

Photoemissivity near a chiral critical point within the quark-meson model

Dissertation
zur Erlangung des wissenschaftlichen Grades
Doctor rerum naturalium

vorgelegt von

Falk Wunderlich
geboren am 24.03.1987 in Dresden

Institut für Theoretische Physik
Fakultät Mathematik und Naturwissenschaften
der Technischen Universität Dresden
2017

Eingereicht am 24.07.2017

1. Gutachter: Prof. Dr. B. Kämpfer
2. Gutachter: Prof. Dr. D. Stöckinger
3. Gutachter: Prof. Dr. B. Friman

Verteidigt am 02.11.2017

Kurzdarstellung

Das Zusammenspiel der thermodynamischen Eigenschaften von stark wechselwirkender Materie und deren Emission von Photonen wird untersucht. Dazu wird die Lagrange-dichte des Quark-Meson-Modells (auch: Linear-Sigma-Modell oder Linear-Sigma-Modell mit Quarks) um einen elektromagnetischen Sektor erweitert. Aus der so erweiterten Lagrange-dichte werden auf konsistente Weise sowohl das großkanonische Potential als auch das erzeugende Funktional der Korrelationsfunktionen ermittelt. Aus ersterem werden die Phasenstruktur des Modells sowie zahlreiche thermodynamische Eigenschaften berechnet. Insbesondere wird die Abhängigkeit einiger Orientierungspunkte (kritischer Punkt, Schnittpunkte der Phasengrenze mit den Koordinatenachsen usw.) des Phasendiagramms von den Modellparametern detailliert untersucht.

Mit Hilfe des erzeugenden Funktionals wiederum kann der Photonenpropagator bestimmt werden, dessen Imaginärteil mit der Emissionsrate von Photonen zusammenhängt. Die führende Ordnung in einer Entwicklung nach der Anzahl der beteiligten Teilchen und der Potenz der Quark-Meson-Kopplung lässt sich durch Baumgraphen-Diagramme darstellen, die ebenfalls berechnet werden. Auf dieser Basis wird die Photon-Emissivität in Abhängigkeit von Temperatur, chemischem Potential und Photon-Frequenz berechnet und unter verschiedenen Gesichtspunkten analysiert.

Die Abhängigkeit der Teilchenmassen von Temperatur und chemischem Potential hinterlässt teilweise ausgeprägte Signaturen in den Emissivitäten der einzelnen sub-Prozesse. Insbesondere ein Phasenübergang erster Ordnung zeigt sich deutlich, da an diesem die Emissivität – abhängig von der Temperatur – um einen Faktor der Größenordnung zehn springen kann. Jedoch finden wir im Rahmen dieser Analyse keine spezifischen Signaturen in den Photonen-Emissivitäten, die einen kritischen Punkt auszeichnen. Des Weiteren wird untersucht von welchen Parametern die Photonen-Emissionsrate in den Bereichen niedriger oder hoher Photonen-Frequenzen abhängt. Mit diesen Ergebnissen kann das Verhalten der Emissivität in Abhängigkeit von Temperatur und chemischem Potential gut verstanden und zahlreiche Auffälligkeiten in den Emissivitäten erklärt werden.

Abstract

The interplay of thermodynamic properties of strongly interacting matter and its emission of photons is investigated. For this purpose the Lagrangian of the quark meson model (in the literature also dubbed “linear sigma model” or “linear sigma model with quarks”) is extended by an electromagnetic sector. Based on this extended Lagrangian both the grand-canonical potential and the generating functional of correlation functions are calculated in a consistent manner. From the former, the phase structure and various thermodynamical properties are determined. Especially, the dependence of certain landmarks (critical point, intersections of the phase boundary with the coordinate axes, *etc.*) of the phase diagram with respect to the model parameters is investigated in detail.

With the help of the generating functional in turn, the photon propagator can be computed whose imaginary part is connected to the emission rate of photons. The leading order of the result with respect to the number of participating particles and the power of the quark-meson coupling is expressed in terms of tree level diagrams, which are calculated likewise. On this basis, the photon emissivity with respect to temperature, chemical potential and photon frequency is calculated and analyzed addressing various questions.

The dependence of the particle masses with respect to temperature and chemical potential leaves notable imprints on the emissivities of the individual production processes. Especially a first-order phase transition can easily be identified, since, there, the emissivity may jump – depending on the temperature – by a factor of about ten. Contrarily, within our analysis, we do not find signatures in the photon emissivities that specifically mark a critical end point. Moreover, it is investigated on which parameters the photon emission rate depends in the low- and high-frequency regions. With these results the behavior of the emissivity with respect to temperature and chemical potential can be understood and many peculiarities of the emissivities can be explained.

Contents

1. Introduction	1
1.1. Quantum Chromodynamics	3
1.2. Effective models	6
1.3. Heavy-ion collisions	7
1.4. Electromagnetic probes	11
1.5. Structure of this work	14
1.6. List of related publications	15
2. The quark-meson model	17
2.1. Model definition	17
2.2. Symmetry breaking pattern of the QMM in the chiral limit	18
2.2.1. Chiral symmetry of QCD	18
2.2.2. Symmetries of the QMM Lagrangian	20
2.2.3. Conserved currents	23
2.2.4. Spontaneous symmetry breaking	24
2.2.5. Explicit symmetry breaking	24
2.3. Parameter fixings	25
2.4. Relation to other effective models	28
2.4.1. Extensions of the QMM	28
2.4.2. Other effective models	28
2.5. Advantages of the QMM	30
3. Basic definitions	31
3.1. The McLERRAN-TOIMELA formula	31
3.2. Path integrals	32
3.2.1. Path integral representation of the partition function	32
3.2.2. Path integral representation of the generating functional	33
3.2.3. Path integrals for quadratic action	34

3.3.	Calculating correlation functions in the path integral framework	35
3.3.1.	Correlation functions	35
3.3.2.	Partition function and generating functional	36
4.	Derivation of the photon rate formula	37
4.1.	Model definition	37
4.2.	Calculating the generating functional	38
4.2.1.	Integrating out the photons	39
4.2.2.	Integrating out the fermions	40
4.2.3.	Derivative expansion of the fermion trace	40
4.2.4.	Quadratic approximation of the meson potential	41
4.2.5.	Isolating the electromagnetic contribution to V	43
4.2.6.	Integrating out the meson fields	44
4.3.	Calculating the imaginary part of the photon propagator	44
4.3.1.	Calculating the photon propagator	44
4.3.2.	Determining the imaginary part of the photon propagator	46
4.4.	Photon emission rate	49
4.4.1.	Phase space integration	49
4.5.	BOLTZMANN approximation	51
4.5.1.	The Gaussian approximation (a)	52
4.5.2.	The exponential approximation (b)	53
4.6.	DOPPLER shift and center-of-mass photon frequency	53
4.7.	Dynamical enhancement mechanism	56
5.	Thermodynamics of the quark-meson model	59
5.1.	Mean field approximation	60
5.1.1.	Derivation of the grand potential	60
5.1.2.	Renormalization of the vacuum term	63
5.1.3.	Thermodynamic quantities in MFA	64
5.2.	The linearized fluctuation approximation	70
5.2.1.	The partition function in LFA	70
5.2.2.	Thermodynamics – standard set of parameters	71
5.2.3.	The sigma mass parameter and the CEP	77
5.3.	Sensitivity with respect to model parameters	79
5.3.1.	Phase contour	79
5.3.2.	Critical end point	81
5.3.3.	Isentropes	84

5.3.4. Phase transition type	85
5.4. Discussion	86
5.4.1. Phase structure and particle masses	86
5.4.2. Thermodynamic quantities	90
5.4.3. Impact of vacuum fluctuations	91
5.4.4. Impact of thermal fluctuations	92
5.4.5. Parameter dependence	92
6. Photon emission within the quark-meson model	95
6.1. Overview	95
6.2. Emissivities for given frequency	100
6.2.1. Low-frequency rates	100
6.2.2. High-frequency rates	103
6.2.3. Rates and masses	103
6.2.4. Cross sections	106
6.2.5. Dynamical enhancement	108
6.2.6. Chiral restoration	110
6.3. Differential spectra	112
6.3.1. Chiral symmetry breaking effects on the spectra	112
6.3.2. Emissivity and phase transition type	113
6.3.3. Spectra in view of adiabatic expansion	113
6.4. Static enhancement	116
6.5. Summarizing the findings	119
6.6. Discussion of the emissivities	120
7. Summary and outlook	127
7.1. Thermodynamics	127
7.2. Photon emission	129
7.3. Outlook and suggested future projects	132
A. Conventions and acronyms	135
A.1. Units	135
A.2. Conventions	135
A.3. Acronyms and shortcuts	136
B. Useful identities	141
B.1. Functional calculus	141
B.1.1. Continuum limit	141

B.1.2. FOURIER transform	142
B.1.3. Functional traces	143
B.2. Epsilon contraction formulas	144
B.3. PAULI matrices	145
B.4. DIRAC matrices	145
B.4.1. Definition and properties of γ^5	145
B.4.2. Trace formulas	145
B.5. Kinematics of two-particle scatterings	147
B.5.1. Energies and momenta in the center-of-mass system	147
B.5.2. Limits for the MANDELSTAM variables	148
B.5.3. Cross section	150
C. Calculation of the fermion determinant	153
C.1. Derivative expansion	153
C.1.1. Leading order	153
C.1.2. First-order correction	155
D. Inverting perturbed matrices	159
E. Thermodynamic formulas in LFA	161
F. Matrix elements	163
F.1. FEYNMAN rules	163
F.2. COMPTON scattering with sigma mesons	163
F.3. COMPTON scattering with pions	167
F.4. Annihilations and anti-COMPTON	170
G. Comments on the photon production formulas	173
G.1. The MCLERRAN-TOIMELA formula	173
G.2. The optical theorem	175
H. Phase space integration	177
H.1. Solving the integrals	177
H.2. Limits of the ν integration	182
H.3. Simplifying the denominator	183
H.4. The rate formula	185
I. Approximations of the rate formulas	187
I.1. BOLTZMANN approximation	187

I.2. Approximations for the s integration	188
I.2.1. Case (a), the Gaussian approximation	189
I.2.2. Case (b), the exponential approximation	190

1. Introduction

To our present knowledge all¹ physical phenomena at the experimentally accessible energy or length scales can be traced back to four fundamental forces and their respective interplay. These forces are gravity, the electromagnetic force, as well as the weak and the strong (nuclear) forces. While gravity is best described with a classical theory – the general theory of relativity –, the theories for the remaining three forces are formulated as quantum field theories. This difference in description reflects the different realms in which they are “living”: Except for space-time regions with extreme curvatures, such as the neighborhood of black holes, gravity is a comparatively weak force for elementary particles, *e.g.* the electromagnetic force between two protons is about 10^{36} times stronger, rendering gravity a negligible effect for earth bound particle physics. Nonetheless, in many astrophysical contexts, such as the HAWKING radiation from black holes [Haw75], stability of neutron stars [SK09, Lat12] or the dynamics of the early universe [She80, KKM05] gravity plays an essential or even dominant role. The remaining interactions are combined into one theory, the Standard Model of particle physics [PS95, CG07, O⁺14]. The fundamental statement of the Standard Model is that – besides the POINCARÉ symmetry of the (flat) MINKOWSKI space-time – the microscopic world is invariant under a set of continuous internal local symmetries forming (mathematically) a group of symmetry transformations, which can be decomposed into three fundamental subgroups. Parallel to the decomposition of the internal symmetry group into fundamental subgroups, the Standard Model can be decomposed into three sectors corresponding to the respective subgroups. The sector corresponding to the largest of these subgroups is responsible for the strong nuclear force and the respective projection of the Standard Model onto this sector is called Quantum Chromodynamics (QCD) – the theory of the strong interaction. In the remaining (electroweak) sectors, there is a complication, namely the symmetry apparently present at high energies ($\gtrsim 100$ GeV) cannot be observed at low energies. Within the Standard Model, this phe-

¹ Probably except dark matter and dark energy, which might or might not be understood within this theoretical framework.

nomenon is explained via the HIGGS mechanism, according to which a weakly² interacting scalar field acquires a non-vanishing vacuum expectation which breaks the gauge symmetry of the electroweak sector down to that of electromagnetism. The projection of the Standard Model onto this remaining gauge symmetry is called Quantum Electrodynamics (QED).³ Besides breaking the electroweak symmetry, the HIGGS mechanism introduces mass terms for the elementary particles. We will discuss implications of this issue below. Apart from the gauge symmetries there are further (global) symmetries present in the various sectors of the Standard Model. In the QCD sector, a particularly important symmetry is the (approximate) flavor symmetry in the light quark sector. This symmetry – the “chiral symmetry” – is spontaneously broken both in vacuum and at temperatures $\lesssim 150$ MeV and baryo-chemical potentials $\lesssim 1$ GeV. Currently, a lot of effort is put into the exploration of the phase diagram both experimentally and theoretically. In Fig. 1.1, a sketch of the QCD phase diagram is shown. Only two features of this phase diagram are well established: these are (i) the crossover transition at small baryo-chemical potential (from lattice QCD calculation, see below) and (ii) the nuclear liquid-gas transition (from nuclear physics). Not shown is the deconfinement transition (*cf.* Section 1.1) which seems to coincide with the chiral transition at small baryo-chemical potential. However, at finite baryo-chemical potential both transitions might separate. Furthermore, at large baryo-chemical potential and small temperatures, perturbative QCD reveals that there are several color superconducting phases. Other peculiarities of the phase diagram such as a first-order phase transition (FOPT in Fig. 1.1) ending at a critical end point (CEP) or further phases might or might not be present. It is thus an important theoretical task to work out signatures for these possible features of the phase diagram that might show up in experiments.

In the corresponding experiments, nuclei are brought to collision creating a region of highly compressed strongly interacting matter that rapidly expands and eventually fragments into a large number of (mostly unstable) hadrons. However, a minor portion of the produced particles is not strongly interacting, but solely couples electromagnetically to the medium. These electromagnetic probes provide valuable information about the hot interior of the expanding strongly interacting medium. This work combines both the chiral phase transition and the emission of photons, both based on the same model and a common approximation scheme. It is primarily aimed at digging out the connection between the chiral phase

² “weak” is here not referring to the strength of the interaction, but to one of the fundamental forces (the weak nuclear force).

³ Several authors use the term QED only for the theory of electrons and photons. Here, this term is used to describe the theory corresponding to the residual gauge symmetry at energy scales at which the electroweak symmetry in the Standard Model is broken via the HIGGS mechanism. With the term ‘weak interaction’ we refer to the effective interactions corresponding to the broken symmetries.

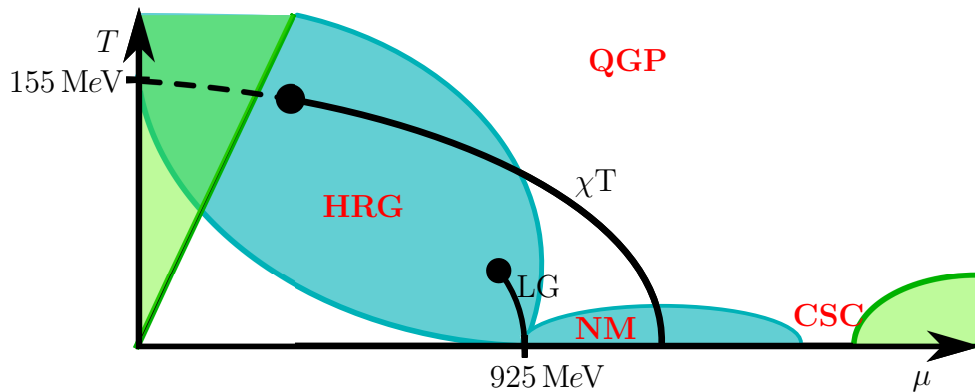


Figure 1.1.: Sketch of the QCD phase diagram. The black dashed curve marks the crossover between the QGP and the hadronic phase (denoted by HRG), and the black solid curves represent first-order phase transitions ending in critical end points (dots). The lower short solid curve depicts the nuclear liquid-gas transition (LG), while the upper curve resembles the chiral transition (χT) which might be partially first-order. The green triangle marks the region that is accessible with ℓ QCD and the green region on the right denotes the region where perturbation theory is applicable. The experimentally accessible regions are highlighted in blue. The large blue “leaf” is accessible in accelerator experiments and the small one via neutron star observations and low energy nuclear physics experiments. The labels NM and CSC denote the regions, where nuclear matter and color superconductivity can be found, both in a variety of different phases.

transition and the emission of photons and addresses the question whether and to what extent peculiarities of the phase diagram, such as a CEP or a curve of first-order phase transitions, affect the production of photons.

The remainder of this introductory chapter is intended to give an overview over recent developments and basic facts about topics related to this work to help properly put it into the context of the research on the strong interaction and hadron physics. At the end of this chapter the structure of this thesis is outlined and the publications on which the presented material is based are listed.

1.1. Quantum Chromodynamics

The strong nuclear interaction governs the physics of nuclear matter. It binds the fundamental degrees of freedom – quarks and gluons – to the large variety of mesons and baryons or their excitations – often called resonances – observed in high energy experiments [O⁺14] and thus makes QCD one of the corner stones in our understanding of particle physics.

The QCD Lagrangian at the classical level reads

$$\mathcal{L}_{\text{QCD}}^{\text{cl}} = \sum_f \bar{\psi}_f (i\gamma^\mu D_\mu - m_f \mathbb{1}) \psi^f - \frac{1}{4} G_{\mu\nu}^a G_a^{\mu\nu}, \quad (1.1.1)$$

with ψ_f denoting the quark field with flavor $f \in \{u, d, s, c, b, t\}$, m_f being the (current) mass of the quarks with flavor f , $D_\mu = \partial_\mu - ig\lambda^a A_\mu^a$ with the GELL-MANN matrices λ^a and the gluon vector potential A_μ^a being the covariant derivative, and $G_{\mu\nu}^a = \partial_\mu A_\nu^a - \partial_\nu A_\mu^a + if_{abc} A_\mu^b A_\nu^c$ being the field strength tensor with the structure constants f_{abc} of the gauge group $SU(3)$. The quark fields ψ^f themselves are elements of a three dimensional internal vector space with the associated degree of freedom called 'color'. However, for ease of notation the color index is suppressed in (1.1.1).

Despite its compact form the evaluation of observables in the low-energy regime is notoriously difficult. The reason is the energy dependence of the renormalized coupling strength g which is decreasing for increasing energy scales. In the limit of infinitely large energy scales the coupling gets arbitrarily small leading to free (*i.e.* non-interacting) theory of quarks and gluons – a phenomenon called asymptotic freedom. Conversely, at low energies the interaction strength becomes large and thus makes a naive perturbative expansion in the coupling strength impossible. The energy scale at which this happens is called Λ_{QCD} – the immanent energy scale of QCD being of $\mathcal{O}(200 \text{ MeV})$. Below this energy scale, the interaction becomes so strong that it binds all (color-)charged particles into color singlet states. QCD at low energies is therefore effectively a theory of color-singlet bound states which can be classified by their spin into baryons (half-integer spin, fermions) and mesons (integer spin, bosons). The effective degrees of freedom thus transform trivially under the gauge symmetry hiding it effectively from observation.

At energy scales much larger than Λ_{QCD} , a perturbative (in the coupling g) treatment of QCD is possible. However, naive summation of Feynman diagrams up to a given loop order may yield gauge dependent results (*e.g.* the imaginary part of the gluon self energy [EHKT88, CHYZ89]). This can be traced back to the thermal masses of the quarks and gluons which – being proportional to g – make different loop orders contributing parametrically to the same order in the strong coupling expansion [BP90]. Such effects can be accounted for by classifying the external momenta p_{ext} as soft ($p_{\text{ext}} \sim gT$) and hard ($p_{\text{ext}} \sim T$) and identifying the subclass of all loop diagrams which lead to a correction of $\mathcal{O}(g^2 T^2 / p_{\text{ext}}^2)$. If all external momenta are soft, these diagrams (the authors of [BP90] termed them 'hard thermal loops') are of the same order as the tree-level amplitude and have to be evaluated exactly and resummed in order to get a result which includes all de-

dependencies on the coupling strength up to a given power of g .⁴ This resummation scheme is dubbed hard thermal loop (HTL) resummation and can successfully be applied for solving most of the above mentioned problems with naive perturbation theory (*e.g.* making the propagators gauge independent, as they should) [BP90, BI02]. Other problems are unsolved and can only be avoided for sufficiently weak couplings. Furthermore, it has been shown that the pressure of a strongly interacting medium composed of quarks and gluons cannot be calculated in perturbation theory beyond $\mathcal{O}(g^6 \ln g)$ [Lin80].⁵ Nevertheless, one may state that at high enough temperatures perturbation theory is applicable to QCD and analytical results for various quantities can be obtained.

Similar considerations apply to very high densities, because small distances (or equivalently high densities) correspond, after FOURIER transformation, to large momenta for which the above considerations apply. The analog to the HTL approximation and resummation scheme is termed hard dense loop (HDL) scheme. One of the most remarkable results at low temperature and very high densities which rigorously can be derived from QCD in such a perturbative approach is the occurrence of a so called color-flavor-locked (CFL) phase. In this phase the $SU(3)$ gauge symmetry of QCD and its approximate $SU(3)_V$ flavor symmetry form a combined symmetry under which pairs of quarks (“COOPER pairs”, analog to the COOPER pairs in the BCS theory of superconductivity) are invariant.⁶ Analogous to superconductivity the appearance of COOPER pairs is accompanied by a gap in the excitation spectrum with similar effects as superconductivity in solid state physics, such as the expulsion of the gauge field modes from the superconductor (MEISSNER effect). Nuclear matter in this phase is therefore called a color superconductor although transferring the concept of conductivity to color degrees of freedom has some conceptual difficulties (*cf.* [Sch03, ASRS08] for a comprehensive discussion of this issue).

At vanishing net baryon densities and – in principle – arbitrary temperatures QCD can be solved on a finite grid of space-time points. To achieve this one constructs a numerical approximation to the path integral representation of the QCD partition function. Fermionic fields can be analytically integrated out yielding real functional determinants depending on the gluon configurations. At vanishing chemical potential the integrand of the gluon

4 Since any observables within QCD is gauge invariant, all expansion coefficients of such an observable *w.r.t.* g cannot depend on the gauge, either. If therefore an observable is calculated such that all (explicit and implicit) dependencies on g up to a given order are included, the result is gauge independent.

5 This is a genuine non-perturbative (even in the limit of small couplings) aspect of QCD, which can be traced back to ‘super-soft’ magnetic modes $p \sim g^2 T$ and moreover cannot be avoided with standard resummation techniques. For details, see [FHK⁺11] and references therein.

6 Because of the multitude of possible quark pairs (three colors, three light flavors and two chiralities for each partner) there are many different possible color superconducting phases. On general grounds however, it can be shown that in the limit of infinite density the CFL phase is favored.

path integral is a positive definite function of the gluon configuration and can thus be interpreted as a probability distribution⁷ for these configurations. The partition function is afterwards calculated using MONTE-CARLO approaches. Such an approach to the QCD thermodynamics is referred to under the name of lattice QCD (ℓ QCD). The computational costs of such a calculation strongly scale with the number of grid points and the inverse fermion masses. State of the art grids are therefore still restricted to grid sizes of $N_\tau \times N_x = 4 \dots 8 \times 64 \dots 256$, with N_τ being the number of grid points in imaginary temporal direction and N_x being that in spatial direction. To improve convergence the action is typically supplemented with terms vanishing in the continuum limit and suppressing discretization errors. Also the handling of fermionic degrees of freedom is quite nontrivial. However, nowadays ℓ QCD calculations agree for many important quantities, *e.g.* the order (crossover) and temperature ($T_c = 154 \pm 8 \text{ MeV}$) of the confinement/deconfinement and chiral transition at vanishing net baryon density [AFKS06, B⁺12].

Analyzing generalized susceptibilities the field content in the respective temperature regions can be derived [DKM15] confirming from first principles the picture of a strongly interacting liquid of quarks and gluons (with some admixture from quarkonia and other hadrons) above the crossover temperature and a gas of hadrons below it. For other quantities, *e.g.* the slope of the crossover temperature *w.r.t.* baryo-chemical potential μ_B , no final conclusion can be drawn with present data.

At finite net densities present standard methods of ℓ QCD fail, since for non-vanishing baryo-chemical potential the fermion determinants receive nonzero imaginary parts inhibiting the interpretation of the integrand of the path integral representation of the partition function as probability distribution. Several techniques have been developed to overcome this obstacle, *e.g.* reweighting [FK02], Taylor expansion in μ_B [KKL⁺11], analytic continuation from imaginary μ_B [dFP02], or density of state methods [FKS07], all of which apply only for sufficiently small μ_B/T ratio. With the present data one tentatively may state that the crossover region seems to stretch at least to $\mu_B/T \sim 2$ [DKM15].

1.2. Effective models

At finite net densities no first principle methods are at hand to evaluate observables of QCD thermodynamics. In order to still capture essential features of QCD thermodynamics at finite net densities a number of different methods is applied besides lattice QCD calculations (*cf.* Section 1.1), which are limited to the proximity of the temperature axis.

⁷ after proper normalization

The most popular of these are the evaluation of DYSON-SCHWINGER equations (DSEs) [RW94, AvS01, Fis06] and the application of the CORNWALL-JACKIW-TOMBOULIS (CJT) formalism [CJT74].

Less rigorously connected to QCD are effective models which are constructed in line with symmetries of QCD present at low energies. Because of confinement the relevant degrees of freedom in this regime are color singlets making the gauge symmetry trivially fulfilled. Therefore effective models are primarily constrained by the LORENTZ symmetry as well as the global symmetries of QCD, especially the (approximate) chiral symmetry. Besides the correct global symmetries the field content of such models has to parallel that of low-energy QCD.

The most important contribution at small baryo-chemical potential comes naturally from the lightest mesons of QCD. In the light sector, these are the pion and, if additionally including the strange sector into the consideration, also the kaons and the eta. The effective models modeling the breaking of chiral symmetry include these fields as pseudo-GOLDSTONE modes of the broken symmetry. As the low-energy physics of QCD are governed by dynamics and interactions of these pseudo-GOLDSTONE modes, which in turn are determined by the pattern of symmetry breaking, the effective models constructed on the basis of these patterns are expected to give reasonable results. This changes at energy scales comparable to the mass of the next mesonic states, from which the probably most important one is the rho meson with a vacuum mass of $m_\rho = 775 \text{ MeV}$ [O⁺14]. More details concerning the pattern of chiral symmetry breaking, with special emphasis on the quark-meson model, are given in Chapter 2.

1.3. Heavy-ion collisions

In collider experiments as they are conducted at the large hadron collider (LHC) at CERN, Geneva, Switzerland and the relativistic heavy-ion collider (RHIC) at BNL, Long Island, New York, USA or former fixed-target experiments at the super proton synchrotron (SPS) at CERN as well as the alternate gradient synchrotron (AGS) at BNL and planned in the future facility for anti-proton and ion research (FAIR) at GSI, Darmstadt, Germany, the nuclotron-based ion collider facility (NICA) at JINR, Dubna, Russia, and with the heavy-ion program at the Japan proton accelerator research complex (J-PARC), Tōkai, Japan, the nuclei of heavy elements are brought to collision at relativistic energies.

The colliding nuclei lose a part of their energy due to inelastic collisions. When the beam energy is not too large ($\lesssim 10 \text{ GeV}$ for colliders [B⁺01]) the nucleons in the collision zone

(“participants”) get stopped completely resulting in net baryon densities several times the nuclear density. For beam energies much larger, the nuclei partially pass through each other leaving behind a region filled with a large energy density but only small net baryon density, *i.e.* with an almost equal number of particles and antiparticles [A⁺05b, TJGS17]. Evidence for an incomplete stopping was already found at SPS energies (*cf.* [A⁺99b] for measurements at $\sqrt{s_{NN}} = 17.2 \text{ GeV}^8$).

Although the system is initially very far from equilibrium, it quickly thermalizes, *e.g.* at the top RHIC energy ($\sqrt{s_{NN}} = 200 \text{ GeV}$) the equilibration time τ_{eq} is estimated as $\mathcal{O}(0.5 \text{ fm}/c)$ [KBHP16]. After equilibration, the system can be described most easily by local thermodynamical variables, *i.e.* space-time dependent temperature, entropy density, net baryon density, energy density, pressure *etc.*, which obey “almost ideal” hydrodynamical expansion dynamics driven by pressure gradients [RR07, Oll08, Hei09]. In this phase, the dynamics are characterized by collective behavior building up correlations between various observables, *e.g.* elliptic and higher order flow.

When the energy density falls below a certain threshold corresponding to an energy per hadron of about 1 GeV [CR99, CORW06] the average collision energy of the constituent degrees of freedom is too small to allow for conversions between different particle species. Thus the chemical equilibrium cannot be maintained anymore and the ratios of the particle species yields are frozen (hence the name “chemical freeze-out”). Thermal equilibrium can be preserved for some time by elastic collisions between the hadrons until the scattering rate at some density threshold is too small to keep the rapidly expanding system in thermal equilibrium (“kinetic freeze-out”). Afterwards the system can be regarded as free streaming particles that move outward and decay or eventually hit the detectors [Hei09].

Analyzing the particle yields, the temperature and the baryo-chemical potential at the chemical freeze-out can be determined (see *e.g.* [ABMRS11] for LHC data). Comparing various experiments one finds that the chemical freeze-out happens to take place on a universal curve that can be characterized with the simple requirement that the energy per hadron is about 1 GeV, *cf.* [CR99, CORW06]. On this curve, the energy density can be calculated yielding a maximum at freeze-out conditions corresponding to $\sqrt{s_{NN}} \sim 8 \text{ GeV}$ [RC06]. Thus to probe the QCD phase diagram at highest possible baryon densities heavy-ion beams with rather moderate energies are needed. Especially well suited for this task will be the beams produced at the upcoming NICA and FAIR projects which will both work in this energy range [RC16] and have the investigation of the phase diagram and the search for an CEP on their respective agenda.

⁸ $\sqrt{s_{NN}}$ is the energy per colliding nucleon pair in the center-of-mass frame.

Scanning through the center-of-mass energies per colliding nucleon pair $\sqrt{s_{NN}}$ the maximally achieved net baryon densities first rise (until $\sqrt{s_{NN}} \approx 10$ GeV [A⁺99b, B⁺01, TJGS17]) and then fall due to the finite stopping power of the nuclei. At high energies, most of the nucleons leave the collision zone and leaving behind a region with high energy density but small net baryon density. Thus by scanning the beam energy, as done *e.g.* in the beam energy scan project at RHIC [Das15, McD15, Sol14, A⁺14a, A⁺13, A⁺14c, A⁺14b, A⁺12a, A⁺12b], different regions of the QCD phase diagram are probed in heavy-ion collisions (HICs). Another adjustable parameter is the system size which can be controlled by the choice of the nuclei brought to collision as well as by the choice of the centrality class of the analyzed ensemble of collisions [Gaz08].

Generally speaking one looks in such scans for the non-monotonous behavior of certain observables. Of particular interest are observables, which can be related to fluctuations of conserved quantities, such as net baryon density, electric charge or strangeness [AHM00]. Deviations of a conserved quantity from its equilibrium value vanish only due to transport processes, which are comparatively slow. Thus, traces of certain peculiarities of the distribution of conserved quantities are expected to survive the hydrodynamical evolution and show up in the detectors [SRS99]. Besides the enhancement of fluctuations at a CEP, which is present even in equilibrium, the phenomenon of critical slowing down introduces deviations from equilibrium that might survive the subsequent hydrodynamical evolution. These distributions are often parametrized by their central moments, which usually are combined to volume independent ratios, such as the scaled variance, the skewness and the kurtosis [VAGP15]. A lot of effort has been put, both theoretically [SFR11, Fri14, MFR15, K⁺16] and experimentally [And16, A⁺14b, Sol14, LX17], into the evaluation of fluctuations of conserved quantities on an event-by-event basis, since it can be shown that the generalized susceptibilities⁹ are related to the cumulants characterizing the event-by-event distribution of this quantity [Nah16].

The fluctuation measurements of conserved quantities can be supplemented by the measurement of particle ratio fluctuations, such as the fluctuations of p/K , p/π or K/π , however only monotonous and slow variations with the beam energy have been found up to now [A⁺15].

Besides fluctuation-based measures it has been argued that the enhancement of certain transport coefficients, such as the bulk viscosity, leaves characteristic imprints of a CEP in the heavy-ion data [MMY17].

The evolution of the strongly interacting matter produced in a HIC follows approximately

⁹ These are the (dimensionless) derivatives, $\chi_q^{(n)} = T^{n-4} \partial^n p / \partial \mu_q^n$ of the pressure p *w.r.t.* the chemical potential μ_q associated to the respective conserved quantity q .

curves with constant entropy per baryon ratio (isentropes) [RR07, Oll08, Hei09]. In [NA05] it is argued that the QCD critical point acts as an attractor for the isentropes (focusing effect). This assumption is used in [ABMN08] to propose the behavior of the \bar{p}/p ratio *w.r.t.* transverse momentum as an observable signaling the QCD CEP. Nonetheless, since the entropy per baryon is not a singular quantity at the CEP, universality arguments are not sufficient for the occurrence of a focusing effect [FHK⁺11]. Studies in the context of the QMM confirm that the focusing effect is not a universal feature, not even within the same universality class [NSS⁺10, WK17]. However, as there are notable differences between the quark hadron phase transition and the QMM transition [SRK14], the possibility of a focusing effect in QCD matter is not ruled out either.

An interesting study based on the STAR data from the beam energy scan project at RHIC and the LHC data finds a non-monotonous behavior of a viscous damping coefficient *w.r.t.* the collision energy [LTJ⁺14]. This might point to a CEP located at quite small baryo-chemical potential. The same conclusion is drawn from two-pion interferometry data and the position of the CEP is suggested to be at $(T^{\text{CEP}}, \mu_b^{\text{CEP}}) = (165 \text{ MeV}, 95 \text{ MeV})$ [Lac15]. However this claim is still controversial because of the scaling relations used for the extraction [ADD16] and because the suggested position is in a region $\mu_B/T < 2$ that is claimed to be accessible with various extrapolation schemes from lattice QCD, which however find no CEP in this region [DKM15].

The CEP search at the SHINE experiment at the SPS, which operates in a fixed target mode (contrary to the beam energy scan at RHIC using collider setups), has not been successful so far. In addition to scanning through beam energies also the type of the colliding nuclei is varied at SHINE. (Presently, p-p, Be-Be and Ar-Sc have been studied at all available beam energies and Xe-La and Pb-Pb as well as the remaining beam energies in the p-Pb system will be studied in the near future.) This makes studies of different system sizes possible without changing the centrality class. Thereby it introduces another promising dimension to the phase diagram studies. Besides studying deconfinement signatures as the “kink”, “horn” and “step” structures – already found by the NA49 collaboration in Pb-Pb collisions [A⁺08c] – also fluctuation measures are studied. As the system volume fluctuates on an event-by-event basis intensive quantities such as the scaled variance of a suitably chosen observable are of special interest. Furthermore, to avoid uncertainties introduced by volume fluctuations, so-called “strongly intensive” quantities are needed. However, the investigation of two of such quantities in the SHINE data yields no clear CEP signature [And16].

In summary, it can be stated that no unambiguous signals for a CEP have been detected up to now, which makes the upcoming NICA and FAIR projects especially exciting and

the task of working out further connections between observable quantities and the phase structure particularly important.

1.4. Electromagnetic probes

By far the most particles produced in a HIC are strongly interacting. Due to their numerous scatterings their (momentum-) distributions are similar to the corresponding equilibrium distributions. The detector signal therefore corresponds to the freeze-out conditions and can especially be analyzed by means of collective phenomena, such as elliptic and higher order flow. Electromagnetic probes, such as photons and (di-)leptons, are produced much less frequently but reach, due to their weak interaction with the surrounding medium, the detector almost unperturbed thus carrying information about the conditions under which they were produced to the detectors. This makes electromagnetic probes a valuable tool for the investigation of the hot and dense interior of the fireball produced in a HIC.

On the other hand the detector signal is a superposition of photons or dileptons coming from every step of the collision: from binary parton collisions, from the locally equilibrated stage, and from final state decays, which makes the extraction of the encoded information a rather complicated task.

The total photon rates (“inclusive photon rates”) are subdivided into rates from decays of long lived (on the strong interaction scale) mesons (“decay photons”) and the rest (“direct photons”), the latter ones being furthermore divided into photons from the stage before local thermal equilibration (“non-thermal” or “primordial” photons) and photons emitted after (“thermal photons”).

At small transverse momentum p_T , the photon spectra are dominated by decay photons mostly from pions and η -mesons, while at high p_T ($\gtrsim 6 \text{ GeV}$) photons from the initial hard processes contribute significantly to the total photon rate. Experimentally these are deduced from the photon transverse momentum spectra measured in proton-proton collisions [A⁺10b, Rey05] and can theoretically be well described with perturbative QCD (pQCD) calculations [vHGR11]. The region between 1 GeV and 3 GeV is presumably best suited for the detection of thermal photons from the QGP phase [TRG04].

The central idea behind the investigation of electromagnetic probes from HICs is that the matter emitting them leaves characteristic imprints in the spectra. A typical example is provided by the peaks in the dilepton invariant mass spectra at the positions of the vector meson masses from which masses and decay widths of these mesons can be deduced. Furthermore, also their modification in nuclear matter, *e.g.* by comparison of these spectra

for proton-proton and nucleus-nucleus collisions, can be studied giving valuable input for theoretical considerations [Fri96, FP97, A⁺08a].

Another illustrative example is the search for a thermal component in the dimuon transverse mass spectra. In the intermediate (transverse) mass range $m_T = 1 - 3 \text{ GeV}$, the spectra obtained from proton-proton collisions can well be described by a mixture of DRELLYAN processes and decays of correlated D and \bar{D} mesons as well as a background contribution from pion and kaon decays [A⁺00a]. In Indium-Indium interactions performed at the SPS at $\sqrt{s_{NN}} = 158 \text{ GeV}$, however, an excess of dimuons with $p_T = 1 - 3 \text{ GeV}$ was found that could not be explained by decays. The spectral slope of these excess dimuons is related to the average temperature of the emitting medium which was analyzed to be $T_{\text{eff}} \sim 190 \text{ MeV}$ and thus above the pseudocritical temperature $T_c \sim 160 \text{ MeV}$, signaling that this emission comes from the QGP phase [A⁺09a].

Since their penetrating nature provides a tool for the investigation of the interior of the fireball created in a HIC, electromagnetic probes have been studied in a large number of heavy-ion experiments. At the BEVALAC at LBL, Berkeley, USA, the DLS experiment [P⁺97] was the first experimental set-up for systematically measuring dilepton (dielectron) production in nucleus-nucleus collisions at relatively low (a few GeV per nucleon) center-of-mass energy. The excess of the dielectron yields in the low-invariant-mass region was notoriously difficult to model leading to the designation “DLS puzzle”. The investigations at low beam energies were followed up by HADES experiment [A⁺08b] at the heavy-ion synchrotron SIS18 (“SchwerIonenSynchrotron”) at GSI, Darmstadt, Germany. At higher center-of-mass energies, $\sqrt{s_{NN}} \sim 10 \text{ GeV}$, dielectron measurements were done by the CERES experiment [A⁺98, A⁺03, A⁺05a] at the SPS and later by the PHENIX [A⁺10a] experiment at RHIC. Dimuons were studied with the HELIOS-3 [A⁺00c] as well as the NA38 [L⁺94], NA50 [A⁺00a], and NA60 [A⁺09a, A⁺09b] experiments at the SPS in detail.

The first measurements of direct photons produced in a HIC were done by the CERES [B⁺96] and the WA80 collaborations [A⁺96], both of which were only able to give upper limits, mostly due to systematic uncertainties. The first successful observation of direct photons was reported by the WA98 collaboration [A⁺00b] for central Pb-Pb collisions at transverse momentum $p_T > 1.5 \text{ GeV}$, however, still only at the $1 - 2\sigma$ confidence level. With PHENIX [A⁺12d, A⁺12c] the search for direct photons was carried on at much larger center-of-mass energies with the measurement of direct-photon collective flow being particularly interesting as it is surprisingly large (see below).

In the future, electromagnetic probes will be studied with the CBM experiment [Heu11, Hö14] (dileptons and direct photons) at the new accelerator complex FAIR as well as with the multi purpose detector (MPD) at the NICA accelerator complex [Mus11] (dielectrons),

both measuring in the region of the conjectured CEP of QCD matter. This discussion of electromagnetic probes in heavy-ion experiments is – of course – not complete. For a comprehensive review on this issue, see [Tse10] and references therein.

Interestingly the elliptic flow¹⁰ v_2 of direct photons is comparable to the one of pions at transverse momenta $p_T < 3 \text{ GeV}$ [A⁺12c]. This points to late emission times when a momentum asymmetry for the pions has built up due to anisotropic pressure gradients in the hydrodynamical stage of the HIC. However, the photon low- p_T spectra suggest relatively high emission temperatures which are present only at early stages of the hydrodynamical evolution [RvHH14, GHJ⁺15]. This discrepancy might be resolved either by a “pseudocritical enhancement” due to the time-evolution of the co-moving volume [vHHR15], different equilibration times for the gluons and the quarks leading to a transient stage of the evolution that is dominated by gluons with quarks being produced with some proper time delay [VKG⁺16, VGS⁺16], or by blue-shifted emission from the hadronic phase, which nevertheless must be supplemented by tuning several evolution and emission parameters to achieve hadron dominance in photon emission rates [vHGR11]. Also a strong asymmetric magnetic background field (such as the magnetic field of the colliding nuclei) might lead to a strong asymmetry of the photon production at early emission times. Other explanations point to synchrotron radiation effects from quarks at the surface of the QGP [GSZ13].

Besides the above mentioned pion and η decays, a large variety of channels has been found to contribute to the photon yields in HICs. In the hadronic phase, these are decay channels, such as the decays of π , η and η' , or those of the vector mesons ρ , ω and ϕ , meson-meson, or meson-baryon bremsstrahlung and pion-pion or pion-rho scattering. From the QGP, photons are emitted in COMPTON and quark annihilation processes [LBC15]. In the case of a hot hadronic gas, π/ρ - K scattering contributes with similar strength as π/ρ - π scattering for temperatures of about 200 MeV [TRG04]. However, for the rapid expansion dynamics of HICs strange channels contribute less than the light flavor channels [BB10b]. In the QGP phase, the emissivity originates to a large extent from COMPTON and $2 \rightarrow 2$ annihilation processes with the quarks acquiring a thermal mass $\propto gT$ that can be accounted for within the HTL resummation scheme [KLS91, BNNR92]. Collinear photon emission parametrically enhances certain bremsstrahlung and $3 \rightarrow 2$ annihilation processes, making the corresponding rates comparable to those from the COMPTON and $2 \rightarrow 2$ annihilations [AGKZ98, AGZ00a]. Finally, the interference of multiple scattering processes during the production time of a collinearly emitted photon (relativistic LANDAU-POMERANCHUK-MIGDAL effect) reduces the rate in certain kinematical regions [AMY02]. The complete leading-order results (in the strong coupling g), including all these effects for the QGP, are

¹⁰ This is the second FOURIER coefficient of the azimuthal distribution of a given particle species.

calculated in [AMY01a].

1.5. Structure of this work

The remainder of this thesis is organized as follows: In the next chapter, an overview of the quark meson model is given, including its precise definition and a discussion of the symmetries as well as its relations to various extensions and related models that are discussed in the literature. Afterwards, in Chapter 3, several relations and formulas that are used in the calculations are collected. In Chapter 4, a detailed derivation of the photon production formula is presented as well as the necessary approximations. As an intermediate step the generating functional of correlation functions is calculated. With minor changes the generating functional for correlation functions is transformed into the grand canonical partition function in Chapter 5. Based on this, the thermodynamics of the model as well as the mass parameters of the fields are calculated and presented in detail. Afterwards, in Chapter 6, the photon emissivities are presented and discussed extensively. The main results of this thesis are summarized in Chapter 7.

A large variety of supplementary material is collected in the appendices. In Appendix A, conventions used in this thesis as well as a list of acronyms and shortcuts is given. In Appendix B, a number of useful identities and formulas concerning PAULI and DIRAC matrices as well as functional calculus are collected. The Appendices C, F and H contain rather technical calculations of the derivative expansion of the fermion determinant, the S -matrix elements and the phase space integrals. In Appendix D, a formula is derived for the inversion of perturbed matrices that is used for the derivation of the photon emissivity. In Appendix E, we quote the formulas for the most important thermodynamical quantities derived within the approximation scheme that is applied in this thesis. For completeness, in Appendix G the derivation of a central formula for the photon emission is sketched and its connection to the optical theorem and the unitarity of the S matrix is discussed. In Appendix I, the approximations for the emission rate discussed in Chapter 6 are explained in some detail.

1.6. List of related publications

In the course of elaborating the material for this thesis, the following publications have been written:

- [WK15b] F. Wunderlich and B. Kämpfer,
“Photon emission within the linear sigma model”,
J. Phys. Conf. Ser. **599** (2015), arXiv:1412.7113 [hep-ph]
- [WK15a] F. Wunderlich and B. Kämpfer,
“Photon emission rates near the critical point in linear sigma model”,
PoS **CPOD2014** (2015), arXiv:1502.02857 [hep-ph]
- [WK16] F. Wunderlich and B. Kämpfer,
“Imprints of a critical point on photon emission”,
Eur. Phys. J. **A52** (2016), arXiv:1511.04941 [hep-ph]
- [WYK16] F. Wunderlich, R. Yaresko and B. Kämpfer,
“Arguing on entropic and enthalpic first-order phase transitions in strongly interacting matter”,
J. Mod. Phys. **7** (2016), arXiv:1604.00179 [hep-ph]
- [WK17] F. Wunderlich and B. Kämpfer,
“Photon emissivity in the vicinity of a critical point - A case study within the quark meson model”,
Nucl. Phys. **A959** (2017), arXiv:1611.10139 [hep-ph]

2. The quark-meson model

Due to the high complexity of QCD, several effective models have been put forward aiming at mimicking certain (conjectured) features or at hoping to have suitable approximations or both. Among such models are the so called chiral models with the most prominent examples being the NAMBU-JONA-LASINIO (NJL) model and the quark-meson model (QMM), often also dubbed linear sigma model, both of which can be equipped by a gluonic sector represented by a POLYAKOV loop in order to capture confinement-deconfinement dynamics. As this work does not primarily aim at a realistic description of low-energy QCD, but at the interplay of spontaneous chiral symmetry breaking and photon emission, the underlying chiral model (the QMM) is not supplemented with such a POLYAKOV loop, here.

2.1. Model definition

There are various versions of the QMM available in the literature. Their common feature is a $SU(N_f) \times SU(N_f)$ flavor-symmetric scalar meson potential with a nontrivial degenerated minimum. The QMM was invented in 1960 [GML60] in order to model spontaneous symmetry breaking and restoration. Later, it was extended with a POLYAKOV loop in order to model also the deconfinement transition. In the original version, the field content was simply an isoscalar LORENTZ-scalar field (the σ) and an isovector LORENTZ-pseudoscalar field (the $\vec{\pi}$), which were later identified with the GOLDSTONE bosons of the chiral symmetry breaking, as well as a doublet of fermions interpreted either as quarks or as nucleons, depending on the field of study. The main reason for applying this model to photon emission of strongly interacting matter is that it, on the one hand, is in some sense minimal but still containing both meson as well as quark fields explicitly and, on the other hand, shows spontaneous symmetry breaking.

On the classical level, the model is defined by the Lagrangian

$$\mathcal{L}_{\text{QMM}} = \mathcal{L}_q + \mathcal{L}_{\text{kin},m} - U, \quad (2.1.1)$$

$$\mathcal{L}_q = \bar{q}^c \left(i \not{\partial} - g(\sigma + i\gamma^5 \vec{\tau} \vec{\pi}) \right) q_c, \quad (2.1.2)$$

$$\mathcal{L}_{\text{kin},m} = \frac{1}{2} \partial_\mu \sigma \partial^\mu \sigma + \frac{1}{2} \partial_\mu \vec{\pi} \partial^\mu \vec{\pi}, \quad (2.1.3)$$

$$U(\sigma, \vec{\pi}) = \frac{\lambda}{4} \left(\sigma^2 + \vec{\pi}^2 - \zeta \right)^2 - H\sigma, \quad (2.1.4)$$

with $q_c = (u_c, d_c)^T$ being a flavor doublet and color triplet of fermion fields called quarks,¹ σ being a flavor singlet of scalar fields and $\vec{\pi}$ being a flavor triplet of pseudo-scalar fields called pions. The parameters of the Lagrangian (meson-quark coupling g , four-meson coupling λ , meson bare mass $\lambda\zeta$ and symmetry breaking parameter H) can be expressed by means of the particle masses and the vacuum expectation values, *cf.* Section 2.3. Since the whole Lagrangian is diagonal in color space (label c), this simply leads to a triplication of the fermionic degrees of freedom.

2.2. Symmetry breaking pattern of the QMM in the chiral limit

Before discussing the chiral symmetries of the QMM, it is helpful to take a look at the (approximate) flavor symmetries of QCD.

2.2.1. Chiral symmetry of QCD

In the limit of vanishing quark masses $m_f \rightarrow 0$, the QCD Lagrangian (1.1.1) is invariant under a set of global flavor symmetries. For the right and left handed quarks, the massless flavors can independently be mixed according to unitary flavor transformations. The corresponding symmetry group is $U(N_f)_L \times U(N_f)_R$ with L and R denoting on which chirality (left (L) or right (R) handedness) the unitary flavor transformations act. Conveniently these symmetry transformations can be rewritten in terms of transformations acting independently on vectors (subscript V) and axial vectors (subscript A) as $U(N_f)_A \times U(N_f)_V$. The elements of these groups $A \in U(N_f)_A$ and $V \in U(N_f)_V$ are related to $L \in U(N_f)_L$

¹ The quarks of the QMM differ from the quarks of QCD, although they share some properties. Throughout this thesis the term 'quarks' – if not stated otherwise – refers to the QMM quarks and not those of QCD.

and $R \in U(N_f)_R$ according to $A = L - R$ and $V = L + R$. Furthermore, the unitary groups $U(N_f)$ can be decomposed into $U(1)$ and $SU(N_f)$ subgroups.

Although present at the classical level, quantum effects break the $U(1)_A$ symmetry. This can be interpreted in terms of instantons, which are associated to the tunneling between locally equivalent but topological different vacuum configurations, characterized by a topological charge called the instanton winding number [Wei05b]. Thus, the low-energy quantum theory based on Lagrangian (1.1.1) with N_f massless flavors is invariant under the $U(1)_V \times SU(N_f)_V \times SU(N_f)_A$ global symmetry group [PW84].

This symmetry has a number of important implications. For instance, meson fields which can be transformed into each other by virtue of these transformations – so called chiral partners – necessarily have to possess identical spectral functions, especially the same masses. An example for such a pair of fields are the ρ and the a_1 mesons. Analyzing the decay of τ leptons into a τ -neutrino and n pions, the axial (for n odd) and vector (for n even) spectral functions can be compared yielding clearly different results for both cases [B⁺98a, A⁺99a, S⁺05]. Also other chiral partners exhibit a mass splitting of $\mathcal{O}(100 \text{ MeV})$. It can thus be concluded that at low energies (especially in the ground state) the symmetry is broken to a remnant $U(1)_V \times SU(N_f)_V$ symmetry corresponding to the baryon number conservation (the $U(1)$ part) and the isospin symmetry (the $SU(N_f)$ part). According to the GOLDSTONE theorem, the breaking of the $SU(N_f)_A$ symmetry is accompanied by the appearance of massless modes carrying the same set of quantum numbers as the current corresponding to this symmetry.

This pattern of symmetry breaking is modified by the nonzero quark masses $m_f > 0$. They explicitly break chiral symmetry as they couple left and right handed degrees of freedom. In the up and down quark sector, this symmetry breaking is relatively weak [Wei05b, PS95], since the up and down quark masses are much smaller than the QCD energy scale Λ_{QCD} . In the strange quark sector, the traces of the chiral symmetry are much harder to detect, since – although the strange quark mass is smaller than Λ_{QCD} – both are of the same order of magnitude, which leads to notable distortions of the patterns derived from the assumption of chiral symmetry. In the charm, bottom and top quark sectors, the explicit symmetry breaking is too large for the application of chiral symmetry [PS95, Wei05b]. In the light quark sector (and with a great deal of caution in the strange sector, too), the smallness of the quark masses can be applied to derive relations between various quantities (*e.g.* meson masses, decay widths, effective couplings *etc.*) in terms of a perturbative series. The systematic approach to an effective theory for the set of the lightest mesons, in this spirit, is termed chiral perturbation theory (χ PT). Within χ PT (among other approaches)

a relation between the quark masses and the pion mass can be established:

$$f_\pi^2 m_\pi^2 = \frac{m_u + m_d}{2} \langle \bar{u}u + \bar{d}d \rangle, \quad (2.2.1)$$

with $m_{u,d}$ being the up and down quark current masses, respectively, m_π being the effective pion mass, f_π being the pion decay constant and $\langle \bar{u}u \rangle$ and $\langle \bar{d}d \rangle$ being the up and down quark condensates [GMOR68]. Since the axial part of the chiral symmetry is broken at low temperatures and densities, the axial current A_a^μ is not conserved. The matrix element of its divergence $\langle 0 | \partial_\mu A_a^\mu(x) | \pi^b(p) \rangle$ does not vanish but is proportional to m_π^2 . Besides the trivial factors δ_a^b and $\exp\{ipx\}$, the proportionality constant is the above mentioned f_π [Koc97, Ynd02]. The axial current A_a^μ is also an important quantity in the weak sector of the Standard Model. Because the weak interaction maximally violates parity² (in other words: chiral symmetry, since parity transformations transform left- into right-handed particles and vice versa) the weak decay of the pions can be shown to be proportional to $\langle 0 | \partial_\mu A_a^\mu(x) | \pi^b(p) \rangle$. Hence, although weak and strong interaction are completely independent from each other (to our present knowledge), measuring the weak decay width of the pion gives access to f_π . Evaluating the divergence of the axial current once more, the coupling strength of the pions to nucleons $g_{\pi NN}$ can be related to f_π according to the GOLDBERGER-TREIMANN relation

$$g_{\pi NN} f_\pi = g_a M_N, \quad (2.2.2)$$

with $g_a = 1.25$ being the renormalization constant for the nucleon current measured in the weak neutron decay and M_N being the nucleon mass.

2.2.2. Symmetries of the QMM Lagrangian

Several aspects discussed in the previous section for QCD also apply to the QMM. For simplicity, we first discuss the symmetries of the model in the chiral limit, where they are exact. The content of this section can be found elsewhere in the literature, *e.g.* in [GML60]. However, because of the great importance of the symmetry breaking pattern we collect here some brief calculations and the main results. In the chiral limit, *i.e.* for $H = 0$ in (2.1.4), the Lagrangian of the QMM (2.1.1) – (2.1.4) possesses a global $U(1) \times SU(2) \times SU(2)$ flavor symmetry. This can be seen most easily by considering infinitesimal transformations for

² The symmetry under space inversions $\vec{x} \rightarrow -\vec{x}$.

the fermion fields

$$q \rightarrow q' = (1 + i\epsilon + i\vec{\tau}\vec{\alpha} + i\gamma^5\vec{\tau}\vec{\beta} + \mathcal{O}(\epsilon^2, \alpha^2, \beta^2))q, \quad (2.2.3)$$

$$\bar{q} \rightarrow \bar{q}' = \bar{q}(1 - i\epsilon - i\vec{\tau}\vec{\alpha} + i\gamma^5\vec{\tau}\vec{\beta} + \mathcal{O}(\epsilon^2, \alpha^2, \beta^2)), \quad (2.2.4)$$

with $\epsilon, \alpha^i, \beta^j$, ($i, j \in [1, 2, 3]$) being infinitesimal real numbers. The kinetic term of the fermions (*cf.* (2.1.2)) is invariant under such a transformation:

$$\mathcal{L}_{\text{kin},q} = \bar{q}i\cancel{\partial}q, \quad (2.2.5)$$

$$\mathcal{L}'_{\text{kin},q} = \bar{q}i(1 - i\epsilon - i\vec{\tau}\vec{\alpha} + i\gamma^5\vec{\tau}\vec{\beta})\gamma^\mu\partial_\mu(1 + i\epsilon + i\vec{\tau}\vec{\alpha} + i\gamma^5\vec{\tau}\vec{\beta})q + \mathcal{O}(\epsilon^2, \alpha^2, \beta^2), \quad (2.2.6)$$

$$= \bar{q}i\gamma^\mu\partial_\mu(1 - i\epsilon - i\vec{\tau}\vec{\alpha} - i\gamma^5\vec{\tau}\vec{\beta})(1 + i\epsilon + i\vec{\tau}\vec{\alpha} + i\gamma^5\vec{\tau}\vec{\beta})q + \mathcal{O}(\epsilon^2, \alpha^2, \beta^2), \quad (2.2.7)$$

$$= \bar{q}i\cancel{\partial}(1 + i\epsilon + i\vec{\tau}\vec{\alpha} + i\gamma^5\vec{\tau}\vec{\beta} - i\epsilon - i\vec{\tau}\vec{\alpha} - i\gamma^5\vec{\tau}\vec{\beta})q + \mathcal{O}(\epsilon^2, \alpha^2, \beta^2), \quad (2.2.8)$$

$$= \mathcal{L}_{\text{kin},q} + \mathcal{O}(\epsilon^2, \alpha^2, \beta^2). \quad (2.2.9)$$

The interaction term is more involved. It can remain invariant only if the fermion transformation is accompanied by corresponding meson transformations $\sigma \rightarrow \sigma' = \sigma + \delta_\sigma$ and $\vec{\pi} \rightarrow \vec{\pi}' = \vec{\pi} + \vec{\delta}_\pi$:

$$\mathcal{L}_{\text{int}} = \bar{q}g(\sigma + i\gamma^5\vec{\tau}\vec{\pi})q, \quad (2.2.10)$$

$$\begin{aligned} \mathcal{L}'_{\text{int}} &= \bar{q}(1 - i\epsilon - i\vec{\tau}\vec{\alpha} + i\gamma^5\vec{\tau}\vec{\beta})g(\sigma + \delta_\sigma + i\gamma^5\vec{\tau}(\vec{\pi} + \vec{\delta}_\pi))(1 + i\epsilon + i\vec{\tau}\vec{\alpha} + i\gamma^5\vec{\tau}\vec{\beta})q \\ &+ \mathcal{O}(\epsilon^2, \alpha^2, \beta^2). \end{aligned} \quad (2.2.11)$$

Keeping only linear terms in the infinitesimal quantities $\vec{\alpha}$, $\vec{\beta}$, ϵ , δ_σ and $\vec{\delta}_\pi$ one finds for $\delta\mathcal{L}_{\text{int}} \equiv \mathcal{L}'_{\text{int}} - \mathcal{L}_{\text{int}}$

$$\begin{aligned} \delta\mathcal{L}_{\text{int}} &= g\bar{q}\left(\left(\delta_\sigma + i\gamma^5\vec{\tau}\vec{\delta}_\pi\right) + \left[\left(\sigma + i\gamma^5\vec{\tau}\vec{\pi}\right), i\vec{\tau}\vec{\alpha}\right] + \left\{\left(\sigma + i\gamma^5\vec{\tau}\vec{\pi}\right), i\gamma^5\vec{\tau}\vec{\beta}\right\}\right)q \\ &+ \mathcal{O}(\epsilon^2, \alpha^2, \beta^2), \end{aligned} \quad (2.2.12)$$

$$\begin{aligned} &= g\bar{q}\left(\left(\delta_\sigma + i\gamma^5\vec{\tau}\vec{\delta}_\pi\right) - \gamma^5\left[\vec{\tau}\vec{\pi}, \vec{\tau}\vec{\alpha}\right] + 2\sigma i\gamma^5\vec{\tau}\vec{\beta} - \left\{\vec{\tau}\vec{\pi}, \vec{\tau}\vec{\beta}\right\}\right)q \\ &+ \mathcal{O}(\epsilon^2, \alpha^2, \beta^2), \end{aligned} \quad (2.2.13)$$

where $(\gamma^5)^2 = \mathbb{1}$ as well as the trivial (anti-) commutation relations with scalars were applied. The (anti-) commutation relations of two PAULI matrices, collected in Appen-

dix B, lead to

$$\begin{aligned} \delta\mathcal{L}_{\text{int}} = g\bar{q} & \left(\left(\delta_\sigma + i\gamma^5 \vec{\tau} \vec{\delta}_\pi \right) - i\gamma^5 \epsilon^{ab} \pi_a \alpha_b \tau^c + 2\sigma i\gamma^5 \vec{\tau} \vec{\beta} - 2\pi_a \beta_b \delta^{ab} \mathbb{1} \right) q \\ & + \mathcal{O}(\epsilon^2, \alpha^2, \beta^2). \end{aligned} \quad (2.2.14)$$

Demanding the first order in the infinitesimal quantities to vanish results in

$$\delta_\sigma = 2\pi_a \beta_b \delta^{ab} = 2\vec{\pi} \vec{\beta}, \quad (2.2.15)$$

$$\delta_\pi^c = \epsilon^{abc} \pi_a \alpha_b - 2\sigma \beta^c \Leftrightarrow \vec{\delta}_\pi = \vec{\pi} \times \vec{\alpha} - 2\sigma \vec{\beta}. \quad (2.2.16)$$

The nature of these mesonic transformations can be recognized most easily when written in terms of the 4-dimensional vectors $\phi := (\sigma, \vec{\pi})^T$ and $\delta_\phi := (\delta_\sigma, \vec{\delta}_\pi)^T$:

$$\begin{pmatrix} \delta_\sigma \\ \delta_\pi^1 \\ \delta_\pi^2 \\ \delta_\pi^3 \end{pmatrix} = \begin{pmatrix} 0 & 2\beta_1 & 2\beta_2 & 2\beta_3 \\ -2\beta_1 & 0 & \alpha_3 & -\alpha_2 \\ -2\beta_2 & -\alpha_3 & 0 & \alpha_1 \\ -2\beta_3 & \alpha_2 & -\alpha_1 & 0 \end{pmatrix} \begin{pmatrix} \sigma \\ \pi^1 \\ \pi^2 \\ \pi^3 \end{pmatrix} \quad (2.2.17)$$

$$= \left[2\beta_1 \begin{pmatrix} 0 & 1 & 0 & 0 \\ -1 & 0 & 0 & 0 \\ 0 & 0 & 0 & 0 \\ 0 & 0 & 0 & 0 \end{pmatrix} + 2\beta_2 \begin{pmatrix} 0 & 0 & 1 & 0 \\ 0 & 0 & 0 & 0 \\ -1 & 0 & 0 & 0 \\ 0 & 0 & 0 & 0 \end{pmatrix} + \dots \right] \begin{pmatrix} \sigma \\ \pi^1 \\ \pi^2 \\ \pi^3 \end{pmatrix}. \quad (2.2.18)$$

Inspecting (2.2.17) one notes that $\delta_\phi \phi^T = 0$ because of the antisymmetry of the infinitesimal matrix, implying the invariance of ϕ^2 under the transformation. Thus, the symmetry must be a subgroup of $O(4)$, which is the group of real transformations keeping the norm of a 4-dimensional vector constant. Counting the number of generators in (2.2.18), necessary for constructing the infinitesimal matrix in (2.2.17), reveals that the algebra of the meson transformation is 6-dimensional and hence must be holomorphic (or even isomorphic) to the full $O(4)$ group. Closer inspection shows that all $O(4)$ elements are necessary for maintaining invariance of \mathcal{L}_{int} under the $SU(2) \times SU(2)$ transformation in the fermionic sector. It is interesting to note that although there is an $SU(2) \times SU(2)$ symmetry in the fermionic sector, only a (smaller) $O(4)$ symmetry in the meson sector is necessary to balance its effect on the interaction term.

One task remains, namely, to show that the induced transformation on the meson fields keeps the mesonic part of the Lagrangian invariant. This invariance can be seen most

easily in terms of the combined meson field ϕ and a general $O(4)$ transformation matrix O :

$$\mathcal{L}_{\text{kin},m} = \frac{1}{2} \partial_\mu \phi^T \partial^\mu \phi, \quad (2.2.19)$$

$$\mathcal{L}'_{\text{kin},m} = \frac{1}{2} \partial_\mu (\phi^T O^T) \partial^\mu (O \phi) = \frac{1}{2} \partial_\mu \phi^T \partial^\mu \phi, \quad (2.2.20)$$

where we used the group property $O^T = O^{-1}$ and that O is a global symmetry (*i.e.* not depending on the space-time coordinates) for commuting it with the derivatives. The interaction potential transforms trivially (as discussed above, the transformation keeps $\phi^T \phi$ invariant) since the potential

$$U(\sigma, \vec{\pi}) = \frac{\lambda}{4} (\sigma^2 + \pi^2 - \zeta)^2 = \frac{\lambda}{4} (\phi^T \phi - \zeta)^2, \quad (2.2.21)$$

depends solely on $\phi^T \phi$ in the chiral limit.

Another comment is in order here. After demonstrating the $U(1)_V \times SU(2)_V \times SU(2)_A$ symmetry, one might ask whether there is another $U(1)_A$ symmetry for this model not discussed yet. This is not the case: The $U(1)_A$ symmetry, which is present at the classical level of light flavor QCD and broken by quantum effects (referred to under the name of “axial anomaly”), is infinitesimally written as ($\eta \ll 1$)

$$q \rightarrow (1 + i\gamma^5 \eta)q, \quad \bar{q} \rightarrow \bar{q}(1 + i\gamma^5 \eta). \quad (2.2.22)$$

The kinetic term indeed is invariant under this symmetry (commuting $\not{\partial}$ with γ^5 changes the sign in one of the η -terms), but in the interaction part it induces contributions $\propto \vec{\tau} \mathbb{1}_D$ and $\propto \gamma^5 \mathbb{1}_f$ (instead of $\mathbb{1}_D \mathbb{1}_f$ and $\vec{\tau} \gamma^5$ as the other infinitesimal transformations discussed above do), which cannot be absorbed into transformations of the meson fields, thus, rendering the interaction not $U(1)_A$ symmetric.

2.2.3. Conserved currents

According to NOETHER’s theorem any continuous symmetry of the Lagrangian is connected to a conserved current. This connection is well known and will not be shown here in detail. The reader is referred to standard textbooks (*e.g.* [Kug97, Sre07, Wei05a, PS95]) for a thorough discussion of this subject. For definiteness the transformation of an n -component field ϕ_a under a continuous symmetry is written as

$$\phi_a \rightarrow \phi'_a = \phi_a(x) + \eta_b G_a^b(\phi_1, \dots, \phi_n), \quad (2.2.23)$$

with real infinitesimal parameters η_b and the generators G_a^b for the respective symmetry (indexed by b). With this definition the corresponding NOETHER current reads

$$j^{b,\mu} = \mathcal{N} \frac{\partial \mathcal{L}}{\partial (\partial_\mu \phi_a)} G_a^b, \quad (2.2.24)$$

where \mathcal{N} denotes an arbitrarily chosen normalization constant. Applied to the symmetries of the QMM one gets

$$\begin{aligned} j_V^\mu &= \bar{q} \gamma^\mu q, \\ j_V^{a,\mu} &= \bar{q} \gamma^\mu \tau^a q + \epsilon^{bca} \pi_b \partial^\mu \pi_c & \Leftrightarrow & \vec{j}_V^\mu = \bar{q} \gamma^\mu \vec{\tau} q + \vec{\pi} \times \partial^\mu \vec{\pi}, \\ j_A^{b,\mu} &= \bar{q} \gamma^\mu \gamma^5 \tau^b q - 2\pi^b \partial^\mu \sigma + 2\sigma \partial^\mu \pi^b & \Leftrightarrow & \vec{j}_A^\mu = \bar{q} \gamma^\mu \gamma^5 \vec{\tau} q - 2\vec{\pi} \partial^\mu \sigma + 2\sigma \partial^\mu \vec{\pi}, \end{aligned} \quad (2.2.25)$$

with the canonical normalization $\mathcal{N} = 1$ for the currents.

2.2.4. Spontaneous symmetry breaking

In the chiral limit, *i.e.* $H = 0$, the meson interaction potential (2.1.4) is minimal on the manifold determined by $\phi^T \phi = \zeta$. Including the fermionic sector into the consideration one finds that the ground state of the model is composed of one of these meson states and an accordingly chosen fermion state. The mesonic part of the ground state typically is chosen to be in σ direction, *i.e.* $\langle \sigma \rangle_0 = \sqrt{\zeta}$ and correspondingly $\langle \vec{\pi}^2 \rangle_0 = 0$. Having fixed the value of σ according to (2.2.15) the symmetry $SU(2)_A$ corresponding to the infinitesimal parameters β^a cannot be applied anymore without changing the ground state. Only the remaining $U(1)_V \times SU(2)_V$ transformations leave the ground state invariant. In other words: The symmetry $U(1)_V \times SU(2)_V \times SU(2)_A$ is not present in the ground state, but instead is broken to $U(1)_V \times SU(2)_V$. The “lost” symmetry $SU(2)_A$ transforms within the infinite set of degenerate ground states. According to the GOLDSTONE theorem this symmetry is realized by massless fields transforming nontrivially under this symmetry [Wei05b, GSW62]. In the case of the QMM, these are the π fields.

2.2.5. Explicit symmetry breaking

Traces of the symmetry breaking pattern can be seen even when the chiral symmetry is broken explicitly by a non-invariant term in the Lagrangian (in (2.1.4), this is the case for $H \neq 0$) provided the symmetry breaking term is small compared to the symmetric part of the meson potential. This somewhat sloppy formulation means that a typical σ -dependence of the Hamiltonian $\Delta \mathcal{H}_{sb}$ originating from the symmetry breaking term

(*i.e.* $\Delta\mathcal{H}_{sb} \sim H|\sigma_1 - \sigma_2|$) is much smaller than the typical σ -dependence already included in the chirally symmetric part of the potential $\Delta\mathcal{H}_\chi \sim |U(\sigma_1) - U(\sigma_2)|$. Choosing for σ_1 and σ_2 the vacuum expectation value of the σ field $\langle\sigma\rangle_{\text{vac}}$ and the σ expectation value in the symmetric phase ($\langle\sigma\rangle = 0$ in the chiral limit), respectively, one arrives at

$$H\langle\sigma\rangle_{\text{vac}} \ll \frac{\lambda\zeta^2}{4} \quad (2.2.26)$$

as condition for an explicit symmetry breaking being small, *i.e.* $\Delta\mathcal{H}_{sb} \ll \Delta\mathcal{H}_\chi$. With the parameters of the Lagrangian expressed by the masses and vacuum expectation values of the fields according to Section 2.3 this condition transforms into

$$8 \frac{(m_\pi^{\text{vac}})^2}{(m_\sigma^{\text{vac}})^2} \frac{\left(1 - \frac{(m_\pi^{\text{vac}})^2}{(m_\sigma^{\text{vac}})^2}\right)}{\left(1 - 3 \frac{(m_\pi^{\text{vac}})^2}{(m_\sigma^{\text{vac}})^2}\right)^2} \ll 1, \quad (2.2.27)$$

which is fulfilled in the limits $(m_\pi^{\text{vac}})^2/(m_\sigma^{\text{vac}})^2 \rightarrow 0$ and $(m_\pi^{\text{vac}})^2/(m_\sigma^{\text{vac}})^2 \rightarrow 1$. However, the latter one representing the noninteracting limit $\lambda \rightarrow 0$ without spontaneous symmetry breaking at all. It thus can be concluded that the explicit symmetry breaking may be regarded small if $(m_\pi^{\text{vac}})^2 \ll (m_\sigma^{\text{vac}})^2$.

2.3. Parameter fixings

Besides the number of colors ($N_c = 3$ in the context of modeling low-energy QCD) there are four parameters in the Lagrangian. Often it is much more convenient to express them in terms of observables which then can be fixed to reasonable (often: QCD-rooted) values. These observables are the vacuum masses of the three fields as well as the pion decay constant determined according to PCAC (partial conservation of axial currents) relations. Using these observables instead of the renormalization scale dependent parameters in the Lagrangian has – besides the independence of the renormalization scale – the advantage that the results are much better comparable between different approaches (*e.g.* renormalization group approaches or the path integral approach in mean field approximation either with or without vacuum terms, *cf.* Section 5).

The ground state of the model corresponds to the minimum of the meson potential determined by

$$0 \stackrel{!}{=} \frac{\partial U}{\partial \sigma} = \lambda(\sigma^2 + \vec{\pi}^2 - \zeta)\sigma - H, \quad (2.3.1)$$

$$0 \stackrel{!}{=} \frac{\partial U}{\partial \pi^a} = \lambda \left(\sigma^2 + \vec{\pi}^2 - \zeta \right) \pi_a. \quad (2.3.2)$$

For non-zero H , (2.3.1) enforces $\sigma^2 + \vec{\pi}^2 - \zeta$ to be non-vanishing, which in turn leads to $\pi_a = \pi^a = 0$ in order to fulfill (2.3.2). In mean field approximation as well as in the linearized fluctuation approximation without vacuum terms, the vacuum masses of the mesons are related to the second derivatives *w.r.t.* the fields evaluated in the vacuum state ($T = \mu = 0$). Thus one gets

$$(m_\sigma^{\text{vac}})^2 = \left. \frac{\partial^2 U}{\partial \sigma^2} \right|_{\substack{(2.3.1) \\ (2.3.2)}} = \lambda \left(3\sigma^2 + \vec{\pi}^2 - \zeta \right) \Big|_{\substack{(2.3.1) \\ (2.3.2)}}, \quad (2.3.3)$$

$$(m_\pi^{\text{vac}})^2_{ab} = \left. \frac{\partial^2 U}{\partial \pi^b \partial \pi^a} \right|_{\substack{(2.3.1) \\ (2.3.2)}} = \lambda \pi_b \pi_a + \lambda \left(\sigma^2 + \vec{\pi}^2 - \zeta \right) \delta_{ab} \Big|_{\substack{(2.3.1) \\ (2.3.2)}}. \quad (2.3.4)$$

Applying $\pi_a = 0$ the mass matrix for the pions in vacuum is diagonal and degenerate, thus all pion fields have the same mass (as they should by symmetry) yielding with $(m_\pi^{\text{vac}})^2_{ab} \equiv (m_\pi^{\text{vac}})^2 \delta_{ab}$

$$(m_\pi^{\text{vac}})^2 = \lambda \left(\sigma^2 + \vec{\pi}^2 - \zeta \right) \Big|_{\substack{(2.3.1) \\ (2.3.2)}}. \quad (2.3.5)$$

In the vacuum, the quark mass is given by

$$m_q = g\sigma \Big|_{\substack{(2.3.1) \\ (2.3.2)}}, \quad (2.3.6)$$

which can be deduced in various ways, *e.g.* applying a derivative expansion *w.r.t.* the meson fields (*cf.* Appendix C) and setting $\partial\sigma = \partial\pi = 0$ in the vacuum. Finally, the vacuum expectation value of the sigma field $\langle \sigma \rangle_{\text{vac}}$ can be related to the pion decay constant. For the matrix element of the axial current sandwiched between the vacuum and a one pion state, one can write

$$\partial_\mu \langle 0 | \vec{j}_A^\mu | \vec{\pi}(p) \rangle = \partial_\mu \langle 0 | -\bar{q} \gamma^\mu \gamma^5 \vec{\tau} q + 2\vec{\pi} \partial^\mu \sigma - 2\sigma \partial^\mu \vec{\pi} | \vec{\pi}(p) \rangle. \quad (2.3.7)$$

With

$$\langle 0 | -\bar{q} \gamma^\mu \gamma^5 \vec{\tau} q | \vec{\pi}(p) \rangle \propto \langle 0 | \text{Tr}_{D,F} \left[G_q \gamma^\mu \gamma^5 \vec{\tau} \vec{\pi}(p) \right] | 0 \rangle \quad (2.3.8)$$

and the full quark propagator G_q according to (4.2.10) together with $\text{Tr} \gamma^\nu \gamma^\mu \gamma^5 = \text{Tr} \gamma^\mu \gamma^5 = \text{Tr} \gamma^\mu = 0$, the quark contribution to the current matrix element vanishes. Within the lin-

earized fluctuation approximation³, the meson sector of the generating functional is Gaussian in the variables π^a and $\Delta = \sigma - \langle\sigma\rangle$. Thus correlation functions with odd powers of these fields vanish. Applying $\partial\langle\sigma\rangle = 0$, the only non-vanishing contribution to (2.3.7) is

$$-2\langle\sigma\rangle\partial_\mu\langle 0|\partial^\mu\vec{\pi}|\vec{\pi}(p)\rangle = -2\langle\sigma\rangle\Box\sqrt{2}\delta_a^a e^{ipx} = 6\sqrt{2}\langle\sigma\rangle m_\pi^2 e^{ipx} \quad (2.3.9)$$

yielding upon comparison with the PCAC relation, *cf.* Section 2.2.1, for the matrix element of an axial vector current between the vacuum and a single pion state (which formally has the same structure)

$$\langle\sigma\rangle_{\text{vac}} = f_\pi. \quad (2.3.10)$$

Equations (2.3.1), (2.3.2), (2.3.3), (2.3.5), (2.3.6) and (2.3.10) are six equations for the four model parameters and the two vacuum expectation values of the meson fields. Rearranging them yields

$$\begin{aligned} H &= (m_\pi^{\text{vac}})^2 \langle\sigma\rangle_{\text{vac}}, & g &= \frac{m_q^{\text{vac}}}{\langle\sigma\rangle_{\text{vac}}}, \\ \lambda &= \frac{(m_\sigma^{\text{vac}})^2 - (m_\pi^{\text{vac}})^2}{2\langle\sigma\rangle_{\text{vac}}^2}, & 2\lambda\zeta &= (m_\sigma^{\text{vac}})^2 - 3(m_\pi^{\text{vac}})^2. \end{aligned} \quad (2.3.11)$$

The quantities on the right hand side can be fixed to “reasonable values”, *e.g.* the PDG values of the respective masses [O⁺14]. The (QMM-)quark mass reflects the σ condensation and the coupling of the mesons to the fermionic sector of the model. It is hence a result of the interactions encoded in the model Lagrangian and thus should not be fixed to the bare (Standard Model) quark mass ($\lesssim 10$ MeV) but rather to an effective (“constituent”) mass, which is about one third of the nucleon mass. With (2.3.10) the expectation value of the σ field can be fixed to the pion decay constant. There is some flexibility in the choice of these parameters, since the model lacks too many degrees of freedom (*e.g.* gluons, strange as well as heavier quarks, vector and axial vector mesons *etc.*) to reach quantitative agreement with QCD predictions or experimental data. Thus the values suggested above for parameter fixing might be taken as a first guess but can be varied over a broad range to study the model behavior. In this spirit, the impact of the vacuum pion mass parameter was studied, *e.g.* in [BK09], that of the vacuum sigma mass parameter in [WK15a] and that of a wide variation of certain parameter combinations in [WK17] (for the two flavor model) and [SW09] (for three flavors).

³ See Chapter 4.

2.4. Relation to other effective models

2.4.1. Extensions of the QMM

For studying the low-temperature properties of the nuclear medium, the QMM is not well suited, *e.g.* the pressure at nuclear density at low temperatures is too small compared to our understanding of neutron star structure [SRK14]. Also, many more mesonic degrees of freedom are known from experiment. A part of the latter objection can be dealt with by increasing the number of flavors to three [LRSB00] or four [DATD16] and by including axial and vector mesons, *cf.* [PGR10, BSSB14] for a case with two, [PKW⁺13] for three and [EGR15, Sas14] for four flavors. However, in order to reproduce the vacuum properties of the QCD matter correctly the flavor symmetries in the strange and in the charm sector (for the $N_f = 4$ models) have to be explicitly broken thus introducing many free parameters into the model, which have to be fitted to QCD results or meson properties [PGR10]. Often the QMM is coupled to a POLYAKOV loop to partially account for the interaction with the gluon field. For the POLYAKOV loop, several potentials are discussed in the literature, *e.g.* [SPW07, HPS11, LFK⁺13, SSB16]. A further possibility to partially include the gluonic degrees of freedom is the introduction of glueballs [SM12].

2.4.2. Other effective models

There is a close connection to the NAMBU-JONA-LASINIO (NJL) model [VW91, HK94, Fuk08, MBC⁺13], being probably the most widely used chiral effective model with the Lagrangian

$$\mathcal{L}_{\text{NJL}} = \bar{q}(i\cancel{\partial} - m)q - g((\bar{q}q)^2 - (\bar{q}\gamma^5\vec{\tau}q)^2). \quad (2.4.1)$$

The partition function of the NJL model reads:

$$Z = \int \mathcal{D}\bar{q}\mathcal{D}q \exp \left\{ \int d^4x \mathcal{L}_{\text{NJL}} - \mu\bar{q}\gamma^0 q \right\}. \quad (2.4.2)$$

Applying HUBBARD-STRATONOVIC transformations (*cf.* [ZJ02])

$$e^{-a/2 \int d^4x \xi_i(x)^2} = \frac{1}{\sqrt{2\pi a}} \int \mathcal{D}\phi_i e^{-\int d^4x \phi_i(x)^2 / (2a) - i\xi_i(x)\phi_i(x)}, \quad (2.4.3)$$

with $\xi_1 \equiv \bar{q}q$ and $\xi_2 \equiv i\bar{q}\gamma^5\vec{\tau}q$ and, correspondingly, $\phi_1 \equiv \sigma$ and $\phi_2 \equiv \vec{\pi}$, we arrive at

$$Z = \int \mathcal{D}\bar{q}\mathcal{D}q\mathcal{D}\sigma\mathcal{D}\pi_a \exp \left\{ \bar{q}(i\cancel{\partial} - m - g(\sigma + i\gamma^5\tau\pi))q - g((\sigma)^2 - (\vec{\pi})^2) \right\} \quad (2.4.4)$$

having the same fermionic terms, especially the same fermion-meson interaction terms as the QMM.

When the fermionic sector \mathcal{L}_q is removed from the Lagrangian (2.1.1) one obtains a purely mesonic model showing the same pattern of symmetry breaking. In the literature, this model is called the $O(4)$ model or the linear sigma model [PS95, LR00]. Since the $O(4)$ model and the QMM share the same meson potential, which ultimately is responsible for the symmetry breaking, the thermodynamics of both models share many common features. Furthermore, many formal properties, such as renormalizability, are identical in both cases. However, there exist important differences due to the lack of fermionic degrees of freedom, *e.g.* in the high-temperature behavior (dominated by quarks in the QMM) or in the dependence on the baryo-chemical potential (there is none in the $O(4)$ model). On the other hand the $O(4)$ model can simply be generalized to the $O(N)$ model (with $N \in \mathbb{N}$) for which the large N -limit can be taken [LR00].

Another model which is related to the QMM is the non-linear sigma model. The most straight forward way to obtain its Lagrangian from the QMM Lagrangian (2.1.1)-(2.1.4) is by imposing the condition $C^2 = \sigma^2 + \vec{\pi}^2$ to eliminate σ . Effectively this restricts the pions to the sphere $S(3)$ and makes the kinetic term of the pions a complicated function of (pion) derivatives and field values leading to nonlinear solutions of the equations of motion (hence the naming of the model). The connection can elegantly be made manifest by the introduction of an auxiliary field α introduced again by a HUBBARD-STRATONOVIC transformation. The mesonic sector Z_m of the partition function of the QMM can be written as [See11]

$$Z_m = \int \mathcal{D}\pi^a\mathcal{D}\sigma\mathcal{D}\alpha \exp \left\{ \frac{1}{2}(\partial\sigma)^2 + \frac{1}{2}(\partial\vec{\pi})^2 - U(\sigma, \vec{\pi}, \alpha) \right\}, \quad (2.4.5)$$

$$U(\sigma, \vec{\pi}, \alpha) = \frac{i}{2}\alpha(\sigma^2 + \vec{\pi}^2 - \zeta) + \frac{\epsilon}{2}\alpha^2 - H\sigma. \quad (2.4.6)$$

Setting $\epsilon \equiv 1/(2\lambda)$ one recovers (2.1.4) while in the limit $\epsilon \rightarrow 0$, (2.4.5) resembles the mesonic sector of the non-linear sigma model. In more physical terms, the transition from the QMM to the non-linear sigma model corresponds to sending the σ mass to infinity. It turns out that this kind of construction leads to a Lagrangian that coincides in leading order with the Lagrangian obtained with chiral perturbation theory *i.e.* the systematic

low-energy expansion of QCD *w.r.t.* quark masses.

2.5. Advantages of the QMM

As discussed above the two-flavor QMM possesses a $U(1)_V \times SU(2)_V \times SU(2)_A$ symmetry. This is to be contrasted with the flavor symmetry of two-flavor QCD. The QCD Lagrangian with two massless quarks is manifestly $SU(2)_A \times U(1)_A \times SU(2)_V \times U(1)_V$ invariant at the classical level. The $U(1)_A$ symmetry again is broken by radiative corrections [PW84] making the flavor symmetry of light QCD isomorphic to that of the QMM.

Besides this satisfying symmetry breaking pattern, the QMM is renormalizable making the introduction of a cut-off by hand unnecessary (in contrast to the NJL model, where such a cut-off has to be introduced in order to make finite predictions). Another advantage of the QMM with respect to the NJL model is that the QMM has mesonic degrees of freedom, so the mesonic properties are much more directly accessible, *e.g.* in the NJL model the pion mass has to be extracted from resonances in loop calculations, while within the QMM the mass can be extracted from the pion propagator.

Compared to more realistic models incorporating a large variety of mesonic degrees of freedom, the QMM is a rather slim model with only a few independent fields. This simplicity allows to relate thermodynamic properties as well as peculiarities in the phase diagram to a small number of model parameters. For the more elaborate model versions, such as those presented in [Sas14, EGR15, KSW16], such a connection is much more difficult to identify because of the large number of possible dependencies as well as the necessity for applying fitting procedures in high-dimensional parameter spaces.

Concluding, it can be stated that the QMM combines the correct symmetry breaking pattern with a small number of free parameters but still explicitly including some relevant degrees of freedom also present in QCD, both for the high-temperature phase (quarks) as well as for the low-temperature phase (pions).

3. Basic definitions

3.1. The MCLERRAN-TOIMELA formula

One of the central formulas needed below in Chapter 4 that allows for connecting the photon emissivity to thermodynamics is the so-called MCLERRAN-TOIMELA formula [MT85]. It relates the emissivity $\omega d^7N/d^3kd^4x$ to the retarded in-medium photon propagator $G_{\gamma,\text{ret}}^{\mu\nu}$ according to

$$\omega \frac{d^7N}{d^3kd^4x} = \frac{g_{\mu\nu}}{(2\pi)^3} \text{Im} G_{\gamma,\text{ret}}^{\mu\nu}(k^2 = 0, \omega) n_B(\omega), \quad (3.1.1)$$

where n_B is the BOSE-EINSTEIN distribution function and $k = (\omega, \vec{k})$ is the 4-momentum of the emitted photons. Although first derived rather technically by studying the electromagnetic current-current correlation function perturbatively [MT85], it was re-derived based on very general assumptions without the use of perturbation theory in the strongly interacting sector [KG06, Gal10]. In Appendix G, this derivation is recalled in some detail, here, however, only the main ingredients are given.

From the definition of the S matrix one finds that the reaction rate for a transition from some initial state $|i\rangle$ to some final state $|f\rangle$ is proportional to the square of the absolute value of the corresponding matrix element $|\langle f|S|i\rangle|^2$. Furthermore, assuming the emitting system to be much smaller than the mean free path of the photons the S matrix element can be written to first order in the electromagnetic coupling in terms of the electromagnetic current. If, on the other hand, the system is much larger than the mean free path of the strongly interacting particles and only slowly changing on this scale, translational invariance can be invoked yielding delta distributions that can be interpreted as energy-momentum conservation for emission and absorption processes. In the resulting expression, the spectral functions associated to photon emission processes can be identified which are finally written in terms of the retarded photon propagator yielding formula (3.1.1).

Formula (3.1.1) is exact to all orders in the strong interaction, yet only to first order in the electromagnetic interaction [Gal10]. This poses the probably strongest limitation of (3.1.1), however, for colliding nuclei, the assumption of the system size being intermediate between the mean free path for strong and electromagnetic interactions is reasonable.

3.2. Path integrals

3.2.1. Path integral representation of the partition function

One major application of the path integral formalism is the representation of fundamental field theoretical or thermodynamical quantities based directly on the Lagrangian and thus manifestly respecting the classical symmetries of the theory, such as LORENTZ and gauge invariance as well as flavor symmetries. A detailed introduction to path integrals and the derivation of the key formulas goes far beyond the scope of this thesis. We will rather focus on the path integral representation of the grand canonical partition function itself and give some formulas which are used in subsequent chapters. For an introduction to the formalism, we refer to the literature, *e.g.* [ZJ02, Das06, KG06].

The grand canonical partition function Z is defined as

$$Z = \text{Tr} e^{-\beta(\hat{H} - \mu\hat{N})} \quad (3.2.1)$$

with \hat{H} being the Hamiltonian, \hat{N} the number operator, μ the chemical potential and β the inverse temperature. For simplicity, we first take a look at a theory with one single scalar field defined at the classical level by the Lagrangian $\mathcal{L} = \mathcal{L}(\phi, \partial_\mu\phi)$. The Hamiltonian is then obtained with a LEGENDRE transformation

$$\mathcal{H} = \pi \frac{\partial\phi}{\partial t} - \mathcal{L}(\phi, \partial_\mu\phi) \quad (3.2.2)$$

with the canonical momentum π defined by $\pi = \frac{\partial\mathcal{L}}{\partial\partial_0\phi}$. The grand canonical partition function can be represented by the path integral

$$Z = \int \mathcal{D}\phi \int \mathcal{D}\pi e^{\int_0^\beta d\tau \int d^3x (\pi \frac{\partial\phi}{\partial\tau} - \mathcal{H}(\pi, \phi) + \mu\mathcal{N})}, \quad (3.2.3)$$

where $\mathcal{N} = \mathcal{N}(\phi)$ denotes the number density of the field configuration ϕ . In this thesis, only Hamiltonians that are quadratic in the canonical momentum are considered, especially

$$\mathcal{H}(\pi, \phi) = \frac{1}{2}\pi^2 + \mathcal{H}^\phi(\phi). \quad (3.2.4)$$

Then the path integral *w.r.t.* the canonical momentum can be carried out exactly yielding

$$Z = \int \mathcal{D}\phi e^{\int_0^\beta d\tau \int d^3x \frac{1}{2} \frac{\partial \phi^2}{\partial \tau^2} - \mathcal{H}(\phi) + \mu \mathcal{N}} \quad (3.2.5)$$

$$= \int \mathcal{D}\phi e^{\int_0^\beta d\tau \int d^3x \mathcal{L}(\phi, \partial \phi) + \mu \mathcal{N}}, \quad (3.2.6)$$

where it was used that if the Hamiltonian can be decomposed according to (3.2.4), then $\mathcal{L} = 1/2(\partial_\tau \phi)^2 - \mathcal{H}$. This easily can be generalized to n fields provided that the Hamiltonian for each field is quadratic in the canonical momentum

$$Z = \int \mathcal{D}\phi_1 \cdots \int \mathcal{D}\phi_n e^{\int_0^\beta d\tau \int d^3x \mathcal{L}(\phi, \partial \phi) + \sum_i \mu_i \mathcal{N}^{(i)}} \quad (3.2.7)$$

with the number density $\mathcal{N}^{(i)}$ for the field ϕ_i and μ_i the corresponding chemical potential. This will apply for all bosonic fields in this thesis. For the fermionic fields, however, the canonical momentum cannot be integrated over since the fermionic Hamiltonian is linear in the canonical momentum. Nonetheless, for the cases interesting for this thesis, the canonical momentum of the fermionic field ψ can be identified with the adjoint DIRAC field $\bar{\psi}$, yielding a factor

$$\int \mathcal{D}\psi \mathcal{D}\bar{\psi} e^{\int_0^\beta d\tau \int d^3x \mathcal{L}_\psi(\psi, \partial \psi) + \mu \mathcal{N}} \quad (3.2.8)$$

for each fermion field. Thus, for a theory with b bosonic degrees of freedom ϕ_i with quadratic kinetic terms and f fermionic degrees of freedom ψ_j one obtains for the partition function

$$Z = \int \mathcal{D}\phi_1 \cdots \mathcal{D}\phi_b \int \mathcal{D}\psi_1 \mathcal{D}\bar{\psi}_1 \cdots \mathcal{D}\psi_f \mathcal{D}\bar{\psi}_f e^{\int_0^\beta d\tau \int d^3x \mathcal{L}(\phi_1, \dots, \psi_f, \partial \phi_1, \dots, \partial \psi_f) + \mu \mathcal{N}}, \quad (3.2.9)$$

where we restricted ourselves to the case of only one conserved particle number with density \mathcal{N} .¹

3.2.2. Path integral representation of the generating functional

Another quantity that will be calculated is the generating functional S of correlation functions. It can be regarded as a computational trick to obtain in a simple manner the correlation functions of a field theory. Analogous to the partition function it has a path

¹ In (3.2.9) we suppressed a possible multiplicative factor, which can be introduced without changing the physics as long as it does not depend on physical quantities. However, such a factor also might be absorbed into the definition of the path integral measure.

integral representation which strikingly is rather similar to those for the partition function. For a theory with b bosonic and f fermionic fields this representation reads

$$S[\eta] = \int \mathcal{D}\phi_1 \dots \mathcal{D}\phi_b \int \mathcal{D}\psi_1 \mathcal{D}\bar{\psi}_1 \dots \mathcal{D}\psi_f \mathcal{D}\bar{\psi}_f \times e^{i \int d^4x \mathcal{L}(\phi_1, \dots, \psi_f, \partial\phi_1, \dots, \partial\psi_f) + \sum_{i=0}^b \eta_i^b \phi_i + \sum_{j=0}^f \bar{\eta}_j^f \psi_j + \bar{\psi}_j \eta_j^f} \quad (3.2.10)$$

with the bosonic sources η_i^b and the fermionic source $\eta_j^f, \bar{\eta}_j^f$. The similarity of (3.2.9) and (3.2.10) is an interesting feature of the path integral formalism. In particular, for the vacuum, *i.e.* at $T = \mu = 0$, and for vanishing sources $\eta_i^b = \eta_j^f = 0$ (for all i and j) the generating functional and the partition function are closely related, the only relevant difference being that the integral in the exponent is – for the partition function – in imaginary direction while that for the generating functional of correlation functions is in real time direction. In order to maintain this connection, one of the central ideas of this thesis is that approximations to the partition function and to the generating functional cannot be made independently but have to be consistent to each other.

3.2.3. Path integrals for quadratic action

Since in the subsequent chapters the path integrations have often to be evaluated for quadratic integrands some relevant results for this case are quoted here. The fundamental formula for bosonic Gaussian path integrals is

$$I_b := \int \mathcal{D}\phi e^{-\frac{1}{2} \int d^4x \int d^4y \phi(x) M(x,y) \phi(y) + \int d^4z B(z) \phi(z)} = \frac{1}{\sqrt{\det M}} e^{\frac{1}{2} \int d^4x d^4y B(x) M^{-1} B(y)} \quad (3.2.11)$$

with M^{-1} being a GREEN's function of the operator M defined by

$$\int d^4z M(x, z) M^{-1}(z, y) = \delta(x - y). \quad (3.2.12)$$

If (3.2.11) resembles the generating functional of a theory or at least all parts of it that depend on the field ϕ , then $M^{-1}(x, y)$ can be identified with the propagator $G_\phi(x, y)$ for that field. We will only consider cases, where M can be diagonalized by transforming to the momentum space. Then – after rewriting the functional determinant with the help of a functional trace – one obtains

$$I_b = e^{-T \sum_{\omega_n} \int d^3p \frac{1}{2} \ln \widetilde{M}(\omega_n, \vec{p}) + \frac{1}{2} T^2 \sum_{\omega_n, \omega_k} \int d^3p d^3q \widetilde{B}(\omega_n, \vec{p}) G_\phi(\omega_n, \vec{p}; \omega_k, \vec{q}) \widetilde{B}(\omega_k, \vec{q})}, \quad (3.2.13)$$

where now the FOURIER transformed functions \widetilde{M} and \widetilde{B} can be regarded as simple functions of ω_n and \vec{p} .

Path integration over fermionic fields, represented by GRASSMANN numbers, obeys a very different algebra. However, the resulting formulas for Gaussian path integrals look rather similar:

$$I_f := \int \mathcal{D}\bar{\psi} \mathcal{D}\psi e^{-\int d^4x \int d^4y \bar{\psi} M(x,y) \psi + \int d^4z \bar{B}(z) \psi + \bar{\psi} B(z)} \quad (3.2.14)$$

$$= \det M e^{\int d^4x d^4y \bar{B}(x) M^{-1}(x,y) B(y)}, \quad (3.2.15)$$

with \bar{B} and B being GRASSMANN valued functions. If $M(x,y)$ can be diagonalized by FOURIER transformation, one obtains

$$I_f = e^{T \sum_{\omega_n} \int d^3p \ln \widetilde{M}(\omega_n, \vec{p}) + T^2 \sum_{\omega_n, \omega_k} \int d^3p d^3q \widetilde{\bar{B}}(\omega_n, \vec{p}) G_{\psi}(\omega_n, \vec{p}; \omega_k, \vec{q}) \widetilde{B}(\omega_k, \vec{q})} \quad (3.2.16)$$

again with \widetilde{M} , $\widetilde{\bar{B}}$ and \widetilde{B} denoting the respective FOURIER transformed functions.

3.3. Calculating correlation functions in the path integral framework

3.3.1. Correlation functions

The correlation functions of a theory can be represented within the path integral framework. A comprehensive discussion of this issue is part of many textbooks on quantum field theory, *cf.* [PS95, ZJ02, Das06, KG06]. In this section, we therefore simply quote the relevant formulas. The time ordered n -field correlation function for an interacting theory with Lagrangian $\mathcal{L}(\Phi)$ depending on the fields $\Phi \equiv \phi_1, \dots, \phi_N$ with ϕ_i being any kind of relativistic quantum field, especially with half-integer or integer spin, is calculated according to the GELL-MANN-LOW formula which has the path integral representation

$$\langle 0 | \mathcal{T} \phi_{k_1}(x^{(1)}) \dots \phi_{k_n}(x^{(n)}) | 0 \rangle = \frac{\int \mathcal{D}\Phi \phi_{k_1} \dots \phi_{k_n} e^{-i \int d^4x \mathcal{L}(\Phi)}}{\int \mathcal{D}\Phi e^{-i \int d^4x \mathcal{L}(\Phi)}} \quad (3.3.1)$$

with $\mathcal{D}\Phi \equiv \mathcal{D}\phi_1 \dots \mathcal{D}\phi_N$ denoting the N dimensional path integral measure over all fields of the theory and k being a list of arbitrary integer numbers with $1 \leq k_i \leq N$. The variable $x^{(j)}$ represents the space-time coordinates of the j th field. This formula can be reformulated by adding source terms $\phi_j(x) \eta^j(x)$ to the Lagrangian. The factors of ϕ_i under

the path integral can then be represented by functional derivatives *w.r.t.* the corresponding sources which can be pulled out of the integral. The denominator is obtained by setting all sources η^j zero. Thus, with the definition

$$S_\eta := \mathcal{D}\Phi e^{-i \int d^4x \mathcal{L}(\Phi) - \phi_j(x) \eta^j(x)} \quad (3.3.2)$$

and S_0 being S_η with all sources set to zero, the n -field correlation function reads

$$\langle 0 | \mathcal{T} \phi_{k_1} \dots \phi_{k_n} | 0 \rangle = \frac{i^n}{S_0} \frac{\delta}{\delta \eta^{k_n}(x^{(n)})} \dots \frac{\delta}{\delta \eta^{k_1}(x^{(1)})} S_\eta. \quad (3.3.3)$$

The quantity S_η from which all time ordered correlation functions of the theory can be calculated by differentiation is called the generating functional of correlation functions.

3.3.2. Partition function and generating functional

As stressed above the partition function and the generating functional formally have quite similar path integral representations. There are only three differences in the respective definitions:

- (i) There are no source terms for the partition function.
- (ii) The term with the chemical potential is missing for the generating functional.
- (iii) The integration measure in both cases differs by a factor of i and the limits of the time integration are different, too ($\tau \in [0, \beta]$ vs. $t \in [-\infty, \infty]$).

However, if all sources are set zero and if the partition function is evaluated in the vacuum, *i.e.* at $T = \mu = 0$, the only difference remaining is that the partition function is calculated in Euclidean space *i.e.* with an imaginary time argument for all fields and the generating functional for correlation function is defined in MINKOWSKI space. The factor i mentioned above reflects this difference which can be seen most easily by writing it as $\sqrt{\det g}$ with g denoting the metric of the space. Despite the differences the dependence on the fields is identical implying that for a consistent treatment of dynamics (derived from the generating functional) and thermodynamics (derived from the partition function) requires for both quantities to apply the same scheme of approximations, regularizations, renormalization *etc.* This is a key observation for this thesis that will later help to define the fermion mass within the approximation scheme under consideration properly – a task formulated by the authors of [MME04] and answered here, *cf.* [WK17].

4. Derivation of the photon rate formula

In this chapter, an expression for the photon emissivity $\omega d^7N/d^3kd^4x$ of the QMM is derived. First the QMM is extended by an electromagnetic sector. Then the generating functional of correlation functions is calculated including lowest-order meson field fluctuations. These have to be included for consistency purposes since their omission (which corresponds to the mean field approximation) violates gauge invariance. This is due to the gauge transformation of the photon field, which is not balanced by the transformation of pion derivatives if these terms are omitted (as it is, if the derivative-terms are included).

With the generating functional at hand, the photon propagator can be calculated within these approximations. Its imaginary part is related to the photon emissivity by virtue of the MCLERRAN-TOIMELA formula. To obtain the imaginary part of the photon propagator a dedicated formula is used that was derived in [Wel83], which is applicable since the propagators corresponding to the approximation scheme used in this work have the same form as those used in [Wel83].

Finally, the nine dimensional phase space is reduced to four dimensions using delta distributions and symmetry arguments. At the end, the result ready for numerical evaluation is given. Supplementary material is collected in Appendices C – I.

4.1. Model definition

The central topic to be addressed in this thesis is to which extent the photon signal can reflect the peculiarities of the phase diagram. In order to discuss this issue for the QMM, the model Lagrangian (2.1.1) has to be supplemented with an electromagnetic sector. This is achieved, following [NS06, MCF10, ALZ15], by replacing the partial derivative ∂^μ with $U(1)$ -covariant derivatives $D^\mu = \partial^\mu - ieQA^\mu$ (e being the electromagnetic coupling and Q

the charge operator) and by adding the conventional kinetic term for the gauge field (the photon field) A^μ , with the field strength tensor $F^{\mu\nu} = \frac{i}{e}[D^\mu, D^\nu] = \partial^\mu A^\nu - \partial^\nu A^\mu$. This procedure corresponds to adding the following terms to the Lagrangian (2.1.1):

$$\begin{aligned}\mathcal{L}_{e\text{QMM}} &= \mathcal{L}_{\text{QMM}} + \mathcal{L}_{k\gamma} + \mathcal{L}_e, \\ \mathcal{L}_{k\gamma} &= -\frac{1}{4}F^{\mu\nu}F_{\mu\nu}, \\ \mathcal{L}_e &= N_c \bar{q}eQ\mathcal{A}q + ieA^\mu\pi^-\partial_\mu\pi^+ - ieA_\mu\pi^+\partial^\mu\pi^- - e^2A_\mu A^\mu\pi^+\pi^-. \end{aligned}\tag{4.1.1}$$

In (4.1.1) the action of the charge operator on the pions π^1 , π^2 and π^3 has been evaluated and the charge eigenstates π^\pm and π^0 have been projected out. The invariance of the pion interaction term in (2.1.2) under chiral transformations requires π^1 , π^2 and π^3 not to be the charge eigenstates, however a change of basis (onto the basis of charge eigenstates) can easily be performed on the pion fields and simultaneously on the matrices τ such that the product $\vec{\tau}\vec{\pi}$ keeps unchanged, *i.e.* $\tau^1\pi^1 + \tau^2\pi^2 + \tau^3\pi^3 = \tau^+\pi^+ + \tau^-\pi^- + \tau^0\pi^0$. The new π^a and τ^a are then defined according to

$$\begin{aligned}\tau^\pm &= \frac{1}{\sqrt{2}}(\tau^1 \pm i\tau^2), & \pi^\pm &= \frac{1}{\sqrt{2}}(\pi^1 \pm i\pi^2), \\ \tau^0 &= \tau^3, & \pi^0 &= \pi^3. \end{aligned}\tag{4.1.2}$$

Having defined the model thus far we can go ahead by calculating the Euclidean generating functional S_η for correlation functions.

4.2. Calculating the generating functional

The derivation in this chapter follows closely that presented in [WK17]. The path integral representation of the generating functional $S_\eta \equiv S[\eta_\sigma, \vec{\eta}_\pi, \eta_q, \bar{\eta}_q, \eta_\gamma^\mu]$ for the QMM is found by inserting the corresponding fields into the general formula (3.2.10):

$$\begin{aligned}S_\eta &= \int \mathcal{D}\sigma \mathcal{D}^3\pi \mathcal{D}\bar{q} \mathcal{D}q \mathcal{D}[A] \\ &\times \exp \left\{ i \int d^4x \mathcal{L}_{e\text{QMM}}(q, \bar{q}, \sigma, \vec{\pi}) + \bar{q}\eta_q + \bar{\eta}_q q + \eta_\sigma \sigma + \eta_a^\pi \pi^a + \eta_\mu^\gamma A^\mu \right\}, \end{aligned}\tag{4.2.1}$$

where $\mathcal{L}_{e\text{QMM}}$ is the Lagrangian given in (4.1.1) and $\eta_\sigma, \vec{\eta}_\pi, \eta_q, \bar{\eta}_q, \eta_\gamma^\mu$ denote the sources of the respective fields. (The measure $\mathcal{D}[A]$ refers to a path integral over gauge independent field configurations according to [FP67].) The source term for the pions, $\vec{\eta}_\pi \vec{\pi} = \eta_\pi^1 \pi_1 + \dots + \eta_\pi^3 \pi_3$, can be rewritten in terms of the charged pions according to $\vec{\eta}_\pi \vec{\pi} = \eta_\pi^- \pi^+ + \eta_\pi^+ \pi^- + \eta_\pi^0 \pi^0$

with $\eta_\pi^\pm = \sqrt{2}^{-1}(\eta_\pi^1 \mp i\eta_\pi^2)$, $\eta_\pi^0 = \eta_\pi^3$ and $\pi^{\pm,0}$ as in (4.1.2).

4.2.1. Integrating out the photons

The path integral over the photon field configurations, being quadratic in the fields (for the gauge fixing, the standard covariant choice $\mathcal{L}_{\text{fix}} = \xi^{-1}(\partial A)^2$ is made) can be evaluated exactly (*cf.* (3.2.11)).

First the action \mathcal{S} (supplemented with the gauge fixing term) and the source terms are split into those terms depending on the photon field and those that are independent:

$$\mathcal{S} = \int d^4x \mathcal{L}_{\text{eQMM}} \quad (4.2.2)$$

$$= \int d^4x \mathcal{L}_{\text{QMM}} + \int d^4x d^4y A^\mu(x) M_{\mu\nu}(x, y) A^\nu(y) + \int d^4x B_\mu A^\mu \quad (4.2.3)$$

with¹

$$M_{\mu\nu}(x, y) = \delta(x - y) \left[g_{\mu\nu} \square - (1 - \xi^{-1}) \partial_\mu \partial_\nu - e^2 \pi^+(x) \pi^-(y) g_{\mu\nu} \right] \quad (4.2.4)$$

$$B_\mu(x) = J_\mu^\gamma(x) + \eta_\mu^\gamma(x) \quad (4.2.5)$$

with the electromagnetic current

$$J_\gamma^\mu(z) = -N_c \bar{q}(z) e \hat{Q} \gamma^\mu q(z) - \pi^+(z) i e \partial^\mu \pi^-(z) + \pi^-(z) i e \partial^\mu \pi^+(z) \quad (4.2.6)$$

and the photon source η_μ^γ . Then the photon path integral can be evaluated as given in (3.2.11) and one obtains

$$\begin{aligned} S_\eta = & \int \mathcal{D}\sigma \mathcal{D}^3\pi \mathcal{D}\bar{q} \mathcal{D}q \sqrt{\det(G_\gamma^0)_{\mu\nu}} \\ & \times \exp \left\{ i \int d^4x (\mathcal{L}_{\text{QMM}} - \mu \bar{q} \gamma^0 q + \bar{\eta}_q q + \bar{q} \eta_q + \eta_\sigma \sigma + \bar{\eta}_\pi \bar{\pi}) \right\} \\ & \times \exp \left\{ i \int d^4z d^4z' (J_\gamma^\mu(z) + \eta_\gamma^\mu(z)) (G_\gamma^0)_{\mu\nu}(z, z') (J_\gamma^\nu(z') + \eta_\gamma^\nu(z')) \right\}, \end{aligned} \quad (4.2.7)$$

where the perturbative photon propagator $(G_\gamma^0)_{\mu\nu}$ is defined by

$$(G_\gamma^0)_{\mu\nu}^{-1} = M_{\mu\nu}. \quad (4.2.8)$$

¹ In order to bring $\int d^4x \mathcal{L}_{k,\gamma} + \mathcal{L}_{\text{fix}}$ into the form $A^\mu(x) M_{\mu\nu}(x, y) A^\nu(y)$ $\mathcal{L}_{k,\gamma}$ and \mathcal{L}_{fix} have to be integrated by parts.

The treatment of the photon path integral is part of many textbooks on quantum field theory, see *e.g.* [PS95, Sre07] for further details.

4.2.2. Integrating out the fermions

After having dealt with the photons the quarks are integrated out resulting in a functional determinant, which is written as the exponential of a functional trace (*i.e.* a momentum integral of traces over internal – *i.e.* DIRAC and flavor – indices) and an exponential with source terms:

$$\begin{aligned}
S_\eta = & \int \mathcal{D}\sigma \mathcal{D}^3\pi \sqrt{\det (G_\gamma^0)_{\mu\nu}} \\
& \times \exp \left\{ i \int d^4x \left(\mathcal{L}_{\text{kin},m} - U - \left(\text{Tr} \ln (G_q^0)_{\sigma,\pi} \right) (x, x) + \eta_\sigma \sigma + \vec{\eta}_\pi \vec{\pi} \right) \right\} \\
& \times \exp \left\{ i \int d^4z d^4z' \left(J_\gamma^\mu(z) + \eta_\gamma^\mu(z) \right) (G_\gamma^0)_{\mu\nu} (z, z') \left(J_\gamma^\nu(z') + \eta_\gamma^\nu(z') \right) \right. \\
& \quad \left. + \bar{\eta}_q(z) (G_q^0)_{\sigma,\pi} (z, z') \eta_q(z') \right\}
\end{aligned} \tag{4.2.9}$$

with the quark propagator defined by

$$(G_q^0)_{\sigma,\pi}^{-1} = i\not{\partial} - g(\sigma + i\gamma^5 \vec{\tau} \vec{\pi}). \tag{4.2.10}$$

Up to now the calculation is exact. But since the remaining mesonic part is not at all Gaussian, an approximation is necessary in order to proceed.

4.2.3. Derivative expansion of the fermion trace

The term $\text{Tr} \ln (G_q^0)_{\sigma,\pi}$ in (4.2.9) is expanded *w.r.t.* derivatives of the meson fields similar to [AF85] yielding

$$\text{Tr} \ln (G_q^0)_{\sigma,\pi} = \text{Tr} \ln \left[i\not{\partial} - m_q(\sigma, \vec{\pi}) \right] + \mathcal{O}(\partial\sigma, \partial\vec{\pi}), \tag{4.2.11}$$

$$m_q^2 = g^2(\sigma^2 + \vec{\pi}^2), \tag{4.2.12}$$

which coincides with the expression of a massive (with mass m_q) non-interacting FERMI gas. Applying standard steps, *cf. e.g.* [KG06], (4.2.11) can be evaluated further ultimately

yielding

$$\mathrm{Tr} \ln (G_q^0)_{\sigma,\pi} = \frac{1}{3(2\pi)^3} \int d^3p \frac{p^2}{E_q} (1 + n_F(E_q) + n_{\bar{F}}(E_q)) + \mathcal{O}(\partial\sigma, \partial\vec{\pi}), \quad (4.2.13)$$

$$E_q^2 = m_q^2 + p^2. \quad (4.2.14)$$

Assuming slowly varying meson fields the terms containing meson derivatives can be regarded small and are thus excluded from further calculations. Details can be found in Appendix C.1.1.

4.2.4. Quadratic approximation of the meson potential

The generating functional in (4.2.9) can be regarded as the generating functional of a purely mesonic theory with the potential V :

$$V(z) = U_{\mathrm{eff}}(\sigma(z), \pi(z)) - \int d^4z' \left(J_\gamma^\mu(z) (G_\gamma^0)_{\mu\nu}(z, z') J_\gamma^\nu(z') \right), \quad (4.2.15)$$

$$U_{\mathrm{eff}} = U(\sigma, \vec{\pi}) - \Omega_{\bar{q}q}(\sigma, \vec{\pi}), \quad (4.2.16)$$

$$\Omega_{\bar{q}q} = \frac{1}{3(2\pi)^3} \int d^3p \frac{p^2}{E_q} (1 + n_F(E_q) + n_{\bar{F}}(E_q)). \quad (4.2.17)$$

Now the effective potential U_{eff} is approximated by a quadratic potential \bar{U} defined by the conditions

$$\langle \bar{U} \rangle = \langle U_{\mathrm{eff}} \rangle, \quad (4.2.18)$$

$$0 = \left. \frac{\partial \bar{U}}{\partial \sigma, \pi} \right|_{\substack{\sigma=v \\ \vec{\pi}=0}}, \quad \text{with } v \text{ determined by} \quad 0 = \left\langle \frac{\partial U_{\mathrm{eff}}(v + \Delta, \vec{\pi})}{\partial \Delta, \pi} \right\rangle. \quad (4.2.19)$$

The condition (4.2.18) fixes the zero-order coefficients in \bar{U} and (4.2.19) the first-order coefficients. For convenience the σ field is shifted by its thermal expectation value v and the shifted field $\Delta = \sigma - v$ is used as the new dynamical field. The non-vanishing second order coefficients (which we name m_σ^2 and m_π^2) have to be chosen according to

$$\frac{\partial^2 \bar{U}}{\partial \Delta^2} \equiv m_\sigma^2 = \left\langle \frac{\partial^2 U_{\mathrm{eff}}(v + \Delta)}{\partial \Delta^2} \right\rangle, \quad \frac{\partial^2 \bar{U}}{\partial \pi^2} \equiv m_\pi^2 = \left\langle \frac{\partial^2 U_{\mathrm{eff}}}{\partial \pi^2} \right\rangle \quad (4.2.20)$$

for being consistent to the respective propagator pole mass, calculated for the approximated

theory with Lagrangian

$$\bar{\mathcal{L}} = \mathcal{L}_{\text{kin},m} - \bar{U}(\Delta, \pi). \quad (4.2.21)$$

The second-order mixed term in U_{eff} vanishes, since U_{eff} is an even function of π as the inspection of (2.1.4), (4.2.12) and (4.2.16) reveals. The thus defined approximative potential

$$\bar{U} = \langle U_{\text{eff}} \rangle + \frac{1}{2}m_\pi^2(\bar{\pi}^2 - \langle \bar{\pi}^2 \rangle) + \frac{1}{2}m_\sigma^2(\Delta^2 - \langle \Delta^2 \rangle) \quad (4.2.22)$$

induces via the accordingly approximated partition function \bar{Z} a probability distribution for the meson fields

$$\begin{aligned} \rho(\Delta, \bar{\pi}) &= \bar{Z}^{-1} \exp \left\{ \int d^4x \mathcal{L}_{\text{kin},m} - \bar{U} \right\} \\ &= \frac{1}{\sqrt{2\pi\langle \Delta^2 \rangle}} \exp \left\{ \frac{-\Delta^2}{2\langle \Delta^2 \rangle} \right\} \sqrt{\left(\frac{3}{2\pi\langle \bar{\pi}^2 \rangle} \right)^3} \exp \left\{ \frac{-3\bar{\pi}^2}{2\langle \bar{\pi}^2 \rangle} \right\}, \end{aligned} \quad (4.2.23)$$

which is independent of the direction of π . Integrating over the angles yields for the probability distribution

$$\rho(\Delta, |\bar{\pi}|) = \frac{1}{\sqrt{2\pi\langle \Delta^2 \rangle}} \exp \left\{ \frac{-\Delta^2}{2\langle \Delta^2 \rangle} \right\} \sqrt{\frac{2}{\pi} \left(\frac{3}{\langle \bar{\pi}^2 \rangle} \right)^3} |\bar{\pi}|^2 \exp \left\{ \frac{-3\bar{\pi}^2}{2\langle \bar{\pi}^2 \rangle} \right\}, \quad (4.2.24)$$

where it was already applied that all relevant functions are even functions of $\vec{\pi}$. This leads to the following form of the variances ($\text{var } f = \langle f^2 \rangle - \langle f \rangle^2$) for the meson fields:

$$\langle \Delta^2 \rangle = \text{var } \sigma = \frac{1}{(2\pi)^3} \int d^3p \left(\frac{1}{2E_\sigma} + \frac{1}{E_\sigma} n_B(E_\sigma) \right), \quad (4.2.25)$$

$$\langle \bar{\pi}^2 \rangle = 3 \text{var } \pi_i = \frac{3}{(2\pi)^3} \int d^3p \left(\frac{1}{2E_\pi} + \frac{1}{E_\pi} n_B(E_\pi) \right) \quad (4.2.26)$$

with the dispersion relations $E_{\sigma,\pi}^2 = m_{\sigma,\pi}^2 + \vec{p}^2$. With (4.2.24) the ensemble averages $\langle f \rangle$ of a meson dependent function can be calculated according to

$$\langle f(\sigma, \bar{\pi}) \rangle = \int d\sigma \int d|\bar{\pi}| \rho(\sigma, |\bar{\pi}|) f(\sigma, |\bar{\pi}|), \quad (4.2.27)$$

where f is only allowed to depend on $|\bar{\pi}|$, since that is the only case relevant for the calculation. The quark source term in (4.2.9) is treated by expanding $(G_q^0)_{\sigma,\pi}$ *w.r.t.* the meson fields (*cf.* Appendix D) and replacing the meson fields afterwards with the variation

w.r.t. the corresponding sources.

Equations (4.2.19), (4.2.20), (4.2.25) and (4.2.26) constitute a set of five equations for the unknown m_σ , m_π , v , $\langle \Delta^2 \rangle$ and $\langle \pi^2 \rangle$. The complete set of equations is given in Appendix E (Eqs. (E.1.1) – (E.1.6)). For a detailed derivation of this set of equations, see [MME04].

4.2.5. Isolating the electromagnetic contribution to V

Due to the relatively small electromagnetic coupling the electromagnetic contribution in (4.2.15) is expected to be only a small perturbation of S_η . Therefore the photon propagator $(G_\gamma^0)_{\mu\nu}$ is expanded (*cf.* Appendix D) *w.r.t.* e^2 and afterwards the exponential of the electromagnetic source term (with the accordingly approximated $(G_\gamma^0)_{\mu\nu}$) is expanded up to linear order of the argument yielding:

$$\begin{aligned} & \exp \left\{ i \int d^4z d^4z' (J_\gamma^\mu(z) + \eta_\gamma^\mu(z)) (G_\gamma^0)_{\mu\nu}(z, z') (J_\gamma^\nu(z') + \eta_\gamma^\nu(z')) \right\} \\ &= 1 + i \int d^4z d^4z' (J_\gamma^\mu(z) + \eta_\gamma^\mu(z)) \left(\overline{G}_{\mu\nu}^\gamma(z, z') \right. \\ & \quad \left. + e^2 \int d^4z'' \overline{G}_{\mu\rho}^\gamma(z, z'') g^{\rho\kappa} \pi^+(z'') \pi^-(z'') \overline{G}_{\kappa\nu}^\gamma(z'', z') + \mathcal{O}(e^4) \right) \\ & \quad \left(J_\gamma^\nu(z') + \eta_\gamma^\nu(z') \right) + \mathcal{O}(J_\gamma^4). \end{aligned} \quad (4.2.28)$$

Since $J_\gamma^\mu = \mathcal{O}(e)$ the terms up to $\mathcal{O}(e^2)$ are

$$\begin{aligned} & \exp \left\{ i \int d^4z d^4z' (J_\gamma^\mu(z) + \eta_\gamma^\mu(z)) (G_\gamma^0)_{\mu\nu}(z, z') (J_\gamma^\nu(z') + \eta_\gamma^\nu(z')) \right\} \\ &= 1 + i \int d^4z d^4z' (J_\gamma^\mu(z) + \eta_\gamma^\mu(z)) \overline{G}_{\mu\nu}^\gamma(z, z') (J_\gamma^\nu(z') + \eta_\gamma^\nu(z')) \\ & \quad + i \int d^4z d^4z' d^4z'' \eta_\gamma^\mu(z) e^2 \overline{G}_{\mu\rho}^\gamma(z, z'') g^{\rho\kappa} \pi^+(z'') \pi^-(z'') \eta_\gamma^\nu(z) \overline{G}_{\kappa\nu}^\gamma(z'', z') \\ & \quad + \mathcal{O}(e^3), \end{aligned} \quad (4.2.29)$$

with $\overline{G}_{\mu\rho}^\gamma$ being the bare photon propagator

$$(\overline{G}_{\mu\nu}^\gamma)^{-1} = [g_{\mu\nu} \square - (1 - \xi^{-1}) \partial_\mu \partial_\nu] \quad (4.2.30)$$

connected to $(G_\gamma^0)_{\mu\nu}$ defined in (4.2.8) by $(\overline{G}_{\mu\nu}^\gamma)^{-1} = ((G_\gamma^0)_{\mu\nu})^{-1} + e^2 \pi^+ \pi^- g_{\mu\nu}$. Finally, the fields are replaced by the variations *w.r.t.* the corresponding sources, *i.e.* $\pi^\pm(z) \rightarrow \delta/\delta\eta_\pi^\mp(z)$, $q(z) \rightarrow \delta/\delta\bar{\eta}_q(z)$ and $\bar{q}(z) \rightarrow \delta/\delta\eta_q(z)$, and (4.2.29) can be pulled out of the path integral

(4.2.9).

4.2.6. Integrating out the meson fields

The remaining integrand of the path integrals in (4.2.9) is Gaussian yielding

$$\begin{aligned}
S_\eta &= \sqrt{\det (G_\gamma^0)_{\mu\nu}} \sqrt{\det G_\pi}^3 \sqrt{\det G_\sigma} \\
&\times \exp \left\{ i \int d^4z d^4z' \left(\widehat{J}_\gamma^\mu(z) + \eta_\gamma^\mu(z) \right) \left(\widehat{G}_\gamma^0 \right)_{\mu\nu}(z, z') \left(\widehat{J}_\gamma^\nu(z') + \eta_\gamma^\nu(z') \right) \right\} \\
&\times \exp \left\{ i \int d^4z d^4z' \bar{\eta}_q(z) \left(\widehat{G}_q^0 \right)_{\sigma,\pi}(z, z') \eta_q(z') + \eta_\sigma(z) G_\sigma(z, z') \eta_\sigma(z') \right. \\
&\quad \left. + \eta_\pi^+(z) G_\pi(z, z') \eta_\pi^-(z') + \eta_\pi^0(z) G_\pi(z, z') \eta_\pi^0(z') \right\},
\end{aligned} \tag{4.2.31}$$

with $\left(\widehat{G}_q^0 \right)_{\sigma,\pi}$, $\left(\widehat{G}_\gamma^0 \right)_{\mu\nu}$ and \widehat{J}_γ^μ obtained from $(G_q^0)_{\sigma,\pi}$, $(G_\gamma^0)_{\mu\nu}$ and J_γ^μ by replacing the fields with the variations *w.r.t.* the corresponding sources, *i.e.* $\sigma \rightarrow \delta/\delta\eta_\sigma$, $\pi^a \rightarrow \delta/\delta\eta_{\pi^a}$, $q(z) \rightarrow \delta/\delta\bar{\eta}_q(z)$ and $\bar{q}(z) \rightarrow \delta/\delta\eta_q(z)$. The momentum space meson propagators can be found by an explicit evaluation of the Gaussian meson path integrals:

$$G_\pi^{a\bar{b}}(p) = \frac{-i\delta^{ab}}{p^2 - m_\pi^2}, \quad G_\sigma(p) = \frac{-i}{p^2 - m_\sigma^2} \tag{4.2.32}$$

with $a, b \in \{0, +, -\}$ denoting the charge of the respective pions, $\bar{b} \equiv -b$ and the mass parameters according to (4.2.20).

4.3. Calculating the imaginary part of the photon propagator

4.3.1. Calculating the photon propagator

The full photon propagator (within the above approximations) \mathcal{G} can be calculated by varying S_η *w.r.t.* the photon sources:

$$\mathcal{G}_{\mu\nu}^\gamma(x, y) = \frac{1}{S} (-i)^2 \frac{\delta^2}{\delta\eta_\gamma^\mu(x) \delta\eta_\gamma^\nu(y)} S_\eta \Big|_{\eta=0}. \tag{4.3.1}$$

Executing the variations yields

$$G_{\mu\nu}^\gamma(x, y) = \overline{G}_{\mu\nu}^\gamma(x, y) + e^2 \frac{1}{S} \int d^4z \overline{G}_{\mu\alpha}^\gamma(x, z) \frac{\delta}{\delta\eta_\pi^-(z)} \frac{\delta}{\delta\eta_\pi^+(z)} g^{\alpha\beta} \overline{G}_{\beta\nu}^\gamma(z, y) S_\eta \Big|_{\eta=0} \quad (4.3.2)$$

$$+ \frac{1}{S} \int d^4z \int d^4z' \overline{G}_{\mu\alpha}^\gamma(x, z) \widehat{J}_\gamma^\alpha(z) \widehat{J}_\gamma^\beta(z') \overline{G}_{\beta\nu}^\gamma(z', y) S_\eta \Big|_{\eta=0}.$$

First the variations *w.r.t.* the fermionic sources hidden within the \widehat{J}_γ terms are executed. To achieve this the $\widehat{J}_\gamma^\alpha(z)$ and $\widehat{J}_\gamma^\beta(z')$ are expanded. Furthermore, one notes that any pair of fermion derivatives which includes both types, $\delta/\delta\eta$ as well as $\delta/\delta\bar{\eta}$, acting on S_η gives a factor $(G_q^0)_{\sigma,\pi}$ with the space-time arguments being that of the respective fermion source variations, since the fermionic sources appear only as $\exp\{\iint d^4z d^4z' \bar{\eta}_q(z) \widehat{(G_q^0)}_{\sigma,\pi}(z, z') \eta_q(z')\}$ in S_η .

If the external points x and y are represented by the end of the external legs, the variables of integration z and z' by dots, $\widehat{(G_q^0)}_{\sigma,\pi}$ by a double line connecting its arguments and the (not yet) evaluated derivatives *w.r.t.* mesonic sources by small dots, (4.3.2) can be represented diagrammatically as exhibited in Fig. 4.2 (upper panel).

Inspecting the upper panel of Fig. 4.2 one notes that several diagrams are not connected which seems rather unconventional for the representation of the photon propagator. It is worth stressing that the upper panel of Fig. 4.2 represents an intermediate step of the calculation and that the disconnected parts can (and will) be connected with meson propagators in the subsequent steps of the calculations. Comparing the upper panel of Fig. 4.2 with (4.3.2) one can identify the first two diagrams with the first two terms in (4.3.2). The rest of the diagrams corresponds to the $\mathcal{O}(e^2)$ contributions of the second line of (4.3.2) with the derivatives *w.r.t.* the fermionic sources carried out.

The fermion propagators $\widehat{(G_q^0)}_{\sigma,\pi}$ are expanded according to (D.1.6). This expansion follows from the decomposition of $(G_q^0)_{\sigma,\pi}$ into a part independent of the dynamical fields Δ and π (but dependent on the average σ field) and an interaction part that depends on Δ and π according to

$$\left((G_q^0)_{\sigma,\pi}\right)^{-1} = \left((G_q^0)_{v,0}\right)^{-1} - g(\Delta + i\gamma^5 \vec{\tau} \vec{\pi}), \quad (4.3.3)$$

$$\left((G_q^0)_{v,0}\right)^{-1} = i\cancel{\partial} - g\langle\sigma\rangle. \quad (4.3.4)$$

This expansion can be represented diagrammatically as depicted in Fig. 4.1. After expanding the fermion propagators the meson source derivatives are evaluated. Every pair of

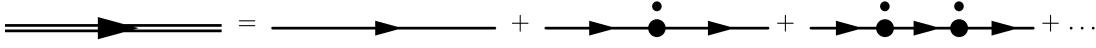


Figure 4.1.: Diagrammatic representation of the quark propagator $\widehat{(G_q^0)}_{\sigma,\pi}$ represented by the double line. Single lines represent $(G_q^0)_{v,0}$ while the dots next to the vertices stand for functional derivatives *w.r.t.* meson sources and the vertices themselves for either ig or $ig\gamma^5\tau^a$ depending on the type of meson source derivative. Precisely, each vertex with dot stands for the expression $ig\delta/\delta\eta_\sigma + ig\gamma^5\tau^a\delta/\delta\eta_\pi^{\bar{a}}$, with $\bar{a} \equiv -a$ as in (4.2.32).

derivatives *w.r.t.* meson sources reduces to a propagator of the respective meson (provided both variations are *w.r.t.* the same field sources). The resulting expression can be represented diagrammatically according to the lower panel of Fig. 4.2. There, each solid line represents $(G_q^0)_{v,0}$ and each wiggly line refers to $\overline{G}_{\mu\nu}^\gamma$. For brevity of notation the meson propagators and vertices are combined such that each dashed line stands for $G_\sigma + G_\pi$ and each dot means the corresponding vertex factor.

4.3.2. Determining the imaginary part of the photon propagator

The propagators G_π , G_σ and $(G_q^0)_{v,0}$, *cf.* (4.2.32) and (4.3.4), have the form discussed in [Wel83]. Following [Wel83] the imaginary part of the diagrams in Fig. 4.2 is calculated by cutting through each diagram in any possible way that separates the two vertices connected to external photon lines. Such a procedure leads to sets of (simpler) diagrams (most of which are at tree-level for the diagrams in the lower panel of Fig. 4.2) corresponding to processes of the type $\phi_1, \dots, \phi_a \rightarrow \Phi_1, \dots, \Phi_b + \gamma$ with a incoming fields and $b+1$ outgoing fields one of which is a photon. Denoting the diagrams in Fig. 4.2 by $\mathcal{M}_{\phi_1+\dots+\phi_a \rightarrow \Phi_1+\dots+\Phi_b+\gamma}^{(i)}$ and the diagrams obtained from cutting these by $\mathcal{M}_{\phi_1+\dots+\phi_a \rightarrow \Phi_1+\dots+\Phi_b+\gamma}^{(i,j)}$ the imaginary part of the photon propagator $\text{Im}\mathcal{G}_{\gamma,\text{ret}}^{\mu\nu} \sim \sum_i \text{Im}\mathcal{M}_{\phi_1+\dots+\phi_a \rightarrow \Phi_1+\dots+\Phi_b+\gamma}^{(i)}$ can be expressed according to [Wel83] as

$$\begin{aligned} \text{Im}\mathcal{G}_{\gamma,\text{ret}}^{\mu\nu} &= 2 \sum_{a,b} \int d\Omega_{ab} |\mathcal{M}_{\phi_1+\dots+\phi_a \rightarrow \Phi_1+\dots+\Phi_b+\gamma}^{(i,j)}|^2 \\ &\quad \times n_{F/B}^{(1)} \cdots n_{F/B}^{(a)} (1 \mp n_{F/B}^{(1)}) \cdots (1 \mp n_{F/B}^{(b)}) (e^{\omega/T} - 1), \\ \int d\Omega_{ab} &= \int \frac{d^3p_1}{2E_p^{(1)}(2\pi)^3} \cdots \frac{d^3p_a}{2E_p^{(a)}(2\pi)^3} \frac{d^3q_1}{2E_q^{(1)}(2\pi)^3} \cdots \frac{d^3q_b}{2E_q^{(b)}(2\pi)^3} \\ &\quad \times (2\pi)^4 \delta\left(k - \sum_i p^i + \sum_j q^j\right) \end{aligned} \quad (4.3.5)$$

with $n_{F/B}^{(i)}$ being FERMI or BOSE distribution functions (depending on the spin of the particle i). The upper sign in the $(1 \mp n_{F/B}^{(i)})$ corresponds to FERMI and the lower sign to

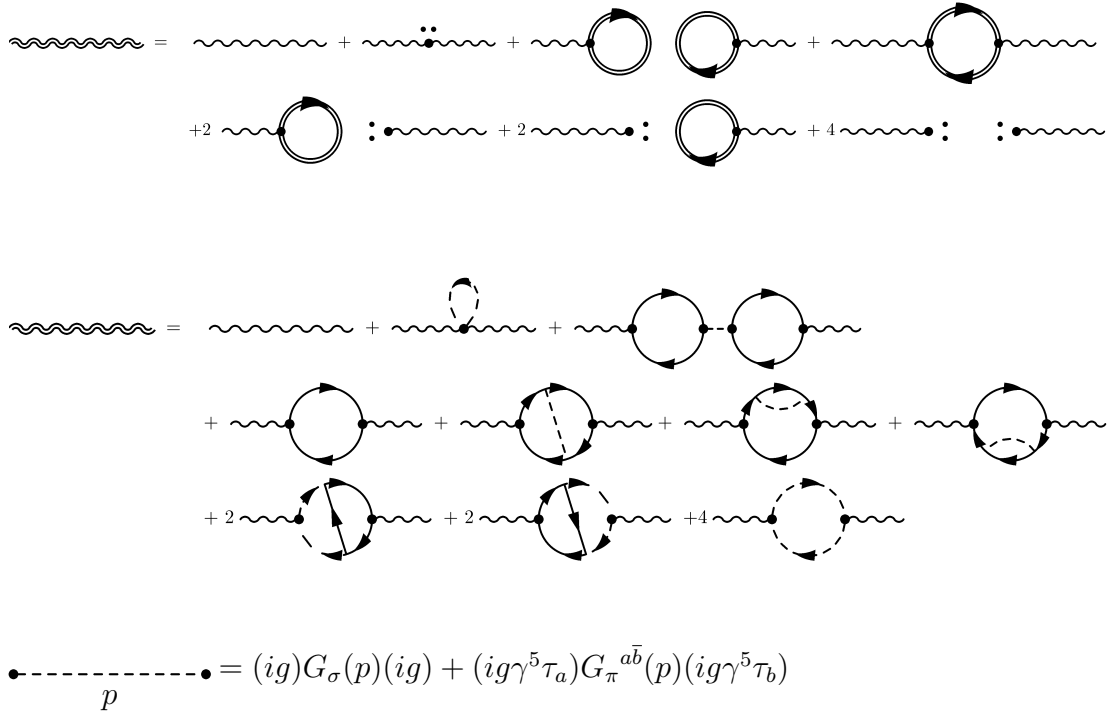


Figure 4.2.: Diagrammatic representation of the electromagnetic current term in (4.3.2) after applying the fermion source derivatives and setting the fermion sources zero (upper panel) and after additionally executing all meson source derivatives, both written down explicitly as dots next to a vertex and implicitly contained in the summed fermion propagator (middle panel). Solid double lines represent the summed fermion propagator $\widehat{(G_q^0)}_{\sigma,\pi}$, the double wavy line represents the full photon propagator up to $\mathcal{O}(e^2)$ and $\mathcal{O}(g^2)$, the single solid lines represents $(G_q^0)_{v,0}$, single wavy lines the perturbative photon propagator $\widehat{G}_{\mu\nu}^\gamma$, dashed lines represent a sum over all meson field propagators G_π, G_σ connected to the fitting vertices (dots), as shown in the lower panel. Arrows on dashed lines denote the direction of charge flow (they appear only at lines connected to a photon vertex, so that only charged pions contribute to the diagram, for which the direction of charge flow is well defined).

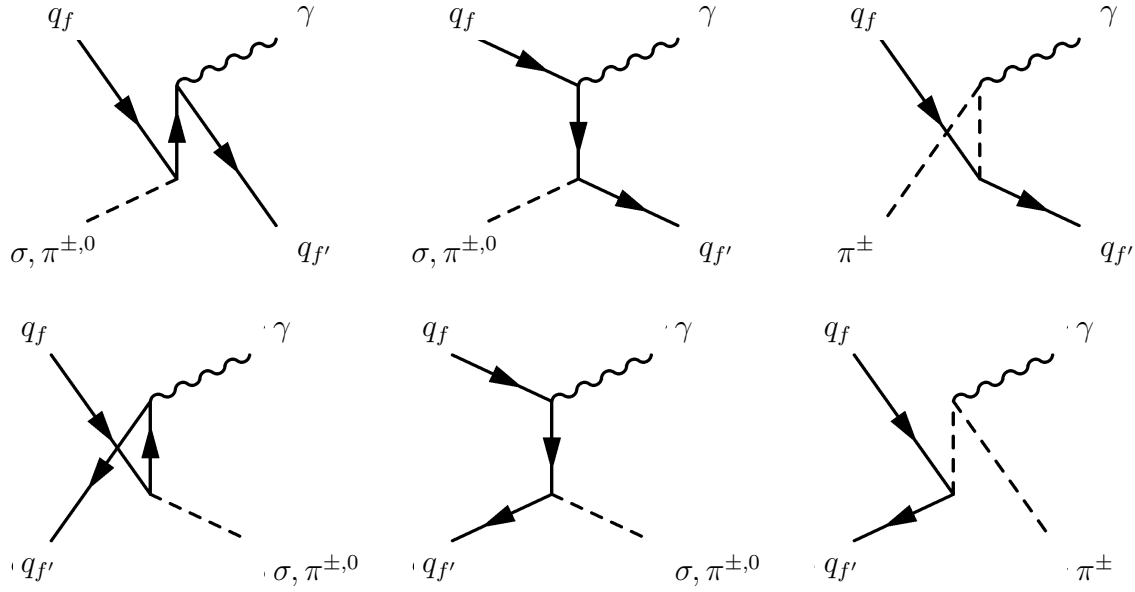


Figure 4.3.: Tree-level diagrams of the reactions (4.3.6) – (4.3.8). Top row: diagrams for COMPTON scattering off quarks; bottom row: annihilations. The matrix elements for COMPTON scattering off antiquarks can be obtained by inverting the direction of the fermion arrows. Note that in the third column there is no σ meson and no neutral pion, since these are uncharged. The indices f and f' at the external quark lines denote the quark flavor. Color and spin indices are suppressed for ease of notation.

BOSE statistics. The summands in (4.3.5) can be sorted *w.r.t.* the number of participating fields ($= a + b + 1$). The inspection of the phase space regions over which one has to integrate on the right hand side of (4.3.5) yields that the summands with $n + N \leq 2$ are zero because the phase space vanishes in these cases at least if all fields except the photons are massive (as it is the case in our model). The first non-zero terms have $a + b = 3$ and correspond to $2 \rightarrow 2$ processes

$$q_i + \sigma, \pi^a \rightarrow q_j + \gamma \quad (\text{COMPTON scattering off quarks}), \quad (4.3.6)$$

$$\bar{q}_i + \sigma, \pi^a \rightarrow \bar{q}_j + \gamma \quad (\text{COMPTON scattering off antiquarks}), \quad (4.3.7)$$

$$q_i + \bar{q}_j \rightarrow \sigma, \pi^a + \gamma \quad (\text{annihilations}) \quad (4.3.8)$$

with the cut diagrams (denoted $M^{(i,j)}$ in (4.3.5)) collected in Fig. 4.3 and given in Appendix F.

4.4. Photon emission rate

From the imaginary part of the photon propagator the photon rate can be determined according to the MCLERRAN-TOIMELA formula (3.1.1), *cf.* Appendix G for a sketch of the derivation. With (4.3.5) we get as the leading terms *w.r.t.* the number of participating particles in the above mentioned expansion

$$\begin{aligned} \omega \frac{d^7 N}{d^3 k d^4 x} &= 2 \frac{g_{\mu\nu}}{(2\pi)^{12}} \int \frac{d^3 p_1}{2E_p^{(1)}} \frac{d^3 p_2}{2E_p^{(2)}} \frac{d^3 q}{2E_q} |\mathcal{M}_{\phi_1+\phi_2 \rightarrow \Phi_3+\gamma}^{(i,j)}|^2 \\ &\times (2\pi)^4 \delta(k+q-p_1-p_2) n_{F/B}^{(1)}(p_1) n_{F/B}^{(2)}(p_2) (1 \mp n_{F/B}^{(3)}(q)) \end{aligned} \quad (4.4.1)$$

which resembles the formula for the production of photons in $2 \rightarrow 2$ processes derived from kinetic theory.

4.4.1. Phase space integration

The final step of the calculation is the evaluation of the phase space integral in (4.4.1). A detailed calculation can be found in Appendix H. Here, only the most important steps are pointed out as well as the final result ready for use in a numerical evaluation.

The q integration is evaluated by the use of the three-momentum conserving δ -distribution. Then the MANDELSTAM variables s and t are introduced by inserting $1 = \int ds \delta(s - (p+q)^2)$ and $1 = \int dt \delta(t - (q-k)^2)$. Afterwards both p_i integrations are transformed into spherical coordinates and the three remaining δ distributions are applied to calculate two of the azimuthal integrations and one of the polar integrations. The second polar integration is trivial since the remaining integrand is independent of this angle. The integrations *w.r.t.* the absolute value of the momenta can be transformed into the corresponding energy integrations. The last step is the simplification of the denominator, which is a straightforward yet lengthy calculation. After that the final results are:

COMPTON processes

$$\begin{aligned} \omega \frac{d^7 N}{d^3 k d^4 x} &= \frac{1}{16\omega(2\pi)^7} \int_{s_0}^{\infty} \frac{ds}{s - m_q^2} \int_{t^-}^{t^+} dt |M(s, t)|^2 \\ &\times \int_{\nu_{\min}}^{\infty} d\nu \int_{E^-}^{E^+} dE \frac{n_F(E) n_B(\nu - E) \bar{n}_F(\omega - \nu)}{\sqrt{(E - E^-)(E^+ - E)}}, \end{aligned} \quad (4.4.2)$$

$$\nu_{\min} = \frac{s - m_q^2}{4\omega} + \frac{\omega s}{s - m_q^2}, \quad (4.4.3)$$

$$s_0 = (m_q + m_{\pi,\sigma})^2, \quad (4.4.4)$$

$$u_{\pm} = m_q^2 - \frac{s - m_q^2}{2s} \left((s + m_q^2 - m_{\pi,\sigma}^2) \pm \sqrt{\lambda(s, m_q^2, m_{\pi,\sigma}^2)} \right), \quad (4.4.5)$$

$$t_{\pm} = 2m_q^2 + m_{\pi,\sigma}^2 - s - u_{\mp}, \quad (4.4.6)$$

$$\Delta^2 = 4\omega(s - m_q^2)s(u_+ - u)(u - u_-)(\nu - \nu_{\min}), \quad (4.4.7)$$

$$E^{\pm} = \bar{E} \pm |\Delta|, \quad (4.4.8)$$

$$\bar{E} = \frac{(s + m_q^2 - m_{\pi,\sigma}^2)\omega(s - m_q^2) + (u - m_q^2)(2\omega s - \nu(s - m_q^2))}{(s - m_q^2)^2}, \quad (4.4.9)$$

where λ is a frequently occurring kinematical function, *cf.* Appendix B.5, defined by

$$\lambda(x, y, z) := x^2 + y^2 + z^2 - 2xy - 2xz - 2yz \quad (4.4.10)$$

and n_B , n_F and \bar{n}_F are the distribution functions for bosons, fermions and anti-fermions, respectively.

Annihilations

$$\begin{aligned} \omega \frac{d^7 N}{d^3 k d^4 x} &= \frac{1}{16\omega(2\pi)^7} \int_{s_0}^{\infty} \frac{ds}{s - m_{\pi,\sigma}^2} \int_{t^-}^{t^+} dt |M(s, t)|^2 \\ &\times \int_{\nu_{\min}}^{\infty} d\nu \int_{E^-}^{E^+} dE \frac{n_F(E) \bar{n}_F(\nu - E) n_B(\omega - \nu)}{\sqrt{(E - E^-)(E^+ - E)}}, \end{aligned} \quad (4.4.11)$$

$$\nu_{\min} = \frac{s - m_{\pi,\sigma}^2}{4\omega} + \frac{\omega s}{s - m_{\pi,\sigma}^2}, \quad (4.4.12)$$

$$s_0 = \max \{ 4m_q^2, m_{\pi,\sigma}^2 \}, \quad (4.4.13)$$

$$u_{\pm} = m_q^2 - \frac{s - m_{\pi,\sigma}^2}{2} \left(1 \pm \sqrt{s^2 - 4sm_q} \right), \quad (4.4.14)$$

$$t_{\pm} = 2m_q^2 + m_{\pi,\sigma}^2 - s - u_{\mp}, \quad (4.4.15)$$

$$\Delta^2 = 4\omega(s - m_{\pi,\sigma}^2)s(u_+ - u)(u - u_-)(\nu - \nu_{\min}), \quad (4.4.16)$$

$$E^{\pm} = \bar{E} \pm |\Delta|, \quad (4.4.17)$$

$$\bar{E} = \frac{s\omega(s - m_{\pi,\sigma}^2) + (u - m_q^2)(2\omega s - \nu(s - m_{\pi,\sigma}^2))}{(s - m_{\pi,\sigma}^2)^2}; \quad (4.4.18)$$

anti-COMPTON processes

$$\begin{aligned} \omega \frac{d^7 N}{d^3 k d^4 x} &= \frac{1}{16\omega(2\pi)^7} \int_{s_0}^{\infty} \frac{ds}{s - m_q^2} \int_{t^-}^{t^+} dt |M(s, t)|^2 \\ &\times \int_{\nu_{\min}}^{\infty} d\nu \int_{E^-}^{E^+} dE \frac{\bar{n}_F(E) n_B(\nu - E) n_F(\omega - \nu)}{\sqrt{(E - E^-)(E^+ - E)}} \end{aligned} \quad (4.4.19)$$

and with ν_{\min} , s_0 , u_{\pm} , t_{\pm} , Δ , E^{\pm} and \bar{E} as for the COMPTON case.

4.5. BOLTZMANN approximation

In large parts of the phase diagram, it turns out that the distribution functions can be approximated by their classical analogon *i.e.* by the BOLTZMANN distribution function:

$$n_F(E, T, \mu) \rightarrow e^{-(E-\mu)/T}, \quad n_B(E, T) \rightarrow e^{-E/T}. \quad (4.5.1)$$

With these replacements, (4.4.1) simplifies considerably (see Appendix I) and one obtains

$$\omega \frac{d^7 N}{d^3 k d^4 x} = C_b \times \begin{cases} e^{\mu/T} \int_{s_0}^{\infty} \frac{ds}{s - m_q^2} e^{-\nu_{\min}(s)/T} \lambda(s, m_q^2, m_{\pi, \sigma}^2) \sigma_{q\sigma/\pi \rightarrow q\gamma}(s) & \text{COMPTON,} \\ \int_{s_0}^{\infty} \frac{ds}{s - m_{\sigma, \pi}^2} e^{-\nu_{\min}(s)/T} s(s - 4m_q^2) \sigma_{q\bar{q} \rightarrow \sigma/\pi \gamma}(s) & \text{annihilations,} \\ e^{-\mu/T} \int_{s_0}^{\infty} \frac{ds}{s - m_q^2} e^{-\nu_{\min}(s)/T} \lambda(s, m_q^2, m_{\pi, \sigma}^2) \sigma_{\bar{q}\sigma/\pi \rightarrow \bar{q}\gamma}(s) & \text{anti-COMPTON} \end{cases} \quad (4.5.2)$$

with

$$\nu_{\min}(s) = \frac{s - (m^{\text{out}})^2}{4\omega} + \frac{\omega s}{s - (m^{\text{out}})^2} \quad (4.5.3)$$

being the minimal incoming (and outgoing) total energy in the rest frame of the heat bath, $C_b = T(2\pi)^{-5}/(4\omega)$ and λ defined according to (4.4.10). The rates (4.5.2) are dominated by the exponential under the integral. The function $\nu_{\min}(s)$ has a minimum at

$$s_1 = 2\omega m^{\text{out}} + (m^{\text{out}})^2 \quad (4.5.4)$$

and there takes the value

$$\nu_{\min}(s_1) = m^{\text{out}} + \omega, \quad (4.5.5)$$

with m^{out} being the mass of the outgoing partner of the photon. The second derivative at the minimum is

$$\nu''_{\min}(s_1) = \frac{1}{4\omega^2 m^{\text{out}}}. \quad (4.5.6)$$

Now, two cases are to be distinguished: (a) $s_1 \geq s_0$ and (b) $s_1 < s_0$. Although both cases lead to very different dependencies of the rates on the photon frequency ω , they are based on the same recipe, namely ν_{\min} is TAYLOR-expanded around its minimum² in the domain of integration up to the first non-vanishing term beyond zero order.

4.5.1. The Gaussian approximation (a)

If $s_1 \geq s_0$ the minimum of ν_{\min} is in the domain of integration. Following the above mentioned recipe ν_{\min} is expanded around s_1 . Because the first derivative vanishes at the minimum the expansion is evaluated to second order in $(s - s_1)$ yielding

$$e^{-\nu_{\min}/T} \approx e^{-(m^{\text{out}}+\omega)/T} e^{-\frac{(s-s_1)^2}{8\omega^2 m^{\text{out}} T}}. \quad (4.5.7)$$

Assuming a slow variation of $|\mathcal{M}|^2$, and the other s -dependent factors in (4.5.2) in the vicinity of s_1 , one arrives at

$$\omega \frac{d^7 N}{d^3 k d^4 x} = C_g \times \begin{cases} \frac{e^{-(m_q - \mu)/T}}{\sqrt{m_q}} \lambda(s_1, m_q^2, m_{\pi, \sigma}^2) \sigma_{q\sigma/\pi \rightarrow q\gamma}(s_1) & \text{COMPTON,} \\ \frac{e^{-m_{\pi, \sigma}/T}}{\sqrt{m_{\pi, \sigma}}} s_1 (s_1 - 4m_q^2) \sigma_{q\bar{q} \rightarrow \sigma/\pi \gamma}(s_1) & \text{annihilations,} \\ \frac{e^{-(m_q + \mu)/T}}{\sqrt{m_q}} \lambda(s_1, m_q^2, m_{\pi, \sigma}^2) \sigma_{q\sigma/\pi \rightarrow q\gamma}(s_1) & \text{anti-COMPTON} \end{cases} \quad (4.5.8)$$

with $C_g := T^{3/2} e^{-\omega/T} (2\pi)^{-9/2} / (4\omega)$. If $m_{\sigma, \pi} > 2m_q$ then $s_1 > s_0$ for all values of ω . In this case the annihilation rate diverges for $\omega \rightarrow 0$.

Since s_1 depends monotonously on ω but s_0 is ω -independent, one can find for any s_0 some value ω_1 for which $s_1(\omega) > s_0$ for all $\omega > \omega_1$. Therefore, this case can be regarded as the high (photon) energy approximation of the rates.

² Since the relevant term in the rate formula (4.5.2) is $\exp\{-\nu_{\min}/T\}$ this minimum corresponds to a maximum of $\exp\{-\nu_{\min}/T\}$ and hence is an estimate for the region where the integrand of the s integration in (4.5.2) is largest.

4.5.2. The exponential approximation (b)

When the minimum of ν_{\min} is not in the domain of integration, *i.e.* $s_1 < s_0$, a different approximation has to be applied: In this case ν_{\min} is smallest at the lower boundary s_0 of the s integration, which is thus chosen as the expansion point. Since the first derivative does not vanish there, an expansion up to linear order is sufficient yielding

$$e^{-\nu_{\min}/T} \approx e^{-a/T - b/T(s-s_0)}, \quad (4.5.9)$$

$$a = \nu_{\min}(s_0), \quad (4.5.10)$$

$$b = \frac{-\omega(m^{\text{out}})^2}{(s_0 - (m^{\text{out}})^2)^2} + \frac{1}{4\omega}. \quad (4.5.11)$$

Assuming that $|\mathcal{M}|^2$ and the other s -dependent factors in (4.5.2) vary slowly with s one obtains.

$$\omega \frac{d^7 N}{d^3 k d^4 x} = \frac{T^2}{(2\pi)^5} \begin{cases} e^{-(a_C - \mu)/T} \frac{(s_0 - m_q^2) \lambda(s_0, m_q^2, m_{\sigma, \pi}^2)}{(s_0 - m_q^2)^2 - 4\omega^2 m_q^2} \sigma_{q\sigma/\pi \rightarrow q\gamma}(s_0) & \text{COMPTON,} \\ e^{-a_A/T} \frac{(s_0 - m_{\sigma, \pi}^2) s_0 (s_0 - 4m_q^2)}{(s_0 - m_{\sigma, \pi}^2)^2 - 4\omega^2 m_{\sigma, \pi}^2} \sigma_{q\bar{q} \rightarrow \sigma/\pi \gamma}(s_0) & \text{annihilations,} \\ e^{-(a_C + \mu)/T} \frac{(s_0 - m_q^2) \lambda(s_0, m_q^2, m_{\sigma, \pi}^2)}{(s_0 - m_q^2)^2 - 4\omega^2 m_q^2} \sigma_{q\sigma/\pi \rightarrow q\gamma}(s_0) & \text{anti-COMPTON} \end{cases} \quad (4.5.12)$$

with

$$a_C = \frac{(m_q + m_{\pi, \sigma})^2}{4\omega} + \omega + \frac{\omega m_q^2}{(m_q + m_{\pi, \sigma})^2}, \quad (4.5.13)$$

$$a_A = \frac{\max\{4m_q^2 - m_{\pi, \sigma}^2, 0\}}{4\omega} + \omega + \frac{\omega m_{\pi, \sigma}^2}{\max\{4m_q^2 - m_{\pi, \sigma}^2, 0\}}. \quad (4.5.14)$$

This approximation is, *e.g.*, applicable for the COMPTON processes in the low frequency limit, since $s_1 \rightarrow m_q^2$ and $s_0 = \max\{(m_q + m_{\sigma, \pi})^2, m_q^2\} \geq s_1$.

4.6. DOPPLER shift and center-of-mass photon frequency

The dominant ω dependence of the rate formulas (4.5.12) within the exponential approximation is due to the factor $\exp\{-a/T\}$, which has – viewed as a function of the photon frequency ω – a (positive frequency) maximum at

$$\omega_2 = \frac{s_0 - (m^{\text{out}})^2}{2\sqrt{s_0}} = \begin{cases} \frac{(m_1^{\text{in}} + m_2^{\text{in}})^2 - (m^{\text{out}})^2}{2(m_1^{\text{in}} + m_2^{\text{in}})} & \text{if } m_1^{\text{in}} + m_2^{\text{in}} > m^{\text{out}} \\ 0 & \text{if } m_1^{\text{in}} + m_2^{\text{in}} \leq m^{\text{out}} \end{cases} \quad (4.6.1)$$

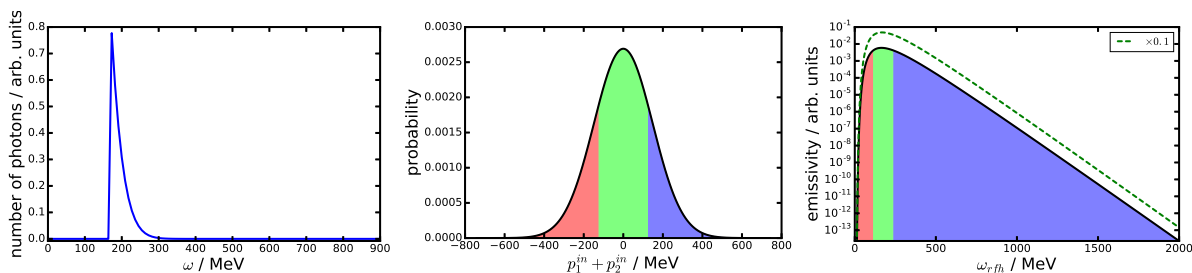


Figure 4.4.: Illustration of the DOPPLER shift generating the (partial) spectra. In the left panel the ω distribution in the CMS of a $q + \sigma \rightarrow q + \gamma$ reaction is displayed and in the middle panel the distribution of the ingoing momenta is shown. In the right panel the function $\exp\{-\gamma_{\text{cms}}^{\text{rfh}}\sqrt{s_0}/T\}$ is depicted with $\gamma_{\text{cms}}^{\text{rfh}} = (\omega_{\text{cms}}(s_0)^2 + \omega_{\text{rfh}}^2)/(2\omega_{\text{cms}}(s_0)\omega_{\text{rfh}})$ being the γ -factor of the transformation from the RFH to the CMS (see text). The parts shaded red correspond to red shifts of the CMS photon frequencies and those shaded blue to blue shifts while green corresponds only to minor DOPPLER shifts. The edges of the shaded regions are located at DOPPLER factors $\nu = \omega_{\text{rfh}}/\omega_{\text{cms}} = 7/10$ and $\nu' = 10/7$. The dashed green curve in the right panel is the function $\exp\{-a_C/T\}$ rescaled by a factor of 0.1 (see text). All curves are calculated with particle masses corresponding to $T = 65 \text{ MeV}$, $\mu = 295 \text{ MeV}$ and parameter set A given in Tab. 6.1.

with the mass of the incoming particles denoted by $m_{1,2}^{\text{in}}$ and that of the outgoing partner of the photon by m^{out} . If the exponential approximation is applicable the spectra are – to a large extent – determined by collisions at the minimal center-of-mass energy s_0 . For an illustrative example, see the left panel of Fig. 4.4, where one may note that the width of the ω_{cms} distribution is rather small.³ It thus is instructive to analyze the spectral shape in terms of such collisions, *i.e.* collisions at $s = s_0$. For $2 \rightarrow 2$ scatterings energy and momenta of all participants can easily be calculated (*cf.* (B.5.5) and (B.5.6)). For minimal center-of-mass energy $\sqrt{s} = \sqrt{s_0}$, the photon frequency in the CMS is precisely ω_2 , *cf.* (B.5.6).

In the rest frame of the heat bath (RFH) the momenta of the particles obey distribution functions that are determined by temperature, chemical potential and the respective mass. This translates into a distribution of the total incoming momentum $p_{\text{tot}} = p_1^{\text{in}} + p_2^{\text{in}}$ for each scattering (middle panel in Fig. 4.4) It is the width of this distribution and not that of the ω_{cms} distribution (*cf.* left panel in Fig. 4.4), which determines the width of the corresponding photon spectrum. For instance, when using parameter set A at $(T, \mu) = (65 \text{ MeV}, 295 \text{ MeV})$ the full width at half maximum (FWHM) of the ω_{cms} -distribution is

³ The term $\exp\{-\nu_{\text{min}}(s)/T\}$ according to the exponential approximation (4.5.9) is considered as an estimate for the probability for a scattering to take place with center-of-mass energy \sqrt{s} . With (B.5.6) this can be converted into a probability for the production of a photon with center-of-mass frequency ω_{cms} . This probability is proportional to the number of produced photons σ with frequency ω_{cms} .

$\text{FWHM}(\omega_{\text{cms}}) \approx 25 \text{ MeV}$ (left panel of Fig. 4.4) and that of the distribution of the total incoming momentum is $\text{FWHM}(p_{\text{tot}}) \approx 350 \text{ MeV}$ (middle panel of Fig. 4.4), which much better fits the width of the actual spectrum $\text{FWHM}(\omega d^7N/d^3kd^4xq + \sigma \rightarrow q + \gamma) \approx 400 \text{ MeV}$ (long-dashed green curve in the right panel of Fig. 6.1). All values as well as the data displayed in Fig. 4.4 are calculated with the particle masses given in Tab. 6.1 for the $q + \sigma \rightarrow q + \gamma$ process. It remains to demonstrate that the shape of a photon distribution based solely on the DOPPLER shift of a narrow ω_{cms} distribution mimics that of the actual distribution or its approximations. This is done in the right panel of Fig. 4.4, where the BOLTZMANN-factor $\exp\{-(E_{\text{rfh}} - \mu)/T\}$ (solid black curve) with $E_{\text{rfh}} = \gamma_{\text{cms}}^{\text{rfh}} \sqrt{s_0}$ is plotted together with $\exp\{-(\nu_{\text{min}}(s_0) - \mu)/T\}$ according to (4.5.9) with $a = a_C$ as in (4.5.13). The ω dependence of E_{rfh} (which is obtained by LORENTZ-transforming the total four-momentum in the CMS $p_{\text{tot}}^{\text{cms}} = (\sqrt{s_0}, \vec{0})^T$ into the RFH) is solely due to $\gamma_{\text{cms}}^{\text{rfh}} = (\omega_{\text{cms}}(s_0)^2 + \omega_{\text{rfh}}^2)/(2\omega_{\text{cms}}(s_0)\omega_{\text{rfh}})$.

This leads to the following interpretation of the spectral shape (*cf.* Fig. 4.4): The differential spectra $\omega d^7N/d^3kd^4x$, measured in the RFH, have a maximum at the photon frequency that equals the center-of-mass frequency, *i.e.* the maximum of $\omega d^7N/d^3kd^4x$ corresponds to the condition that the RFH and the CMS coincide⁴. If $\omega_{\text{rfh}} \not\approx \omega_{\text{cms}}(s_0)$, CMS and RFH differ and move relative to each other with velocity $v = (\omega_{\text{cms}}(s_0)^2 - \omega_{\text{rfh}}^2)/(\omega_{\text{cms}}(s_0)^2 + \omega_{\text{rfh}}^2)$ corresponding to a DOPPLER shift $\nu = \omega_{\text{rfh}}/\omega_{\text{cms}}(s_0)$. Boosting the center-of-mass momenta of the particles leads to a multiplication of the energies with the corresponding gamma-factor $\gamma_{\text{cms}}^{\text{rfh}} = (\omega_{\text{cms}}(s_0)^2 + \omega_{\text{rfh}}^2)/(2\omega_{\text{cms}}(s_0)\omega_{\text{rfh}})$ and thus to a suppression $\sim \exp\{-\gamma_{\text{cms}}^{\text{rfh}} E_{\text{cms}}/T\}$ *w.r.t.* the rate, when CMS and RFH coincide (*i.e.* the maximum rate). For the heat bath being at rest in the frame of an observer (detector) this can be formulated in terms of red and blue shifts of the photon frequencies:

- (i) For the rate at the maximum: RFH and CMS of the collisions with minimal center-of-mass energy coincide (green regions in the right panel of Fig. 4.4).
- (ii) At the low-frequency side of the maximum: In order to measure these photon frequencies, there must be a red shift, *i.e.* the CMS has to move away from the detector (red regions in the right panel of Fig. 4.4).
- (iii) At the high-frequency side of the maximum: In order to measure these photon frequencies, there must be a blue shift, *i.e.* the CMS has to move towards the detector (blue regions in Fig. 4.4).

⁴ Contrary to the CMS, where *all* photons produced in minimal center-of-mass $2 \rightarrow 2$ collisions have the same energy, namely $\omega_{\text{cms}}(s_0)$, the photons measured in the RHF are distributed according to the rate formulas (4.4.1) or its approximations, such as (4.5.12). Those photons that correspond to the peaks of the spectra, *i.e.* that with $\omega_{\text{rfh}} \approx \omega_2$, have approximately the same photon frequency as in the CMS, which means they are not DOPPLER shifted, *i.e.* CMS and RFH coincide for them

This discussion should be regarded as an interpretation concerning the form of the photon spectra to point out what the physical origin of the maximum in the rate is. One major assumption for this interpretation is that the form (especially the position of the maximum) is determined by the factor $\exp\{-\nu_{\min}(s_0)/T\}$ only.

The s -dependent factors (in particular, the cross section) may shift the maximum of the spectrum, but do not change the form of the spectrum qualitatively. If the width of the Gaussian $2\omega\sqrt{m^{\text{out}}T}$ (in case (a)) is small or the damping rate of the exponential b/T (in case (b)) is large, such an assumption is well justified. In the limit $T \rightarrow 0$ these conditions are fulfilled, thus the corrections to the behavior described above vanish and the spectra get the form of sharp peaks at the kinematically determined positions.

Another interesting feature of the spectral shape is that the height of the maximum of the function $\exp\{-a/T\}$ is simply

$$e^{-a(\omega=\omega_2)/T} = e^{-\sqrt{s_0}/T} = \exp\left\{-\frac{\max\{m_1^{\text{in}} + m_2^{\text{in}}, m^{\text{out}}\}}{T}\right\}. \quad (4.6.2)$$

In principle, it is possible for m^{out} to become larger than the sum of the masses of the incoming particles. Within the QMM and considering only $2 \rightarrow 2$ processes there are certain regions of the phase diagram, where $2m_q < m_{\sigma,\pi}$. Then, for the annihilations the outgoing partner of the photon (which in this case is one of the mesons) can have a larger mass than both incoming (anti-) quarks together. However, then automatically $s_1 > s_0$, and the Gaussian approximation has to be applied instead of the exponential approximation, for which this shape of the spectra (and hence position and height of the maximum) were deduced. Thus, one finds within the exponential approximation for the maximum of the partial spectrum located at ω_2 , *cf.* (4.6.1), that the height is $\propto \exp\{-(m_1^{\text{in}} + m_2^{\text{in}})/T\}$.

It is worth pointing out that this discussion relies on kinematics only and thus is applicable to very different underlying theories, *e.g.* in QED the leading contribution to photon production comes from electron annihilation into two photons $e^+ + e^- \rightarrow \gamma + \gamma$. The discussion above yields for the position of the maximum in the photon spectrum at $T \rightarrow 0$ $\omega = m_e$, which is what one finds with an exact calculation (*cf.* [YMK10]).

4.7. Dynamical enhancement mechanism

Having identified the ratio m^{out}/T for large values of ω and the quotient $(m_1^{\text{in}} + m_2^{\text{in}})/T$ for small values of ω (*i.e.* ω is not too far away from the maxima of the spectra – if there

are any – which means that ω is of the order of the particles masses $m_{q,\sigma,\pi}$) as the relevant parameter whose change over the phase diagram modulates the rates, we will now explain a dynamical enhancement mechanism for the photon rate. With “dynamical enhancement” we term the relative increase of the rate along different isentropes when one of them goes through the continuous regions of the phase diagram only, and the other one crosses the phase transition line.⁵

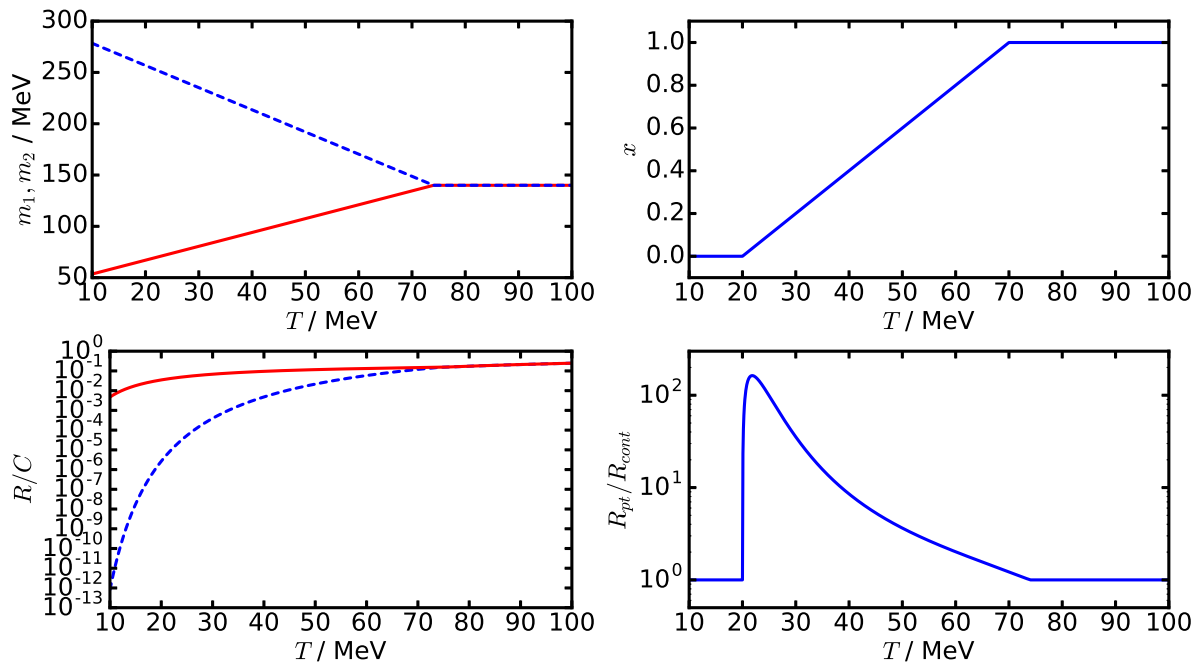


Figure 4.5.: Visualization of the toy model introduced for explaining the dynamical enhancement mechanism. Upper left panel: masses of the outgoing partner of the photon according to (4.7.1), with the parameters $m_1^0 = 40$ MeV, $m_2^0 = 300$ MeV, $m_c = 140$ MeV and $T_c = 74$ MeV. Upper right panel: phase fraction of the phase 1 for the expansion path through the first-order phase transition curve according to (4.7.2), with parameters $T_1^x = 20$ MeV and $T_2^x = 70$ MeV. Lower left panel: Rates R divided by the normalization C for the pure phases 1 and 2 according to (4.7.1). Lower right panel: dynamical enhancement, *i.e.* the ratio $R_{\text{pt}}/R_{\text{cont}}$ of the rate $R_{\text{pt}} = x(T)R(m_1(T), T) + (1 - x(T))R(m_2(T), T)$ along a path crossing the FOPT curve and the rate $R_{\text{cont}}(T) \equiv R_2(T)$ along a path avoiding the phase transition.

The enhancement phenomenon is based on the fact that, in the high-frequency region, the rate is to a large extent determined by the factor $\exp\{-m_{\text{out}}/T\}$ (see (4.5.8)). However, analogous considerations apply also for the low-frequency case. In this case the only

⁵ The term “dynamical” refers to the fact that the emission is compared for different isentropes, which are a reasonable estimate for the evolution of the hot and dense strongly interacting medium created in a heavy-ion collision.

relevant change in the below discussion is to replace m^{out} by $m_1^{\text{in}} + m_2^{\text{in}}$. For the discussion of the dynamical enhancement, a simplified model is introduced, without μ -dependence and a linear T -dependence of the masses:

$$m_{1,2}(T) = \frac{m_{1,2}^0(T_c - T) + m_c T}{T_c}, \quad R_{1,2} = C e^{-m_{1,2}/T} \quad (4.7.1)$$

with $m_{1,2}$ and $R_{1,2}$ being the masses of the outgoing partner of the photon and the photon rate, in phases 1 and 2, respectively. The phase fraction x of the phase 1 for a path through the phase diagram, which crosses the FOPT curve between temperatures T_1^x and T_2^x shall also be linear in T :

$$x = \begin{cases} 1 & \text{for } T > T_1^x, \\ \frac{T - T_1^x}{T_2^x - T_1^x} & \text{for } T_2^x \leq T \leq T_1^x, \\ 0 & \text{for } T < T_2^x. \end{cases} \quad (4.7.2)$$

In the upper row of Fig. 4.5 and the left panel in the lower row, these quantities are displayed. In the lower right panel, the ratio of the rate through a continuous region of the phase diagram (we choose phase 2) and the rate on a path crossing the phase transition line are displayed. The latter path enters the phase transition line from phase 1 at $T = T_1^x$ and leaves it to phase 2 at $T = T_2^x$. Of course, this toy model is extremely crude, but it serves to illustrate the mechanism behind the dynamical enhancement: The rate R_1 in phase 1 is larger than in phase 2 by a factor of $\exp\{(m_2 - m_1)/T\}$. In the coexistence region the phase fraction of phase 1 adds a considerable amount to the rate R_{pt} . The interplay between the phase fraction of phase 1 (which tends to zero for $T \rightarrow T_2^x$) and the ratio of the rates $\exp\{(m_2 - m_1)/T\}$ (which diverges at $T \rightarrow 0$) produces a peak close to the temperature, when the respective path leaves the phase transition line (*i.e.* T_2^x in this toy model). We will see this mechanism working in the QMM, too (see Section 6.2.5 below).

5. Thermodynamics of the quark-meson model

One major field of application for chiral models of strongly interacting matter, and especially for the QMM, is to study such matter at finite temperature and densities, where no first-principle approaches to QCD are applicable. Often, these models can be tuned to yield a first-order phase transition (FOPT) at low temperatures and finite chemical potential that terminates in a critical end point (CEP). In this chapter, various thermodynamical observables of the QMM as well as the masses of the particles are shown *w.r.t.* temperature and quark chemical potential. For many applications it is favorable to use the best possible approximation scheme¹ to evaluate the thermodynamics of the model, however, this thesis does not aim at the best possible approximation but at the connection between peculiarities of the phase diagram and the associated photon spectra. Of special interest is a CEP at temperatures which are $\mathcal{O}(100 \text{ MeV})$ and relatively small chemical potential. It turns out that some of the approximations frequently done for the QMM, lead to the CEP being at $T \lesssim 50 \text{ MeV}$ [SW05, NSS⁺10]. Although being more realistic from a purely thermodynamical point of view, they are thus less suitable for our purpose. The approximation schemes discussed in this chapter can therefore be seen as methods for achieving a threefold goal: Firstly, they provide, in a thermodynamically self-consistent manner, the pressure p as function of temperature T and quark chemical potential μ . Secondly, the phase structure, which can be extracted from $p(T, \mu)$ includes a curve of FOPTs that ends at a CEP at $T_{\text{CEP}} \sim 100 \text{ MeV}$. Lastly, it is possible to calculate the photon emissivity consistently to the thermodynamics.

Before proceeding with the presentation of the thermodynamics of the QMM, it is necessary to introduce some terminology. In principle a symmetry present in a field theory can be realized in two distinct ways: Either it is an invariance of the physical state (WIGNER-

¹ “best” in the sense that it is as close as possible to an exact solution

WEYL realization)² or as the formation of equivalence classes of states with the symmetry being the corresponding equivalence relation (NAMBU-GOLDSTONE realization)³. The latter case is often phrased as the symmetry being “spontaneously broken”. In the case of the QMM the relevant symmetries are the flavor symmetries discussed in Chapter 2. In the chiral limit (*i.e.* for $H = 0$) – where these symmetries are exact – the phases can be labeled by the respective realization type of the symmetry (*i.e.* WIGNER-WEYL or NAMBU-GOLDSTONE type). For $H \neq 0$ thy symmetries are only approximate and the phases not even separated entirely by a curve of genuine phase transitions. However, for the purpose of a simple nomenclature the regions of the QMM phase diagram where the (approximate) symmetries are (approximately) realized in the WIGNER-WEYL sense is dubbed pseudo-WIGNER-WEYL (PWW) phase, while the region where it is (approximately) realized in the NAMBU-GOLDSTONE sense is named pseudo-NAMBU-GOLDSTONE (PNG) phase.

5.1. Mean field approximation

5.1.1. Derivation of the grand potential

The mean field approximation (MFA) of the QMM is well documented in the literature, see *e.g.* [SMMR01, SDF⁺01, PSD03, SW09, KT09, GT12, SM12, Tiw12, FGP12, CBS14, SR15]. For completeness we sketch it in this paragraph. The grand potential Ω for the QMM is given by the following path integral, obtained by specifying the relevant fields in the general formula (3.2.9):

$$\Omega = -\frac{1}{\beta V} \ln \int \mathcal{D}\bar{q}\mathcal{D}q\mathcal{D}^3\pi\mathcal{D}\sigma e^{\int_0^\beta d\tau \int d^3x \mathcal{L}_q(q, \bar{q}, \sigma, \vec{\pi}) + \mathcal{L}_{\text{kin},m}(\sigma, \vec{\pi}) - U(\sigma, \vec{\pi}) + \mu\bar{q}\gamma^0 q}, \quad (5.1.1)$$

with the inverse temperature $\beta = T^{-1}$, the volume V and \mathcal{L}_q , $\mathcal{L}_{\text{kin},m}$ and U defined in (2.1.2) – (2.1.4). Based on the assumption that the largest contribution to the path integral originates from states corresponding to meson field configurations differing only slightly from their respective thermal expectation values an approximate solution can be obtained. Any occurrence of the meson field variable is replaced by the corresponding expectation value and the meson path integrations are omitted. Since the Lagrangian is space-time indepen-

² Mathematically this manifests in all generators of the symmetry annihilating the vacuum.

³ This manifests in generators which do not annihilate the vacuum but transform between different states with identical physical properties.

dent the expectation values do not depend on the coordinates within this approximation⁴ and thus the kinetic terms for the mesons vanish, yielding

$$\Omega_{\text{MFA}} = -\frac{1}{\beta V} \ln \int \mathcal{D}\bar{q}\mathcal{D}q e^{\int_0^\beta d\tau \int d^3x \mathcal{L}_q(q, \bar{q}, \sigma_0, \vec{\pi}_0) - U(\sigma_0, \vec{\pi}_0) + \mu \bar{q} \gamma^0 q}, \quad (5.1.2)$$

with $\sigma_0, \vec{\pi}_0$ being the thermal expectation values of the σ and the $\vec{\pi}$ fields. These have to be determined by minimizing the potential *w.r.t.* the fields:

$$0 = \frac{\partial \Omega_{\text{MFA}}}{\partial \sigma_0}, \quad 0 = \frac{\partial \Omega_{\text{MFA}}}{\partial \pi_0^i}. \quad (5.1.3)$$

The curvature of Ω_{MFA} at the minimum is interpreted in terms of mass parameters for the meson fields according to

$$(m_\sigma^{\text{MFA}})^2 = \frac{\partial^2 \Omega_{\text{MFA}}}{\partial \sigma_0^2}, \quad (m_\pi^{\text{MFA}})^2 \equiv (m_{\pi^i}^{\text{MFA}})^2 = \frac{\partial^2 \Omega_{\text{MFA}}}{\partial (\pi_0^i)^2}, \quad (5.1.4)$$

where it was used that by symmetry the masses of all pions coincide.

The mesonic part of the Lagrangian can be pulled out of the path integral and afterwards the fermionic path integral can be solved in terms of a functional determinant, *cf.* (3.2.15).

$$\Omega_{\text{MFA}} = -\frac{1}{\beta V} \ln e^{-\int_0^\beta d\tau \int d^3x U(\sigma_0, \vec{\pi}_0)} - \frac{1}{\beta V} \ln \int \mathcal{D}\bar{q}\mathcal{D}q e^{\int_0^\beta d\tau \int d^3x \mathcal{L}_q(q, \bar{q}, \sigma_0, \vec{\pi}_0)} \quad (5.1.5)$$

$$= U(\sigma_0, \vec{\pi}_0) - \frac{1}{\beta V} \ln \det \left[i\not{\partial} - \mu\gamma^0 - g(\sigma_0 - i\vec{\tau}\pi_0\gamma^5) \right]. \quad (5.1.6)$$

The argument of the determinant is a direct product of a matrix in DIRAC space, one in flavor space and one in functional (configuration) space. Therefore, the determinants can be evaluated independently yielding after the evaluation of the DIRAC and flavor parts of

⁴ There are, however, calculations showing that periodic modulations of the expectation values can produce configurations with even smaller free energy in a region close to the chiral transition at not too large temperatures. These calculations reveal that there is a competition between two contributions to the free energy having different signs. On the one hand, the modulation of the σ expectation value modulates the effective quark mass which can lower the total energy and, on the other hand, these modulations give rise to contributions to the kinetic terms since, by definition, they have non-vanishing derivatives. Close to the chiral transition the interplay of these effects can produce thermodynamically stable periodic field configurations, see [NT05, AIS12, BC15, CBS14]. Besides these configurations, other types of modulations, such as periodic domain walls and simple or dual chiral density waves, are known to exist within chiral models [LNT⁺15].

the determinant

$$\Omega_{\text{MFA}} = U(\sigma_0, \vec{\pi}_0) - \frac{1}{\beta V} \ln \det_{\mathbf{x}} \left[(i\partial_0 - \mu)^2 - (i\vec{\nabla})^2 - g^2(\sigma_0^2 + \pi_0^2) \right] \quad (5.1.7)$$

$$= U(\sigma_0, \vec{\pi}_0) - \frac{1}{\beta V} \text{Tr}_{\mathbf{x}} \ln \left[(i\partial_0 - \mu)^2 - (i\vec{\nabla})^2 - g^2(\sigma_0^2 + \pi_0^2) \right], \quad (5.1.8)$$

where the determinant and the trace is understood in the functional sense, *cf.* Appendix B.1. The trace is most conveniently evaluated after applying a coordinate transformation in functional space. The best choice is a FOURIER transformation, since it diagonalizes the operator argument of the logarithm. Then one obtains

$$\Omega_{\text{MFA}} = U(\sigma_0, \vec{\pi}_0) - \frac{1}{\beta V} \text{Tr}_{\mathbf{p}} \ln \left[(i\omega_n - \mu)^2 - \vec{p}^2 - g^2(\sigma_0^2 + \pi_0^2) \right], \quad (5.1.9)$$

where

$$\text{Tr}_{\mathbf{p}} = T \sum_{\omega_n} \frac{V}{(2\pi)^3} \int d^3p \quad (5.1.10)$$

and $\omega_n = (2n + 1)\pi T$ (with integer n) are the fermionic MATSUBARA frequencies. After a number of standard steps (*cf.* [ZJ02, KG06]) one finds

$$\Omega_{\text{MFA}} = U(\sigma_0, \vec{\pi}_0) - \frac{2N_c N_f}{(2\pi)^3} \int d^3p \left[E_p + T \ln(1 + e^{(E_p - \mu)\beta}) + T \ln(1 + e^{(E_p + \mu)\beta}) \right], \quad (5.1.11)$$

$$E_p^2 = m_q^2 + \vec{p}^2, \quad (5.1.12)$$

$$(m_q^{\text{MFA}})^2 = g^2(\sigma_0^2 + \pi_0^2), \quad (5.1.13)$$

where $N_c = 3$ denotes the number of colors and $N_f = 2$ the number of flavors. The logarithmic terms in (5.1.11) are the thermal contributions and vanish in the vacuum ($T = \mu = 0$). The remaining term under the integral contributes to the grand potential density even in the vacuum. It is the sum of all energies possible in the system. This formally is a term which can be interpreted as the contribution of the DIRAC sea and is often ignored, because it represents a high-momentum effect and is thus considered to be of little importance to the spontaneous chiral symmetry breaking mechanism. However, dedicated investigations reveal that this is not always justified [SFN⁺10, Tiw12]. This issue is discussed in greater detail below, *cf.* Section 5.1.2.

The pion field appears only squared in (5.1.11). Therefore, the derivative *w.r.t.* π_i in (5.1.3)

is proportional to π_i itself. Thus, $\pi_i = 0$ fulfills the second condition in (5.1.3). There is also another solution to this equation with non-zero π_i . However, such a non-vanishing π_i is in conflict with the condition for σ_0 (left equation in (5.1.3)), unless $H = 0$ (which will not be discussed in this thesis). Thus the expectation value for the pion fields vanish. For further convenience we also substitute $v \equiv \sigma_0$.

5.1.2. Renormalization of the vacuum term

In Section 5.1.1 it was stated that often the vacuum terms are ignored since these contributions are regarded as a high-momentum effect with little importance for effective theories. There are, however, topics for which these vacuum contributions are important. For instance, in [SFN⁺10], the chiral phase transition of the QMM is investigated in the chiral limit. The analysis reveals that logarithmic terms present in the low-quark-mass expansion can change the order of the phase transition if the vacuum terms are omitted, provided the quark mass in the chirally restored phase is sufficiently small near the phase transition curve. As the authors in [SSFR10] note this resembles the well known COLEMAN-WEINBERG fluctuation-induced FOPT [CW73]. In particular, close to the chiral limit, *i.e.* for $H \rightarrow 0$ or equivalently $m_\pi^{\text{vac}}/m_\sigma^{\text{vac}} \rightarrow 0$, the quark mass becomes small, $m_q \rightarrow 0$, right beyond the phase transition curve in the PWW phase. Therefore, sufficiently close to the chiral limit the phase transition at $\mu = 0$ becomes first-order (instead of second-order as it is expected for Mexican-hat-like potentials [KG06]). Especially, if one is interested in the remnants of the critical behavior present in the chiral limit [KR11, FKRS11, SFR12], this change of the phase transition order has to be circumvented by properly including and renormalizing the vacuum contributions. This is possible indeed, since the QMM is renormalizable [Lee69, PS95] and thus, the vacuum terms can be treated properly using standard techniques.

We sketch the main steps of this procedure following [GT12]. Dimensional regularization in $d + \epsilon$ dimension yields for the fermion part of the partition function in MFA

$$\Omega_{\text{MFA}}^{\text{vac}} = \frac{2N_f N_c}{(2\pi)^3} \int d^3p E_p \quad (5.1.14)$$

$$= \frac{2N_f N_c}{32\pi^2} m_q^4 \left(\frac{1}{\epsilon} - \frac{1}{2} \left[-3 + 2\gamma_E + 2 \ln \left(\frac{m_q^2}{4\pi M^2} \right) \right] \right). \quad (5.1.15)$$

In MFA, one has $m_q = g\sigma_0$. Thus the term

$$g^4 \sigma_0^4 \frac{2N_f N_c}{32\pi^2} \left(\frac{1}{\epsilon} - \frac{1}{2} [-3 + 2\gamma_E - 2 \ln(4\pi)] \right) \quad (5.1.16)$$

can be absorbed by re-adjusting λ and $\lambda\zeta$. Only the term

$$\Omega_{\text{vac},q}^{\text{ren}} = -\frac{2N_f N_c}{32\pi^2} m_q^4 \ln\left(\frac{m_q^2}{M^2}\right) = -\frac{2N_f N_c}{32\pi^2} g^4 \sigma_0^4 \ln\left(\frac{g^2 \sigma_0^2}{M^2}\right) \quad (5.1.17)$$

remains depending on the renormalization scale M . This term is all that is left at $T = \mu = 0$ from the momentum integral in (5.1.11) and hence $\Omega_{\text{MFA}}(T = \mu = 0) = \Omega_{\text{vac},q}^{\text{ren}} + U$. With the help of (5.1.3) and (5.1.4) the parameters λ and ζ can be expressed as functions of m_π^{vac} , m_σ^{vac} , $m_{\text{nuc}}^{\text{vac}} = N_c m_q^{\text{vac}}$, σ_0^{vac} and the renormalization scale M . However, when inserting these expressions into Ω_{MFA} the dependence on M drops out and one finds for the renormalized grand potential

$$\begin{aligned} \Omega_{\text{MFA}}^{\text{ren}} = & -U(\sigma_0, \vec{\pi}_0) + \frac{2N_f N_c}{(2\pi)^3} \int d^3p \left[\ln(1 + e^{(E_p - \mu)\beta}) + \ln(1 + e^{(E_p + \mu)\beta}) \right] \\ & - \frac{2N_f N_c}{16\pi^2} g^4 \sigma_0^4 \ln\left(\frac{\sigma_0}{\langle \sigma \rangle_{\text{vac}}}\right) + \frac{\lambda_r}{4} (\sigma_0^2 - \zeta_r)^2 - H\sigma_0, \end{aligned} \quad (5.1.18)$$

The renormalized constants λ_r and ζ_r can be related to the vacuum properties of the fields according to

$$\lambda_r = \frac{(m_\sigma^{\text{vac}})^2 - (m_\pi^{\text{vac}})^2}{2(\sigma_0^{\text{vac}})^2} + \frac{32N_f N_c}{16\pi^2} \left(\frac{m_{\text{nuc}}^{\text{vac}}}{N_c \sigma_0^{\text{vac}}}\right)^4, \quad (5.1.19)$$

$$\lambda_r \zeta_r = \frac{(m_\sigma^{\text{vac}})^2 - 3(m_\pi^{\text{vac}})^2}{2} + \frac{2N_f N_c}{8\pi^2} \left(\frac{m_{\text{nuc}}^{\text{vac}}}{N_c \sigma_0^{\text{vac}}}\right)^4 (\sigma_0^{\text{vac}})^2, \quad (5.1.20)$$

where the terms $\propto (m_{\text{nuc}}^{\text{vac}}/N_c \sigma_0^{\text{vac}})^4$ come from the renormalization procedure. Compared to the MFA grand canonical potential without vacuum fluctuations the renormalized grand potential given in (5.1.18) contains an additional term ($\propto \ln \sigma_0/\sigma_0^{\text{vac}}$). This term compensates in the above mentioned low- m_q expansion the logarithmic terms that cause the phase transition to be first-order in the chiral limit.

5.1.3. Thermodynamic quantities in mean field approximation

To be specific one has to fix the parameters of the Lagrangian. This is done by requiring the particle masses and the σ expectation value to coincide with appropriately chosen values in the vacuum. Nonetheless, it is certainly questionable to fix the QMM parameters to standard model or QCD vacuum properties, since the QMM constitutes not a realistic description of the QCD vacuum. However, such parameter fixings are commonly used in the literature and can be calculated directly from the parameters of the Lagrangian (and vice versa) according to (2.3.11). Even more important, the vacuum masses have

[MeV]	$m_{\text{nuc}}^{\text{vac}}$	m_{σ}^{vac}	m_{π}^{vac}	$\langle\sigma\rangle_{\text{vac}}$	T_{pc}	μ_c^0	T_{CEP}	μ_{CEP}
A	936.0	700.0	138.0	92.4	148.3	328	72.5	279.5
A _{MFA}	936.0	700.0	138.0	92.4	161.0	328	104.0	234.0
B	1170.0	1284.4	138.0	90.0	194.6	430	97.0	377.5
C	1080.0	700.0	138.0	90.0	140.3	324	98.0	216.0
D	936.0	900.0	138.0	71.8	155.0	333	64.0	296.0
E	936.0	500.0	138.0	129.3	144.9	325	82.0	264.0

Table 5.1.: Parameter sets used for the analysis (all quantities given in MeV). The parameters $m_{\text{nuc}}^{\text{vac}}$, m_{σ}^{vac} , m_{π}^{vac} , $\langle\sigma\rangle_{\text{vac}}$ can be mapped to the parameters of the Lagrangian (2.1.1) g , λ , ζ , H according to (2.3.11). Running a simulation with these parameters yields the pseudocritical temperature T_{pc} at vanishing chemical potential, the critical chemical potential at zero temperature μ_c^0 and the coordinates for the critical point $(T_{\text{CEP}}, \mu_{\text{CEP}})$ given in the last two columns.

a clear physical interpretation and are independent of the renormalization scale (which does not hold for the parameters of the Lagrangian g, λ, ζ and H), which permits the comparison of the results between different approximation and/or renormalization schemes. For instance, typically these quantities are given for approximations based on the functional renormalization group (FRG) as well as for path integral based approaches (MFA and LFA) which does not hold for the parameters of the Lagrangian as they are not easily accessible within FRG approaches. In Tab. 5.1 the parameter sets used in this thesis are collected.

We now present the thermodynamic quantities in MFA, calculated without the quark vacuum term and based on parameter set A_{MFA} given in Tab. 5.1.

Masses of the particles

In Fig. 5.1, the masses of the particles are depicted (upper row: sigma meson mass m_{σ} (left panel) and pion mass m_{π} (right panel); lower left panel: quark mass m_q) *w.r.t.* temperature and quark chemical potential. In the spirit of the LANDAU theory of phase transitions [Cow80],⁵ the quark mass resembles an order parameter of the chiral phase transition. For clarification the lower right panel in Fig. 5.1 displays the phase structure (crossover region, CEP and the curve of FOPTs) as well as the position of the PWW and PNG phases. In Section 5.3.2, the model parameters influencing the position of the phase boundary as well

⁵ In the LANDAU theory of phase transitions, the order parameter is required to be zero in one phase. This is true in the chiral limit, where the quark mass in the WIGNER-WEYL phase is exactly zero, but due to the explicit symmetry breaking ($H \neq 0$) this requirement is not fulfilled for the parameter sets under discussion. The finite order parameter in the PWW phase thus represents the imperfect symmetry restoration.

as the CEP are discussed in some detail.

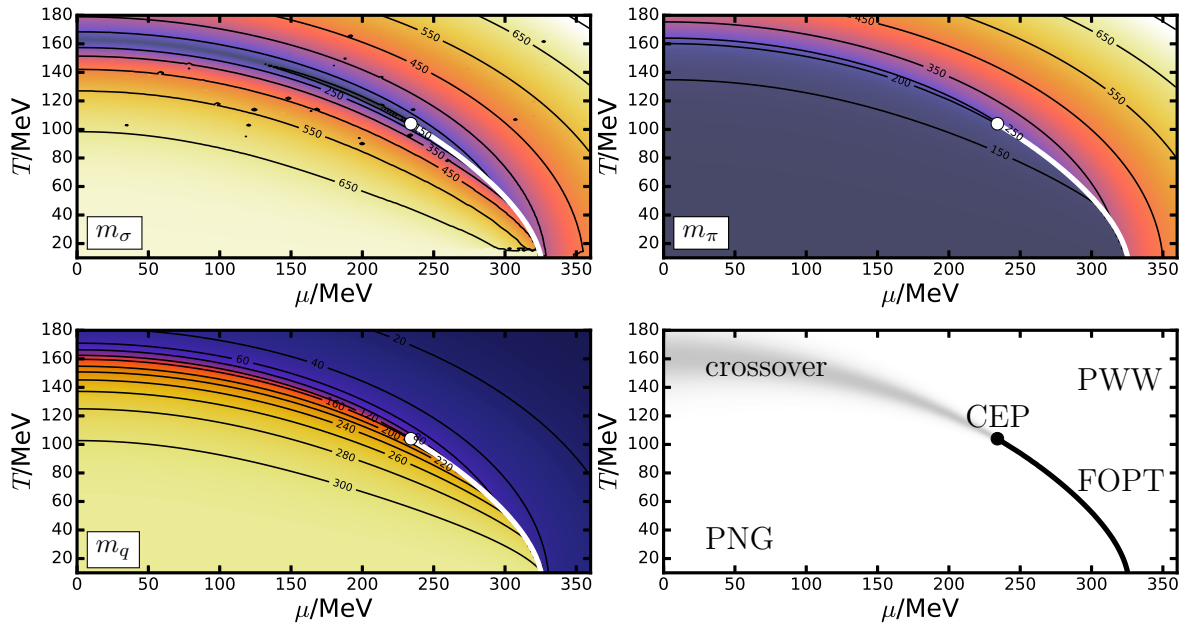


Figure 5.1.: Masses of the fields and the phase structure in MFA (without vacuum fluctuations). Depicted are the sigma mass (upper left panel) and the pion mass (upper right panel) and the quark mass (lower left panel) in units of MeV. The solid white line in these panels denotes the curve of FOPTs ending in a CEP (white dot). In the lower right panel the phase structure is displayed for clarification. Shown are the crossover region (shaded in gray), the FOPT (solid black curve) and the CEP (black dot). The shortcuts PWW and PNG mark the respective phases.

While the pion mass m_π monotonously increases with T and μ , the sigma mass m_σ exhibits a minimum at the CEP where it is exactly zero. The correlation length being inversely proportional to the lightest particle mass thus diverges at the CEP. This is a requirement for the medium to show all kinds of critical behavior (*e.g.* critical opalescence, diverging compressibility, diverging fluctuation scales *etc.*). The divergence of the correlation length implies that the physical properties get independent of the underlying microscopic theory and show universal features largely determined by dimensionality of space and the global symmetries of the Lagrangian. For the QMM this means that at the CEP shows the same critical behavior (*e.g.* the same critical exponents) as other $O(4)$ -symmetric models in three dimensional space putting the QMM into the universality class of the three dimensional HEISENBERG model.⁶

⁶ Since the QMM's chiral symmetry is identical to that of light QCD (*cf.* Section 2.5), this also is the universality class of light QCD itself.

Thermodynamic quantities

A selection of thermodynamic quantities *w.r.t.* temperature and quark chemical potential is presented in Figs. 5.2 and 5.3. The pressure (as a function of T and μ), which is the

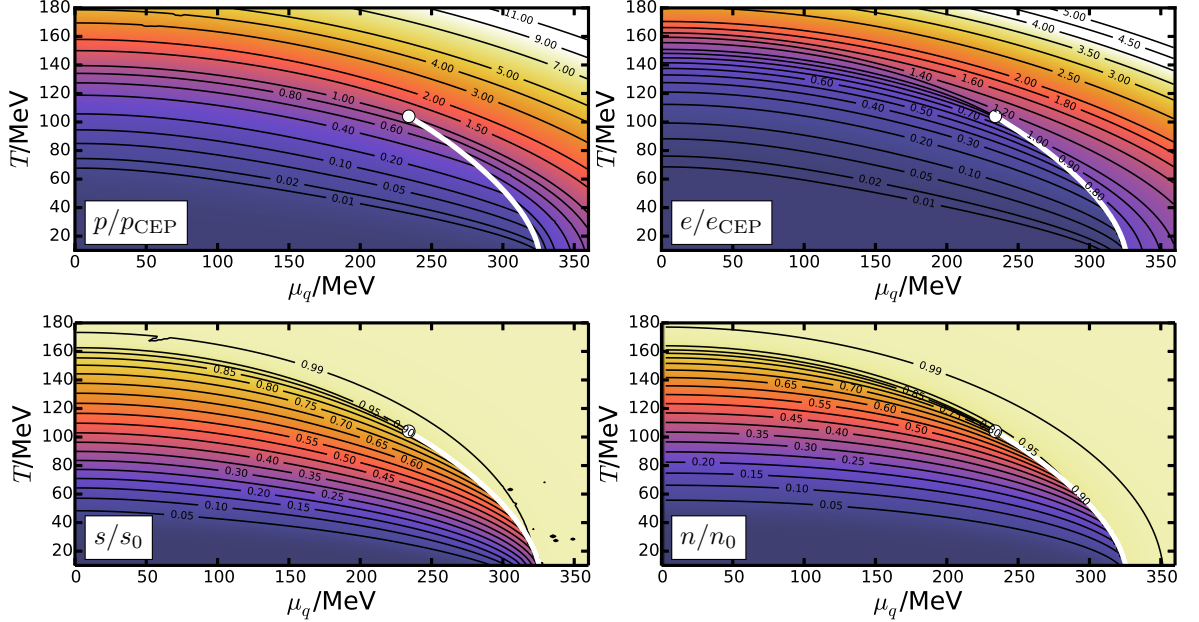


Figure 5.2.: Thermodynamic quantities in MFA (without vacuum fluctuations). Upper row: pressure p (left panel) and energy density e (right panel) scaled with their respective value at the CEP. Lower row: entropy density s (left panel) and net quark density (right panel), scaled with the entropy density s_0 or the net fermion density n_0 of a noninteracting ultrarelativistic FERMION gas with the same number of degrees of freedom. Phase contour as in Fig. 5.1.

central quantity from which many other quantities can be derived by differentiation, is a monotonously increasing function of its arguments. The inspection of the curves $T_p(\mu)$ of constant pressure (isobars) reveals further information. Since $dp = s dT + n d\mu = 0$ on these curves, their slope can be expressed in terms of the net quark density and the entropy density according to $dT_p/d\mu = -n/s$ providing a nice check for the calculation of the isentropic curves, *i.e.* curves with constant s/n ratio. At the FOPT curve the isobars are kinked such that their slope decreases when crossing the FOPT from below, *i.e.* $dT_p/d\mu|_{\mu_c-\epsilon} > dT_p/d\mu|_{\mu_c+\epsilon}$ with ϵ being an infinitesimal shift and μ_c the chemical potential at the FOPT. This is a consequence of the pressure being maximal in the thermodynamically stable phase. Furthermore, relating the slope of the isobars to the entropy per net quark ratio as discussed above this translates into $s^+/n^+ < s^-/n^-$, where s^\pm, n^\pm denote the entropy and net quark density slightly above (+) or below (-) the FOPT curve. Together with $n^+ > n^-$ which also follows from thermodynamical stability the slope of the

critical pressure p_c *w.r.t.* μ is positive for this parameter set (and as it turns out, for the QMM in general), *cf.* (5.4.2), which puts the QMM's FOPTs into the class of enthalpic FOPTs in the classification scheme of [Jos15].

In the lower row of Fig. 5.2, the entropy density and the net quark density are scaled with the respective quantities for an ideal ultrarelativistic FERMI gas with the same number of degrees of freedom. The most remarkable feature of these plots is that both scaled quantities tend to unity in the PWW phase, making a noninteracting gas of massless quarks a good approximation of this phase.

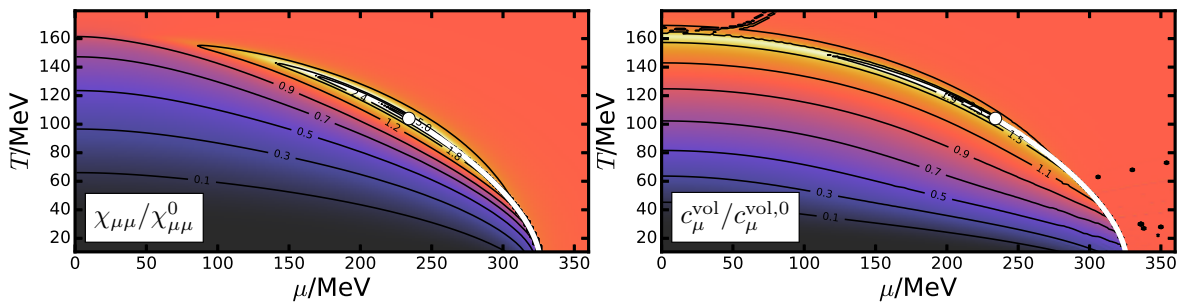


Figure 5.3.: Quark number susceptibility $\chi_{\mu\mu} = \partial^2 p / \partial \mu^2$ (left panel) and heat capacity $c_{\mu}^{\text{vol}} = T \partial^2 p / \partial T^2$ (right panel) in MFA scaled by the same quantities for an ideal FERMI gas with the same number of degrees of freedom. Phase contour as in Fig. 5.1.

A similar conclusion can be drawn from Fig. 5.3, where the quark number susceptibility $\chi_{\mu\mu}$ and the volume-specific (volumetric) heat capacity⁷ c_{μ}^{vol} at constant chemical potential defined according to

$$\chi_{\mu\mu} = \frac{\partial^2 p(T, \mu)}{\partial \mu^2}, \quad c_{\mu}^{\text{vol}} := T \frac{\partial^2 p(T, \mu)}{\partial T^2} = T \frac{\partial s}{\partial T} \quad (5.1.21)$$

and scaled by the same quantities for an noninteracting ultrarelativistic FERMI gas are shown. However, the most remarkable feature of these quantities is their increase in the transition region. While the scaled heat capacity is increased mostly in the crossover region, the scaled quark number susceptibility peaks in the region surrounding the CEP. While the former thus provides a measure for the crossover region the latter can be applied to characterize the size of the critical region.

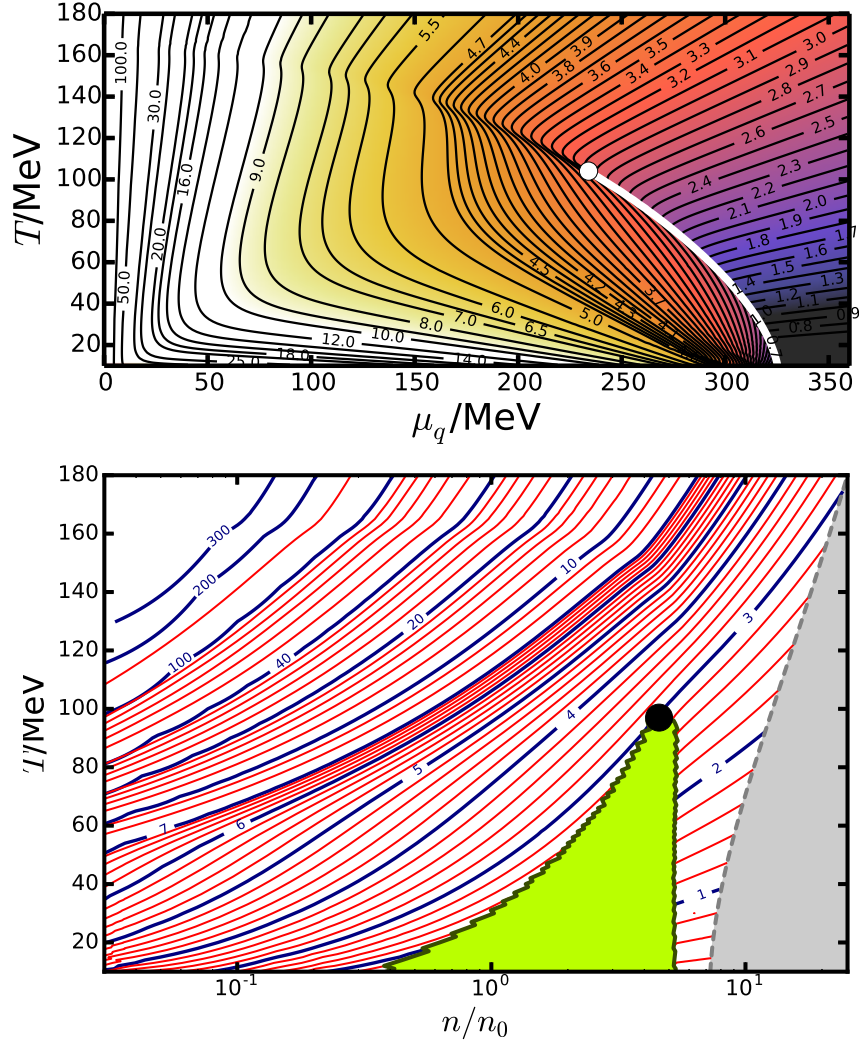


Figure 5.4.: Contour plot of the entropy per quark s/n within the MFA *w.r.t.* temperature T and quark chemical potential μ (upper panel). The FOPT curve as well as the CEP are denoted by a white curve and a white dot, respectively. Lower panel: The same, but *w.r.t.* temperature and net quark density n . The green region is the coexistence region with the CEP (black dot) at its border. The net quark density is scaled by the nuclear saturation density $n_0 = 0.16 \text{ fm}^{-3}$. In the gray region, which corresponds to $\mu \geq 360 \text{ MeV}$, no data has been calculated.

Isentropes

In Fig. 5.4, the isentropes within the MFA are depicted, both in the T - μ diagram (upper panel) as well as in the T - n diagram (lower panel). Two features of the isentropic curves are apparent: (i) in the PWW phase, the isentropes in the T - μ plane are well approximated by straight lines pointing toward the origin and (ii) for $T \rightarrow 0$ all isentropes merge at the

⁷ The heat capacity normalized to the volume.

point $(T, \mu) = (0, m_q^{\text{vac}})$. In contrast, no such patterns are present in the T - n diagram (lower panel). The same observations will be made and discussed in more detail within the LFA below.

5.2. The linearized fluctuation approximation

5.2.1. The partition function in linearized fluctuation approximation

The formal similarity of the grand canonical partition function Z (*cf.* Section 3.2.1) and the generating functional for correlation functions S_η (*cf.* Section 3.2.2) in Euclidean space makes a derivation of Z from S_η in LFA a comparatively simple task.

Setting in (4.2.1) all sources to zero and replacing $i\partial/\partial t$ by $\partial/\partial\tau - \mu$ as well as $i \int dt$ by $\int d\tau$ transforms S_η formally into the grand canonical partition function Z . As our goal is to study systems much smaller than the mean free path of photons (which is a reasonable assumption in the context of heavy-ion collisions) the photons do not contribute to the pressure and hence to the thermodynamic potential and the partition function. Thus, all terms containing the photon field A are removed from (4.2.1), which corresponds to setting the electromagnetic coupling e zero (explicitly, and implicitly in J_γ^μ) as well as removing $\det G_\gamma$ from (4.2.31). Then one gets

$$Z = \sqrt{\det G_\pi}^3 \sqrt{\det G_\sigma} \exp \left\{ - \int d\tau d^3x \left(\langle U_{\text{eff}} \rangle + \frac{1}{2} m_\pi^2 \langle \vec{\pi}^2 \rangle + \frac{1}{2} m_\sigma \langle \Delta^2 \rangle \right) \right\}. \quad (5.2.1)$$

Since $\langle U_{\text{eff}} \rangle, \langle \vec{\pi}^2 \rangle, \langle \Delta^2 \rangle$ and $m_{\sigma,\pi}$ do not depend on the space-time coordinates, the integration in the exponent yields a factor of the Euclidean volume $V\beta$. For the grand canonical potential $\Omega(T, \mu) = -p(T, \mu) = (\beta V)^{-1} \ln Z$ one gets

$$\Omega = \frac{3}{2} \ln \det G_\pi + \frac{1}{2} \ln \det G_\sigma - \langle U_{\text{eff}} \rangle - \frac{1}{2} m_\pi^2 \langle \vec{\pi}^2 \rangle - \frac{1}{2} m_\sigma \langle \Delta^2 \rangle. \quad (5.2.2)$$

Applying $\ln \det G_{\pi,\sigma} = \text{Tr} \ln G_{\pi,\sigma}$ and using standard techniques for solving these functional traces [KG06] one arrives at

$$\Omega = \Omega_\pi + \Omega_\sigma + \langle U \rangle + \langle \Omega_{\bar{q}q} \rangle - \frac{1}{2} m_\pi^2 \langle \vec{\pi}^2 \rangle - \frac{1}{2} m_\sigma \langle \Delta^2 \rangle, \quad (5.2.3)$$

$$\Omega_\pi = \frac{3}{3(2\pi)^3} \int d^3p \frac{p^2}{E_\pi} (1 + n_B(E_\pi)), \quad (5.2.4)$$

$$\Omega_\sigma = \frac{1}{3(2\pi)^3} \int d^3p \frac{p^2}{E_\sigma} (1 + n_B(E_\sigma)), \quad (5.2.5)$$

$$E_{\pi,\sigma}^2 = m_{\pi,\sigma}^2 + \vec{p}^2 \quad (5.2.6)$$

and $\Omega_{\bar{q}q}$ according to (4.2.17)⁸ in agreement with [MME04, BK09, FKP10]. From the thermodynamic potential the thermodynamic quantities (energy density, net quark density, entropy density, susceptibilities, etc.) follow by differentiation. The explicit formulas have been worked out in [MME04, BK09, FKP10]. For completeness the relations for several thermodynamic quantities are quoted in Appendix E. Following the nomenclature of [WK16, WK17] this approximation is named “linearized fluctuation approximation” (LFA) in the rest of this thesis.

5.2.2. Thermodynamics – standard set of parameters

In the following, an overview of the thermodynamics of the QMM in LFA is presented applying the parameter set A given in Tab. 5.1. Modifications of the patterns *w.r.t.* the model parameters are discussed in Section 5.3.

In Fig. 5.5, the masses of the mesons are depicted *w.r.t.* temperature T and chemical potential μ . The behavior is similar to the MFA result: the pion mass increases monotonously for increasing temperatures or chemical potential, while the sigma mass is minimal in the crossover region with a global minimum at the CEP. In the PWW phase, both masses are approximately degenerate, while in the PNG phase there is a large mass splitting in the meson sector. For the fermion mass it is less obvious what the correct mass parameter is. The derivation of the photon rate formulas (4.4.1) in Section 4 shows that in the corresponding FEYNMAN diagrams the fermion propagator has $m_q = g\langle\sigma\rangle$ as its mass parameter. On the other hand, a fermion mass can be determined by averaging either the meson field dependent $m_q(\sigma, \pi)$ (see (4.2.12)) or a power of it over the meson field configurations (and taking the corresponding root of the result), *i.e.*

$$M_q^{(n)} := \sqrt[n]{\langle m_q(\sigma, \pi)^n \rangle}. \quad (5.2.7)$$

The thus defined mass parameters $M_q^{(n)}$ are reasonable choices in the thermodynamic context. However, especially in the high temperature $T \gtrsim 100 \text{ MeV}$ region, there are notable differences to the propagator mass parameter m_q . In Fig. 5.6, $M_q^{(n)}$ and m_q for different choices of n are plotted over the phase diagram. Apparently, the choice of n has little effect

⁸ Strictly speaking n_F and $n_{\bar{F}}$ in (4.2.17) are evaluated at $\mu = 0$ and thus coincide there. The additional term $\mu\bar{q}\gamma^0 q$ to the Lagrangian in the integrand of the partition function leads to the well known shifts of the argument $E_q \rightarrow E_q \pm \mu$ in the fermion distribution functions making one of them the distribution function for particles and the other one that for antiparticles.

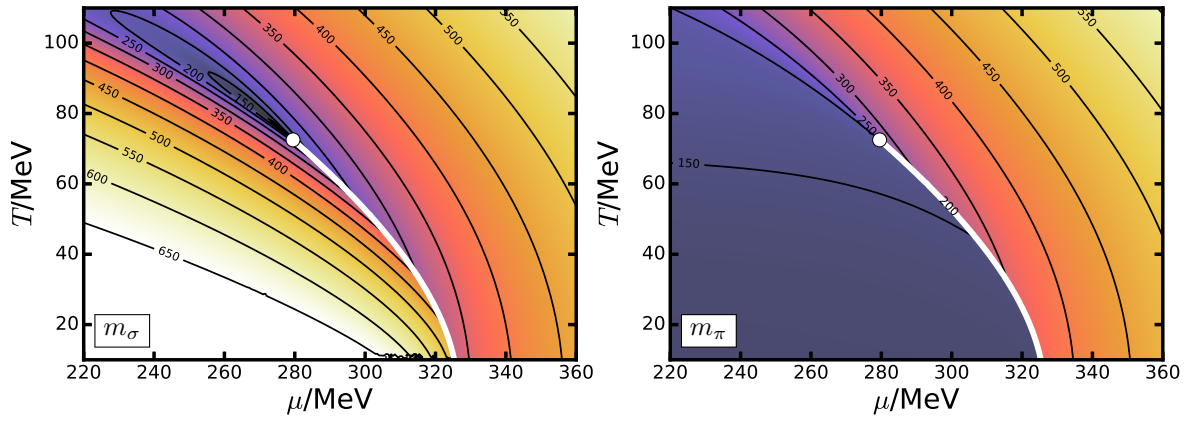


Figure 5.5.: Contour plots of the masses of the sigma meson m_σ (left panel) and the pions m_π (right panel) calculated within the LFA and given in units of MeV. For a simpler comparison the color codes are the same in both panels. The solid white curve denotes the FOPT which ends in a CEP (white dot).

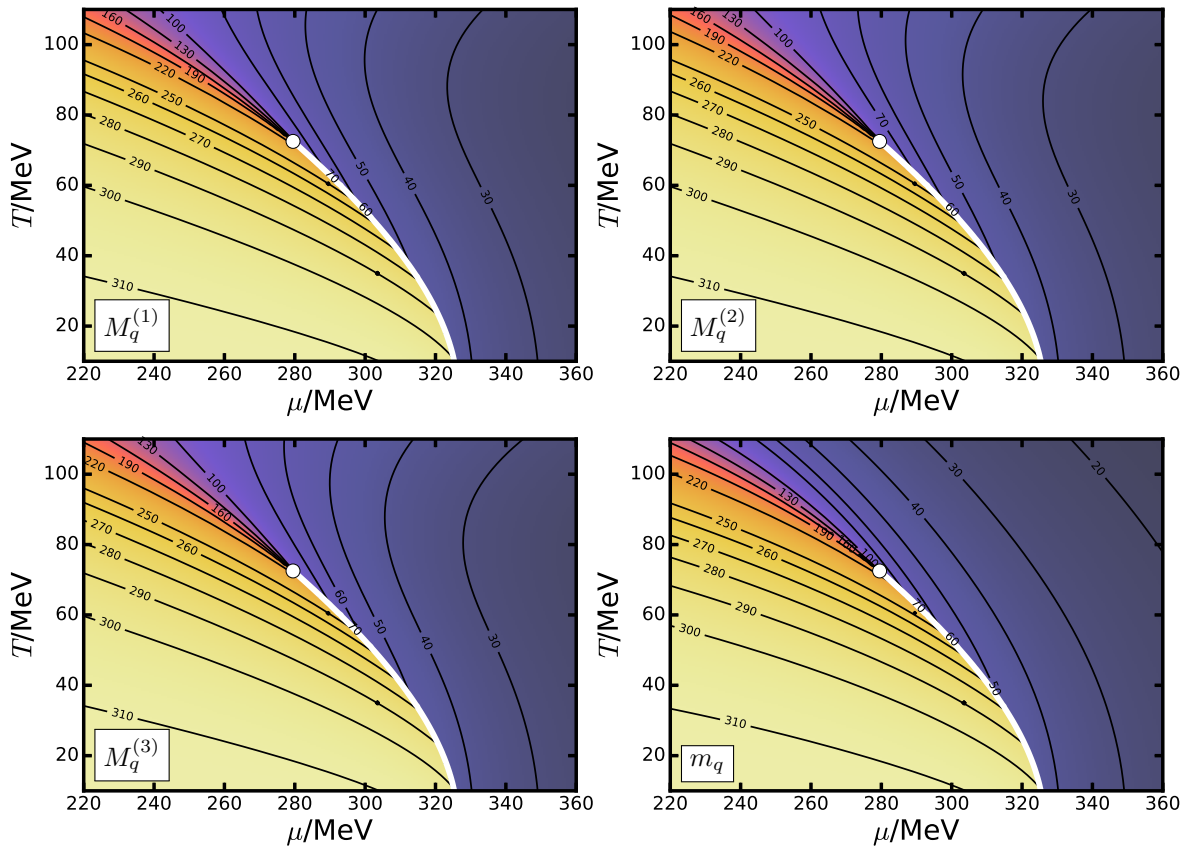


Figure 5.6.: Contour plots for different choices for the quark mass parameter (in MeV): $M_q^{(n)} = \sqrt[n]{\langle m_q^n \rangle}$ with $n = 1$ (upper left), 2 (upper right), 3 (lower left). The lower right panel shows $m_q = g\langle\sigma\rangle$, which is the correct mass to be used in FEYNMAN diagrams. Phase contour as in Fig. 5.5.

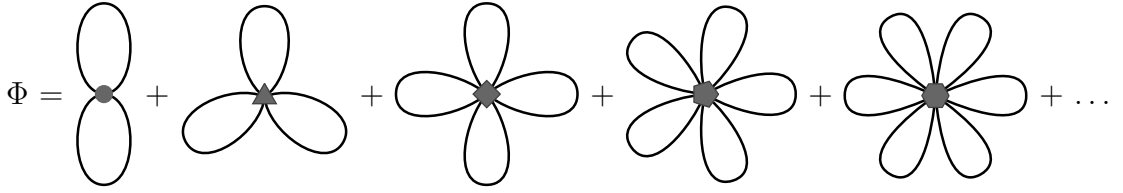


Figure 5.7.: Schematic diagrammatic representation of the Φ -functional of the effective mesonic theory with interaction potential U_{eff} according to (4.2.16).

on $M_q^{(n)}$ as was already reported for $\mu = 0$ in [MME04]. A particularly interesting feature of $M_q^{(n)}$ is the fact that these quantities – after their decrease in the low temperature region – increase again for high temperatures (when increasing the temperature). This is caused by meson field fluctuations, which can be seen most easily for $M_q^{(2)}$ after explicitly carrying out the averaging procedure for the fermion mass:

$$(M_q^{(2)})^2 = \left\langle g^2 \left((v + \Delta)^2 + \pi^2 \right) \right\rangle = g^2 \left(v^2 + \langle \Delta^2 \rangle + \langle \pi^2 \rangle \right). \quad (5.2.8)$$

For the propagator mass parameter m_q , the fluctuation-induced terms $\propto \langle \Delta^2 \rangle$ and $\propto \langle \pi^2 \rangle$ are absent. For this reason m_q decreases for increasing T and μ contrary to the thermal mass parameters $M_q^{(n)}$, *cf.* Fig. 5.6.

The separation of the fermion mass into an effective thermal mass and a dynamical (propagator) mass is caused by the LFA not being Φ -derivable⁹ in the fermion sector. Contrarily, in the meson sector the approximation is Φ -derivable (the corresponding Φ -functional is diagrammatically depicted in Fig. 5.7) and hence thermal and dynamical mass parameters coincide for both meson fields. In Fig. 5.7, lines represent the full meson propagators and the dots are the vertices extracted from U_{eff} . In order to reduce the number of depicted diagrams in this expansion only diagrams that differ topologically are depicted. In a full representation of the Φ -functional corresponding to the LFA, sigma and pion propagators have to be written separately (*e.g.* by representing sigma propagators with dashed and pion propagators with full lines) which leads, for a diagram with l loops, to 2^l topologically identical diagrams. The essential feature of the Φ -functional associated to the LFA, namely that all diagrams have only one vertex (however, the vertex factors are not identical for all diagrams), can already be seen in the compressed notation depicted in Fig. 5.7.

In Fig. 5.8, a selection of thermodynamic quantities calculated for parameter set A within the LFA is shown. All of the displayed quantities show a similar qualitative behavior as within the MFA, *cf.* Fig. 5.2. Especially the ratios s/s_0 and n/n_0 with the entropy density

⁹ The concept of Φ derivable approximations is introduced in the pioneering works [BK61, Bay62, CJT74]. A modern introduction can be found, *e.g.*, in [vHK02].

s , the net quark density n and the same quantities evaluated for an ideal ultrarelativistic FERMI gas s_0 and n_0 show a similar behavior as in the MFA, *i.e.* in the PWW phase these ratios tend to unity.

The entropy per quark ratio s/n is displayed in Fig. 5.9. Here, we only want to stress that this plots are quite similar to the corresponding plots shown in Fig. 5.4. For a further discussion of the isentropes, *i.e.* the curves of constant s/n ratio, we refer to Section 5.3.3.

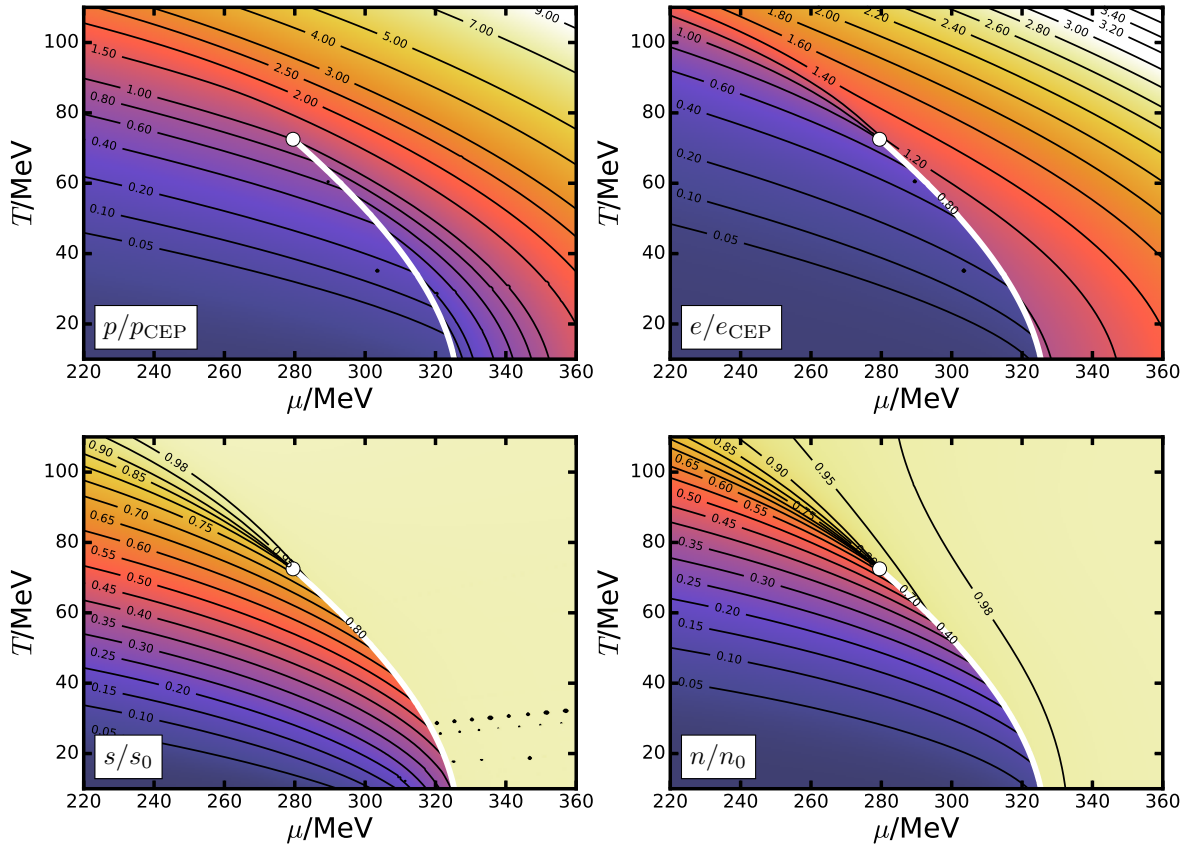


Figure 5.8.: Contour plots of pressure p (top left panel) and energy density e (top right), scaled with their respective values – p_{CEP} and e_{CEP} – at the CEP as well as entropy density s (bottom left) and net quark density n (bottom right) scaled with the same quantities – s_0 and n_0 – for an ideal ultrarelativistic FERMI gas. The data was calculated within the LFA using the parameter set A given in Tab. 5.1. The thick white curve in each panel denotes the FOPT curve and the white dot is the point with minimal sigma mass as a measure for the CEP position.

The size of the critical region is not a precisely defined quantity. In the literature, several prescriptions based on the quark number susceptibility $\chi_{\mu\mu} = \partial^2 p / \partial \mu^2$ or the chiral susceptibility $\chi_m = \partial^2 p / \partial m^2$ as well as fluctuation measures are used, *cf.* [SW12, Tiw12, VAGP15]. In all these cases the respective quantities are enhanced in the critical region relative to some reference. These reference quantities are not uniquely defined either, which

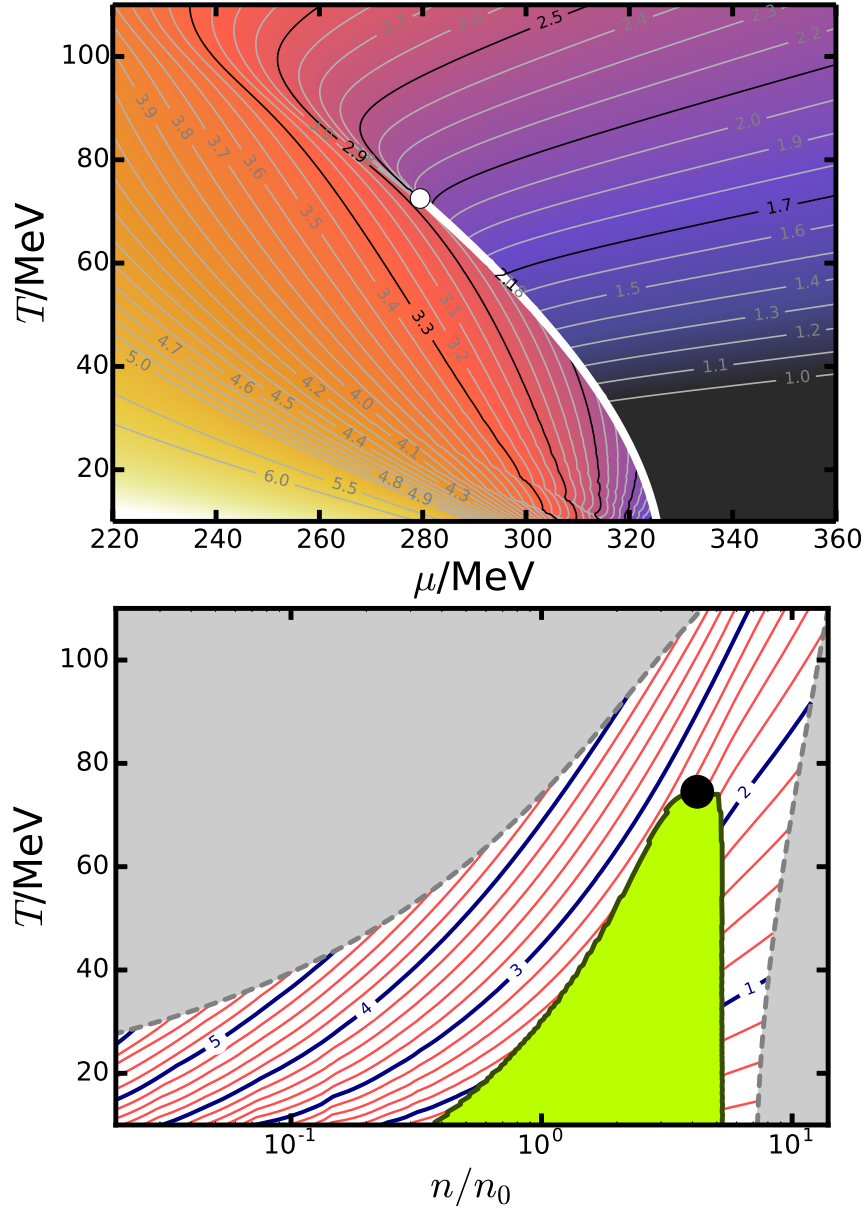


Figure 5.9.: Contour plots of the entropy per quark ratio s/n displayed *w.r.t.* temperature T and quark chemical potential μ (upper panel) and *w.r.t.* temperature and net quark density n (lower panel), respectively. In the upper panel, the FOPT curve as well as the CEP are denoted by a white curve and a white dot, respectively. In the lower panel, the green region is the coexistence region with the CEP (black dot) at its boundary. The net quark density is scaled by the nuclear saturation density $n_0 = 0.16 \text{ fm}^{-3}$. In the gray regions, which are characterized by the conditions $\mu \leq 220 \text{ MeV}$ (left region) and $\mu \geq 360 \text{ MeV}$ (right region), no data has been computed.

introduces a certain amount of arbitrariness to the discussion of the critical regions. Possible choices for the reference quantities are the same quantities averaged over a region of

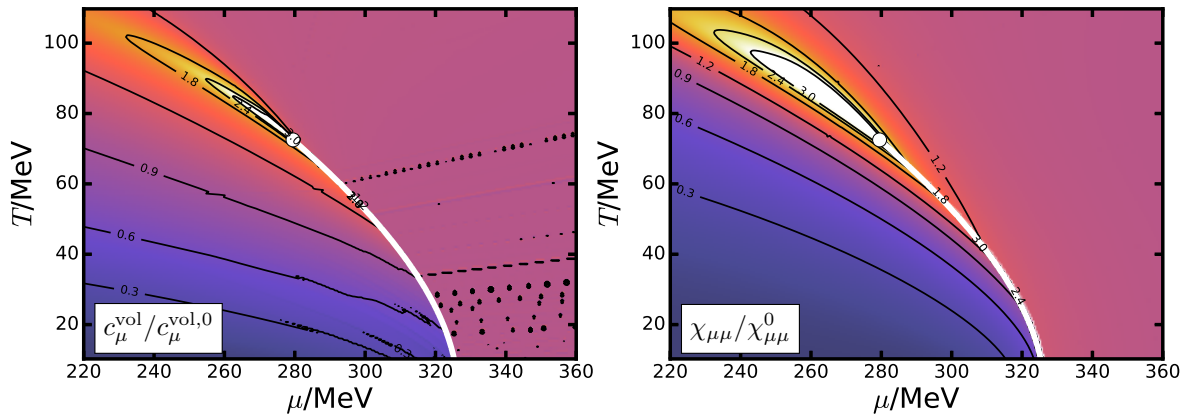


Figure 5.10.: Normalized heat capacity (left panel) $c_\mu^{\text{vol}}/c_\mu^{\text{vol},0} = (c_\mu^{\text{vol},0})^{-1}\partial s/\partial T$ and normalized quark number susceptibility (right panel) $\chi_{\mu\mu}/\chi_{\mu\mu}^0 = 1/\chi_{\mu\mu}^0\partial n/\partial\mu$ for parameter set A. The normalization factors c_0 and $\chi_{\mu\mu}^0$ are the corresponding quantities for an ideal ultrarelativistic FERMI gas with the same number of degrees of freedom.

the phase diagram of intermediate size or the same quantities for an ideal ultrarelativistic gas. In the right panel of Fig. 5.10, the quark number susceptibility $\chi_{\mu\mu}$ normalized to the quark number susceptibility $\chi_{\mu\mu}^0$ of an ultrarelativistic ideal FERMI gas with the same number of degrees of freedom is displayed. This is the procedure also applied, *e.g.* in [SW12]. Clearly, one notes that, within the LFA, $\chi_{\mu\mu}/\chi_{\mu\mu}^0$ is enhanced around the CEP. Such an enhancement is also observed in the MFA, *cf.* Fig. 5.3. However, size and shape of the critical region differ in both approximation schemes.

In the crossover region, the heat capacity can be used to estimate the pseudocritical curve. The volumetric heat capacity (at constant quark chemical potential) c_μ^{vol} , when normalized to the heat capacity of an ideal ultrarelativistic FERMI gas $c_\mu^{\text{vol},0}$, exhibits an increase in the crossover region. Nevertheless, other choices such as the peak position of the chiral susceptibility or the maximum slope of the renormalized chiral condensate $\langle\bar{q}q\rangle$ are conceivable; see [AFKS06, BDM⁺14] for a discussion of the influence of the precise definition.

In [VAGP15], the scaled variance $\tilde{\sigma}(N) = (\langle N^2 \rangle - \langle N \rangle^2)/\langle N \rangle$, with N denoting the baryon number, and higher moments of the quark distribution, such as the skewness, are suggested for the identification of a critical region. The central moments $\langle (N - \langle N \rangle)^i \rangle$ can be calculated from the (dimensionless) cumulants k_i characterizing the quark distribution (in general: the distribution of a conserved quantity,¹⁰ such as baryon number, electric charge or strangeness) by differentiation of the pressure *w.r.t.* the chemical potential according

¹⁰ Conserved *w.r.t.* the strong interaction.

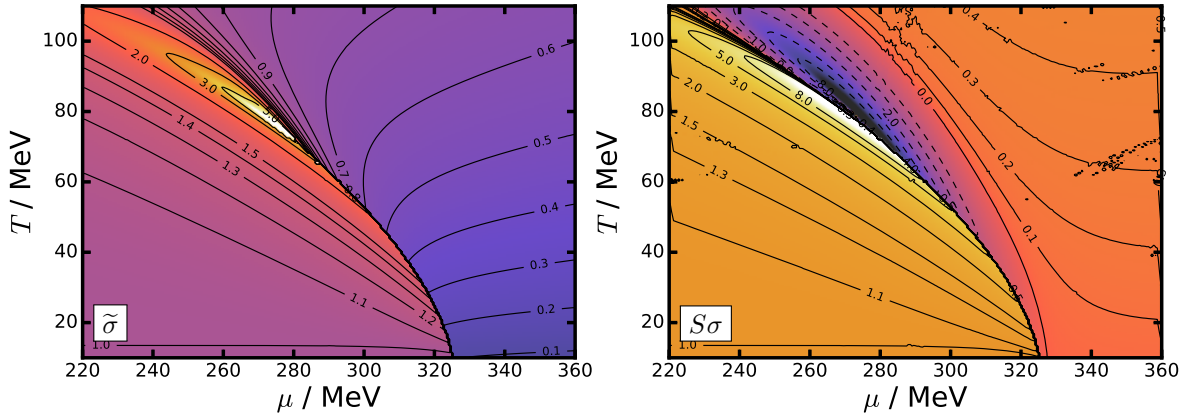


Figure 5.11.: Central moments characterizing the distribution of quarks according to [VAGP15]. Depicted are the scaled variance $\tilde{\sigma} = \langle(N - \langle N \rangle)^2\rangle/\langle N \rangle$ (left panel) and the skewness $S\sigma = \langle(N - \langle N \rangle)^3\rangle/\langle(N - \langle N \rangle)^2\rangle$ (right panel) *w.r.t.* temperature T and quark chemical potential μ .

to $k_i = T^{i-4}\partial^i p/\partial\mu^i$. The idea behind using the distributions of a conserved quantity (characterized by its cumulants) is that correlation functions become scale-independent at a critical point, a phenomenon incompatible with a Gaussian distribution for which the standard deviation constitutes an immanent scale. The scale-independence leads to the divergence of certain fluctuation measures such as the cumulants of the distribution. Since the degree of divergence increases with the order of the cumulants it may be possible to observe even imperfect criticality (*e.g.* due to experimental limitations) through its impact on the high-order cumulants.

Because of the difficulty of properly defining an effective volume of the strongly interacting medium produced in heavy-ion collisions (HICs) it is convenient to use volume independent (intensive) quantities to characterize the fluctuations of conserved quantities measured in these experiments [FAR17]. Therefore, in Fig. 5.11 the scaled variance $\tilde{\sigma} = (\langle N^2 \rangle - \langle N \rangle^2)/\langle N \rangle = k_2/k_1$ (left panel) and the skewness $S\sigma = \langle(N - \langle N \rangle)^3\rangle/\langle(N - \langle N \rangle)^2\rangle = k_3/k_2$ (right panel) are displayed in the vicinity of the CEP, both being such volume independent fluctuation measures. Both quantities show striking features close to the CEP. The increase of the scaled variance ω in the vicinity of the CEP can be attributed to the above mentioned enhancement of fluctuations related to criticality, while the skewness $S\sigma$ encodes certain deviations from a Gaussian distribution [Bul79].

5.2.3. The sigma mass parameter and the CEP

At the end of the FOPT curve, one expects a point where the phase transition is of second order. For such transitions the correlation length diverges and in turn the microscopic

physics becomes less important. This leads to universal behavior which is conveniently quantified by critical exponents characterizing the critical behavior of a multitude of quantities, such as heat capacity, correlation length or the order parameter of the phase transition. The divergence of the correlation length requires the mass of at least one mode to vanish.¹¹ In the QMM, this mode is the deviation Δ of the σ field from its thermal expectation value v . However, within the LFA, the masses of all particles are nonzero at the CEP. This is an artifact of the approximation scheme and can be understood by considering the interplay of Eqs. (4.2.25) and (4.2.20). On the one hand, low masses lead to large field fluctuations according to (4.2.25). On the other hand, large fluctuations lead to positive contributions to the masses, because of the fourth-order increase of the meson interaction potential which only contribute significantly to the m_σ , if the sigma field deviates strongly from its expectation value. Therefore, it is only possible to fulfill both, (4.2.25) and (4.2.20), if the σ mass is larger than some lower limit, which is of the order of the temperature. For the parameter set A, the minimal σ mass is $m_\sigma^{\text{CEP}} = 72 \text{ MeV}$. Consequently, the correlation length at the CEP $\xi_{\text{CEP}} \sim 1/m_\sigma^{\text{CEP}}$ is of order 3 fm. For the application to HICs, this is presumably enough as it is at least of the same order of magnitude as the system size which constitutes an upper limit for the correlation length. The correlation length in a HIC is furthermore limited by non-equilibrium effects [SRS99, BR00]. For instance, the expansion time scale $\tau_{\text{exp}} = R/\dot{R}$ (with R characterizing the size of the strongly interacting medium)¹² being of the order of a few fm/ c prevents the correlation length from becoming larger than a few fm.¹³ Another point of view on this issue is that close to the CEP the time scale for the relaxation to equilibrium increases, a phenomenon commonly called critical slowing down.¹⁴ Sufficiently close to the critical point the equilibration time scale τ_{eq} thus becomes larger than the expansion time scale τ_{exp} driving the system off equilibrium and making equilibrium properties difficult to access in the critical region. It thus can be concluded that although in the direct neighborhood of the CEP the LFA cannot reproduce the static properties in an entirely satisfying manner, the results of dynamic calculations

11 For a theory with a mass gap Δm the correlation functions are bounded by $C \exp\{|\vec{r}|\Delta m\}$. This allows a divergence of the corresponding length scale (the correlation length ξ) only for $\Delta m \rightarrow 0$. Furthermore, the mass gap is at least twice the mass of the lightest mode in the system.

12 Equally well one could use $\tau_{\text{exp}}^s := -s/\dot{s}$ or $\tau_{\text{exp}}^V := V/\dot{V}$. If the system expands adiabatically, both definitions yield the same results, *i.e.* $\tau_{\text{exp}}^s = \tau_{\text{exp}}^V$.

13 Maintaining thermal equilibrium requires the relaxation time scale τ_{eq} not to exceed the expansion time scale τ_{exp} . Since τ_{eq} is related to the correlation length ξ according to $\xi \sim \tau_{\text{eq}}^z$ with z being the dynamical critical exponent this implies $\xi \leq C\tau_{\text{exp}}^{1/z}$ with some constant C .

14 Qualitatively, this can be understood by noting that close to the CEP the effective potential for the critical mode (in case of the QMM, this is Δ) becomes flat which causes the entropic forces that drive the system back to equilibrium to be of higher than first order in Δ (as they are away from the CEP) and thus increasing the relaxation time scale.

(in the context of HICs) still might be sufficiently accurate.

Due to the limitations of the LFA the sigma mass is not vanishing at the CEP. However it still is minimal there. Therefore, in the figures of this and the subsequent chapters the global minimum of m_σ is used as an estimate for the location of the CEP.

5.3. Sensitivity with respect to model parameters

The properties of the medium described with the QMM depend strongly on the precise values of the parameters λ , ζ , H and g in the Lagrangian. These parameters possess several drawbacks which make them less practical for comparisons. An important example for such a drawback is the limited comparability of these parameters between different approximations. For instance, within the functional renormalization group (FRG) framework the model parameters have to be defined at some UV momentum scale as initial conditions for the renormalization group flow. These numbers are difficult to compare already within the FRG framework, and even less comparable to the MFA or LFA values. However, typically the vacuum masses of the particles and the vacuum expectation value of the σ field derived from these different starting points are given, which makes these four parameters best suited for the discussion of the parameter sensitivity. Furthermore, the parameters of the Lagrangian are not observable and depend on regularization scheme as well as the renormalization scale. Therefore, the parameter sets in Tab. 5.1 are characterized by the vacuum masses m_π^{vac} , m_σ^{vac} and $m_{\text{nuc}}^{\text{vac}}$, the later one being related to the vacuum quark mass by $m_{\text{nuc}}^{\text{vac}} = N_c m_q^{\text{vac}}$, as well as the vacuum expectation value of the sigma field $\langle\sigma\rangle_{\text{vac}}$.

5.3.1. Phase contour

To a large extent the phase transition curve (FOPT curve and crossover region) is determined by the meson potential at zero meson fields. This follows from realizing that the fermionic contribution to the pressure in the PWW phase is much larger than the fermionic and bosonic contributions in the PNG phase. The difference is compensated at the phase transition curve by a change in the average meson potential switching from $\langle U(\sigma \approx \langle\sigma\rangle_{\text{vac}}) \rangle$ in the PNG phase to $\langle U(\sigma \ll \langle\sigma\rangle_{\text{vac}}) \rangle$ in the PWW phase. Thus, with the pressure p_{PNG} in the PNG phase given by $p_{\text{PNG}} = -U(v) + \text{FERMI} + \text{BOSE terms} \approx U(\langle\sigma\rangle_{\text{vac}})$ and in the PWW phase by $p_{\text{PWW}} \approx -U(0) + p_F$, where p_{PWW} and p_F are the pressures in the PWW phase and that of an ideal ultrarelativistic FERMI gas¹⁵, respectively, one finds that at the

¹⁵ p_F is expected to be a good approximation of the fermionic contribution to p_{PWW} , since in the PWW phase m_q is significantly smaller than T and/or μ .

FOPT

$$-U(\langle\sigma\rangle_{\text{vac}}) \approx -U(0) + 2N_f N_c \left(\frac{7\pi^2}{890} T^4 + \frac{1}{24} \mu^2 T^2 + \frac{1}{48\pi^2} \mu^4 \right), \quad (5.3.1)$$

$$U(0) = \frac{\langle\sigma\rangle_{\text{vac}}^2 ((m_\sigma^{\text{vac}})^2 - 3(m_\pi^{\text{vac}})^2)^2}{8 (m_\sigma^{\text{vac}})^2 - (m_\pi^{\text{vac}})^2} \quad (5.3.2)$$

$$= \frac{(m_\sigma^{\text{vac}})^2 \langle\sigma\rangle_{\text{vac}}^2}{8} \left(1 - 5 \frac{m_\pi^{\text{vac}2}}{m_\sigma^{\text{vac}2}} + \mathcal{O}\left(\frac{m_\pi^{\text{vac}4}}{m_\sigma^{\text{vac}4}}\right) \right), \quad (5.3.3)$$

$$U(\langle\sigma\rangle_{\text{vac}}) = \frac{(m_\sigma^{\text{vac}})^2 \langle\sigma\rangle_{\text{vac}}^2}{8} \left(-8 \frac{(m_\pi^{\text{vac}})^2}{(m_\sigma^{\text{vac}})^2} + \mathcal{O}\left(\frac{m_\pi^{\text{vac}4}}{m_\sigma^{\text{vac}4}}\right) \right) \quad (5.3.4)$$

leading to

$$T_c^2 = \frac{1}{7\pi^2} \left(2\sqrt{30} \sqrt{\frac{42\pi^2(U(0) - U(\langle\sigma\rangle_{\text{vac}}))}{2N_f N_c}} + \mu^4 - 15\mu^2 \right) \quad (5.3.5)$$

as an estimate for the critical temperature T_c *w.r.t.* the quark chemical potential. Since the ratio $(m_\pi^{\text{vac}})^2/(m_\sigma^{\text{vac}})^2$ is small in realistic scenarios one may apply the chiral limit value of $U(0) - U(\langle\sigma\rangle_{\text{vac}}) = (m_\sigma^{\text{vac}})^2 \langle\sigma\rangle_{\text{vac}}^2/8$ as a good estimate. Although this estimation is rather crude and in the crossover region not even justified it is a surprisingly accurate result for the phase transition curve (*cf.* Fig. 5.12). To achieve a more quantitative agreement of the approximation with the actual phase boundary it is convenient to rescale the prediction according to (5.3.5) (where m_π^{vac} is set zero¹⁶) by the result for some reference parameter set. In Fig. 5.12,

$$T_{\text{pc}}^{0,\text{ref}} = 150 \text{ MeV}, \quad \mu_c^{0,\text{ref}} = 330 \text{ MeV}, \quad \text{for } m_\sigma^{\text{vac}} \langle\sigma\rangle_{\text{vac}} = 260^2 \text{ MeV}^2. \quad (5.3.6)$$

were chosen as reference for the pseudocritical temperature at zero chemical potential T_{pc}^0 and the critical chemical potential at zero temperature μ_c^0 . Inspecting (5.3.5) together with (5.3.3) and (5.3.4) yields $T_{\text{pc}}^0, \mu_c^0 \propto \sqrt{m_\sigma^{\text{vac}} \langle\sigma\rangle_{\text{vac}}}$. Keeping the dependence on model parameters and adjusting the prefactor accordingly, yields the estimates

$$T_{\text{pc}}^0 \approx 150 \text{ MeV} \frac{\sqrt{m_\sigma^{\text{vac}} \langle\sigma\rangle_{\text{vac}}}}{260 \text{ MeV}}, \quad \mu_c^0 \approx 330 \text{ MeV} \frac{\sqrt{m_\sigma^{\text{vac}} \langle\sigma\rangle_{\text{vac}}}}{260 \text{ MeV}}. \quad (5.3.7)$$

These estimates are marked with small arrows in Fig. 5.12 with the color referring to the respective value of $m_\sigma^{\text{vac}} \langle\sigma\rangle_{\text{vac}}$.

¹⁶ This restriction is not necessary. However it simplifies the approximation considerably with little influence on the results, as long as $(m_\pi^{\text{vac}})^2/(m_\sigma^{\text{vac}})^2$ is small.

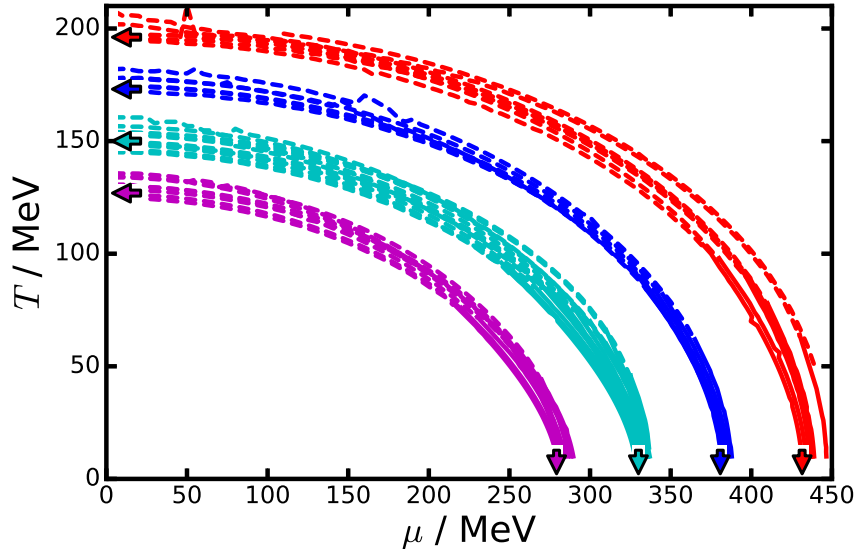


Figure 5.12.: Demonstration of the estimate of the critical curve. Shown are the critical curves for several parameter sets varying $\langle\sigma\rangle_{\text{vac}}$ from 60 MeV to 120 MeV and $\mu_c^0 - m_{\text{nuc}}^{\text{vac}}/N_c$ from -100 MeV to 100 MeV. In each group of phase transition lines the product $m_{\sigma}^{\text{vac}}\langle\sigma\rangle_{\text{vac}}$ is kept fixed: $m_{\sigma}^{\text{vac}}\langle\sigma\rangle_{\text{vac}}/\text{GeV}^2 = 0.1156$ (red), 0.09 (dark blue), 0.0676 (light blue) and 0.048 (violet). The arrows mark the pseudocritical temperature T_{pc}^0 at vanishing density and the critical chemical potential μ_c^0 at vanishing temperature calculated according to (5.3.7) for the respective (same color) group of phase contours with fixed $m_{\sigma}^{\text{vac}}\langle\sigma\rangle_{\text{vac}}$.

5.3.2. Critical end point

To get a feeling of what determines the position of the critical point within the QMM one may resort to the MFA. In this approximation, the pressure depends on the meson fields only via the expectation value v of the sigma field:

$$p_{\text{MFA}}(v) = -\frac{\lambda}{4}(v^2 - \zeta)^2 + Hv - \frac{2N_f N_c T}{(2\pi)^3} \int d^3p \left[\ln(1 + e^{(\mu - E)/T}) + \{\mu \rightarrow -\mu\} \right]. \quad (5.3.8)$$

The thermal expectation value of the sigma field is obtained by maximizing p_{MFA} *w.r.t.* v :

$$\begin{aligned} 0 &= \frac{\partial p_{\text{MFA}}}{\partial v} \\ &= -\lambda(v^2 - \zeta)v + H + \frac{2N_f N_c g^2 v}{2\pi^2} \int d|\vec{p}| \frac{|\vec{p}|^2}{E} (n_F(E) + n_{\bar{F}}(E)) \end{aligned} \quad (5.3.9)$$

where $n_{F,\bar{F}} = (1 + \exp\{(E \mp \mu)/T\})^{-1}$ denote the distribution functions for fermions (-) and antifermions (+), respectively. The occurrence of an FOPT and the position of the critical point is understandable in view of (5.3.9). An FOPT requires multiple (precisely: three)

solutions of (5.3.9). One of these solutions will have a small value of v leading to a dominant fermion term (the momentum integral in (5.3.9)) corresponding to the PWW phase. One solution will be thermodynamically unstable and the third one will be relatively close to the vacuum value corresponding to the PNG phase. For this solution, the derivative of the meson potential (the first two terms in (5.3.9)) gives important contributions. Such a pattern of solutions requires

$$\frac{2N_f N_c g^2}{2\pi^2} \int_{v \lesssim \langle \sigma \rangle_{\text{vac}}} d|\vec{p}| \frac{|\vec{p}|^2}{E} (n_F(E) + n_{\bar{F}}(E)) < -\lambda(v^2 - \zeta) + \frac{H}{v}. \quad (5.3.10)$$

If this inequality is not fulfilled or at least strongly violated the fermion contribution dominates in (5.3.9) supporting only a single solution of (5.3.9) instead of the above described triple solutions. At zero temperature, there are two cases: (i) The fermion mass $m_q = gv$ close to the critical curve (or its estimate according to (5.3.1)) is so small that the fermionic integral in (5.3.9) is dominant and no FOPT occurs. In the opposite case there is an FOPT irrespective of m_q being smaller (case (iia)) or larger (case (iib)) than the critical chemical potential. According to (5.3.5) the critical curve bends toward the temperature axis and already at relatively small temperatures the critical chemical potential gets smaller than the vacuum fermion mass. Thus, only case (iib) is discussed in the following, however, it can be regarded as an upper limit for (iia).

In case (iib), substantial contributions to the momentum integral in (5.3.9) come from the edge of the FERMI distributions or their proximity, *i.e.* from the range $(\mu - xT, \mu + xT)$ with $x = 2 \dots 4$. Since the minimal energy-argument for the FERMI distributions is $E = m_q$ the energy interval that contributes significantly to the fermion term in (5.3.9) is $[m_q, \mu + xT)$. If the vacuum quark mass is larger than $\mu + xT$ the momentum integral in (5.3.9) is too small to be of significance.

The above considerations provide the possibility to judge the impact of $m_{\text{nuc}}^{\text{vac}}$ on the FOPT curve. Applying parameter set A but scanning through a wide variety of values for $m_{\text{nuc}}^{\text{vac}}$, one finds with $x = 4$ and $m_{\text{nuc}}^{\text{vac}} \gtrsim 1700$ that the momentum integral is small for all temperatures at the critical curve yielding a curve of FOPTs, which surrounds the PNG phase completely. This gives rise to an important observation: If the vacuum nucleon mass and hence the quark mass is sufficiently large the FOPT curve can be made to extend from the μ -axis even to the temperature axis. However, a large fermion mass means that the isentropes end on the FOPT curve (see discussion below), which is typically not a desired feature.¹⁷ If one needs isentropes exiting the critical curve at some non-zero temperature,

¹⁷ According to general arguments, the endpoint of an (approximate adiabatic) expansion is at $T = 0$ and $n = 0$, *i.e.* in the vacuum. The vacuum in turn cannot be in direct contact to the chiral FOPT

one is limited to a vacuum quark mass $m_q^{\text{vac}} = m_{\text{nuc}}^{\text{vac}}/N_c$ less than the critical chemical potential μ_c^0 at zero temperature (determined from (5.3.7)). Then, there is an upper limit for the critical temperature corresponding to a critical end point at $T_{\text{CEP}} = \mathcal{O}(100 \text{ MeV})$ ¹⁸ and corresponding μ_{CEP} .

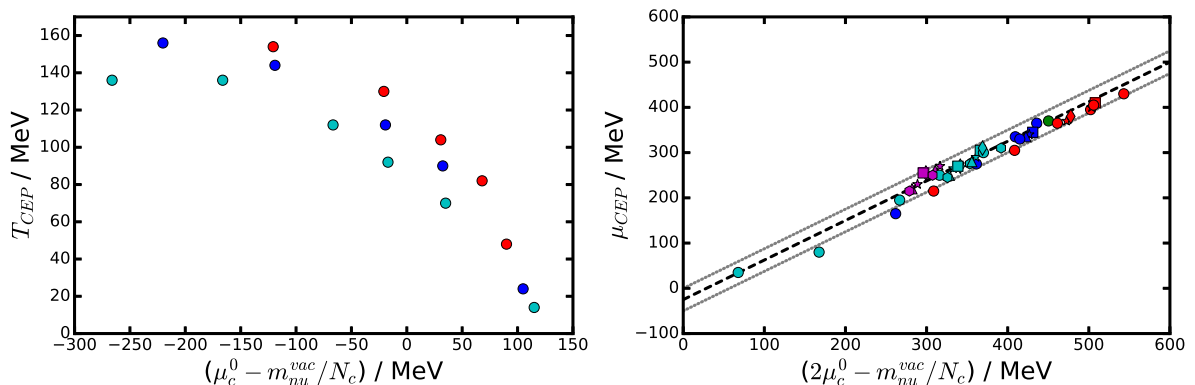


Figure 5.13.: Dependence of the coordinates of the CEP (T_{CEP} on the left panel and μ_{CEP} on the right) on model parameters. The color code is the same as in Fig. 5.12. The symbols denote $\langle\sigma\rangle_{\text{vac}}/\text{MeV} = 60$ (hexagons), 70 (triangles), 90 (stars), 100 (circles), 110 (squares), 120 (diamonds). The black dashed line is the function $f(x) = -25 \text{ MeV} + 7x/8$ with $x = 2\mu_c^0 - m_{\text{nuc}}^{\text{vac}}/N_c$ and the grey dotted lines are $f_{\pm}(x) = f(x) \pm 25 \text{ MeV}$.

With this considerations the behavior of the temperature of the critical point is understandable (*cf.* left panel of Fig. 5.13). In this figure, the positions of the CEP *w.r.t.* a variety of model parameters is plotted. In both panels, the vacuum pion mass m_{π}^{vac} is kept fixed at 138 MeV since the impact of this parameter is discussed rather comprehensively in [BK09] and [SFN⁺10].

The results presented in these works can be summarized by the following: The shape and position of the phase boundary between the PNG and the PWW phases is rather insensitive to the value of m_{π}^{vac} , at least if the explicit chiral symmetry breaking is small, *i.e.* for $(m_{\pi}^{\text{vac}})^2/(m_{\sigma}^{\text{vac}})^2 \ll 1$. However, m_{π}^{vac} shifts the CEP along the phase boundary in such a way that T_{CEP} increases for decreasing m_{π}^{vac} . For sufficiently small m_{π}^{vac} (in [BK09] it was found $m_{\pi}^{\text{vac}} \lesssim 35 \text{ MeV}$, which translates with their value of m_{σ}^{vac} into $(m_{\pi}^{\text{vac}})^2/(m_{\sigma}^{\text{vac}})^2 \lesssim 1/400$) a second curve of FOPTs forms, which also follows the phase boundary curve but starts at the temperature axis, bends towards the chemical-potential-axis and ends at second CEP. For small enough m_{π}^{vac} both curves of FOPTs merge and separate the PNG and the PWW phase completely. The reason for this behavior in the chiral limit is given in [SFN⁺10]

since ordinary nuclear matter is located *between* both landmarks in the phase diagram.

¹⁸ See left panel of Fig. 5.13. The condition that isentropes exit the FOPT at $T > 0$ corresponds approximately to $\mu_c^0 - m_{\text{nuc}}^{\text{vac}}/N_c > 0$.

where it is argued that the transition being of first order at the temperature axis in the chiral limit is an artifact of the omission of the fermion vacuum term in (4.2.17).

Apart from m_π^{vac} in the left panel of Fig. 5.13 also $\langle\sigma\rangle_{\text{vac}}$ is held fixed (at $\langle\sigma\rangle_{\text{vac}} = 100 \text{ MeV}$) and m_σ^{vac} as well as $m_{\text{nuc}}^{\text{vac}}$ are varied. The sigma vacuum mass m_σ^{vac} there takes the values 1156 MeV (red), 900 MeV (dark blue) and 676 MeV (light blue) corresponding to the color code used in Fig. 5.12. The vacuum mass of the nucleons $m_{\text{nuc}}^{\text{vac}}$ is varied from 600 MeV to 1800 MeV. With the discussion above as well as by looking at Fig. 5.12 one notes that the critical chemical potential μ_c^0 at zero temperature is approximately the same in each of the three groups (the red, the dark and the light blue) of phase transitions. Within each group, in turn, the CEP temperature T_{CEP} decreases for increasing $\mu_c^0 - m_{\text{nuc}}^{\text{vac}}/N_c$, *i.e.* for decreasing $m_{\text{nuc}}^{\text{vac}}$ or m_q^{vac} . Furthermore, T_{CEP} becomes zero if the vacuum quark mass is more than about 100 MeV smaller than μ_c^0 . If $m_{\text{nuc}}^{\text{vac}}/N_c$ is more than about 200 MeV larger than μ_c^0 then T_{CEP} is comparable (and eventually identical) to the critical temperature T_{pc}^0 at zero chemical potential (*cf.* (5.3.7)), which means that the curve of FOPTs stretches all the way from the μ axis to the T axis which is the behavior theoretically discussed in terms of (5.3.9) above.

When plotted *w.r.t.* the variable $x := 2\mu_c^0 - m_{\text{nuc}}^{\text{vac}}/N_c$ the CEP chemical potentials μ_{CEP} approximately collapse to a small band centered around the line $f(x) = 7x/8 - 25 \text{ MeV}$, which has a width of approximately 50 MeV, *cf.* right panel of Fig. 5.13. With (5.3.7) the variable x can be expressed in terms of the vacuum properties only, which makes this observation (the linear dependence of μ_{CEP} on x) very useful for the search of parameter sets that obey restrictions on the position of the CEP.

Including thermal meson fluctuations, *e.g.* by considering the LFA, the CEP shifts towards larger μ and smaller T . This is expected since even within the MFA stronger fermion field fluctuations,¹⁹ *i.e.* higher temperatures, tend to weaken the phase transition (*i.e.* reducing the latent heat). The additional fluctuations present in LFA have a similar effect, *i.e.* they also weaken the phase transition and thus move the CEP along the boundary towards smaller temperatures. A similar reasoning applies to the inclusion of vacuum fluctuations, which also push the CEP towards smaller temperatures.

5.3.3. Isentropes

Of special interest for the hydrodynamic simulation of HICs are the isentropes – curves of a constant entropy per baryon (or quark) ratio s/n – since the strongly interacting medium

¹⁹ There are no meson fluctuations in MFA.

behaves as an almost perfect fluid [RR07, ST09] and consequently the expansion is almost adiabatic and thus s/n is constant [Oll08, Flo10].

The behavior of the isentropes can be understood in the two limits (i) $T \rightarrow 0$ as well as (ii) $m_q \rightarrow 0$. In the PWW phase the pressure of the model is well approximated by the pressure of an ideal ultrarelativistic FERMI gas, for which the entropy per quark is given by

$$\frac{s}{n} = \pi^2 \frac{7\pi^2 \tan^3(\phi) + 15 \tan(\phi)}{15\pi^2 \tan^2(\phi) + 15}, \quad (5.3.11)$$

with the polar angle ϕ determined by $\tan(\phi) = T/\mu$. The mesonic contributions are suppressed because the mesons acquire large masses in the PWW phase [SMMR01]. According to (5.3.11), for every choice of s/n the isentropes of an ideal massless FERMI gas, and thus for the QMM in the high temperature phase, follow curves with $\tan(\phi) = \text{const}$.

The isentropes at $T \rightarrow 0$ can be obtained by considering the various contributions in (5.2.3) to the thermodynamic potential. It turns out that for $T \rightarrow 0$ the only term in (5.2.3) without negligible T or μ derivative is the (averaged) fermion pressure (except at the FOPT, where also the (averaged) meson potential jumps). Approximating the FERMI distribution function for small T and $(\mu - m_q^{\text{vac}})$ by

$$n_F(E, T, \mu) \approx \begin{cases} 1 & \text{for } E < \mu - 2T \\ \frac{1}{2} - \frac{E-\mu}{4T} & \text{for } \mu - 2T \leq E \leq \mu + 2T, \\ 0 & \text{for } \mu + 2T < E \end{cases}, \quad (5.3.12)$$

one can show that all isentropes approach the point $(T = 0, \mu_1 = m_q^{\text{vac}})$ in the phase diagram, at least if vacuum fluctuations are omitted.

5.3.4. Phase transition type

In the limit $(m_\pi^{\text{vac}})^2/(m_\sigma^{\text{vac}})^2 \rightarrow 0$ (*i.e.* in the chiral limit, *cf.* (2.2.26) and (2.2.27)), the FOPT at zero temperature occurs at a chemical potential given by (5.3.7), which is also a good approximation for a small but nonzero value of $(m_\pi^{\text{vac}})^2/(m_\sigma^{\text{vac}})^2$. Thus, by tuning the model parameters (or equivalently the vacuum values for the masses and $\langle \sigma \rangle_{\text{vac}}$, *cf.* (2.2.27)) the endpoints of the isentropes *i.e.* $(T = 0, \mu = m_{\text{nuc}}^{\text{vac}}/N_c = m_q^{\text{vac}})$, and the critical chemical potential μ_c^0 at zero temperature, can be shifted relative to each other making the model flexible enough for the study of different dynamical situations. In particular, it is possible to move from the scenario of the endpoints of the isentropes being in the PNG phase to the one with the endpoints on the phase contour (in the T - μ plane).

However, these endpoints cannot be shifted into the PWW phase. This is because for $T \rightarrow 0$, the bosonic contributions to the pressure are negligible and thus the T and μ dependence of the pressure is governed by the fermionic contribution. For a massive FERMI gas thermodynamic stability in the vicinity of the FOPT²⁰ requires that the quark mass in the high-density-phase (here: the PWW phase) is smaller than in the low-density-phase (here: the PNG phase). If the endpoint for the isentropes $(T, \mu) = (0, m_q^{\text{vac}})$ is in the PWW phase, then in both phases m_q is greater than μ_c^0 at $T = 0$. Analyzing the FERMI pressure for vanishing temperatures yields for both phases that the thermodynamical properties are those of the vacuum, *i.e.* identical. This is incompatible with a phase transition at $T = 0$.

In Fig. 5.14, the central statements of this paragraph are visualized: The left panels depict an example for the first class of parameter sets, in which all isentropes end in the PNG phase. The right panels in turn show the other possible class in which the isentropes end on the phase contour (in the T - μ diagram) or in the coexistence region (in the T - n diagram), respectively. As briefly discussed in Section 5.3.2 there are also parameter sets with no FOPT at all. For these parameter sets the momentum integral in (5.3.9) dominates for $T = 0$ over the other two terms. This happens if m_q^{vac} is sufficiently small. Inspecting the left panel of Fig. 5.13 one finds that the FOPT vanishes (*i.e.* $T_{\text{CEP}} \rightarrow 0$) if m_q^{vac} is more than about 100 MeV smaller than μ_c^0 .

5.4. Discussion

5.4.1. Phase structure and particle masses

In the meson sector, the most striking feature is the approximate degeneracy of the meson masses m_π and m_σ in the PWW phase. This reflects the approximate chiral symmetry present in this phase. (In the chiral limit, $H \rightarrow 0$, the symmetry (2.2.17) transforms the σ field into the π field, which implies that the masses for both fields are identical.) In the PNG phase, the chiral symmetry is broken by the non-vanishing expectation value v of the sigma field. This induces a mass term for the quarks, $m_q \sim gv$, as well as a mass splitting term, $\delta m^2 \sim 2\lambda v^2$, for the mesons.²¹ Therefore, the mass splitting in the meson sector and the large quark mass have the same physical origin, namely the σ field acquiring a finite thermal expectation value. The different expectation values of the sigma field in the two phases are caused by two competing contributions to the effective meson

²⁰ Precisely: within the spinodal region.

²¹ There are additional terms in the LFA (*cf.* (E.1.1)-(E.1.5) in Appendix E) but they are less important in the chirally broken phase.

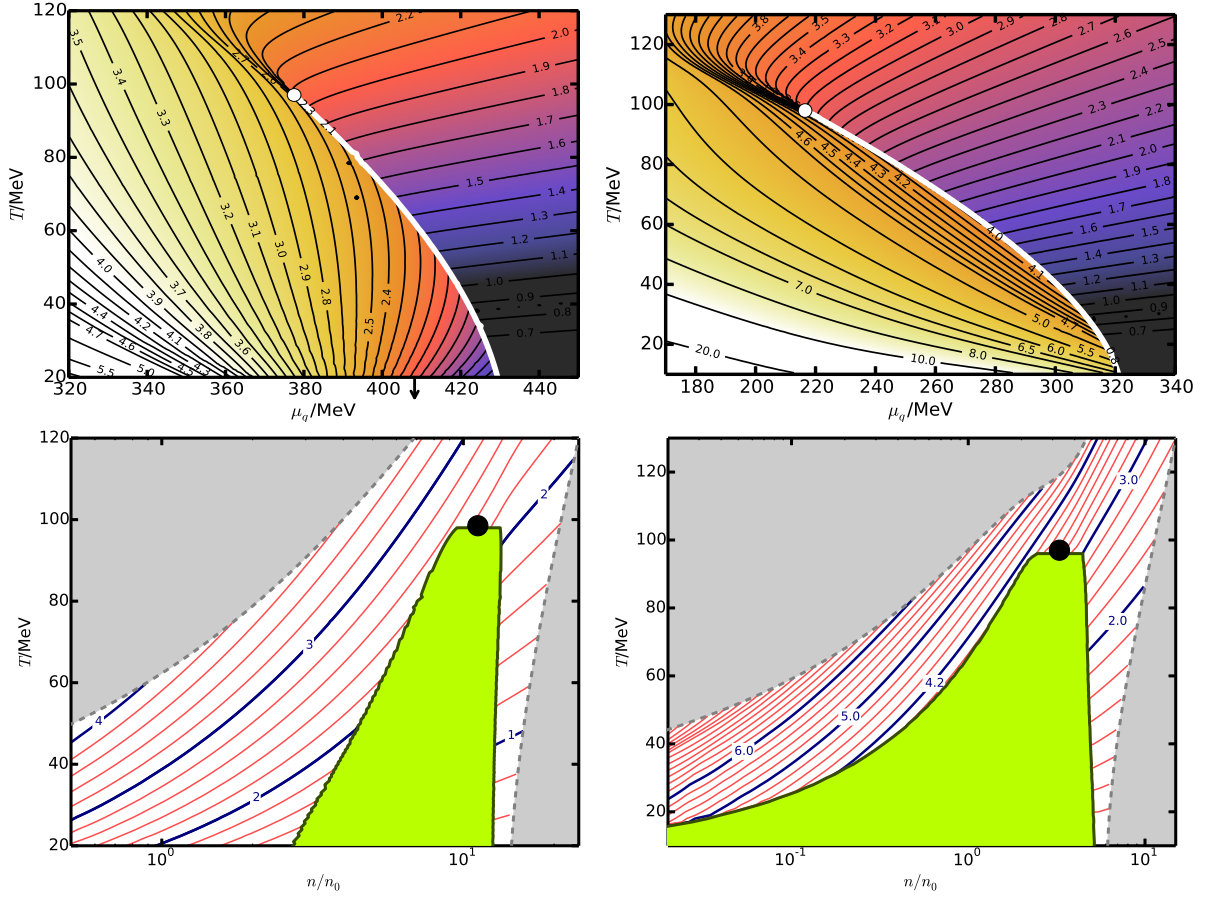


Figure 5.14.: Phase diagrams for parameter sets B (left panels) and C (right panels) (*cf.* Tab. 5.1.) The black curves are the isentropes labeled by their corresponding entropy per quark ratio s/n . The FOPT is denoted by a solid white curve (in the upper panels, *i.e.* in the T - μ plane) and the thick green curves surrounding the coexisting region (light green area, *i.e.* in the T - n plane) in the lower panels. The CEP is depicted by white and black dots, respectively.

potential: (i) The fundamental meson interaction potential U in the Lagrangian (2.1.1), which has a minimum at finite σ and (ii) the quark contribution $\Omega_{\bar{q}q}$ tending to produce another minimum of U_{eff} at $\sigma \sim 0$ for large chemical potentials μ and thus causing the system to undergo a phase transition at high enough chemical potential, *cf.* left panel of Fig. 5.15. In principle, the same takes place for increasing temperature at fixed μ . However, at small μ and $T \sim 100$ MeV, the fermionic contribution $\Omega_{\bar{q}q}$ is much broader (in σ direction) than for small T and large μ , *cf.* right panel of Fig. 5.15. This difference is the reason that U_{eff} exhibits two minima in the latter case and only one in the former. This competition of temperature and chemical potential dependent effects introduces for realistic²² parameter sets the following phase structure: At low temperatures and chemical

²² In a QCD-related context.

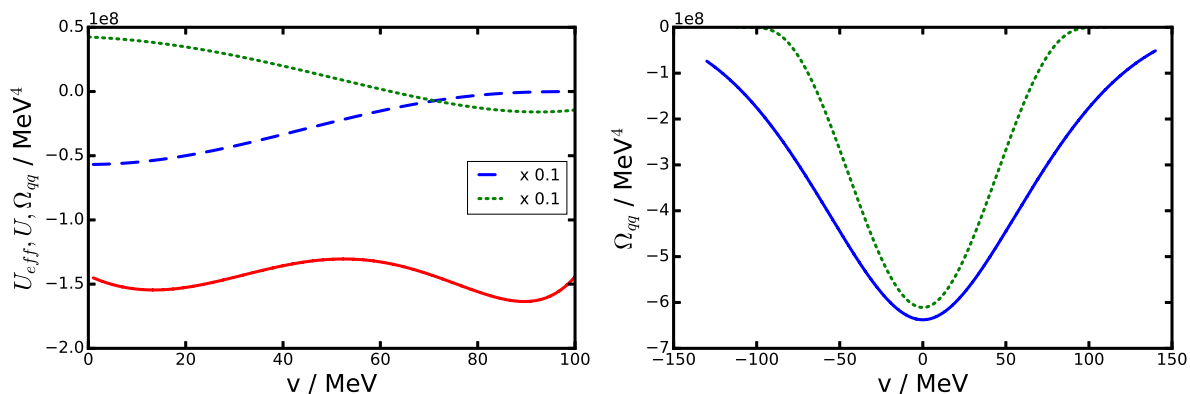


Figure 5.15.: Sketches of the effects determining the phase structure. Left panel: Decomposition of the effective meson potential U_{eff} (solid red curve) into the fundamental potential U (short dashed green) and the quark contribution $\Omega_{\bar{q}q}$ (long dashed blue) in the vicinity of the FOPT. The latter curves are scaled with a factor 0.1. Right panel: Comparison of the fermionic contribution $\Omega_{\bar{q}q}$ to the effective potential U_{eff} on two positions close to the phase transition curve: at $\mu = 0$ (blue solid) and at $T \approx 0$ (green dashed).

potentials (the scale is set by the difference between the local maximum and the (global) minimum of the fundamental meson interaction potential U) there is a phase with large effective quark mass and a large mass splitting of the meson masses with an approximate (due to the explicitly symmetry breaking term $H\sigma$ (2.1.4)) $U(1)_V \times SU(2)_V$ flavor symmetry. At high temperatures or large chemical potentials, the quark mass as well as the meson mass splitting are small, and the fields obey an approximate $U(1)_V \times SU(2)_V \times SU(2)_A$ symmetry. The phases are partially separated by a sequence of FOPTs forming a curve which extends from finite chemical potential μ_c^0 at $T = 0$ to higher temperatures bending towards the temperature axis (corresponding to a negative slope of the critical curve) and ending at a CEP.

The negative slope of the FOPT curve $T_c(\mu)$ is a typical feature of chiral models for strongly interacting matter and can be related to the discontinuities Δn and Δs of the net quark density n and the entropy density s by the following relation of the CLAUSIUS-CLAPEYRON kind:

$$\frac{\partial T_c}{\partial \mu} = - \frac{\Delta n}{\Delta s}. \quad (5.4.1)$$

Both discontinuities, Δn and Δs , are positive within the QMM, such that n and s increase, when crossing the FOPT curve from the PNG phase to the PWW phase. The increase of the net quark density at the phase transition can be attributed to the quark mass which drops significantly at the phase boundary. Thus Δn is positive. For the entropy, the total

number of active degrees of freedom is relevant, and therefore the mesons have to be taken into account. In the PNG phase, the lightest particles are the pions (although still having a larger mass m_π than the temperature T). Due to their non-negligible mass the effective number of degrees of freedom is less than the total number of pion types (three). As discussed above, in the PWW phase, the thermodynamics (especially the entropy density) is well approximated by that of an ideal ultrarelativistic FERMION gas with $2 \times N_f \times N_c$ fermionic degrees of freedom. As the number of effective degrees of freedom thus strongly increases at the phase boundary, the entropy density does the same. In summary, both, the entropy density and net quark density, increase at the phase boundary, *i.e.* Δn and $\Delta s \geq 0$ as claimed above.

The slope of the critical pressure p_c *w.r.t.* the temperature can be determined by another version of the CLAUSIUS-CLAPEYRON equation,

$$\frac{\partial p_c}{\partial T} = \frac{s_{\text{PNG}}/n_{\text{PNG}} - s_{\text{PWW}}/n_{\text{PWW}}}{1/n_{\text{PNG}} - 1/n_{\text{PWW}}}, \quad (5.4.2)$$

where s_i and n_i are the entropy density and the net quark density, both infinitesimally close to the critical curve, yet in the two phases $i = \text{PNG}, \text{PWW}$. For the QMM, the slope is positive, which according to [SRK14, Ios15] makes the transition liquid-gas-like (enthalpic) rather than quark-hadron-like (entropic). The slope of $p_c(T)$ can be related with the relative slope of the curves of constant pressure $T_p(\mu)$ (isobars) and the critical curve $T_c(\mu)$ in the T - μ phase diagram with the result that isobars having a smaller slope (evaluated at the FOPT) than the critical curve correspond to the liquid-gas (enthalpic) type of transition and, conversely, a larger slope of the isobars corresponds to hadron-quark (entropic) type of transition. Present lattice QCD calculations give no definitive answer to what the relative slope of the isobars and the pseudocritical curve at moderate values of μ_B ($\mu_B/T = 1 \dots 3$, with the baryon chemical potential μ_B) is, although it is widely accepted that at $\mu \approx 0$ the pseudocritical curve bends towards the μ axis [KKL⁺11, BBF⁺15, B⁺17].

As this issue has not been settled yet, the QMM can still be considered as a relevant model for the chiral transition if other constraints are fulfilled. One of these constraints is that isentropes arriving at the FOPT from the PWW phase have to leave the FOPT into the PNG phase. In [WYK16] we classified such transitions as type I and the complementary case when isentropes stay on the FOPT as type II. Type I is subdivided into two classes: IA corresponds to isentropes leaving the FOPT at higher temperatures and IB corresponds to isentropes leaving FOPT at lower temperatures. It turns out that type IA is equivalent to the class of entropic phase transitions and types IB and II constitute the class of enthalpic phase transitions. With the present knowledge, type II can be considered unrealistic since

it implies that the adiabatic expansion ends on the chiral phase transition curve, which is not what is observed. This classification scheme is visualized in Fig. 5.16.

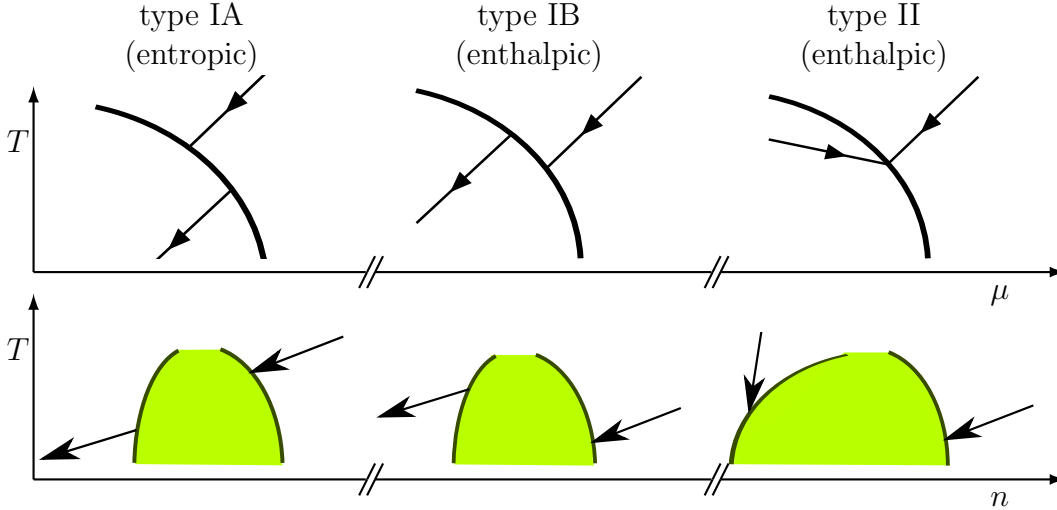


Figure 5.16.: Schematic representation of isentropes (lines with arrows indicate the path of adiabatically expanding matter) for the FOPT types IA (left, $s/n = \text{const}$ along the isentrope), IB (middle, $s/n = \text{const}$) and II (right, two separate isentropes ending both on the FOPT curve with $s_1/n_1 > s_2/n_2$) in the T - μ plane (upper row) and the T - n plane (lower row). States 1 and 2 are to the left and right of the phase border line (fat curves in the upper row), respectively. The green areas in the lower row depict a part of the two-phase coexistence regions for the respective types. Note that the coexistence regions (green areas) can appear in quite different shapes. The figure is reproduced from [WYK16].

5.4.2. Thermodynamic quantities

In the PWW phase, the fermionic contribution $\Omega_{\bar{q}q}$ to the pressure dominates over the mesonic contributions U , Ω_σ , Ω_π etc. Since furthermore, the quark mass in this phase is much smaller than T and/or μ , the derivatives of the pressure – especially net quark density, entropy density and the susceptibilities – are very close to the corresponding quantities of an ultrarelativistic (*i.e.* massless) ideal FERMION gas as can be seen in Figs. 5.8 and 5.10. For the pressure to be approximated with similar accuracy it is necessary to subtract a constant, analogous to the bag constant in bag model approaches [CJJ⁺74].²³ In the low-temperature region $T \lesssim 50$ MeV the pressure is almost entirely determined by two terms: (i)

²³ The interpretation of the constant as the pressure of the (non-perturbative) vacuum against which bubbles with bound states are formed is not applicable for the QMM since the mesons are no bound states but regarded as fundamental within this model. Nevertheless, the subtraction constant corresponds to the energy density that is gained by forming the sigma condensate v .

the fermionic contribution $\Omega_{\bar{q}q}$ and (ii) the meson interaction potential U . Because, except at the FOPT, the latter one varies slowly *w.r.t.* T and μ the derivatives of the pressure *w.r.t.* these quantities – *i.e.* entropy density, net quark density and the susceptibilities – are essentially those of an ideal massive FERMI gas, with the mass jumping at the FOPT. This explains why it is not possible with parameter adjustments to achieve for the FOPT to be of type *IB* (*cf.* Fig. 5.16). To achieve this type of transition with fermionic pressure contributions only, the fermions in the high chemical potential phase (*i.e.* the PWW phase) must have a larger mass than in the low chemical potential phase (*i.e.* the PNG phase). In order for the pressure of both phases to be equal at the phase transition curve and the phase with larger mass being the thermodynamically stable one above the phase transition, the number of (massive) fermionic degrees of freedom must be larger in the PWW phase than in the PNG phase. However, this is not the case within the QMM.

The isentropes form a pattern which is understandable in two distinct limits: (i) for $m_q \rightarrow 0$, which is applicable in the PWW phase, and (ii) for $T \rightarrow 0$. As discussed above (see also Fig. 5.8), in the PWW phase, the entropy density and the net quark density can well be approximated by the corresponding quantities for an ultrarelativistic FERMI gas. Applying the corresponding formulas one finds that the entropy per quark s/n depends only on the ratio μ/T in this limit, *i.e.* the curves $s/n=\text{const}$ are straight lines pointing to the origin with a slope corresponding to the polar angle ϕ in the T - μ plane.

The second derivatives of the pressure *w.r.t.* temperature T or quark chemical potential μ , *i.e.* the temperature times the volumetric heat capacity c_μ^{vol} at constant μ (left panel of Fig. 5.10) and the quark number susceptibility $\chi_{\mu\mu}$ (right panel of Fig. 5.10) show similar behavior as in the MFA case, *cf.* Section 5.1.3. The heat capacity (normalized to that of an ideal ultrarelativistic FERMI gas) is increased in the crossover region and thus can be applied to estimate the pseudocritical temperature $T_{pc}(\mu)$ while the quark number susceptibility (also normalized to that of an ideal ultrarelativistic FERMI gas) peaks at the CEP and can be applied to quantify the size of the critical region. Compared to the MFA result, the critical region is less elongated but of comparable width.

5.4.3. Impact of vacuum fluctuations

In this thesis, the vacuum terms of the mesonic and fermionic contributions to the grand canonical potential Ω (*i.e.* the terms without FERMI or BOSE distribution functions in (4.2.17), (5.2.4) and (5.2.5)) have been omitted. However, for certain purposes they must be included. For instance, if the chiral limit of the QMM is to be investigated or the question whether properties present in the chiral limit “survive” the explicit symmetry

breaking is to be addressed, these vacuum fluctuations are crucial to prevent the chiral transition from becoming first-order in the chiral limit [SFN⁺10]. The difference of the phase transition order in the two cases, (i) with and (ii) without the inclusion of vacuum terms, also has some impact on the form of the isentropes in the crossover region. In the case without vacuum fluctuations, the isentropes passing the crossover region not too far away from the CEP are kinked in this region. This can be attributed to the remnants of the first-order transition present in the chiral limit and the relatively weak explicit symmetry breaking if the value of m_π^{vac} is close to the PDG value. On the contrary, in the case with vacuum terms, the isentropes are smooth and no peculiarities occur in the crossover region [NSS⁺10]. Furthermore, the inclusion of vacuum fluctuations shifts the CEP to smaller temperatures and larger chemical potentials. While without vacuum fluctuations the CEP temperature is about $T_{\text{CEP}} \sim 100 \text{ MeV}$ for realistic parameter sets, it takes values in the region $T_{\text{CEP}} \sim 10 \dots 50 \text{ MeV}$ if these fluctuations are included [NSS⁺10, SFR11, Tiw12]. Including further fluctuations, *e.g.* with the application of functional renormalization group (FRG) methods [Gie12, TSvSW14], does not influence the CEP location much, however shifts of T_{CEP} of about 20 MeV are possible (relative to the result with vacuum fluctuations only) [NSS⁺10].

5.4.4. Impact of thermal fluctuations

Basically, the LFA and the MFA produce similar results. The position and shape of the phase transition curve (FOPT and crossover estimate) are qualitatively similar. Since increasing temperatures (and hence thermal fluctuations) tend to weaken the phase transition (*i.e.* at higher temperature the latent heat and the jumps in thermodynamic quantities, such as entropy density, net quark density *etc.*, get smaller) one might expect that additional fluctuations have a similar effect on the strength of the phase transition. Indeed, when comparing LFA and MFA one notices that the CEP is shifted to lower temperatures if fluctuations are included (*i.e.* for the LFA).

5.4.5. Parameter dependence

For realistic parameter sets, the shape of the phase transition curve (FOPT and crossover estimate) is essentially determined by the difference ΔU of the meson interaction potential U at its local maximum and its local minima. In the chiral limit, this difference can be expressed with the help of the sigma vacuum mass m_σ^{vac} and the sigma vacuum expectation value $\langle \sigma \rangle_{\text{vac}}$ according to $\Delta U = (m_\sigma^{\text{vac}})^2 \langle \sigma \rangle_{\text{vac}}^2 / 8$. The (pseudo-) critical temperature T_c

can then be expressed by (5.3.5). The explicit chiral symmetry breaking term, $-H\sigma$, is of minor importance for this issue. The position of the CEP on the phase transition curve is controlled by the parameter combination $x = 2\mu_c^0 - m_{\text{nuc}}^{\text{vac}}/N_c$, with which the CEP chemical potential μ_{CEP} can be estimated as $\mu_{\text{CEP}} \approx 7x/8 - 25 \text{ MeV}$. One can distinguish three groups of parameter sets with qualitatively different model properties.

- (i) $m_{\text{nuc}}^{\text{vac}}/N_c \geq \mu_c^0$: In this case, there are only incoming isentropes on the FOPT curve. Additionally, all isentropes that enter the PNG (through the cross-over region) merge with the FOPT curve from the low-chemical-potential side and run down on it afterwards. In the classification scheme introduced in [WYK16], the transition is of type II. At $T = 0$, pressure, energy density, net quark density as well as all masses and field expectation values have their vacuum value directly next to the FOPT curve. Sometimes this is phrased as the PWW phase being in equilibrium with the vacuum on the FOPT curve at vanishing temperature. Since ordinary nuclear matter at $T = 0$ is neither in direct contact to the vacuum nor to the chiral transition (and hence the vacuum cannot be in contact to the chiral transition either) we regard such parameter sets as unrealistic, even when particle masses and field expectation values have reasonable values.
- (ii) $\mu_c^0 - 100 \text{ MeV} \lesssim m_{\text{nuc}}^{\text{vac}}/N_c < \mu_c^0$: In this case, all isentropes end in the PNG phase at $\mu = m_{\text{nuc}}^{\text{vac}}/N_c$. The isentropes cross the FOPT curve and the vacuum is always well separated from the FOPT curve. The phase transition is enthalpic²⁴ (type IA). Such a scenario is presently not ruled out for QCD, neither by experiment nor by first principle calculations, albeit there are some indications that the chiral transition is better described by an entropic²⁴ (type IB) phase transition [SRK14].
- (iii) $m_{\text{nuc}}^{\text{vac}}/N_c \lesssim \mu_c^0 - 100 \text{ MeV}$: In this case there is no FOPT at all.

With the results on the parameter dependence one can use the following procedure for tuning the model parameters to physically reasonable values:

- First, $T_{\text{pc}}^{0,\text{ref}}$ and $\mu_c^{0,\text{ref}}$ as well as $m_{\sigma}^{\text{vacref}}$ and $\langle \sigma \rangle_{\text{vac}}^{\text{ref}}$ are calculated for some reference parameter set. If the QMM is used to model low-energy QCD the reference values given in (5.3.6) are reasonable choices.
- Then one has to decide which value for the pseudocritical temperature at zero chemical potential T_{pc}^0 is realistic.
- Use $T_{\text{pc}}^0 = T_{\text{pc}}^{0,\text{ref}} \sqrt{m_{\sigma}^{\text{vac}} \langle \sigma \rangle_{\text{vac}}} / \sqrt{m_{\sigma}^{\text{vacref}} \langle \sigma \rangle_{\text{vac}}^{\text{ref}}}$ to determine the product $m_{\sigma}^{\text{vac}} \langle \sigma \rangle_{\text{vac}}$ that provides such a transition temperature. This also gives a good approximation for the

²⁴ The terms enthalpic/entropic refer to the nomenclature in [Ios15].

shape of the phase boundary $T_c(\mu)$ and via $\mu_c^0 = \mu_c^{0,\text{ref}} \sqrt{m_\sigma^{\text{vac}} \langle \sigma \rangle_{\text{vac}} / \sqrt{m_\sigma^{\text{vac,ref}} \langle \sigma \rangle_{\text{vac}}^{\text{ref}}}}$ also the critical chemical potential at zero temperature. As reference the values given in (5.3.6) can be chosen.

- With $T_c(\mu)$ any restriction on the CEP temperature T_{CEP} can be converted into a restriction on μ_{CEP} .
- Using $\mu_{\text{CEP}} \approx 7x/8 - 25 \text{ MeV}$ with $x = 2\mu_c^0 - m_{\text{nuc}}^{\text{vac}}/N_c$ a value for $m_{\text{nuc}}^{\text{vac}}$ can be calculated that fits the requirements for the CEP position. Comparing μ_c^0 and $m_{\text{nuc}}^{\text{vac}}/N_c$ determines to which class of parameter sets (see above) the result belong.
- The ratio $m_\pi^{\text{vac}}/m_\sigma^{\text{vac}}$ determines the degree of explicit symmetry breaking and one remaining parameter can be used for fine tuning.
- If the result does not fit the requirements sufficiently well, one may specifically tune $m_\sigma^{\text{vac}} \langle \sigma \rangle_{\text{vac}}$, $m_{\text{nuc}}^{\text{vac}}$ or m_π^{vac} depending on which feature (T_{pc}^0, μ_c^0 , μ_{CEP} or the degree of explicit symmetry breaking) of the model needs further fine tuning.

Such a procedure is meant to be used as a guide for specifically manipulating the phase diagram of the QMM and fitting it to the respective needs of the user. The dependencies and numbers refer to the LFA evaluated without vacuum terms and can be applied with minor changes only also to the MFA if the vacuum terms are omitted. If the vacuum terms are included, however, the dependencies and numbers given above need to be modified, *e.g.* in this case T_{pc}^0 and μ_c^0 depend also on $m_{\text{nuc}}^{\text{vac}}$ which can shift the value for μ_c^0 by 30 . . . 50 MeV.

6. Photon emission within the quark-meson model

6.1. Overview

In this section, the emissivities calculated according to (4.4.1) are presented and discussed in some detail. As the emissivities depend essentially on three independent physical quantities (temperature, chemical potential, and photon frequency) plus all model parameters it is impossible to put all information into one plot. Instead, we first discuss a few representatively chosen differential spectra to demonstrate what is to be expected and define on this basis at which area of the phase diagram and at which photon energy a closer look is necessary.

Before proceeding in this manner, some words on the nomenclature are necessary: In the following chapter, the term “emissivity” refers to the differential production rate $\omega d^7N/d^3kd^4x$. When discussed in terms of temperature and chemical potential, also the term “rate” is used for the same quantity. However, when discussed as a function of the photon frequency, the emissivity will be referred to as the “differential (photon) spectrum”. The emissivities/rates/spectra for the individual production processes under consideration will be termed “partial”.

In Fig. 6.1, differential spectra at two representatively chosen positions in the phase diagram are displayed. Several typical features can be observed:

- (i) At high photon energies ($\omega \gtrsim 600 \text{ MeV}$), all displayed partial differential spectra decrease exponentially $\propto e^{-\omega/T}$.
- (ii) At small photon energies ($\omega \rightarrow 0$), two cases are possible: either the spectra approach zero or they diverge. The differential spectra for COMPTON and anti-COMPTON processes do not diverge.
- (iii) In the PWW phase, the rates for the processes of the same type (COMPTON, an-

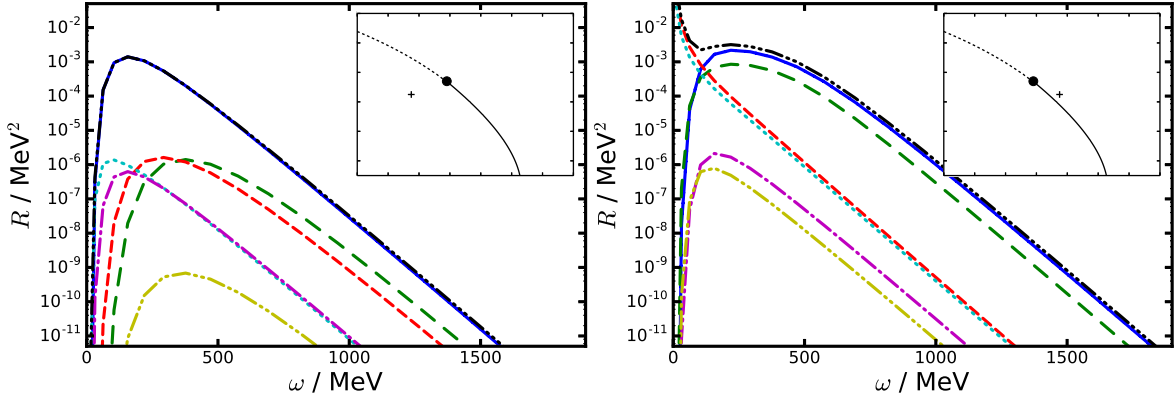


Figure 6.1.: Representative differential spectra $R = \omega d^7 N / d^3 k d^4 x$ from the PNG phase at $T = 65$ MeV and $\mu = 255$ MeV (left panel) and the PWW phase at $T = 65$ MeV and $\mu = 295$ MeV (right panel) (parameter set A). The insets mark their respective position in the phase diagram. The curves denote the partial spectra from the six contributing processes $q + \pi \rightarrow q + \gamma$ (solid blue curve, in the left figure it is almost entirely hidden behind the dash-triple-dotted black curve), $q + \sigma \rightarrow q + \gamma$ (long-dashed green curve), $q + \bar{q} \rightarrow \pi + \gamma$ (short-dashed red curve), $q + \bar{q} \rightarrow \sigma + \gamma$ (dotted light blue curve), $\bar{q} + \pi \rightarrow \bar{q} + \gamma$ (dash-dotted violet curve), $\bar{q} + \sigma \rightarrow \bar{q} + \gamma$ (dash-double-dotted golden curve), and the sum of all of these (dash-triple-dotted black curve).

annihilation, anti-COMPTON differ only by a constant factor of order unity. For the COMPTON and anti-COMPTON processes, this factor is about three.

- (iv) In the PWW phase at sufficiently high photon energies, there is a hierarchy emerging:
 $\omega d^7 N_{\text{COMPTON}} / d^3 k d^4 x > \omega d^7 N_{\text{annihil.}} / d^3 k d^4 x > \omega d^7 N_{\text{anti-COMPTON}} / d^3 k d^4 x$.

All of these features have to be understood and their validity in the whole phase diagram has to be checked. In order to give a complete overview for the emissivities as well as limiting the figures to a reasonable number, the data will be looked at from two different points of view:

- (a) The emissivities are shown and discussed depending on the position in the phase diagram for two fixed photon energies ω_{low} and ω_{high} . One of these photon energies will be in the exponentially decreasing region and one will be at a low frequency (with 'low' being defined below). This approach is intended to identify regions in the phase diagram where the photon rates exhibit peculiarities of any kind.
- (b) The differential spectra, *i.e.* the emissivities depending on the photon energies at fixed positions in the phase diagram, are shown and discussed. The positions are chosen in accordance with a number of different topics. This approach should point out whether the form of the spectra differs on opposite sides of the phase transition

T/MeV	μ/MeV	m_q/MeV	m_σ/MeV	m_π/MeV	
65	255	282	504	151	Figs. 6.1 and 4.4
65	295	55	283	333	
55	255	294.0	564.5	146.0	Fig. 6.14
55	335	30.1	427.7	444.9	
95	335	26.9	508.5	516.5	
50	280	287	506	146	Tab. 6.2

Table 6.1.: Quark, sigma meson and pion masses (m_q , m_σ and m_π , respectively) calculated with parameter set A (Tab. 5.1) The masses are calculated at the temperatures and quark chemical potentials given in the first two columns. The last column displays the position of their usage in this thesis.

curve and at which photon frequencies the imprints of the phase structure on the photon rates are presumably most prominent.

High- and low-frequency regions

For photon frequencies larger than the maximum of the respective partial differential spectrum, the partial spectra quickly approach their asymptotic behavior (*cf.* Section 4.5.1), *i.e.* they become exponentially decreasing curves $\propto \exp\{-\omega/T\}$ (see Fig. 6.1). One important implication of this observation is that the relative strength of the partial emissivities is invariant under the change of the photon frequency ω , provided ω is high enough for all partial emissivities to be on their respective exponential tails. Fig. 6.2 illustrates the approximate positions of the maxima of the differential spectra according to (4.6.1) for the processes under consideration. The true maximum of the rates may be shifted by $\Delta\omega \sim 100 \text{ MeV}$ due to the precise form of the cross section and other power-law corrections to the dominant exponential factor as discussed in Section 4.5. Furthermore, the maxima are rather broad structures with a full width at half maximum being $\mathcal{O}(400 \text{ MeV})$. If one chooses $\omega \gtrsim 1000 \text{ MeV}$, however, one can be sure of being at the exponential tails on the high-frequency side of the maxima for all processes.

The major differences between the various partial spectra in the very-low-energy region (*i.e.* on the left side of all the maxima in the partial spectra, $\omega \lesssim 150 \text{ MeV}$) are related to infrared (IR) divergencies of the photon rates, which can appear in certain regions of the phase diagram for the annihilation processes. They can be traced back to the ω^{-1} -divergence of the prefactor in the rate formulas (see eqs. (4.4.2), (4.4.11) and (4.4.19)) coming from the evaluation of the phase space integrals (see Appendix H). These, in turn, can presumably be attributed to IR divergencies of the matrix elements caused by the internal propagators, which get on-shell for $\omega \rightarrow 0$. However, if the sum of the effective masses of

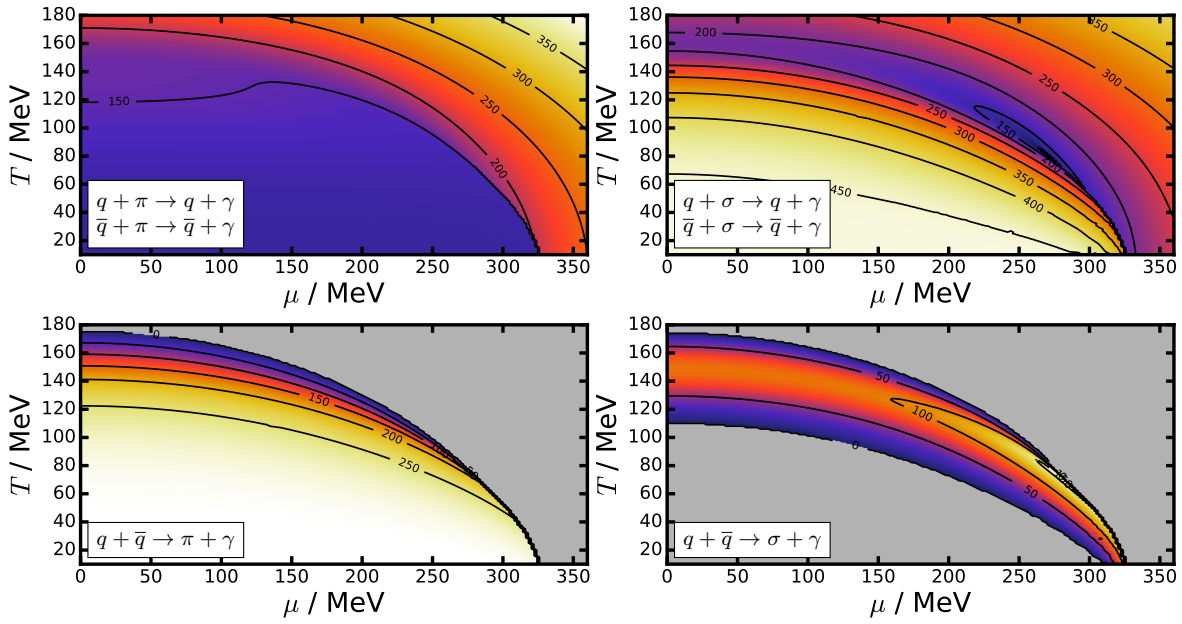


Figure 6.2.: Contour plots of the positions of the local maxima of the various differential spectra, according to the approximation (4.6.1). Upper row: (anti-) COMPTON processes; lower row: annihilations; left column: with pions; right column: with σ mesons. In the gray regions, the partial emissivity has no local maximum.

the incoming particles is larger than the mass of the outgoing partner of the photon, these divergencies get regularized by a strong thermal suppression $\propto \exp\{-(s - (m^{\text{out}})^2)/(4\omega)\}$ in the relevant phase space region. This is seen most easily for the BOLTZMANN-approximated rates (4.5.2). There the only ω dependencies are in the prefactor $C_b \propto \omega^{-1}$ and within $\nu_{\text{min}} \propto (s - (m^{\text{out}})^2)/(4\omega)$ for $\omega \rightarrow 0$. In the limit of vanishing ω the integrand of the s integration is thus made arbitrarily small by the $\exp\{-\nu_{\text{min}}/T\}$ -suppression. As long as the mesons are not massless¹ the COMPTON processes always satisfy the condition of the incoming masses being larger than the outgoing mass, $m_1^{\text{in}} + m_2^{\text{in}} > m^{\text{out}}$.

Therefore, divergencies in the partial differential spectra appear only for the annihilation processes in those areas of the phase diagram, where $s_0 \equiv \max\{(m_1^{\text{in}} + m_2^{\text{in}})^2, m^{\text{out}}\} = (m^{\text{out}})^2$. These regions, *i.e.* those, where the sum of the effective masses of the incoming (anti-) quarks is smaller than the mass of the outgoing (non-photon) particle, are marked in the left panel of Fig. 6.3. There, the area with $m_\pi < 2m_q < m_\sigma$ is hatched diagonally, and the area $2m_q < m_\pi, m_\sigma$ is shaded in light gray without hatching. In the former case, only the partial spectrum for the process $q + \bar{q} \rightarrow \gamma + \sigma$ shows IR divergencies, while in

¹ There are essentially only two cases for which this constraint is of importance: (i) For the PNG phase in the chiral limit the pions and (ii) at the CEP the sigma mesons are massless. Since in this thesis we do not consider photon production in the chiral limit and because of the limitation of the considered approximation that inhibits $m_\sigma \rightarrow 0$ at the CEP both cases are not relevant for this work.

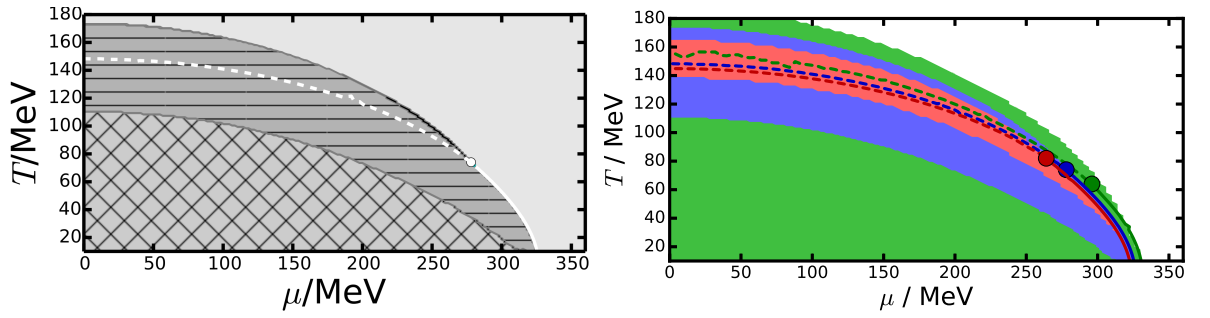


Figure 6.3.: Kinematic regions for several parameter sets. Left panel: Parameter set A; displayed are the regions with $m_\pi < 2m_q < m_\sigma$ (medium gray, diagonally hatched), $2m_q > m_\sigma, m_\pi$ (dark gray, horizontally hatched), $2m_q < m_\sigma, m_\pi$ (light gray, unhatched) and $m_\pi > m_\sigma$ (small black area close to the CEP). Right panel: Influence of the model parameters. Displayed are the regions with $2m_q > m_\sigma$ for parameter sets A, D, E, *cf.* Tab. 5.1. In the red region the inequality $2m_q > m_\sigma$ is fulfilled for all of the three parameter sets, while in the blue region it is fulfilled only for parameter set A and E and in the green region only for parameter set E. The phase contours are displayed red for D, in blue for A and in green for E with the line style denoting the order of the transition: first-order (solid), CEP (dot) and crossover (dashed).

the latter case both annihilation processes do so.

On the other hand, the partial spectra for the considered processes at low photon frequencies are (from an experimental point of view) less important than at higher frequencies, since for $\omega \lesssim m_\pi^{\text{vac}}$ the spectra are dominated by DALITZ decays of the pions as well as other pion decay channels. Thus, the frequencies below some lower bound $\omega_{\text{IR}} \sim m_\pi^{\text{vac}}$ are discarded from the discussion. In the region of interest at $\omega > \omega_{\text{IR}}$, the IR divergencies and their proper regularization/renormalization are expected to have little impact on the spectra and therefore can be ignored in this discussion. It thus seem reasonable to regard the value $\omega_{\text{IR}} = 150 \text{ MeV}$ as the lower limit of the region of interest for this thesis.

As a representative photon frequency for the presentation of the low-frequency rates, $\omega = 200 \text{ MeV}$ is chosen, *cf.* Figs. 6.4 – 6.7, because on the one hand, this frequency is small enough not to be on the exponential tails of the partial spectra but rather in the region where various partial spectra have peaks and, on the other hand, it is still large enough to be within the region of interest $\omega > \omega_{\text{IR}}$.

6.2. Emisivities for given frequency

6.2.1. Low-frequency rates

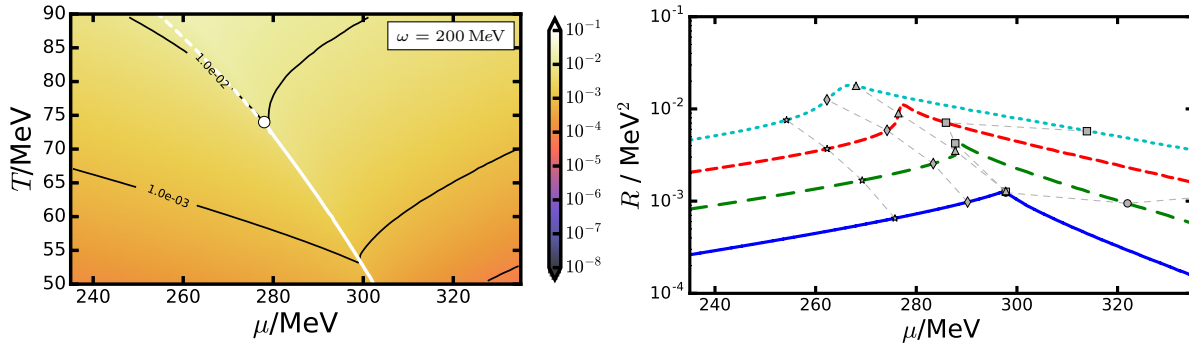


Figure 6.4.: Total photon emission rates $R = \omega d^7 N / d^3 k d^4 x$ in the proximity of the CEP for $\omega = 200$ MeV. Left panels: contour plots of the rates; right panels: rates at constant temperature $T/\text{MeV} = 55, 65, 75, 85$ (bottom to top). The symbols denote the rates at isentropes with $s/n = 1.7$ (dots), 2.1 (squares), 2.5 (triangles), 2.9 (diamonds), 3.3 (stars) and the thin gray lines are for guiding the eyes. The solid white lines in the left plot depicts the FOPT curve, and the white dashed line is an estimate of the crossover region based on the heat capacity. The dot depicts the position of the CEP, numerically determined by the coordinates of the minimum of the sigma mass.

In Figs. 6.4 – 6.7 the photon rates $\omega d^7 N / d^3 k d^4 x$ are displayed *w.r.t.* temperature and quark chemical potential for the photon frequency $\omega = 200$ MeV. The comparison of Figs. 6.4 – 6.7 reveals that the dominating contribution to the total rate comes from the COMPTON processes. The reason can be understood in terms of the BOLTZMANN approximation described in Section 4.5. Because the explicit μ -dependence of the PAULI blocking and BOSE enhancement factors is weak (they are almost one), only the μ dependence of the distribution functions for the incoming particles is relevant which introduces a factor (relative to the annihilation rates) of $\exp\{\mu/T\}$ for the COMPTON processes, and a factor of $\exp\{-\mu/T\}$ for the anti-COMPTON processes (see Section 4.5). Since the rates are displayed in the vicinity of the CEP, which is located at $\mu/T \approx 3.9$, this enhancement/suppression factors are about $\exp\{\mu/T\} \approx 50$ in the regions displayed in the left panels of Figs. 6.4 – 6.7 which explains the dominant role played by the COMPTON processes.

Inspecting the total rate for fixed temperature as a function of quark chemical potential μ , *cf.* the right panel of Fig. 6.4, one observes that the rate first increases with increasing μ , then jumps (slightly) at the FOPT (or quickly increases in the crossover region) and afterwards decreases again. Such a pattern also applies for all partial rates with the

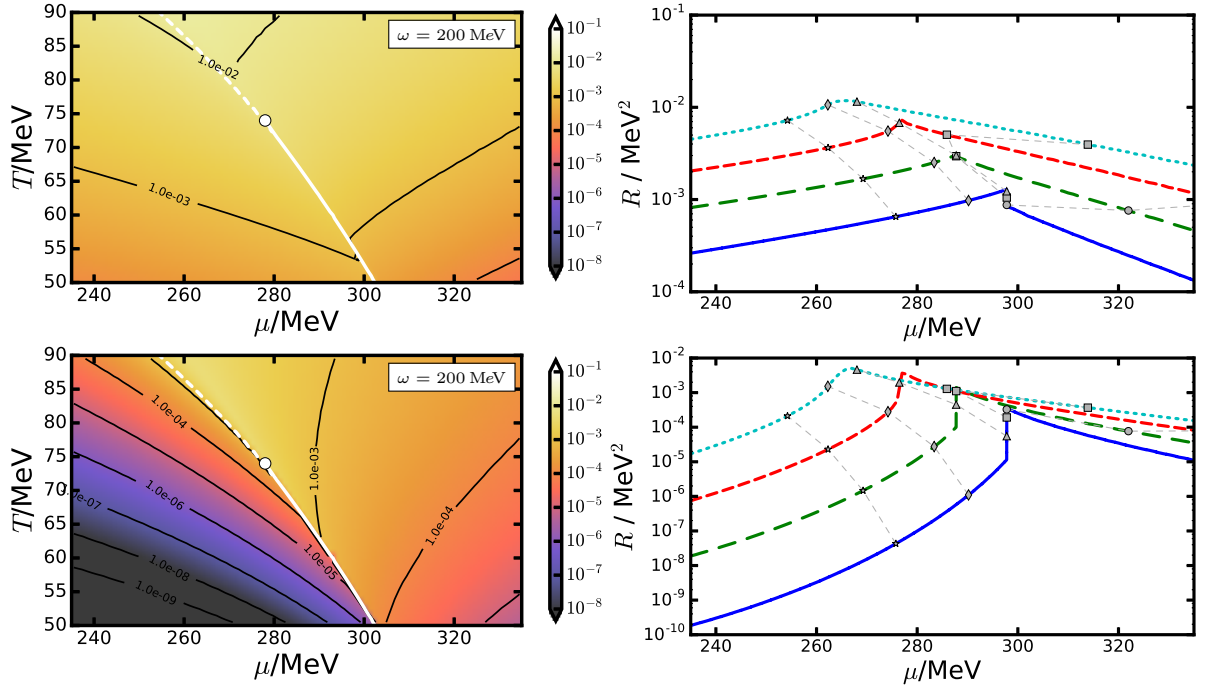


Figure 6.5.: As Fig. 6.4, but for the partial rate corresponding to the COMPTON processes $q + \pi \rightarrow q + \gamma$ (upper row) and $q + \sigma \rightarrow q + \gamma$ (lower row).

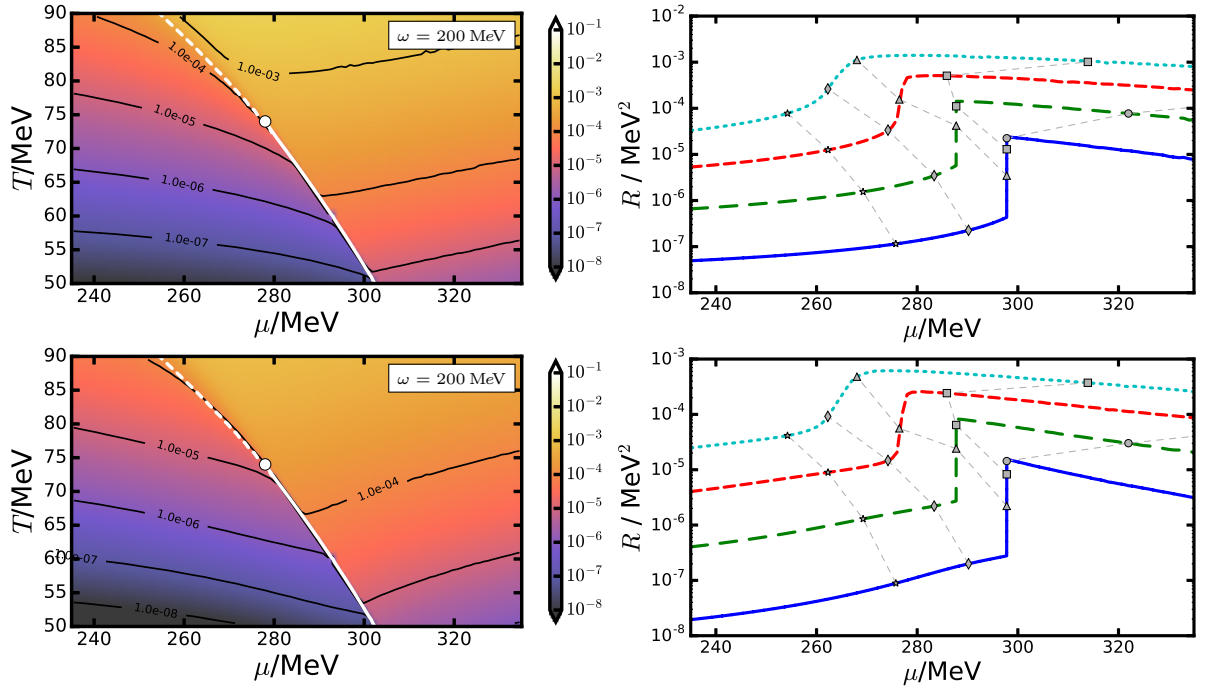


Figure 6.6.: As Fig. 6.5, but for the annihilation processes $q + \bar{q} \rightarrow \pi + \gamma$ (upper row) and $q + \bar{q} \rightarrow \sigma + \gamma$ (lower row).

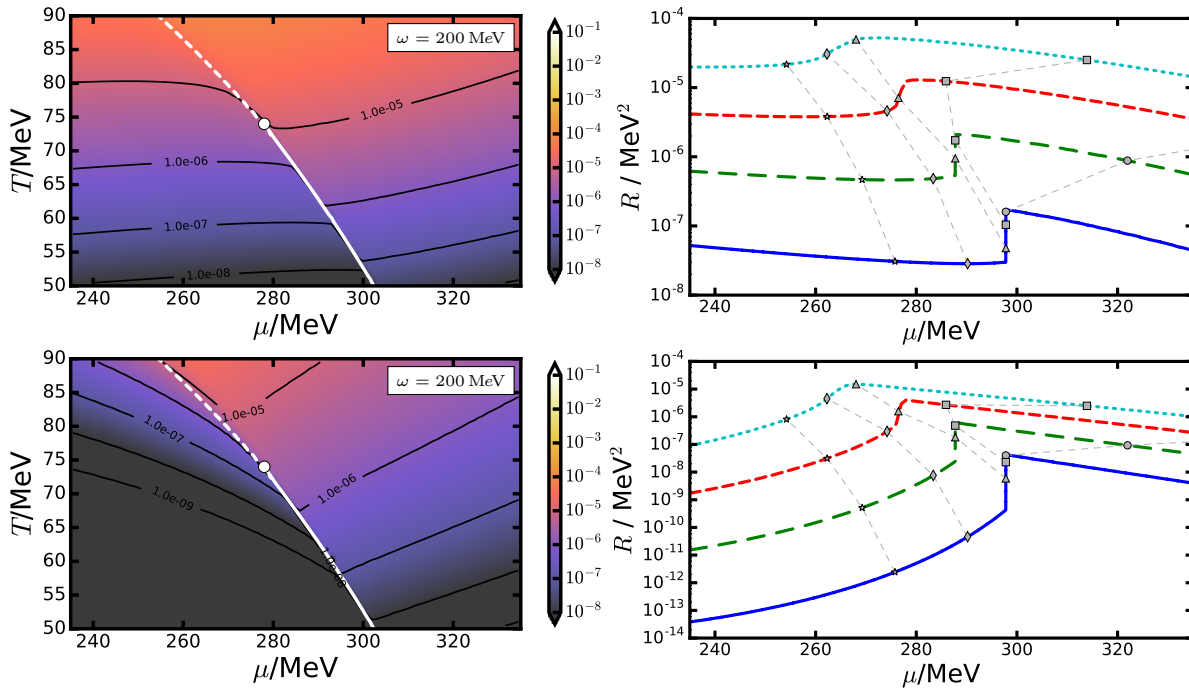


Figure 6.7.: As Fig. 6.5, but for the anti-COMPTON processes $\bar{q} + \pi \rightarrow \bar{q} + \gamma$ (upper row) and $\bar{q} + \sigma \rightarrow \bar{q} + \gamma$ (lower row).

exception of the process $\bar{q} + \pi \rightarrow \bar{q} + \gamma$ where the rate is decreasing also before the phase boundary. The partial rates jump at the phase boundary – depending on the process – either up or down. This and other aspects of the calculated emissivities as functions of temperature and quark chemical potential can be understood within the BOLTZMANN approximation of the rate formula, *cf.* Section 4.5 and discussion below. Although the total rate at fixed temperature shows moderate peak structures at the FOPT as well as at the CEP, there are no peaks in the temperature direction (the curves in the right panel of Fig. 6.4) do not cross but rather are ordered according to their temperature). However, if the asymptotic behavior $\propto \exp\{-\omega/T\}$ is scaled out of the data, then an enhancement around the CEP can be seen.

Comparing the total rate with the COMPTON-type partial rates (which are the dominating contributions according to the discussion above) one notes that in the PNG phase the $q + \pi \rightarrow q + \gamma$ process is the only relevant channel. In the PWW phase, on the other hand, both COMPTON processes as well as the annihilations contribute with similar strength. That the annihilation rates are of the same order of magnitude as the COMPTON rates although they suffer an suppression of the order $\exp\{-\mu/T\}$ is understandable within the exponential approximation, *cf.* Section 4.5.2. Within this approximation the rate can be related to the masses of the incoming particles and since the mesons are much heavier than the quarks the above mentioned $\exp\{-\mu/T\}$ -suppression can be compensated. More

details are given below.

6.2.2. High-frequency rates

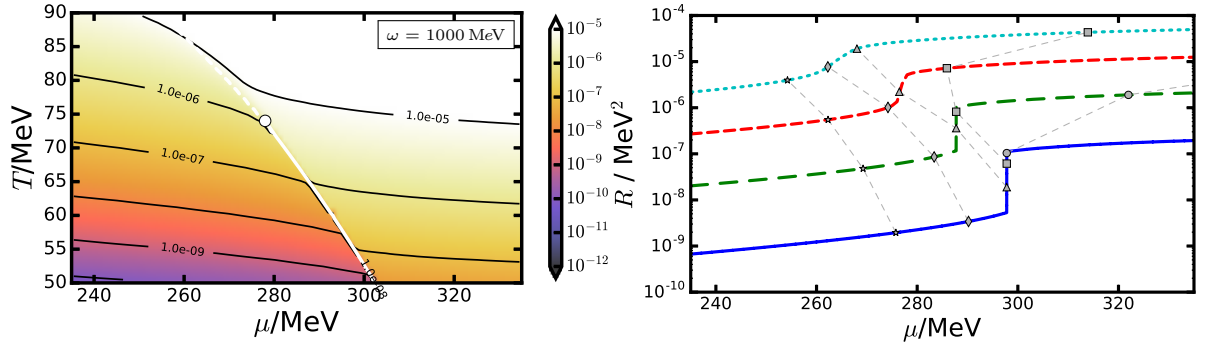


Figure 6.8.: Total photon emission rate $R = \omega d^7N/d^3kd^4x$ in the proximity of the CEP for $\omega = 1000 \text{ MeV}$. Lines and symbols as in Fig. 6.4.

In Section 4.5, it was shown that the high-frequency tail of the partial spectra behaves $\propto \exp\{-m^{\text{out}}/T\}$. Inspecting Figs. 6.9 and 6.11 reveals that in the high-frequency range $\omega \gtrsim 1000 \text{ MeV}$ all the displayed partial emissivities have a similar qualitative behavior: They are continuously changing and jump up at the first-order phase transition. In the crossover region and at the CEP, this jump is smeared out. Applying the BOLTZMANN approximation we were able to show that the emissivities are dominated by the behavior of the mass of the outgoing partner of the photon. In all the cases depicted in Figs. 6.9 and 6.11, this particle is a quark or antiquark, which explains the similar form of the emissivities.

The annihilation rates behave differently: For the annihilation into a pion and a photon, the partial emissivity drops at the phase boundary (corresponding to an increase of the pion mass) and for the annihilation into a sigma meson and a photon, the rate exhibits a weak maximum. Both annihilation rates drop with similar slopes in the PWW phase.

6.2.3. Rates and masses

In Fig. 6.12, the behavior of the partial emissivities according to the Gaussian approximation (*cf.* Section 4.5.1) is displayed. Their qualitative μ -dependency should be compared with the appropriate curves of Figs. 6.9 – 6.11 (the color code and the line styles are the same as in these figures). In doing so one may note several features of the rates that are also present in the Gaussian approximation: (i) The partial emissivities for both COMPTON processes are similar even in the PNG phase. An equivalent comment can be made for the

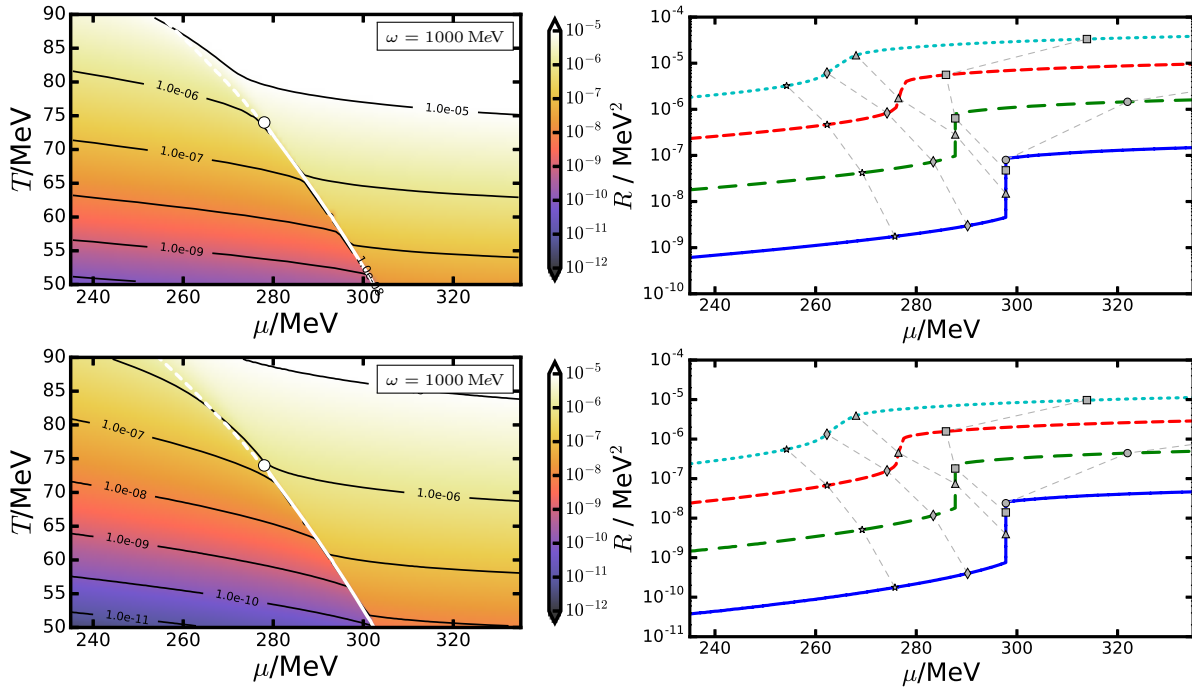


Figure 6.9.: As Fig. 6.8, but for the COMPTON processes $q + \pi \rightarrow q + \gamma$ (upper row) and $q + \sigma \rightarrow q + \gamma$ (lower row).

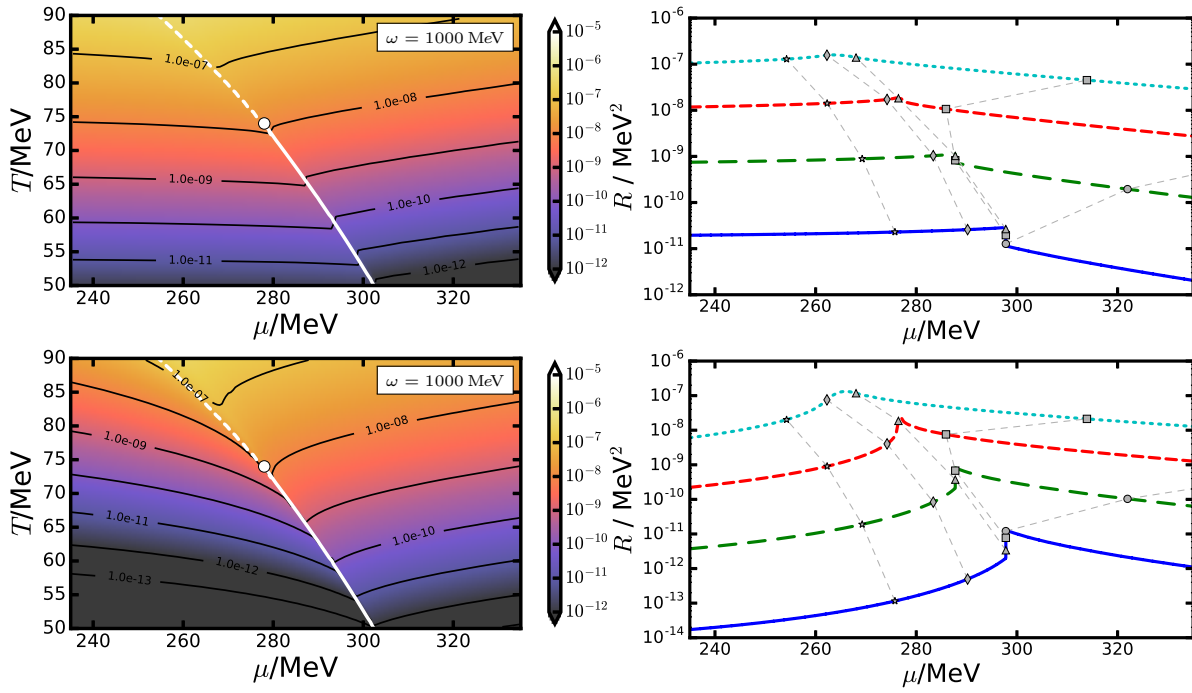


Figure 6.10.: As Fig. 6.8, but for the annihilation processes $q + \bar{q} \rightarrow \pi + \gamma$ (upper row) and $q + \bar{q} \rightarrow \sigma + \gamma$ (lower row).

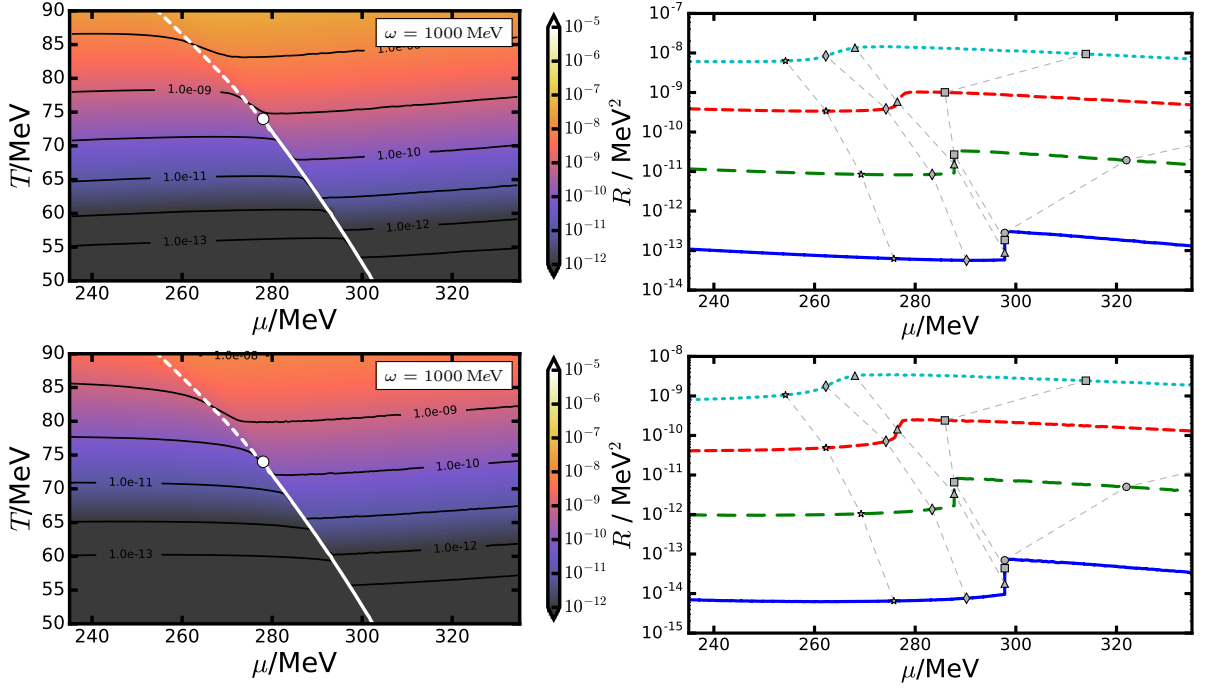


Figure 6.11.: As Fig. 6.8, but for the anti-COMPTON processes $\bar{q} + \pi \rightarrow \bar{q} + \gamma$ (upper row) and $\bar{q} + \sigma \rightarrow \bar{q} + \gamma$ (lower row).

anti-COMPTON processes. (ii) The emissivity for the annihilation into a photon and a pion is almost independent of μ in the PNG phase and decreasing in the PWW phase where it approximately coincides with the partial emissivity for annihilations into photons and sigma mesons. (iii) For all processes the emissivity of the Gaussian-approximated rates jumps at the FOPT into the correct direction (up/down). (iv) The slope of the emissivities in the continuous regions is qualitatively well reproduced. Thus one can conclude that the essential features of the partial emissivities in the high-frequency region can be understood in terms of the Gaussian approximation.

For those partial spectra that exhibit a maximum, the exponential approximation described in Section 4.5.2 can be applied. Doing so, one finds that the height of the maximum is $\propto \exp\{-(m_1^{\text{in}} + m_2^{\text{in}})/T\}$ (*cf.* (4.6.2)), which also governs the low-frequency region. Thus, in the low-frequency region, the emissivities show a different behavior compared to the high-frequency region. (There, the rates are $\propto \exp\{-m^{\text{out}}/T\}$, see above.) Therefore, in Fig. 6.13 the ratios of the partial emissivities $\omega d^7 N_i / d^3 k d^4 x$ (with i labeling the channel) and $\exp\{-(m_1^{\text{in}} + m_2^{\text{in}} - \epsilon_i \mu)/T\}$ are plotted. The curves shown in Fig. 6.13 should be compared with the right panels of Figs. 6.5 – 6.7. Doing so one notes that for all processes the general behavior of all partial rates, except for the process $q + \pi \rightarrow q + \gamma$, agrees with the approximation. The reason of the disagreement for the process $q + \pi \rightarrow q + \gamma$ is the breakdown of the BOLTZMANN approximation in the PWW phase at low and intermediate

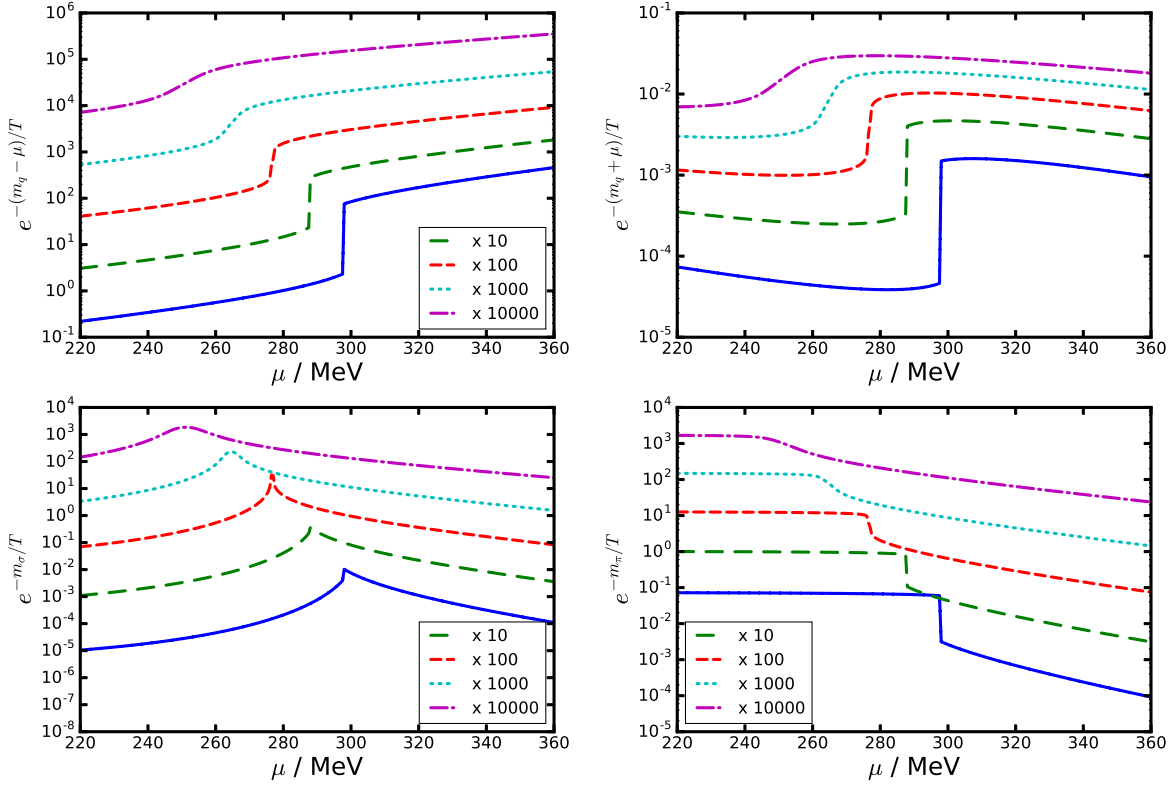


Figure 6.12.: Analytical behavior according to the BOLTZMANN approximation of $R_i = \omega d^7 N_i / d^3 k d^4 x$ in the high-frequency region (*i.e.* the function $\exp\{-(m_i^{\text{out}} - \epsilon_i \mu) / T\}$), with i denoting the processes $q + \sigma \rightarrow q + \gamma$ and $q + \pi \rightarrow q + \gamma$ (upper left panel), $\bar{q} + \sigma \rightarrow \bar{q} + \gamma$ and $\bar{q} + \pi \rightarrow \bar{q} + \gamma$ (upper right panel), $q + \bar{q} \rightarrow \sigma + \gamma$ (lower left panel), $q + \bar{q} \rightarrow \pi + \gamma$ (lower right panel), and ϵ_i discriminating between COMPTON processes ($\epsilon = +1$), annihilations ($\epsilon = 0$) and anti-COMPTON processes ($\epsilon = -1$) at $\omega = 1000$ MeV. When indicated, the curves are multiplied with the given factors to avoid crossings. Color code and linestyles denote the same temperatures as in Fig. 6.8. (For details, see text.)

temperatures for the quark distribution function (but not for the anti-quarks and mesons), which occurs because in this region many quarks occupy (since $m_q \ll \mu$) states with $E < \mu$ for which the BOLTZMANN approximation is not applicable. We thus conclude that indeed the general behavior of the rates can be understood in terms of kinematics and thermal suppression only.

6.2.4. Cross sections

With the BOLTZMANN approximation and the subsequent approximations for the s -integration the emissivities can be related to the cross sections of the contributing processes, *cf.* Section 4.5. The corresponding cross sections are shown in Fig. 6.14. The cross sections

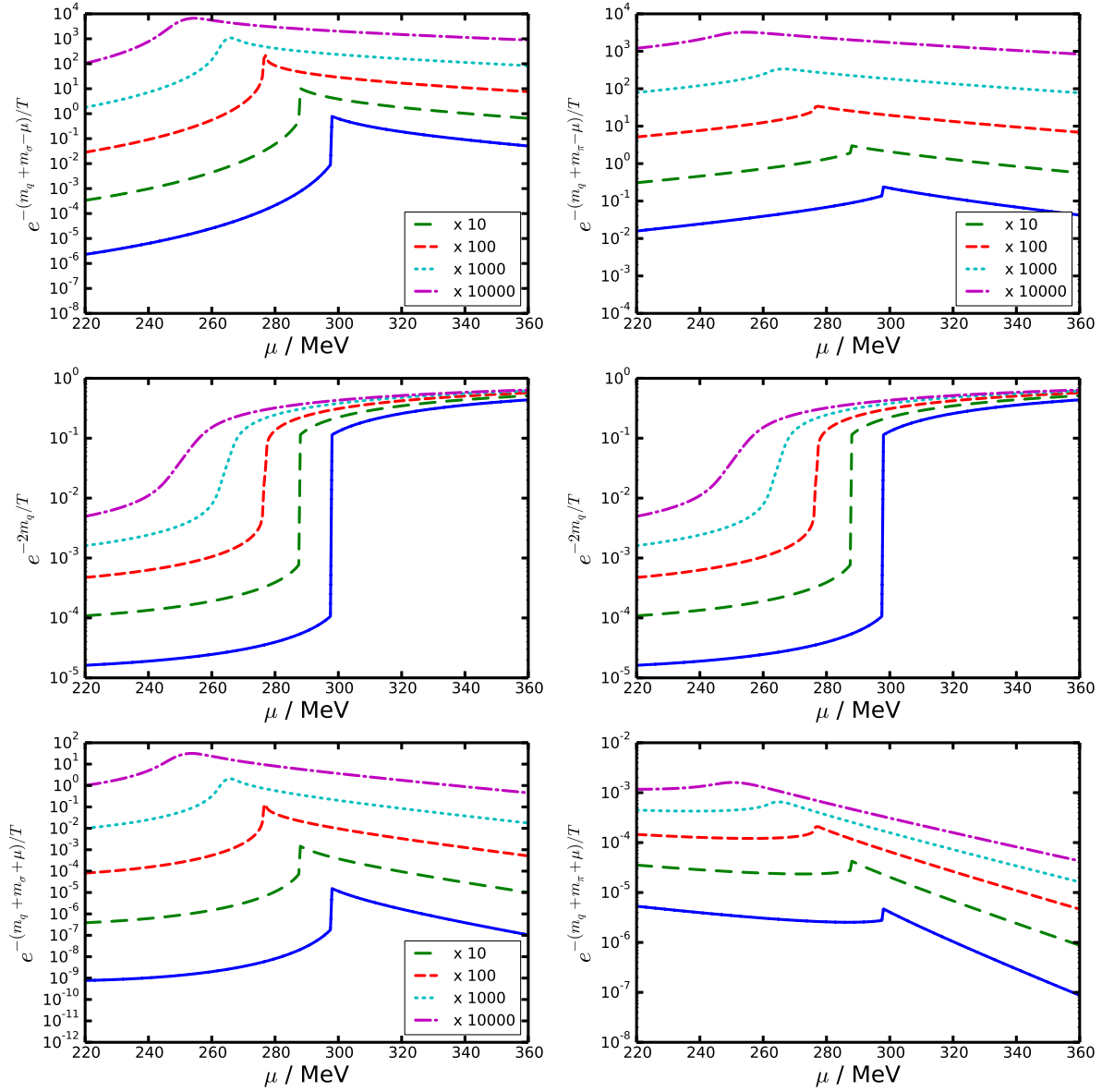


Figure 6.13.: Shape of the function $\exp\{-(m_1^{\text{in}} + m_2^{\text{in}} - \epsilon_i \mu)/T\}$ that encodes the dominant dependencies of the partial emissivities $R_i = \omega d^7 N_i / d^3 k d^4 x$, with i denoting the processes in the low-frequency region, according to the BOLTZMANN approximation $q + \sigma \rightarrow q + \gamma$ (upper left panel), $q + \pi \rightarrow q + \gamma$ (upper right panel), $q + \bar{q} \rightarrow \sigma + \gamma$ (middle left panel), $q + \bar{q} \rightarrow \pi + \gamma$ (middle right panel), $\bar{q} + \sigma \rightarrow \bar{q} + \gamma$ (lower left panel), $\bar{q} + \pi \rightarrow \bar{q} + \gamma$ (lower right panel) and ϵ_i discriminating between COMPTON processes ($\epsilon = +1$), annihilations ($\epsilon = 0$) and anti-COMPTON processes ($\epsilon = -1$) at $\omega = 200$ MeV. When indicated, the curves are multiplied with the given factors to avoid crossings. For details, see the text.

shown in the left column are identical to the respective ones in the right column since the cross section is independent of ω . However, the s -intervals from which the largest contributions to the emissivities come differ for the two displayed photon frequencies since the

widths of $\exp\{-\nu_{\min}/T\}$ (*cf.* Section 4.5) are proportional to ω . In Fig. 6.14, the cross sections are plotted fat in the regions which contribute most. If the Gaussian approximation (*cf.* Section 4.5.1) is applicable this is the interval $s \in [s_1 - \Delta s, s_1 + \Delta s]$ with s_1 as in (4.5.4) and the width of the Gaussian $\Delta s = 2\omega\sqrt{m_z T}$ (m_z is the mass of the outgoing partner of the photon). If, on the other hand, the exponential approximation (*cf.* Section 4.5.2) is applicable this is the interval $s \in [s_0, s_0 + 2T/b]$ with the lower bound s_0 of the s integration given by (B.5.12) or specified for the individual processes in (4.4.4) and (4.4.13) and b defined by (4.5.11). Inspecting Fig. 6.14 one might question the validity of the Gaussian and the exponential approximations because, there, we assumed that the s -dependent prefactor of $\exp\{-\nu_{\min}/T\}$ varies slowly with s , which seems to be in conflict with the divergent cross sections for $s \rightarrow s_0$. Nonetheless, in the rate formulas the cross sections are multiplied with factors that approach zero in this limit which makes the prefactors of $\exp\{-\nu_{\min}/T\}$ finite for all s .

6.2.5. Dynamical enhancement

It is somewhat difficult to estimate the dynamical enhancement of the rate within one model, because one parameter set in a single model gives rise only to one of the two curves that have to be compared. Nevertheless, one can compare within one parameter set the rate along an expansion path that goes only through areas of the phase diagram where all quantities are continuously changing, and the rate along a path that crosses the FOPT curve.

To this end we show in Fig. 6.15 the ratio of the total rate along an isentrope – with $s/n = 2.2$ – that crosses the FOPT curve and an isentrope – with $s/n = 2.8$ – that passes it.² In the left panel, this ratio is plotted for $\omega = 200$ MeV and, in the right panel, for $\omega = 1000$ MeV. For better judgment of the influence the phase transition has on such ratios, the ratio along the isentropes with $s/n = 3.4$ and $s/n = 2.8$ is also shown in the figure (in red) not exhibiting a strong peak. Comparing left and right panel one notices that only for the high photon frequency $\omega = 1000$ MeV the ratio exhibits such a pronounced peak. This peak is a result of the $\propto \exp\{-m_q/T\}$ -dependence of the partial rate for the dominating (COMPTON) processes valid for high photon frequencies (see Section 4.7). Looking at the red curves in both panels of Fig. 6.15 one notes that, if two neighboring isentropes only pass continuous regions of the phase diagram, the emissivities are of similar size for all temperatures. However, if one of the isentropes crosses the FOPT curve, the corresponding

² For an adiabatic expansion (which is suitable for the expansion dynamics in heavy-ion collisions), the system evolves through the phase diagram along curves with constant entropy per baryon ratio s/n .

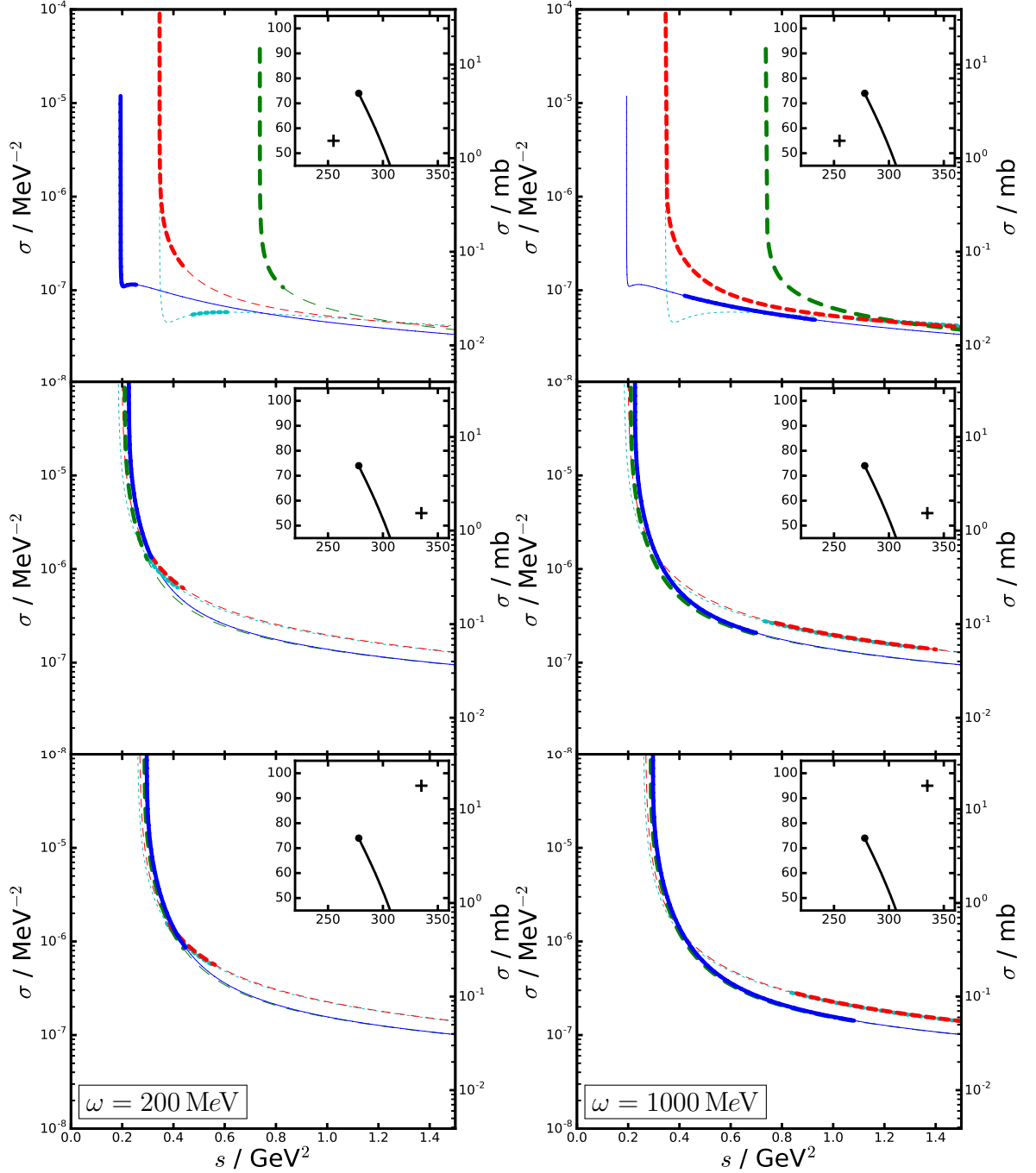


Figure 6.14.: Cross sections σ_i calculated according to (B.5.30) for the processes $q + \pi \rightarrow q + \gamma$ (blue solid curves), $q + \sigma \rightarrow q + \gamma$ (green long dashed), $q + \bar{q} \rightarrow \pi + \gamma$ (red short dashed) and $q + \bar{q} \rightarrow \sigma + \gamma$ (light blue dotted). The curves are plotted fat in the s -interval that contributes most to the approximate rates: The left column is for $\omega = 200$ MeV and the right column for $\omega = 1000$ MeV. The insets mark the positions $(T, \mu) = (55, 255)$, $(55, 335)$, and $(95, 335)$ (in MeV) in the phase diagram, where the cross sections are evaluated. The particle masses at these positions are collected in Tab. 6.1.

emissivity can be several orders of magnitude larger depending strongly on the temperature at which one compares the emissivities as well as on the photon frequency.

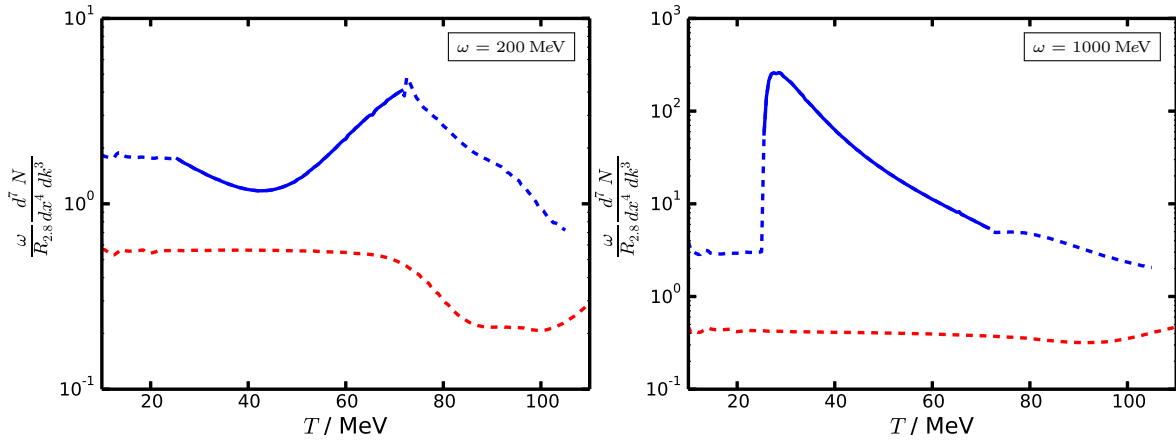


Figure 6.15.: Dynamical enhancement of the photon emissivities. Left panel: ratio $R(s/n = x)/R(s/n = 2.8)$ with $x = 2.2$ (blue) and 3.4 (red), $\omega = 200$ MeV and $R = \omega d^7 N / d^3 k d^4 x$ being the total photon rate. Right panel: the same quantities, but for $\omega = 1000$ MeV. The curves are depicted solid for those temperatures for which the $s/n = 2.2$ isentrope runs on the FOPT curve and dashed otherwise.

6.2.6. Chiral restoration

Since the QMM possesses an approximate chiral symmetry this symmetry is reflected/absent in the rates for the PWW/PNG phase. In the context of the model, the (approximate) chiral symmetry implies the (approximate) degeneracy of the meson masses. In Section 4.5, it was found that kinematics dominate by far the rates, because the masses appear in the exponent, while dynamical differences (*e.g.* spin and couplings which influence the cross section) are only power-law corrections. Accordingly, in Fig. 6.16, one sees that in the PWW phase the ratio of the sums of the COMPTON, anti-COMPTON and annihilation processes with pions and sigma mesons, respectively is approximately unity, but in the PNG phase it is significantly smaller.

In the left panel of Fig. 6.16, this ratio is plotted for $\omega = 200$ MeV, while in the right panel it is shown for $\omega = 1000$ MeV. The comparison of both panels suggests that the low photon frequencies are better suited to distinguish both phases. *e.g.*, in the left panel of Fig. 6.16, at $T = 50$ MeV, $\mu = 280$ MeV the processes involving pions contribute three orders of magnitude stronger to the total rate than the sigma-involving processes, while in the right panel at the same point there is only a factor of about 3.

This is understandable in view of the approximations discussed in Section 4.5. In the

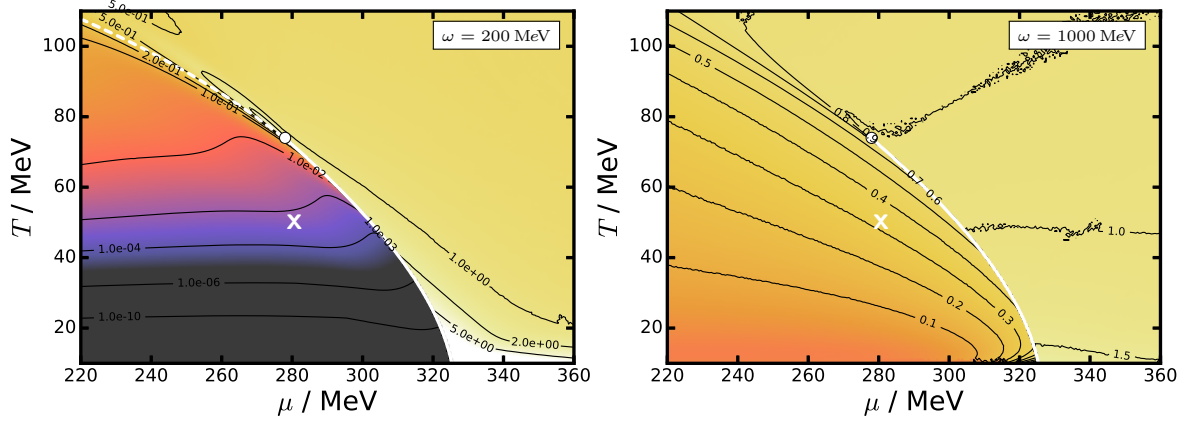


Figure 6.16.: Ratio $(R_{q\bar{q}\rightarrow\gamma\sigma} + R_{q\sigma\rightarrow\gamma q} + R_{\bar{q}\sigma\rightarrow\gamma\bar{q}})/(R_{q\bar{q}\rightarrow\gamma\pi} + R_{q\pi\rightarrow\gamma q} + R_{\bar{q}\pi\rightarrow\gamma\bar{q}})$ over the phase diagram. These ratios are shown for the photon frequencies $\omega = 200$ MeV (left panel) and $\omega = 1000$ MeV (right panel). The white crosses mark the point $(T, \mu) = (50$ MeV, 280 MeV).

low-frequency region, the scale for the emissivity is set by the height of the maximum of the respective partial spectra which, in turn, is $\propto \exp\{-(m_1^{\text{in}} + m_2^{\text{in}} - \epsilon\mu)/T\}$, with the masses of the incoming particles denoted by m_1^{in} and m_2^{in} , respectively and $\epsilon = +1$ for COMPTON processes, $\epsilon = 0$ for annihilations and $\epsilon = -1$ for anti-COMPTON processes (*cf.* Section 4.5.2 and Section 4.6). In the high-frequency region, on the other hand, the scale is set by the term $\exp\{(m^{\text{out}} - \epsilon\mu)/T\}$ with m^{out} denoting the mass of the outgoing partner of the photon (*cf.* Section 4.5.1). The $\epsilon\mu$ terms present in both approximation schemes make the COMPTON processes the dominant contributions to the photon rate, however, in the high-frequency region both COMPTON processes are dominated by the same exponential factor $\exp\{-(m_q - \mu)/T\}$, since in both cases the outgoing particle is the quark. Contrary, in the low-frequency region the masses of the incoming particles are

	$e^{(m_1^{\text{in}}+m_2^{\text{in}}-\epsilon\mu)/T}$	$e^{(m^{\text{out}}-\epsilon\mu)/T}$
$q + \sigma \rightarrow q + \gamma$	3.5×10^{-5}	0.87
$q + \bar{q} \rightarrow \sigma + \gamma$	1.0×10^{-5}	4.0×10^{-5}
$\bar{q} + \sigma \rightarrow \bar{q} + \gamma$	4.8×10^{-10}	1.2×10^{-5}
$q + \pi \rightarrow q + \gamma$	0.047	0.87
$q + \bar{q} \rightarrow \pi + \gamma$	1.0×10^{-5}	0.054
$\bar{q} + \pi \rightarrow \bar{q} + \gamma$	6.4×10^{-7}	1.2×10^{-5}

Table 6.2.: Comparison of the dominating exponential factors in the photon rate for the processes under consideration. (For masses, temperature and chemical potential, see Tab. 6.1). The largest numbers in each quadrant of the table are highlighted marking the dominant contributions to the total emissivity.

the relevant parameters and these differ for both COMPTON processes since pion and sigma masses are very different in the PNG phase. In Tab. 6.2, the corresponding numbers are collected. The rightmost two columns contain the two exponential factors corresponding to the two approximation schemes and show the behavior discussed above: In the low-frequency region, for both COMPTON processes the exponential factors setting the scale (highlighted in blue) differ by three orders of magnitude but in the high-frequency region the exponential factors (highlighted in green) are identical.

6.3. Differential spectra

As a complementary view, now the partial spectra as well as their sum over a broad frequency range are presented at representatively chosen locations in the phase diagram. These locations are chosen for studying several questions of interest.

6.3.1. Chiral symmetry breaking effects on the spectra

The principal difference between the spectra in the PNG and PWW phases, respectively can already be seen in the figures of the overview section 6.1. As discussed above in some detail, the emissivities are dominated by the kinematics, especially by the masses of the incoming and outgoing particles. Since the masses of the mesons are approximately degenerate in the PWW phase, this explains the striking similarity of the partial spectra for processes that differ only in the participating mesons (such as $q + \sigma \rightarrow q + \gamma$ and $q + \pi \rightarrow q + \gamma$).

In the PWW phase, the mass of the mesons is always larger than twice the quark mass, since the quark mass quickly drops at the phase boundary. With the considerations in Section 4.5 this leads to the conclusion that the IR divergency of the annihilation rates is not thermally regularized and thus appears at tree-level in the rates. Even when properly treated, the partial rate due to annihilations is non-zero, while the partial rates for the (anti-) COMPTON processes approaches zero due to thermal suppression. On the other hand, in the PNG phase, two cases are possible: Depending on the precise parameter set (especially, on the ratio $m_\sigma^{\text{vac}}/m_{\text{nuc}}^{\text{vac}}$) there are regions in the phase diagram with $2m_q > m_\sigma$ and $2m_q < m_\sigma$ (for $2m_q = m_\sigma$ a separate analysis is necessary). In the former case, all partial spectra approach zero in the IR, but for the latter case the same considerations as in the PWW phase apply making the annihilation rate into a photon and a sigma meson IR-divergent at tree-level. Even after properly regularizing the IR divergency there is a large difference between the annihilation spectra at $\omega \rightarrow 0$ for the cases $2m_q > m_\sigma$ and

$2m_q < m_\sigma$. Thus, for parameter sets with $2m_{\text{nuc}}^{\text{vac}}/3 = 2m_q^{\text{vac}} > m_\sigma^{\text{vac}}$ in the limit $\omega \rightarrow 0$, the annihilation spectra differ strongly between both phases, however, since for $\omega < 150$ MeV the photons from different sources, especially from DALITZ decays of pions, are expected to dominate the spectra by many orders of magnitude such a signal of chiral symmetry restoration or breaking seems hardly detectable.

6.3.2. Emissivity and phase transition type

Another question of interest is whether the spectral shape differs for different types of phase transitions. To attempt an answer to this, the partial and total spectra are plotted in Fig. 6.17 for the crossover region ($\mu = 255$ MeV, $T = 95$ MeV, top left panel), on the FOPT curve ($\mu = 293$ MeV, $T = 60$ MeV, top right panel) and at the CEP (bottom panels).

Since the rate on the FOPT curve is not unique as it depends on the mixing ratio of the coexisting phases, this ratio must be fixed for definiteness. This is done by specifying $s/n = xs_-/n_- + (1-x)s_+/n_+ = 2.4$ for the entropy per quark, s/n , averaged over both phases with the phase fraction of the PNG phase denoted by x and the entropy per quark ratios of the two phases defined as $s_\pm/n_\pm = s(\mu \pm \delta\mu)/n(\mu \pm \delta\mu)$ (with infinitesimal $\delta\mu$).

The underlying parameters for the rate calculation differ in the bottom panels. In the left panel, m_σ is the sigma mass determined in LFA (as all other masses). As discussed in Section 5.2.3 the m_σ has a lower bound in LFA determined from the interplay between formulas (4.2.25) and (4.2.20). To estimate the influence of this unwanted feature of the LFA on the photon spectra, the spectra at the CEP are shown in the bottom right panel again, but with m_σ set to a small value ($= 1$ MeV) by hand (and all other masses and parameters kept fixed). Comparing both bottom panels in Fig. 6.17 one notes that the strongest effect is on the process $q + \sigma \rightarrow q + \gamma$. However, it is relevant only for the frequency region $\omega \lesssim m_\pi$ which is kept out of consideration due to the expected strong background of DALITZ type decays, *cf.* Section 6.2.1.

6.3.3. Spectra in view of adiabatic expansion

In the course of an heavy-ion collision (HIC), pieces of the initially very hot and dense strongly interacting medium expand and cool down following a path in the phase diagram that can be modeled with relativistic hydrodynamics. Analyzing the azimuthal anisotropy of the particle momentum distributions one was able to constrain the ratio of shear viscosity over entropy density [RR07]. This turned out to be extremely small, in fact very close to a conjectured lower bound believed to exist for strongly coupled media, which was calculated

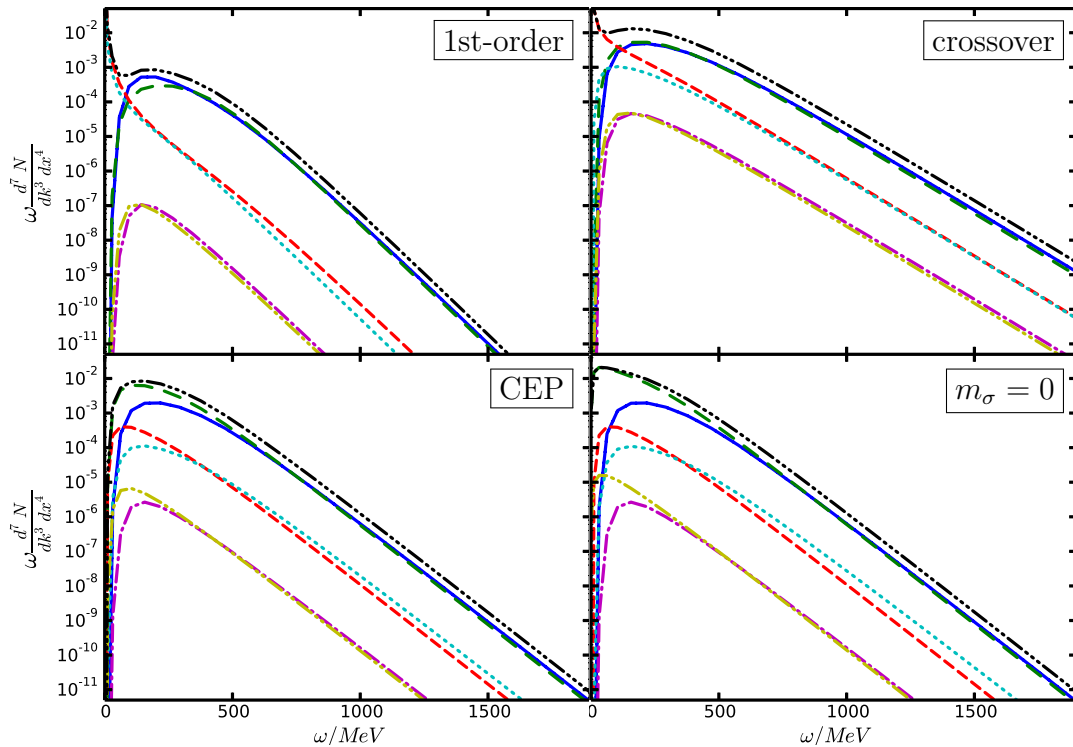


Figure 6.17.: Partial and total differential spectra $\omega d^7 N / d^3 k d^4 x$ evaluated at representatively chosen positions on the phase contour. Top left panel: spectra in the cross over region ($\mu = 255$ MeV, $T = 95$ MeV); top right panel: spectra on the FOPT curve ($\mu = 293$ MeV, $T = 60$ MeV) with a phase fraction corresponding to $s/n = 2.4$; bottom left panel: spectra at the CEP ($\mu = 278$ MeV, $T = 74$ MeV); bottom right panel: same parameters and position as in the bottom left panel, but with m_σ manually set to 1 MeV. The phase diagram and the particle masses are calculated with parameter set A (see Tab. 5.1). Colors and line styles as in Fig. 6.1.

applying the AdS/CFT correspondence [KSS05, ST09]. Because of the smallness of the viscous corrections, ideal hydrodynamics is a good approximation [KH, Hei09, Flo10] for the dynamics. One of the consequences is that an isotropically expanding medium evolves along isentropic curves (or: isentropes) which are defined by the condition $s/n = \text{const}$, with s being the entropy density and n being the net quark or net baryon density [Oll08].

In order to get a first impression of the strength of the distortion the curve of FOPTs imposes on the photon spectra, the total spectra are shown for a selection of temperatures T and values for the entropy per quark ratio s/n in Fig. 6.18. The isentropes with $s/n = 2.0$ and 2.4 cross the FOPT curve, while the isentropes with $s/n = 2.8$ and 3.2 traverse exclusively continuous regions of the phase diagram. For a reliable estimate of such a distortion the emissivities have to be folded with the hydrodynamic evolution and the signal has to be properly red (or blue) shifted. Furthermore, there are contributions from the phase prior to thermal equilibration as well as from final state decays. A comprehensive

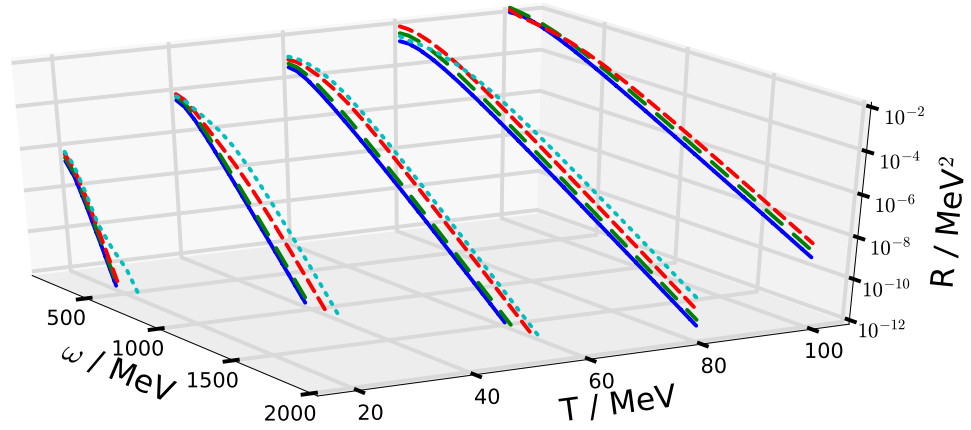


Figure 6.18.: Total spectra $R = \omega d^7 N / d^3 k d^4 x$ as a function of the photon frequency ω for several values of the temperature T . Linestyle and color refer to the entropy per quark ratio s/n : 2.0 (dotted light blue), 2.4 (short dashed red), 2.8 (long dashed green) and 3.2 (solid blue). For an estimate of the corresponding μ values, *cf.* Fig. 5.9. The missing curves for $s/n = 2.0$ at $T \geq 80 \text{ MeV}$ correspond to values for μ larger than 360 MeV , for which no emissivity was calculated.

analysis is therefore beyond the scope of this thesis.

Nonetheless, some insight can be gained even from the rather overview-type of plot. In the high-frequency region, at each temperature the curves are ordered according to their s/n value: The emissivity is larger for smaller entropy per quark. A strong difference between emissivities at the FOPT and away from it shows up only for the $T = 20 \text{ MeV}$ case. At this temperature the emissivity on the $s/n = 2.0$ isentrope at $\omega \gtrsim 500 \text{ MeV}$ is larger than the other emissivities for this temperature depicted in Fig. 6.18 by a factor of about ten thousand. However, at these (comparatively) low temperatures the emissivity is smaller than the emissivities for the other depicted temperatures by many orders of magnitude and thus probably less relevant from an experimental point of view. At higher temperatures, the emissivities from the FOPT (which correspond to the $s/n = 2.0$ and 2.4 isentropes for $T = 40 \text{ MeV}$ and 60 MeV) are only slightly enhanced. Although small, this enhancement is visible and increases in the low-frequency region $\omega \lesssim 500 \text{ MeV}$. At about $\omega \sim 500 \text{ MeV}$ it reaches its maximal value and keeps constant for larger frequencies. Thus, from such considerations, large photon frequencies seem better suited for the identification of a phase transition signal than low frequencies.

6.4. Static enhancement

For the search for an FOPT, one is in need of a quantity that characterizes the distortion of the emissivities by the FOPT. To construct such a quantity, the actual emissivity is compared to a fictitious one, which is determined by a linear extrapolation. This should be regarded as a hypothetical emissivity without an FOPT. In the continuous regions of the phase diagram, such a procedure is mathematically well defined, but on the FOPT curve the emissivity is not unique. This can be seen most easily by looking at a different representation of the phase diagram, *e.g.* the phase diagram in the T - n plane. The one-dimensional FOPT curve in the T - μ phase diagram corresponds to the two-dimensional coexistence region in the T - n phase diagram (*cf.* the schematic sketches in Fig. 5.16 or the lower panel in Fig. 5.9). The additional dimension corresponds to a parameter characterizing the decomposition into the two coexisting phases. This parameter can be chosen to be the fraction of one of the phases, the net quark or baryon density, the entropy density, energy density or any non-trivial combination of these as well as other, even more complex quantities. Because of the importance of the isentropes for the dynamics of HICs, the ratio s/n is a particularly well suited variable parameterizing the position in the coexisting region. Thus we propose the following prescription for an enhancement factor F :

- (i) Transform $R(T, \mu)$ to $R(T, s/n)$. This is unique everywhere except on the phase transition curve. On the transition line, the phase fraction x is calculated from $s/n = xs_+/n_+ + (1-x)s_-/n_-$ with $s_{\pm}, n_{\pm} = s(\mu_{\pm}), n(\mu_{\pm})$ and μ_- (μ_+) being the chemical potential infinitesimally smaller (larger) than the critical chemical potential $\mu_c(T)$. Then $R(T, s/n) = xR(T, \mu_+) + (1-x)R(T, \mu_-)$.
- (ii) Calculate the extrapolated rate $R^e(T, s/n) = 2R(s/n - \Delta_{s/n}) - R(s/n - 2\Delta_{s/n})$ for a suitable chosen grid size $\Delta_{s/n}$.
- (iii) Calculate the ratio $F(T, s/n) := R(T, s/n)/R^e(T, s/n)$.

As F is determined from equilibrium properties only, it is termed in the following the static enhancement factor. In Fig. 6.19, this factor is plotted for two choices of the entropy per quark ratio and a step size $\Delta_{s/n} = 0.4$. Comparing the left and right panels of Fig. 6.19 one notes that only in the left figure the ratio $F(T, s/n)$ is significantly different from unity. This is what was expected since in the right panel all three isentropes ($s/n = 2.8$, $3.2 = 2.8 + \Delta_{s/n}$ and $3.6 = 2.8 + 2\Delta_{s/n}$) traverse only regions of the phase diagram with continuously changing properties (especially the particle masses). On the other hand, in the left panel one isentrope (with $s/n = 2.4$) follows between $T = 35$ MeV and $T = 74$ MeV the FOPT curve. Thus, the rate along the $s/n = 2.4$ isentrope cannot be well approximated by an extrapolation from $s/n = 3.2$ and $s/n = 2.8$ between these temperatures.

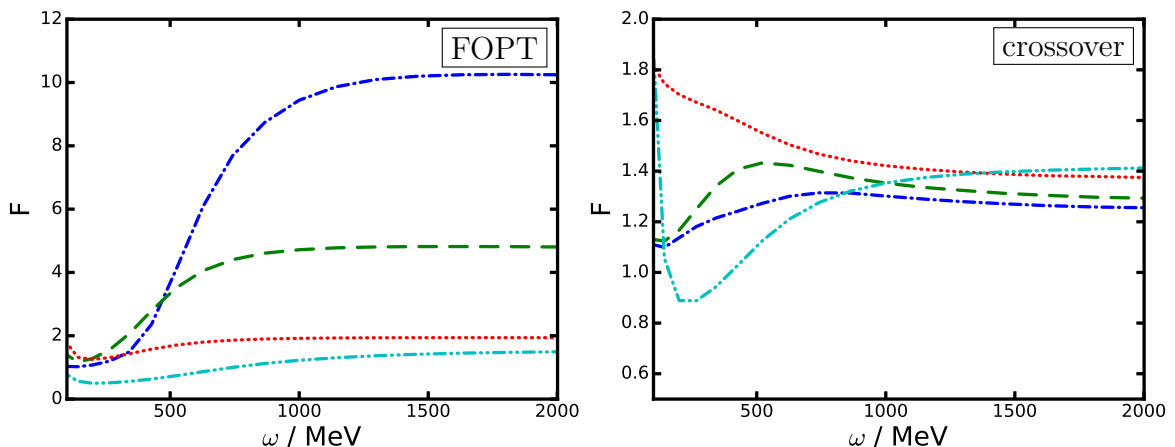


Figure 6.19.: Ratio F of the calculated total spectra for two selected isentropes and the (from below) extrapolated total spectra applying a grid-size $\Delta_{s/n} = 0.4$ (see text). Left panel: The curves correspond to $T/\text{MeV} = 40$ (dark blue dash-dotted curve), 60 (green dashed curve), 80 (red dotted curve) and 100 (light blue dash-double dotted curves). Here, the isentropes with $s/n = 2.4$ is chosen for the evaluation of the spectra and $s/n = 2.8$ and 3.2 for the extrapolation. Right panel: The same as on the left panel, but for the isentropes with $s/n = 2.8$ and the extrapolation based on $s/n = 3.2$ and 3.6.

Inspecting Fig. 6.19 one notes that the enhancement saturates in the high-frequency region, which is the expected behavior as all partial spectra decrease $\propto \exp\{-\omega/T\}$ at high enough photon frequencies. Furthermore, one sees that the enhancement is largest for $\omega \gtrsim 1000 \text{ MeV}$. Thus it can be concluded that in a static system the effect of the FOPT is largest in the high-frequency region $\omega \gtrsim 1000 \text{ MeV}$.

It is an interesting question whether this enhancement at the phase transition curve persists for a hydrodynamically expanding system such as the medium produced in HICs. To be at least approximately exact several aspects have to be considered in such a case: (i) One needs a sufficiently precise hydrodynamical model and a numerical code to calculate the dynamics (*cf.* [KHB14] and references therein). (ii) At the FOPT curve, non-equilibrium effects such as nucleation or spinodal decomposition in a rapidly expanding medium have to be treated properly [SDF⁺01, Ran04]. (iii) The blue/red shifts from the rest frame of the fluid elements to the lab frame have to be calculated for each fluid element and then be summed up. A proper treatment of this aspects is beyond the scope of this thesis and is left for further dedicated research.

Nevertheless, it is interesting whether the position of the FOPT curve can be determined – at least in principal – experimentally. The result would be a baseline that can be compared to a dynamic calculation respecting the considerations of the preceding paragraph.

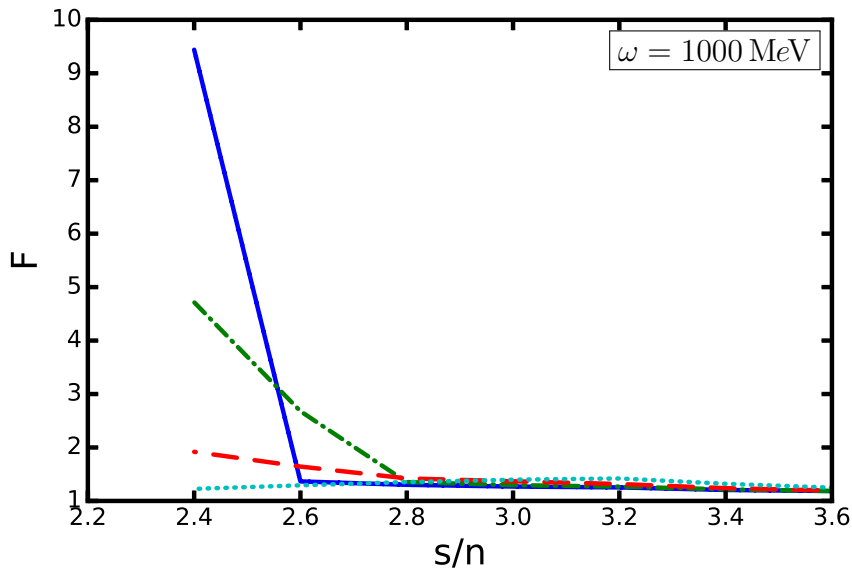


Figure 6.20.: Illustration of the detection strategy of a hypothetical FOPT curve from photon emissivities. Shown is the static enhancement factor F for the temperatures $T/\text{MeV} = 40$ (solid dark blue curve), 60 (dash-dotted green curve), 80 (dashed red curve), 100 (dotted light blue curve) and $\omega = 1000 \text{ MeV}$.

To achieve this, the static enhancement factor F seems a promising quantity. For its determination the photon yield has to be calculated as a function of s/n . The entropy per baryon ratio, s/n , could be estimated by statistical model fits to the particle yields measured in heavy-ion experiments.³ Then the photon yields obtained for two values of s/n and a photon frequency $\omega \gtrsim 1000 \text{ MeV}$ are extrapolated to a third value and compared to the actual photon yield at this point to obtain an integrated version of F . As the photon emissivity strongly depends on the temperature and the enhancement factor is at most $\mathcal{O}(10)$ this is a very challenging measurement, which probably requires to only use data sets with comparable initial temperatures (which has to be estimated on an event-by-event basis by a backwards hydrodynamical calculation).

As a precursory study for such a project, in Fig. 6.20, the static enhancement factor is shown for $\omega = 1000 \text{ MeV}$ and several temperatures. Clearly, one notes that for $s/n \geq 2.8$ F is almost unity for all temperatures, while at $s/n = 2.4$ it is significantly larger for $20 < T < 80 \text{ MeV}$. This is the signature from the $s/n = 2.4$ isentrope touching the FOPT. As $F(T = 80, s/n = 2.4)$ is only slightly larger than unity, one even can deduce that $T_{\text{CEP}} \lesssim 80 \text{ MeV}$ from this plot.

³ In principle, from such fits only properties on the chemical freeze-out curve can be deduced, but as discussed above, the s/n ratio is approximately constant during the evolution.

6.5. Summarizing the findings

In the previous section, a comprehensive overview was given on the photon emission within the QMM. This was done by first distinguishing two ranges of the photon frequency with different emission characteristics. These are the high-frequency region $\omega \gtrsim 1000 \text{ MeV}$ and the low-frequency region $\omega \sim \omega_{\text{peak}}$, with ω_{peak} being the average position of the maxima of the partial spectra. Since the thermal emission from the considered processes is expected to be masked by DALITZ decays of the final state pions the region $\omega < \omega_{\text{IR}} = 150 \text{ MeV}$ is excluded from the analysis. In doing so, also the frequency range was removed in which IR divergencies of the matrix elements can distort the results.

After this separation into a low-frequency and a high-frequency region, the emissivities in each region for one representatively chosen photon frequency ($\omega = 200 \text{ MeV}$ and 1000 MeV , respectively) were studied, finding essentially that in the low-frequency region for $2 \rightarrow 2$ processes the emissivities are governed by the sum of the incoming masses while in the high-frequency region the mass of the outgoing partner of the photon is the relevant quantity. In the high-frequency region, there is an ordering *w.r.t.* the type of the considered processes (COMPTON, annihilation, and anti-COMPTON), while in the low-frequency region the annihilation and COMPTON processes contribute in the same order of magnitude to the emissivity. Studying the effect of chiral symmetry restoration/breaking on the emissivities a much larger effect was found in the low-frequency region.

Besides analyzing the emissivities *w.r.t.* the position in the phase diagram with photon frequencies held constant, we took a complementary view by keeping the position in the phase diagram fixed and analyzed the partial spectra in a wide ω range. These positions were chosen in order to search for signatures of the chiral symmetry restoration and breaking and it was found that in the PWW phase the partial spectra for processes differing only in the meson differ only by a factor of about three. This factor is approximately constant in the whole ω region and can be attributed to the pions being an isospin triplet while the sigma represents a singlet. In the PNG phase, no such similarity of the partial spectra is observed.

Another question that was addressed is whether the order of the phase transition can be related to features of the partial spectra. However, no evidence for this conjecture was found. In this context, it was checked to which extent a vanishing sigma mass influences the spectra since, when releasing the linearized fluctuations approximation, one expects that $m_\sigma = 0$ at the CEP, which is necessary for the correct critical behavior at this point. It was found that the only differences between the spectra with a CEP according to the LFA and the spectra with $m_\sigma \rightarrow 0$ appear in the very low-frequency region $\omega < \omega_{\text{IR}}$, which

we excluded from our analysis.

Finally, we connected the rates to the adiabatic expansion paths through the phase diagram and found only a small, if any, effect of the FOPT. Nevertheless, since the emissivities are (inversely) ordered *w.r.t.* the entropy per quark the differences between neighboring isentropes might persist after integrating the emissivities over the whole hydrodynamic stage of an HIC. However, even in this case it seems a rather small effect. In this context, a quantity was constructed that estimates the influence of an FOPT on the photon rates by comparing the actual rate to an extrapolated rate. By looking for values significantly different from unity this quantity can be applied for locating an FOPT using only observables that are – at least in principal – experimentally accessible.

6.6. Discussion of the emissivities

Infra-red divergencies

As a systematic investigation of the real photon emissivity in context of the QMM has not been done in the literature many aspects of the approach presented in this thesis are of explorative nature. Yet it can be assumed that several observations are robust features which also apply to other approximation schemes or other models for strongly interacting matter at finite density and temperature. One obvious objection is that the problem of IR divergencies of the emissivities was ignored completely. They can be traced back to IR divergencies of the matrix elements for which there are several standard ways to treat them. The authors in [KLS91, BNNR92] regularize the IR divergencies in the weak-coupling (high-temperature) limit of massless two-flavor QCD by equipping the low-momentum propagators with the hard thermal loop (HTL) self-energies. To achieve this a IR cut-off for the internal momenta is introduced, but in the final result the cutoff dependence of the high-momentum (perturbative) parts and the low-momentum parts (HTL) of the calculation neatly cancel. A close inspection shows that the IR divergencies are canceled by contributions to the propagator originating from branch cuts, which are attributed to LANDAU damping effects. Nonetheless, the HTL self-energies seem not to represent an appropriate approximation for the low-momentum propagators within the QMM. To clarify the argument, it is necessary to take a look on the key ingredient of the HTL resummation (see [BP90, BI02] for a comprehensive discussion of the HTL resummation scheme): the separation between hard $\gtrsim T$ and soft momenta $\sim gT$ and the thermal mass being of order gT in the weak coupling limit $g \rightarrow 0$. Contrary, within the QMM, the coupling g between quarks and mesons is of order unity rendering the HTL-like resummed self energies not

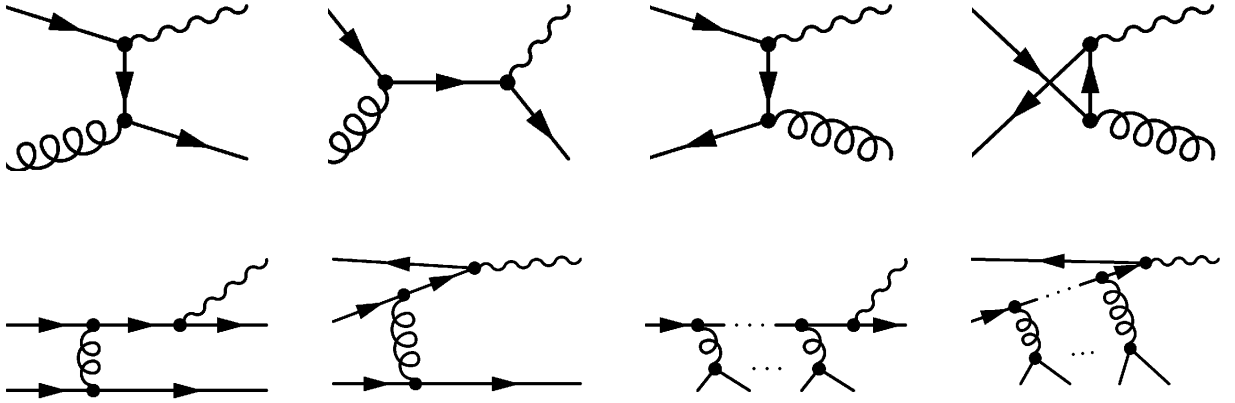


Figure 6.21.: Diagrams for the leading order (*w.r.t.* the strong coupling g_s) contributions to photon emission of the QGP. Top panels: standard COMPTON and annihilation diagrams; bottom left panels: collinear bremsstrahlung and annihilation processes contributing parametrically to the same order as the processes in the top panels; bottom right panels: processes also relevant for the relativistic LPM effect.

the leading terms in a controlled expansion. Related to this issue is that neither mesons nor quarks are massless but are relatively heavy objects. Both facts make the use of a HTL-like regularization of the matrix elements questionable.

Another way is more likely to be applicable for treating the IR divergencies of the matrix elements: One postulates a finite detector sensitivity and adds all possible soft photon emission processes to the production rate. For complete calculation and an exhaustive discussion see, *e.g.* [YFS61, Wei65, PS95].

However, independent of the precise scheme applied for regularizing the IR divergencies of the matrix elements, still a huge difference in the IR region remains between annihilations and (anti-)COMPTON rates in certain regions of the phase space (in some regions even between annihilations with σ mesons and those with π mesons, respectively), because the thermal suppression – present for the (anti-)COMPTON processes, but absent for annihilation processes if $2m_q < m_{\sigma,\pi}$ – leads in these cases to two very different $\omega \rightarrow 0$ limits.

Photon emission from the QGP and the QMM

In the context of a high-temperature (perturbative) QGP, the photon emission was first calculated with the inclusion of the processes depicted in the upper row of Fig. 6.21. The corresponding matrix elements are similar to those used in this thesis. With the HTL resummation method, the high-temperature QCD could systematically be evaluated mak-

ing it possible to regularize the IR divergent parts of the matrix elements based on first principles. Kapusta *et al.* [KLS91] and Baier *et al.* [BNNR92] independently performed this calculations and the problem seemed settled. About ten years later, Aurenche *et al.* [AGKZ98, AGZ00a, AGZ00b] identified further processes to be of similar importance, even if they are only next-to-leading order in the coupling strength of the strong interaction. Their calculations are extended in [AMY01b, AMY01a, AMY02] by the inclusion of the LANDAU-POMERANCHUK-MIGDAL (LPM) effect to arrive at the complete leading order results for photon emission from a QGP in the weak coupling limit.

As described above, in order for obtaining the complete leading order result for the photon emission from the QGP several other processes had to be evaluated besides the $2 \rightarrow 2$ scattering processes depicted in the upper row of Fig. 6.21. It therefore is natural to ask whether the calculations presented in this chapter need similar extensions in order to be complete. Although such considerations are of great importance in the case of QCD at high temperature, it seems that they are not applicable in the context of the QMM within the LFA. This is not caused by the missing gluons, whose role could be played by massless or very light scalar mesons, as spin is no essential feature for the reasoning in [AGKZ98] and [AMY01a], but because neither the QMM coupling g is small compared to unity, nor the thermal quark mass m_q is proportional to T . The large meson mass in many parts of the phase diagram also prevents the mesons to take over the role played by the gluons in the original line of reasoning. In order for processes of the type depicted in the lower row of Fig. 6.21 (but with the gluons replaced by the QMM mesons) to be of importance, both internal particle propagators have to be almost on-shell. This is possible only if the meson is (at least nearly) massless. Thus the only regions in the phase diagram where the conclusions of [AGKZ98, AMY01a, AMY02] have to be considered are the chirally broken phase in the chiral limit (there, the pions as the GOLDSTONE bosons are massless) and at the CEP (there, the σ -meson being the critical mode is massless). Still, even in these cases, the quark-meson coupling is not at all a small number and it is not clear if the considerations can be modified to apply in such a case. Therefore, this issue is left for future work.

Relevant photon production channels

One obvious difficulty in transferring our findings to more realistic models is the limited number of particle fields in the QMM. In modern transport approaches, such as UrQMD [B⁺98b], GiBUU [BGG⁺12] or PHSD [CB09], a large number of possible channels contributing to the photon yields is implemented. In [LKCB13, LKS⁺15], the photon production

processes in the PHSD model are listed and p_T -spectra as well as centrality and beam energy dependence are discussed. Ignoring final state hadronic decays, they find large (depending, of course, on the beam energy and other experimental variables) contributions from COMPTON scattering and annihilations in the QGP, and also significant contributions from $2 \rightarrow 2$ scatterings including pions, vector mesons and nucleons as well as resonances. As these processes are structurally similar to the $2 \rightarrow 2$ processes discussed above for the QMM one may tentatively say that a transfer to realistic models is possible to some extent.

The main reason for such a claim is that the dominant influence of the phase structure on the photon emissivities comes from the different behavior of the particle masses over the phase diagram (and therefore from kinematics) and not from dynamical issues (*i.e.* the cross sections). A similar picture is obtained in hybrid models [BB10a]. Therefore, even though there are, *e.g.*, no vector mesons and no baryons in the QMM, basic kinematic results from our analysis will still persist for $2 \rightarrow 2$ processes including those in other models. This issue will be discussed below in more detail.

In the weak coupling/high temperature limit of the strong interaction, one finds [AGKZ98, AMY01b] that collinear bremsstrahlung and annihilation processes (*cf.* the first two panels in the lower row of Fig. 6.21) contribute parametrically to the same order (up to logarithmic corrections) as the fundamental tree level COMPTON and annihilation processes (*cf.* upper row of Fig. 6.21). Within transport approaches also a large contribution from meson and baryon bremsstrahlung processes is obtained. Thus, future work considering these channels will be of particular interest.

Calculations based on the assumption of vector meson dominance (VMD) find important contributions to the photon yields originating from a direct $\rho/\omega/\phi$ -photon coupling and thus relating the imaginary part of the photon propagator (related by (3.1.1) to the photon emissivity) to the imaginary part (and thus their spectral width) of the vector meson spectral functions [GK91, KKW96, Rap11]. On the other hand, comparisons between calculations based on kinetic theory emission rates and calculations based on the imaginary part of vector meson propagators (and thus VMD) demonstrate the equivalence of both approaches [HHR16]. Especially, a good agreement is found when the kinetic theory part of the calculation is solely based on tree-level $2 \rightarrow 2$ processes, which obey similar kinematics as the processes we analyzed for the QMM. Nonetheless, VMD calculations often focus on dilepton yields since the invariant mass spectra of dileptons reflect properties of the vector meson spectral functions more directly.

QED and the QMM

One further issue that has to be discussed in the context of real photon emission is the coupling of the strongly interacting sector of the QMM to the electromagnetic one. In our opinion, the QED-like minimal coupling is the most reasonable one albeit other, phenomenologically rooted, coupling schemes are also discussed in the literature [SAR⁺98]. Not only such a coupling respects the gauge symmetry of QED, it is separately successfully applied in the individual sectors of the QMM; in the fermionic sector by QED itself and in the mesonic sector by scalar QED which was used for modeling the pion coupling to the electromagnetic field [BKM99]. Another reason for preferring this coupling scheme is its application to investigations concerning static magnetic fields and chiral symmetry breaking [NS06, FM07, MCF10, FGP12, ALZ15]. Thus one can conclude that although other coupling schemes might be possible the minimal coupling can be regarded as the most reliable one.

Transfer of the findings

As the QMM is quite different to realistic models for the strong interaction, especially in the hadronic phase, we need to discuss the applicability of our findings. First, one has to keep in mind that the strength of the QMM is not in its field content, but in its minimalistic formulation, yet including explicitly hadronic and quark degrees of freedom. We now want to comment on the properties of the photon emissivities within the QMM which might be transferable to other models:

- (i) As mentioned above, it was found that, due to the exponential thermal suppression, the general behavior of the photon emissivities is dominated by certain combinations of the mass parameters which have to be seen in relation to temperature and chemical potential. In the high photon frequency region, the rate is dominated by contributions for which the total energy in the rest frame of the heat bath (called ν_{\min} in Section 4.5) is minimal *w.r.t.* the center-of-mass energy s . Both, the position of this minimum as well as the value of ν_{\min} at this point depend primarily on properties of the out-states (*i.e.* on photon frequency and the mass of the other outgoing particle). More specifically, for investigations of the chiral symmetry breaking at photon frequencies $\omega \gtrsim 1000$ MeV, channels with the particle having the largest mass change being outgoing are presumed to be most promising.
- (ii) While in the high-frequency region the outgoing particles determine the overall behavior of the emissivities, in the low-frequency region the incoming particles take

over this role.

- (iii) The hierarchy appearing in the emissivities (rate from COMPTON processes \gg rate from annihilations \gg rate from anti-COMPTON processes) on the other hand is probably less transferable, because it is restricted to processes including quarks or baryons. Often, many important photon production processes (*e.g.* $\pi\pi \rightarrow \rho\gamma$) do take place without participation of quarks or baryons, which reduces the importance of this observation. Nevertheless comparing (anti-) COMPTON processes and annihilations involving the same particles (or their anti-particles) a hierarchy comparable to the one in the QMM is expected to show up for such a subset of emission processes.
- (iv) Chiral symmetry restoration / breaking is expected to show stronger signals in the $\omega \rightarrow 0$ limit, because in this limit the emissivity change drastically if certain inequalities for the masses of the participating particles are fulfilled / violated. The most relevant distinction is between two cases: (a) The minimum, s_1 , of the minimal total energy ν_{\min} (measured in the rest frame of the heat bath) *w.r.t.* the squared center-of-mass energy s (*cf.* (4.5.4)) is smaller, *i.e.* $s_1 < s_0$, and (b) it larger or equal to the minimal center-of-mass energy s_0 , *i.e.* $s_1 \geq s_0$. (*cf.* Section 4.5 for the respective definitions.)

In case (a), the exponential approximation (*cf.* Section 4.5.2) is applicable, while for case (b), the Gaussian approximation (*cf.* Section 4.5.1) is appropriate. In physical terms, the former approximation means that the largest contributions to the photon production origins from processes with minimal center-of-mass energy $s = s_0$ (which in turn is determined from the sum of the masses of the incoming or outgoing particles, depending on which of both is larger). In case (b), the dominant contribution is from processes with center-of-mass energy $\approx s_1$, which corresponds to the production of the outgoing partner of the photon at rest in the heat bath rest frame. Both approximations have very different limits $\omega \rightarrow 0$: In (a), the emissivity approaches zero faster than any power of ω , while in case (b) the limit is divergent (without proper IR regularization) or finite (with proper IR treatment), making the rate for processes according to the Gaussian approximation many orders of magnitude larger than the rate according to the exponential approximation for small photon frequencies. Thus, at low frequencies, the partial emissivities can drastically change when the masses of the particles jump at the phase transition and by chance changing the order of s_1 and s_0 . With minor changes to this argumentation, the same is expected to hold true in a variety of models even for a larger class of processes than the $2 \rightarrow 2$ processes for which it was derived.

Contrary, the result that the low-frequency region $150 \text{ MeV} \lesssim \omega \lesssim 500 \text{ MeV}$ is better

suitable for the investigation of chiral symmetry than the high-frequency region $\omega \gtrsim 1000 \text{ MeV}$ relies strongly on the above mentioned hierarchy of photon production channels which is limited to processes involving fermions as well as to the CEP being located at a relatively large μ/T ratio.

- (v) It was found that the ratio of the total rates on both sides of the phase transition curve is of the order of magnitude $\exp\{-\Delta_m(T)/T\}$ with $\Delta_m(T)$ being the scale of the mass jumps across the FOPT at temperature T . This implies that the effect of the phase transition is larger for small temperatures. On the other hand, at low temperatures the absolute emissivities are small, so the best temperature range for detecting effects of the FOPT is determined by the interplay of these competing effects. For a realistic model of QCD-like matter the effective masses have to be of the same order of magnitude as Λ_{QCD} (in principle, probably also of $\mathcal{O}(T)$ or $\mathcal{O}(\mu)$). However, close to the phase transition curve at least one of the thermodynamic quantities T and μ is of $\mathcal{O}(\Lambda_{\text{QCD}})$. Therefore, for a wide variety of models $\Delta_m(T) = \mathcal{O}(\Lambda_{\text{QCD}})$ and therefore $\Delta_m(T)$ is thus of the same order of magnitude as in the QMM. Concerning the size of the jump of the emissivities at the phase transition line, the main difference between many models is up to which temperature the curve of FOPTs extends, *i.e.* the temperature T_{CEP} of the critical end point. For $\Delta_m \sim 200 \text{ MeV}$, the ratio between the emissivities on both sides of the phase transition line at $T = 50 \text{ MeV}$ is of $\mathcal{O}(50)$, while for $T = 100 \text{ MeV}$ it is less than 10. This makes the detectability of an FOPT in the photon emission at high temperatures much more challenging.

7. Summary and outlook

In this thesis, the photon emission from the quark meson model (QMM) was analyzed in detail. We applied an approach based on path integrals including leading order mesonic fluctuations, the so-called linearized fluctuation approximation (LFA), which ensured consistency between thermodynamics and matrix element calculations in terms of FEYNMAN diagrams. To this end, it was necessary to re-derive the kinetic theory expression for the photon emissivity and to read off at the intermediate steps of the calculation which mass parameters have to be applied in the matrix element calculations. It turned out that in the mesonic sector the mass parameters applied in the momentum distribution function for the grand canonical potential are the same as the mass parameters showing up in the meson propagators used for the matrix elements. However, the fermionic mass parameters differ for both applications. In the thermodynamical sector, a mass parameter averaged over the meson configurations is a reasonable choice, but the correct mass parameter for the fermionic propagator depends only on the averaged meson fields, at least within the LFA.

7.1. Thermodynamics

The general behavior of the thermodynamical quantities, such as pressure, energy density, entropy density, net quark density *etc.*, is similar to that well known from other compilations of the QMM or other chiral effective models with similar degrees of freedom. However, within the LFA it has only partially been studied before. The major compilations are [MME04] (restricted to the temperature axis), [BK09] (focusing on the phase transition curve *w.r.t.* the pion vacuum mass parameter) and [FKP10] (analyzing the fine structure of the CEP).

Analyzing the thermodynamics of the QMM *w.r.t.* to a large number of parameter sets the following behavior in the $T-\mu$ -diagram has been observed:

- (i) At $T = 0$ and $|\mu_q| \leq m_{\text{nuc}}^{\text{vac}}/N_c$, all thermodynamical quantities and field parameters attain their vacuum values, especially pressure, energy density, entropy density and net quark density vanish, while all mass parameters and field expectation values coincide with the vacuum values.
- (ii) There are three major classes of parameter sets. In the first class, the vacuum quark mass is larger than the critical chemical potential μ_c^0 at zero temperature, in the second class it is smaller and in the third class there is no first-order phase transition (FOPT) whatsoever. In the first class, the region in which all thermodynamical quantities and field parameters retain their vacuum mass extends to the FOPT curve. This is sometimes phrased as the system being in equilibrium with the vacuum at the FOPT, which is not regarded realistic for the chiral transition, but fits better to the nuclear liquid-gas transition. In the T - μ phase diagram all isentropic curves merge at some temperature with the FOPT curve and run down on it, even the isentropes that traverse the crossover region.

In the second class of parameters, the thermodynamical quantities at the FOPT are different from their vacuum values, even at $T = 0$, and the isentropic curves all merge at the point $(T, \mu) = (0, m_{\text{nuc}}^{\text{vac}}/N_c)$ after passing the crossover region or the FOPT curve.

As it is the aim of this thesis to study the impact of an FOPT or CEP on the photon emission the third class of parameter sets was not included in the analysis. Albeit not shown explicitly in Chapter 5, also for these parameter sets the isentrope merge at the point $(T, \mu) = (0, m_{\text{nuc}}^{\text{vac}}/N_c)$.

- (iii) The position and shape of the phase transition curve is related to a particular parameter combination, namely $m_\sigma^{\text{vac}} \langle \sigma \rangle_{\text{vac}}$. Phenomenologically, the chemical potential μ_{CEP} of the CEP linearly depends on the parameter combination $m_{\text{nuc}}^{\text{vac}}/(2N_c) - \mu_c^0$. At chemical potentials larger than μ_{CEP} , the transition is of first order and at smaller chemical potential it is a crossover. If the difference of the critical chemical potential at zero temperature and the vacuum quark mass $m_{\text{nuc}}^{\text{vac}}/N_c$ exceeds a certain threshold (about 100 MeV) the CEP ceases to exist and the transition becomes a crossover for all temperatures (third class of parameters according to (ii)). Conversely, for arbitrarily large $m_{\text{nuc}}^{\text{vac}}$, the CEP chemical potential μ_{CEP} can be made arbitrarily small eventually reaching $\mu_{\text{CEP}} = 0$ at some large $m_{\text{nuc}}^{\text{vac}}$ being of $\mathcal{O}(600 \text{ MeV} \times N_c)$ and thus completely separating the two phases by a FOPT curve.
- (iv) The sigma mass parameter m_σ is minimal in a valley surrounding the phase transition curve. The global minimum is at the CEP. In an exact calculation, m_σ should be

zero there, but the LFA enforces a strict relation between the fluctuation measures and m_σ which inhibits m_σ from becoming zero at the CEP.

In the pseudo NAMBU-GOLDSTONE (PNG) phase (*i.e.* the phase with broken chiral symmetry), there is a large mass splitting between m_σ and m_π , while, in the pseudo WIGNER-WEYL (PWW) phase (*i.e.* the phase with restored chiral symmetry), both mass parameters are approximately degenerate. This reflects the approximate chiral symmetry, which (approximately) transforms both fields into each other and thus requires (approximately) identical masses for both fields. On the other hand, the quark mass is large in the PNG phase (between $m_{\text{nuc}}^{\text{vac}}/N_c$ and approximately $m_{\text{nuc}}^{\text{vac}}/(2N_c)$) but considerably smaller in most parts of the PWW phase (in the chiral limit it is zero), which also reflects chiral symmetry. This behavior of the quark mass is reflected by a corresponding behavior of the sigma thermal expectation value, which can be regarded an order parameter of the phase transition.

- (v) In the PWW phase, entropy density and net quark density are almost equal to the corresponding quantities of a free FERMI gas with the same number of degrees of freedom, while in the PNG phase, they are considerably smaller. However, the pressure is much smaller than that of a FERMI gas, which can be parametrized with a temperature and chemical potential independent offset. This can be interpreted – analogous to the MIT bag model – in terms of the pressure of a nontrivial vacuum state.
- (vi) Compared to the mean field thermodynamics the general behavior is similar (albeit with a shift of the CEP), with some differences in the critical region: In mean field approximation the mass m_σ of the sigma field vanishes at the CEP, contrary to the LFA. Also, the critical region in LFA is less elongated than within the mean field approximation. For zero temperature both approximations coincide.

Although the leading meson fluctuations are included, there are still important features missing. The approximation of the effective meson potential U_{eff} by a quadratic potential \bar{U} is a severe simplification. If higher-order terms were included the meson self energy would not be momentum independent and nontrivial dispersion relations are possible.

7.2. Photon emission

Several aspects of the QMM thermodynamics are reproduced imperfectly, if vacuum fluctuations are omitted. However, this thesis is aimed at a different goal: to work out connections between the photon spectra and features of the phase diagram. In order to achieve

this goal it is more important to work with an approximation that permits the CEP to be located at temperatures in the order of 100 MeV at realistic pion and nucleon masses rather than to use the best approximation scheme available for the QMM. Furthermore, the applied approximation scheme is especially well suited to derive both, thermodynamics as well as photon emissivities, on the same footing, namely, the similar path integral representations of the partition function and the generating functional of correlation functions. Studying photon emissivity at finite temperature and density within the QMM is especially interesting as, the QMM, despite its popularity for modeling the chiral transition, has not been applied to the calculation of direct photon emission before. The only (albeit very interesting) application to electromagnetism being the influence of strong nuclear magnetic fields on the phase diagram.

In the high-frequency region ($\omega \gtrsim 1000$ MeV) the behavior of the rates is determined (for $2 \rightarrow 2$ processes) essentially by the mass of the outgoing partner of the photon, *i.e.* for the (anti-)COMPTON processes by the mass of the (anti-)quarks and for the annihilations by either the sigma or the pion mass. This makes annihilations into a photon and a sigma meson an interesting channel for the detection of CEP signatures since the critical mode at the CEP is sigma meson, which hence becomes massless there. However, the momentum distributions of the incoming particles lead to a factor $\sim \exp\{\mu/T\}$ suppressing this channel *w.r.t.* the COMPTON processes by this amount and making the detection of this channel in the total rate a challenging task. Nevertheless, for hypothetical CEP positions at small values of the chemical potential this suppression becomes less important and the peak structure of the partial emissivity from annihilations into a photon and a sigma meson might show up even in the total emissivity.

Contrary, in the low-frequency region, *i.e.* for $\omega = 150$ MeV \dots 500 MeV, the emissivities are determined essentially by the sum of the incoming particle masses. This difference in the dominant parameter dependency leads to the following conclusion: Since the COMPTON emissivities are enhanced by the above mentioned factor $\exp\{\mu/T\}$ they constitute the dominant contribution to the total emissivity. For the COMPTON processes, in turn, the sigma meson being most intimately connected to the CEP (since it constitutes the critical mode) is an incoming particle and thus the low-frequency region is expected to show stronger signals of the CEP than the high-frequency region (for which the outgoing masses are the most relevant quantities).

On the other hand, when being interested in obtaining a clear signal of the FOPT the high-frequency region seems better suited since the quark mass shows the strongest jump of all mass parameters when crossing the FOPT curve. As the COMPTON processes dominate the total emissivities and the quarks are outgoing particles for these processes the high-

frequency region is best suited for getting a clear signal. This conjecture is furthermore supplemented by the static enhancement factor constructed for quantifying the influence of the FOPT on the photon spectra.

At the FOPT curve, the emissivities are discontinuous due to the jumps of the particle masses. These discontinuities vanish at the CEP and in the crossover region, but quickly increase on the FOPT curve with the distance to the CEP, *e.g.* 10 MeV below the CEP-temperature T_{CEP} , the COMPTON rate increases at the FOPT by a factor of about ten. From the point of detectability this is good, since it implies that already at relatively high temperatures the difference in the emissivity between both phases is large. This is especially important since the emissivity strongly scales with the temperature and thus the FOPT has the largest effect on the total photon yield at high temperatures, *i.e.* close to the CEP.

Since the partial emissivities are dominated by kinematics and thus the respective particle masses, chiral symmetry restoration and breaking manifest themselves in the photon emissivity. To this end the sum of COMPTON, anti-COMPTON and annihilation processes with or without pions (*i.e.* without or with sigma mesons) were calculated separately. In the PWW phase, the ratio of both quantities is approximately one third (corresponding to the three pions compared to one sigma meson), while, in the PNG phase, it is several orders of magnitude smaller depending on the precise position in the phase diagram as well as on the photon frequency. It was found that the chiral restoration gives a clearer signal when observed at low photon frequencies, *i.e.* the partial emissivities with pions differ stronger from those with sigma meson at low-photon frequencies.

The character of the phase transition leaves no clear signal in the functional form of the partial spectra. Nevertheless, close to the transition region the mass ratios m_q/m_σ , m_q/m_π , m_π/m_σ *etc.* change, which has some impact on the low-frequency region of the photon spectra. However, the thus induced changes may or may not occur on the phase transition curve and the crossover region.

Finally, the enhancement of the photon emissivity due to the FOPT was quantified by a static enhancement factor. This quantity is constructed in a way that enables – at least in principle – the comparison with experimental data. Nonetheless, due to the limitations of the QMM as well as the applied approximations and the necessity for supplementing the emissivities with many other ingredients that were not focus of this thesis (hydrodynamical evolution of the expanding medium produced in a heavy-ion collision, freeze-out, final state decays *etc.*) we refrained from doing so. Nonetheless, two points are worth mentioning: Firstly, the effect of the FOPT saturates in the high frequency region $\omega \gtrsim 1000$ MeV and is much smaller in the low-frequency region. Secondly, the influence is rather moderate

with the enhancement factor being about three: Only at small temperatures $T \lesssim 40 \text{ MeV}$ the enhancement factor becomes larger reaching values of about 10 at $T \sim 20 \text{ MeV}$. Due to the strong temperature dependence of the total photon emissivity the absolute numbers are small, though.

7.3. Outlook and suggested future projects

This thesis should be seen as an explorative study dedicated to the determination of the extent to which the photon emissivities are sensitive to the chiral symmetry breaking and restoration. In the following, a few improvements are listed that should be incorporated for refining the analysis of photon emission of strongly interacting matter. This discussion is restricted to the chiral sector keeping out confinement/deconfinement issues, *e.g.* the inclusion of a POLYAKOV loop variable and its potential.

To make quantitative predictions several further issues have to be considered: First, more degrees of freedom must be included; especially the vector mesons and (due to chiral symmetry) the axial vector mesons are expected to contribute considerably. Of course, one could think about including strangeness into the model. However, in doing so the number of mesonic degrees of freedom has to be increased strongly (from 4 to 18) in order to maintain chiral symmetry. Furthermore, several explicitly symmetry breaking terms (*e.g.* for $SU(3)$ flavor symmetry the axial $U(1)$ symmetry, absent for the $SU(2)$ case, has to be broken explicitly to respect the axial anomaly of QCD) have to be introduced in order to reproduce QCD vacuum properties adequately [SW09, SWW10]. Similarly, the number of parameters increases even more when including vector and axial vector mesons in the model [PGR10, PKW⁺13]. Thus, for increasing the flavor dimension or adding further kinds of mesons to the model, many additional parameters have to be included reducing the predictive power of the resulting model and complicating the analysis considerably. Furthermore, with much more path integrals to be evaluated the method of linearized fluctuations requires to include further equations to be solved self consistently, such that the numerical solution on a fine grid spanning the relevant parts of the phase diagram becomes impractical. In order to still do thermodynamical calculations one uses the mean field approximation, *i.e.* setting the meson fields to their respective thermal expectation value. However, then the coupling to the photon sector is far less elegant. As an immediate future project we thus recommend to include axial and vector mesons, however sticking to two flavors and furthermore keeping the number of parameters in the meson sector as small as possible.

Besides extending the model, also the applied approximations can be relaxed or refined. In this respect, the inclusion of vacuum fluctuations seems quite important, since, on one hand, it shifts the CEP considerably pushing it well outside the experimentally accessible region and, on the other hand, respects one of the major formal advantages of the QMM, namely its renormalizability. Furthermore, the derivative expansion of the fermion trace can be improved by including higher order derivative terms. Especially the terms up to second order in the derivatives seem to be easily compatible to the LFA. (Third or higher order terms can include third or higher powers of the meson fields which are in conflict with the (second order) approximated effective meson potential, *cf.* (4.2.22).) Also for the calculation of the probability distributions higher order meson derivatives can be incorporated. Yet, probably the most restrictive approximation in our calculation is the replacement of the effective meson potential U_{eff} including the fermionic contribution by the second-order potential \bar{U} as this effectively makes the mesonic sector of the model noninteracting. It is not clear whether an inclusion of third- or fourth-order terms into \bar{U} improves the approximation since the effect of the higher-than-second order terms has most likely to be calculated applying perturbation theory with these terms representing interaction vertices. In general, the effective coupling constants in these additional terms are no small numbers which makes a naive perturbative approach questionable. Nevertheless, momentum dependent meson self energies can be introduced in this way and the correct critical behavior at the CEP might be recovered. Furthermore, the inclusion of additional terms in a systematic way preserving symmetries is a nontrivial task which is best done following dedicated formalisms such as the CJT [CJT74] or the Φ -functional [BK61, Bay62, vHK02] formalisms or working within the FRG framework [Gie12].

Besides improving the LFA or modifying the underlying QMM, one can include further processes in the photon emissivity. The matrix elements, however, have to be first order in the electromagnetic coupling (otherwise the connection of the photon propagator with the emissivity cannot be made with the MCLERRAN-TOIMELA formula introducing rather involved modifications to the rate formulas applied in this thesis) but may be higher order in the quark-meson coupling. Especially, $2 \rightarrow 3$ bremsstrahlung and $3 \rightarrow 2$ annihilation processes seem interesting channels as modern transport codes suggest [LKCB13, BB10a]. In the case that the QMM is supplemented by a vector/axial vector sector, scatterings with ρ and ω mesons are of great interest, too [HHR16].

Finally, we want to point out that within this thesis we illuminated the close relation of photon emission with the underlying thermodynamics especially with dynamical mass generation. In passing, we studied the parameter dependence of certain features of the QMM phase diagram, revealing some simple relations between the vacuum properties and

the phase transition. These relations provide simple tools, which can be used on the one hand to specifically manipulate the model and thus make desired features show up in the phase diagram or, on the other hand, to manifest the limitations of the QMM.

A. Conventions and acronyms

A.1. Units

Throughout this work, exclusively natural units are used in which

$$c = \hbar = k_B = 1. \tag{A.1.1}$$

In the electromagnetic sector, HEAVISIDE-LORENTZ units are used in which

$$e^2 = 4\pi\alpha\hbar c, \tag{A.1.2}$$

$$\stackrel{(A.1.1)}{=} 4\pi\alpha. \tag{A.1.3}$$

A.2. Conventions

- If not stated otherwise, the EINSTEIN sum convention is applied, *i.e.* we implicitly sum over each pair of identical indices one of which must be covariant and the other one contravariant.
- For the MINKOWSKI metric the following sign convention is used :

$$g_{\mu\nu} = \text{diag}(1, -1, -1, -1). \tag{A.2.1}$$

- The LEVI-CIVITA symbol is defined with $\epsilon^{0123} = +1$.
- The prefactor in the definition of the (n -dimensional) FOURIER transform is chosen such that the FOURIER transform is unitary, and the prefactor is real and positive (see Appendix B), *i.e.* $C_n = (2\pi)^{-n/2}$.
- The matrix γ^5 is defined with the following sign: $-1/4!\sqrt{|\det g|}\epsilon_{\mu\nu\rho\kappa}\gamma^\mu\gamma^\nu\gamma^\rho\gamma^\kappa$.

- The invariant matrix elements $\mathcal{M}_{i \rightarrow f}$ for scatterings from initial states $|i\rangle$ into final states $|f\rangle$ are connected to the corresponding T matrix element T_{fi} according to $T_{fi} = (2\pi)^4 \delta^{(4)}(P_f - P_i) \mathcal{M}_{i \rightarrow f}$ with the total momenta of the initial and final states denoted by P_i and P_f , respectively.

A.3. Acronyms and shortcuts

AGS	Alternating Gradient Synchrotron	Former storage ring at the BNL , now a injector for the RHIC ; operating time: 1960 - today.
ALEPH	Apparatus for LEP PHysics	Collider experiment at the LEP at the CERN ; operating time: 1989 - 2000.
ALICE	A Large Ion Collider Experiment	Collider experiment at the LHC dedicated to heavy-ion collisions; operating time: 2010 - today.
BCS	Bardeen Cooper Schrieffer (theory)	Theory for conventional (type I) superconductors, which explains superconductivity by pairing of electrons.
BEVALAC	merged from BEVATRON and (Super) HILAC	Accelerator at the LBL ; operating time: 1971 - 1993.
BNL	Brookhaven National Laboratory	Accelerator center on Long Island, New York, USA.
CBM	Compressed Baryonic Matter	Fixed target experiment at the FAIR facility; under construction .
CEP	Critical End Point	Ending point of a curve of first-order phase transitions.
CERES	ChErenkov Ring Electron Spectrometer	Fixed target experiment at the SPS ; operating time: 1992 - 2000.
CERN	Conseil Européen pour la Recherche Nucléaire	European center for nuclear research; Geneva, Switzerland.
CFL	Color Flavor Locked (phase)	High density phase of strongly interacting matter. The relevant degrees of freedom are COOPER-pairs of quarks with a combined flavor and color symmetry.

CJT	C ornwall J ackiw T omboulis (formalism)	
χ PT	Chiral Perturbation Theory	Effective theory being the result of a systematic expansion of QCD <i>w.r.t.</i> the (light) quark masses.
CMS	C enter of M ass S ystem	
DLS	DiLepton Spectrometer	Fixed target experiment at the BE-VALAC ; operating time: 1986 - 1993.
EoS	E quation of S tate	Thermodynamic relation between derivatives of the thermodynamic potential and certain thermodynamic quantities. In context of ultrarelativistic hydrodynamics often $e = e(p)$ is meant.
FAIR	F acility for A ntiproton and I on R esearch	Accelerator complex at the GSI Helmholtz-Center for Heavy Ion Research; under construction .
FOPT	F irst- O der P hase T ransition	
FRG	F unctional R enormalization G roup	
FWHM	F ull W idth at H alf M aximum	
HADES	H igh- A cceptance D i E lectron S pectrometer	Fixed target experiment at the SIS18 accelerator; operating time: 2004 - today.
HELIOS-3	H igh E nergy L epton and I On S pectrometer - 3	Fixed target experiment at the SPS accelerator, Synonym: NA34-3; operating time: 1988 - 1990.
HIC	H eavy I on C ollision	
HTL	H ard T hermal L oop	Refers to the approximation and resummation scheme developed by Braaten and Pisarski, <i>cf.</i> [BP90].
IR	I nfra R ed	Here: the $\omega \rightarrow 0$ limit
JINR	J oint I nstitute for N uclear R esearch	Russian center for nuclear research; Dubna, Russia.
J-PARC	J apan P roton A ccelerator R esearch C omplex	Japanese center for nuclear research; Tōkai, Japan.

LBL	Lawrence Berkeley National Laboratory	Research center in Berkeley, California, USA.
LEP	Large Electron-Positron collider	Accelerator for electrons and positrons at the CERN ; operating time: 1989 - 2000.
LHC	Large Hadron Collider	Accelerator at the CERN ; operating time: 2009 - today.
LSM	Linear Sigma Model	Field theoretical model for studying the spontaneous chiral symmetry breaking or restoration.
LFA	Linearized Fluctuation Approximation	Approximation scheme applied in this thesis to the QMM .
MFA	Mean Field Approximation	
MPD	Multi Purpose Detector	Future experiment at the NICA accelerator complex; under construction .
NA##	North Area ##	Shortcut for the experiments (distinguished by the number following the letters) located at the northern experimental side at the SPS .
NICA	Nuclotron-based Ion-Collider Facility	Planned accelerator at the JINR ; under construction .
OPAL	Omni-Purpose Apparatus at LEP	Collider experiment at the LEP ; operating time: 1989 - 2000.
QCD	Quantum Chromodynamics	theory of the strong interaction, one of the building blocks of the Standard Model of particle physics.
QED	Quantum Electrodynamics	Quantum theory of electromagnetism.
QGP	Quark Gluon Plasma	high temperature phase of the QCD matter. The relevant degrees of freedom are quarks and gluons.
QMM	Quark Meson Model	Field theoretical model for studying the spontaneous chiral symmetry breaking or restoration.
PHENIX	Pioneering High Energy Nuclear Interaction eXperiment	Collider experiment at the RHIC ; operating time: 2000 - today.
PHSD	Parton Hadron String Dynamics	Microscopic transport model often applied to HICs .

PNG	P seudo N AMBU- G OLDSTONE (phase)	Phase with the NAMBU GOLDSTONE realization of the approximate symmetry, <i>i.e.</i> the conserved charges do not annihilate the thermal equilibrium state, <i>i.e.</i> phase with spontaneously broken approximate symmetry
PWW	P seudo W IGNER- W EYL (phase)	Phase with the WIGNER WEYL realization of the approximate symmetry, <i>i.e.</i> the conserved charges annihilate the thermal equilibrium state, <i>i.e.</i> phase with approximately restored symmetry.
RFH	R est F rame of the H eat bath	
RHIC	R elativistic H eavy I on C ollid- er	Accelerator at the BNL ; operating time: 2000 - today.
SIS	S chwer- I onen S ynchrotron	Accelerator at the GSI Helmholtz-Center for Heavy Ion Research, the number following this shortcut specifies the magnetic rigidity and is used to discriminate different upgrades of the machine.
SPS	S uper P roton S ynchrotron	Storage ring at the CERN , now a injector into the LHC; operating time: 1976 - today.
STAR	S olenoidal T racker A t R HIC	Collider experiment at the RHIC accelerator; operating time: 2000 - today.
UrQMD	U ltrarelativistic Q uantum M olecular D ynamics model	Microscopic transport model often applied to HICs .
VMD	V ector M eson D ominance	Refers to the (phenomenological) assumption that the photon emission is dominated by conversions from vector mesons into photons.
WA##	W est A rea ##	Shortcut for the experiments (distinguished by the number following the letters) located at the western experimental side at the SPS .

B. Useful identities

B.1. Functional calculus

B.1.1. Continuum limit

Several times in this work, functional traces or determinants have to be evaluated. Since they are defined as special limits of their finite dimensional counterparts a precise understanding of the relation of these functions and matrices is required. In this section, the question: “What is the relation of a function $k(x, y)$ and the matrix K , if both are representing the same quantity?” is addressed. For simplicity, this matter is discussed in one dimension. Nevertheless, the results are easily generalized. Obviously for a finite spatial grid (with step size $\epsilon = L/(N - 1)$, where L is the total length of the system and N the number of grid points) $x_n = a + n\epsilon$, $y_m = a + m\epsilon$ the function k evaluated at the grid points form a matrix with matrix elements $k(x_n, y_m)$. The product of two of such matrices k_m^n, f_r^m equals then

$$h(x_n, z_r) = \sum_m k(x_n, y_m) \cdot f(y_m, z_r). \quad (\text{B.1.1})$$

In order for this to have a finite limit $N \rightarrow \infty$, each summand has to be multiplied by a factor ϵ . If we define therefore the corresponding matrix to be $K_{nm} := \epsilon k(x_n, y_m)$ then in the continuum limit a matrix product KF corresponds to

$$h(x, z) = \int dy k(x, y) f(y, z). \quad (\text{B.1.2})$$

Consistent with this definition for continuum matrix multiplication is the following scalar product $\langle \cdot, \cdot \rangle$:

$$\langle V, U \rangle := (V_n^*)U^n = \sum_n v^*(x_n)\sqrt{\epsilon}u(x_n)\sqrt{\epsilon} \rightarrow \int dx v^*(x)u(x). \quad (\text{B.1.3})$$

The complex conjugation of the first argument ensures that the product of a vector with itself yields a non-negative real number. The factors of $\sqrt{\epsilon}$ are necessary, because the direct product of two vectors is a matrix which corresponds to function of two variables multiplied by the step size ϵ .

A scalar product can also be written as the trace of the direct product of the two vectors. Thus the trace can be consistently defined as

$$\text{Tr} [U \circ V^\dagger] = V^\dagger U = \langle V, U \rangle \rightarrow \int dx v^*(x)u(x) \quad (\text{B.1.4})$$

which can be generalized by replacing the special matrix UV^\dagger with an arbitrary matrix M and correspondingly $v^*(x)u(y)$ into the function $m(x, y)$ ¹ yielding

$$\text{Tr} M \rightarrow \int dx m(x, x). \quad (\text{B.1.5})$$

B.1.2. FOURIER transform

There is an arbitrariness in defining the FOURIER transform F of a function f in n dimensions concerning the prefactor C_n of the integral:

$$\tilde{f}(p) := F_{c,n}[f](p) := C_n \int f(x)e^{ipx} d^n x \quad (\text{B.1.6})$$

with the inverse transformation

$$F_{c,n}^{-1}[\tilde{f}](x) := \frac{1}{C_n(2\pi)^n} \int \tilde{f}(q)e^{-iqx} d^n q. \quad (\text{B.1.7})$$

¹ This follows from replacing U and V with basis elements b_i and b_j of the vector space in which U and V “live”. The set of all possible combinations $b_i \circ b_j$ constitute a basis of the space of all quadratic matrices M of corresponding size. Applying the linearity of the trace the above statement then follows.

One particular useful choice for the constant C_n is such that the transformation is unitary, *i.e.*

$$F_{c,n}^\dagger[\tilde{f}](x) = C_n^* \int f(x) e^{-ipx} d^n x \stackrel{!}{=} F_{c,n}^{-1}[\tilde{f}] \quad (\text{B.1.8})$$

leading to

$$|C_n| = (2\pi)^{-n/2}. \quad (\text{B.1.9})$$

A convenient choice is then further demanding C_n to be real and positive. The advantage of a unitary FOURIER transform is that for such a choice a functional determinant is unchanged when the corresponding fields are transformed from configuration to momentum space.

B.1.3. Functional traces

When evaluating a Gaussian path integral $I = \int \mathcal{D}\phi \exp\{-\int dx \int dy \phi(x) A(x, y) \phi(y)\}$ the result is most easily expressed in form of a functional determinant, which, in turn, can be expressed with the help of $\ln \det A = \text{Tr} \ln A$ as a functional trace. In Chapter 4, such a functional trace is then absorbed into the interaction potential. However, in order for this to be mathematically well defined the trace has to be transformed into momentum space.² In this section the central equality

$$\text{Tr} M = \text{Tr} \tilde{M} \quad (\text{B.1.10})$$

with the functional matrices M and \tilde{M} being related by FOURIER transform and $C \equiv C_4$ being the prefactor in the definition of the FOURIER transform (B.1.6) is demonstrated.

With the same reasoning as in Section B.1.1 it is sufficient to show (B.1.10) for matrices of the form

$$M = U \circ V^\dagger. \quad (\text{B.1.11})$$

² This transformation does not have to be done at precisely this point in the calculation, but since the function $A(x, y)$ corresponds to the kinetic operator, it is fixed by the definition of the Lagrangian, which is done in configuration space. The final result however, is represented by a momentum integral. Therefore, the FOURIER transformation has to be done at some point in the calculation.

Applying the functional representations for U, V according to Section B.1.1 one may write

$$\mathrm{Tr} U \circ V^\dagger = \int d^4x v^*(x)u(x) \quad (\text{B.1.12})$$

$$= \int d^4x C^* \int d^4p \tilde{v}^*(p)e^{-ipx} C \int d^4q \tilde{u}(q)e^{iqx} \quad (\text{B.1.13})$$

$$= C^* C \int d^4p \int d^4q (2\pi)^4 \delta(p - q) \tilde{v}^*(p) \tilde{u}(q) \quad (\text{B.1.14})$$

$$= |C|^2 (2\pi)^4 \int d^4p \tilde{v}^*(p) \tilde{u}(p) \quad (\text{B.1.15})$$

$$= |C|^2 (2\pi)^4 \mathrm{Tr} \tilde{U} \circ \tilde{V}^\dagger, \quad (\text{B.1.16})$$

where the functions $u(x)$ and $v(x)$ were FOURIER transformed according to (B.1.6) and \tilde{U} and \tilde{V} correspond to this functions according to the correspondence outlined in Section B.1.1. If, for the prefactor C_n in the definition of the FOURIER transform, the unitary choice is made (*cf.* (B.1.9)) then (B.1.10) follows immediately.

B.2. Epsilon contraction formulas

Often, products of LEVI-CIVITA symbols occur, which can be simplified considerably by applying the identity [LL80]

$$\epsilon^{\mu\nu\rho\kappa} \epsilon_{\alpha\beta\lambda\eta} = \begin{vmatrix} g_\alpha^\mu & g_\beta^\mu & g_\lambda^\mu & g_\eta^\mu \\ g_\alpha^\nu & g_\beta^\nu & g_\lambda^\nu & g_\eta^\nu \\ g_\alpha^\rho & g_\beta^\rho & g_\lambda^\rho & g_\eta^\rho \\ g_\alpha^\kappa & g_\beta^\kappa & g_\lambda^\kappa & g_\eta^\kappa \end{vmatrix}. \quad (\text{B.2.1})$$

Often, one or several index pairs are contracted, which simplifies (B.2.1) considerably [PS95]:

$$\epsilon^{\mu\nu\rho\kappa} \epsilon_{\kappa\beta\lambda\eta} = g_\beta^\nu g_\lambda^\rho g_\eta^\mu - g_\beta^\nu g_\lambda^\mu g_\eta^\rho - g_\beta^\rho g_\lambda^\nu g_\eta^\mu + g_\beta^\rho g_\lambda^\mu g_\eta^\nu + g_\beta^\mu g_\lambda^\nu g_\eta^\rho - g_\beta^\mu g_\lambda^\rho g_\eta^\nu, \quad (\text{B.2.2})$$

$$\epsilon^{\mu\nu\rho\kappa} \epsilon_{\rho\kappa\lambda\eta} = -2g_\lambda^\mu g_\eta^\nu + 2g_\eta^\mu g_\lambda^\nu, \quad (\text{B.2.3})$$

$$\epsilon^{\mu\nu\rho\kappa} \epsilon_{\nu\rho\kappa\eta} = -6g_\eta^\mu, \quad (\text{B.2.4})$$

$$\epsilon^{\mu\nu\rho\kappa} \epsilon_{\mu\nu\rho\kappa} = -24. \quad (\text{B.2.5})$$

B.3. PAULI matrices

In this thesis, the PAULI matrices never have to be used explicitly. However, occasionally some relations concerning them are very helpful:

$$\left[\tau^a, \tau^b \right] = i \epsilon^{ab}{}_c \tau^c, \quad (\text{B.3.1})$$

$$\left\{ \tau^a, \tau^b \right\} = 2 \delta^{ab} \mathbb{1}, \quad (\text{B.3.2})$$

$$\tau^a \tau^b = i \epsilon^{ab}{}_c \tau^c + \delta^{ab} \mathbb{1}, \quad (\text{B.3.3})$$

$$\text{Tr} \left[\tau^a \right] = 0, \quad (\text{B.3.4})$$

$$\det \tau^a = 1. \quad (\text{B.3.5})$$

B.4. DIRAC matrices

B.4.1. Definition and properties of γ^5

The matrix γ^5 is defined as

$$\gamma^5 := -\frac{1}{4!} \sqrt{\det g} \epsilon_{\mu\nu\rho\kappa} \gamma^\mu \gamma^\nu \gamma^\rho \gamma^\kappa. \quad (\text{B.4.1})$$

Since the calculations in this work are all done in flat space-time (MINKOWSKI or Euclidean) $\epsilon_{\mu\nu\rho\kappa}$ simply denotes the LEVI-CIVITA symbol and not the ϵ tensor of general relativity. We explicitly define γ^5 with the factor of $\sqrt{\det g}$ to make the difference between Euclidean ($\det g = +1$) and MINKOWSKI ($\det g = -1$) space, as well as its invariance under coordinate transformations (especially LORENTZ transformations) apparent.

$$\begin{aligned} (\gamma^5)^2 &= \mathbb{1}, \\ (\gamma^5)^\dagger &= \gamma^5, \end{aligned} \quad (\text{B.4.2})$$

$$\left\{ \gamma^5, \gamma^\mu \right\} = 0.$$

B.4.2. Trace formulas

For completeness, the well known trace formulas [PS95, Ynd06, Sre07] for products of γ -matrices are collected here:

$$\text{Tr}_{\text{Dirac}} \left[\text{odd number of } \gamma\text{'s} \right] = 0, \quad (\text{B.4.3})$$

$$\mathrm{Tr}_{\mathrm{Dirac}} \left[\gamma^\mu \gamma^\nu \right] = 4g^{\mu\nu}, \quad (\text{B.4.4})$$

$$\mathrm{Tr}_{\mathrm{Dirac}} \left[\gamma^\mu \gamma^\nu \gamma^\rho \gamma^\kappa \right] = 4g^{\mu\nu} g^{\rho\kappa} - 4g^{\mu\rho} g^{\nu\kappa} + 4g^{\mu\kappa} g^{\nu\rho}, \quad (\text{B.4.5})$$

$$\mathrm{Tr}_{\mathrm{Dirac}} \gamma^5 = 0, \quad (\text{B.4.6})$$

$$\mathrm{Tr}_{\mathrm{Dirac}} \left[\gamma^5 \gamma^\mu \gamma^\nu \right] = 0, \quad (\text{B.4.7})$$

which can be derived by successive use of the anti-commutation relations for the DIRAC matrices and the cyclicity of the trace. Another useful formula is the trace of a product of four DIRAC matrices and one γ^5 . If there is a pair of identical indices, the corresponding matrices can be anti-commuted next to each other giving twice the unity matrix and thus reducing the trace to (B.4.7). In order not to vanish all indices must be different, but in this case all matrices anti-commute (at least if the metric is diagonal, which is true for our purpose), which means that the trace must be a multiple of the LEVI-CIVITA symbol, *i.e.* $\mathrm{Tr} \left[\gamma^\mu \gamma^\nu \gamma^\rho \gamma^\kappa \gamma^5 \right] = C \epsilon^{\mu\nu\rho\kappa}$. Equations (B.2.5), (B.4.1) and (B.4.2) then yield:

$$C \sqrt{\det g} = -\frac{1}{4!} \sqrt{\det g} \epsilon_{\mu\nu\rho\kappa} \mathrm{Tr}_{\mathrm{Dirac}} \left[\gamma^\mu \gamma^\nu \gamma^\rho \gamma^\kappa \gamma^5 \right] \quad (\text{B.4.8})$$

$$= \mathrm{Tr}_{\mathrm{Dirac}} (\gamma^5)^2 = 4, \quad (\text{B.4.9})$$

$$\Rightarrow \mathrm{Tr}_{\mathrm{Dirac}} \left[\gamma^\mu \gamma^\nu \gamma^\rho \gamma^\kappa \gamma^5 \right] = \frac{4}{\sqrt{\det g}} \epsilon^{\mu\nu\rho\kappa}. \quad (\text{B.4.10})$$

With the formulas (B.4.2)-(B.4.10), one can show that the set of matrices

$$\frac{1}{2} \mathbb{1}, \frac{1}{2} \gamma^\mu, \frac{1}{4} \left(\gamma^\mu \gamma^\nu - \gamma^\nu \gamma^\mu \right), i \frac{1}{2} \gamma^\mu \gamma^5, \frac{1}{2} \gamma^5 \quad (\text{B.4.11})$$

constitutes an orthogonal basis for the linear space of all 4×4 matrices with the scalar product $\langle A, B \rangle$ being defined as the trace of the matrix product $\mathrm{Tr} [AB]$. With the general decomposition of a matrix (especially a product of three DIRAC matrices) into this basis and formulas (B.4.2)-(B.4.10) one derives the useful identity

$$\gamma^\mu \gamma^\nu \gamma^\rho = 4g^{\mu\nu} \gamma^\rho - 4g^{\mu\rho} \gamma^\nu + 4g^{\nu\rho} \gamma^\mu + i \epsilon^{\mu\nu\rho\kappa} \gamma_\kappa, \quad (\text{B.4.12})$$

which can be used to reduce the product of n DIRAC matrices to a sum of products with $(n-2)$ DIRAC matrices. Equation (B.4.12) along with the epsilon determinant (B.2.1) and the properties of γ^5 collected in (B.4.2) are sufficient to reduce any structure composed of DIRAC matrices into a sum of traces of at most two DIRAC matrices and one γ^5 which afterwards can be evaluated according to Eqs. (B.4.3) – (B.4.7) and simplified by the use of Eqs. (B.2.1) – (B.2.5) [PS95, Ynd06, Das06]. Such a procedure was implemented for

the evaluation of the matrix elements.

B.5. Kinematics of two-particle scatterings

The kinematics of $2 \rightarrow 2$ processes have been worked out in the literature (*cf.* [BK73, IZ05] for extensive discussions). For completeness, we give short derivations of several relations needed in this thesis.

B.5.1. Energies and momenta in the center-of-mass system

Because the MANDELSTAM variables s , t and u are LORENTZ-invariant quantities they can be evaluated in any frame of reference. For convenience, the center of mass system (CMS) is chosen. The incoming particles are indexed with A and B , while the outgoing particles are labeled by 1 and 2. The first goal is the determination of expressions for energies and momenta in the CMS. Energy-momentum conservation in the CMS reads:

$$\begin{pmatrix} E_A + E_B \\ \vec{0} \end{pmatrix} = \begin{pmatrix} E_1 + \sqrt{m_2^2 + |\vec{p}_2|^2} \\ \vec{0} \end{pmatrix} = \begin{pmatrix} \sqrt{s} \\ \vec{0} \end{pmatrix}. \quad (\text{B.5.1})$$

In this section, the MANDELSTAM variables are defined according to

$$s = (p_A + p_B)^2, \quad u = (p_1 - p_A)^2, \quad t = (p_2 - p_A)^2. \quad (\text{B.5.2})$$

Squaring the energy conservation (B.5.1),

$$s = m_1^2 + |\vec{p}_1|^2 + m_2^2 + |\vec{p}_2|^2 + 2\sqrt{m_1^2 + |\vec{p}_1|^2}\sqrt{m_2^2 + |\vec{p}_2|^2}, \quad (\text{B.5.3})$$

leads after a bit of algebra to

$$|\vec{p}_1| = |\vec{p}_2| = \sqrt{\frac{\lambda(s, m_1^2, m_2^2)}{4s}} \quad (\text{B.5.4})$$

with λ defined as in (4.4.10). Analogous for the incoming momenta:

$$|\vec{p}_A| = |\vec{p}_B| = \sqrt{\frac{\lambda(s, m_A^2, m_B^2)}{4s}}. \quad (\text{B.5.5})$$

The corresponding energies $E_i^2 = \vec{p}_i^2 + m_i^2$ ($i \in \{1, 2, A, B\}$) are:

$$\begin{aligned} E_1^2 &= \frac{(s + m_1^2 - m_2^2)^2}{4s}, & E_2^2 &= \frac{(s - m_1^2 + m_2^2)^2}{4s}, \\ E_A^2 &= \frac{(s + m_A^2 - m_B^2)^2}{4s}, & E_B^2 &= \frac{(s - m_A^2 + m_B^2)^2}{4s}. \end{aligned} \quad (\text{B.5.6})$$

B.5.2. Limits for the MANDELSTAM variables

The center of mass energy s has a lower bound:

$$s = (p_A + p_B)^2 = p_A^2 + p_B^2 + 2\sqrt{p_A^2 + |\vec{p}_A|^2}\sqrt{p_B^2 + |\vec{p}_B|^2} - 2\cos(\theta_{AB})|\vec{p}_A||\vec{p}_B| \quad (\text{B.5.7})$$

$$\geq p_A^2 + p_B^2 + 2\sqrt{p_A^2 + |\vec{p}_A|^2}\sqrt{p_B^2 + |\vec{p}_B|^2} - 2|\vec{p}_A||\vec{p}_B| \quad (\text{B.5.8})$$

$$\geq p_A^2 + p_B^2 + 2\sqrt{p_A^2}\sqrt{p_B^2} \quad (\text{B.5.9})$$

$$\geq \left(\sqrt{p_A^2} + \sqrt{p_B^2}\right)^2 = (m_A + m_B)^2, \quad (\text{B.5.10})$$

where θ_{AB} is the angle between the momentum vectors \vec{p}_A and \vec{p}_B and with the equal signs being valid for $|\vec{p}_A| = |\vec{p}_B| = 0$. Energy-momentum conservation dictates $s = (p_1 + p_2)^2$, too, which by an analogous calculation is bounded from below also by

$$s \geq (m_1 + m_2)^2. \quad (\text{B.5.11})$$

Since both inequalities must be fulfilled, one finds as the lower bound

$$s \geq \max\{(m_A + m_B)^2, (m_1 + m_2)^2\}. \quad (\text{B.5.12})$$

For u we find

$$u = (p_1 - p_A)^2 = m_1^2 + m_A^2 - 2E_1E_A + 2\cos(\theta_{1A})|\vec{p}_1||\vec{p}_A|. \quad (\text{B.5.13})$$

Thus, ($|\cos(\theta_{1A})| \leq 1$) u lies within the interval $[u_-, u_+]$ with

$$u_{\pm} = m_1^2 + m_A^2 - 2E_1E_A \pm 2|\vec{p}_1||\vec{p}_A|. \quad (\text{B.5.14})$$

Applying (B.5.6),(B.5.4) and (B.5.5) one finds

$$u_{\pm} = m_1^2 + m_A^2 - \frac{(s + m_1^2 - m_2^2)(s + m_A^2 - m_B^2)}{2s} \pm \frac{1}{2s} \sqrt{\lambda(s, m_1^2, m_2^2)\lambda(s, m_A^2, m_B^2)}. \quad (\text{B.5.15})$$

Analogously, one finds for $t = (p_1 - p_B)^2$

$$t_{\pm} = m_1^2 + m_B^2 - \frac{(s + m_1^2 - m_2^2)(s - m_A^2 + m_B^2)}{2s} \pm \frac{1}{2s} \sqrt{\lambda(s, m_1^2, m_2^2)\lambda(s, m_A^2, m_B^2)}. \quad (\text{B.5.16})$$

Two special cases are of interest: a) $p_1^2 = 0$ and $p_A^2 = p_B^2$ and b) $p_1^2 = 0$ and $p_A^2 = p_2^2$.

case a)

This case is relevant, when particle 1 is a photon, particle 2 is either the sigma meson or the pion with masses m_{σ} and m_{π} , respectively and the incoming particles are a quark-antiquark pair both with masses m_q . In this case, the limits of the MANDELSTAM variables read

$$s_{\min} = \max\{m_{\sigma,\pi}^2, 4m_q^2\}, \quad (\text{B.5.17})$$

$$u_{\pm} = m_q^2 - \frac{s - m_{\sigma,\pi}^2}{2} \pm \frac{1}{2}(s - m_{\sigma,\pi}^2) \sqrt{1 - \frac{4m_q^2}{s}}, \quad (\text{B.5.18})$$

$$t_{\pm} = m_q^2 - \frac{s - m_{\sigma,\pi}^2}{2} \pm \frac{1}{2}(s - m_{\sigma,\pi}^2) \sqrt{1 - \frac{4m_q^2}{s}}. \quad (\text{B.5.19})$$

case b)

This case in turn is relevant, when particle 1 is a photon, particle B is a sigma meson or a pion and particles A and 2 are either a pair of quarks or a pair of antiquarks. Then the limits of the MANDELSTAM variables are

$$s_{\min} = (m_q + m_{\sigma,\pi})^2, \quad (\text{B.5.20})$$

$$u_{\pm} = m_q^2 + \frac{(s + m_q^2 - m_{\sigma,\pi}^2)(s - m_q^2)}{2s} \left(-1 \pm \sqrt{1 - \frac{4sm_q^2}{(s + m_q^2 - m_{\sigma,\pi}^2)^2}} \right), \quad (\text{B.5.21})$$

$$t_{\pm} = m_{\sigma,\pi}^2 + \frac{(s - m_q^2 + m_{\sigma,\pi}^2)(s - m_q^2)}{2s} \left(-1 \pm \sqrt{1 - \frac{4sm_{\sigma,\pi}^2}{(s - m_q^2 + m_{\sigma,\pi}^2)^2}} \right). \quad (\text{B.5.22})$$

B.5.3. Cross section

For $2 \rightarrow 2$ processes, the phase space of the outgoing particles is six-dimensional. Energy-momentum conservation can be applied to execute four of the corresponding momentum integrals. The remaining integrals can be parametrized by a polar and an azimuthal angle of one of the outgoing particles. For processes symmetric to the beam axis (which is true for point-like particles), the result is independent of the polar angle. Thus, the integration over this angle gives just a factor of 2π and the azimuthal angle integration is the only one remaining.

Calling the phase space integral Π_2 , defined according to

$$\Pi_2 := \frac{1}{(2\pi)^6} \int \frac{d^3p_1}{2E_1} \frac{d^3p_2}{2E_3} (2\pi)^4 \delta(s - E_1 - E_2) \delta^3(\vec{p}_{\text{tot}} - \vec{p}_1 - \vec{p}_2), \quad (\text{B.5.23})$$

and calculating in the CMS one obtains with the help of (B.5.4) and (B.5.6) after some algebra

$$\Pi_2 = \frac{\sqrt{\lambda(s, m_1^2, m_2^2)}}{8(2\pi)s} \int_{-1}^1 d \cos \theta. \quad (\text{B.5.24})$$

The azimuthal integration can be expressed in terms of the MANDELSTAM variable t : With the definition of t (see (B.5.2)) and the energies and momenta in the CMS given by eqs. (B.5.4) and (B.5.6) one obtains:

$$t = m_A^2 + m_1^2 - \frac{2}{4s} (s + m_A^2 - m_B^2)(s + m_1^2 - m_2^2) + \frac{2}{4s} \sqrt{\lambda(s, m_A^2, m_B^2) \lambda(s, m_1^2, m_2^2)} \cos \theta, \quad (\text{B.5.25})$$

from which the infinitesimal t -element can be read off:

$$dt = \frac{1}{2s} \sqrt{\lambda(s, m_A^2, m_B^2) \lambda(s, m_1^2, m_2^2)} d \cos \theta. \quad (\text{B.5.26})$$

One obtains for the phase space integral

$$\Pi_2 = \frac{1}{8\pi \sqrt{\lambda(s, m_A^2, m_B^2)}} \int_{t_-}^{t_+} dt. \quad (\text{B.5.27})$$

The (vacuum) cross section is related to the matrix element \mathcal{M} according to [PS95]

$$\sigma = \frac{1}{4E_A E_B |v_A - v_B|} \int \frac{d^3 p_1}{2E_1 (2\pi)^3} \frac{d^3 p_2}{(2\pi)^3 2E_2} (2\pi)^4 \delta^{(4)}(p_A + p_B - p_1 - p_2) |M(s, t)|^2.$$

With the help of (B.5.27) this can be written compactly as

$$\sigma = \frac{1}{4E_A E_B |v_A - v_B|} \Pi_2 |M(s, t)|^2. \quad (\text{B.5.28})$$

In the CMS, the prefactor can be expressed in terms of s :

$$\frac{1}{4E_A E_B |v_A - v_B|} = \frac{1}{2\sqrt{\lambda(s, m_A^2, m_B^2)}}. \quad (\text{B.5.29})$$

Thus, one gets for the cross section:

$$\sigma = \frac{1}{16\pi\lambda(s, m_A^2, m_B^2)} \int_{t_-}^{t_+} |M(s, t)|^2 dt. \quad (\text{B.5.30})$$

C. Calculation of the fermion determinant

C.1. Derivative expansion

C.1.1. Leading order

In the case of a ϕ^4 theory, the method is explained in [Fra85, AF85]. For the reader's convenience it is outlined and applied to the QMM here. The quantity to be approximated is

$$\Omega_{\bar{q}q} = -\text{Tr} \ln \left[(G_{\psi}^0(\sigma, \vec{\pi}))^{-1} \right] \quad (\text{C.1.1})$$

with $(G_{\psi}^0(\sigma, \vec{\pi}))^{-1}$ defined according to (2.1.2). Formally, one can expand

$$\Omega_{\bar{q}q} = -\text{Tr} \ln [i\not{\partial} - g(\sigma + i\gamma^5 \vec{\tau} \vec{\pi})] \quad (\text{C.1.2})$$

$$= -\text{Tr} \ln \left[i\not{\partial} \left(1 - \frac{1}{i\not{\partial}} g(\sigma + i\gamma^5 \vec{\tau} \vec{\pi}) \right) \right] \quad (\text{C.1.3})$$

$$= -\text{Tr} \ln \not{p} - \text{Tr} \ln(1 - \not{p}^{-1} M) \quad (\text{C.1.4})$$

$$\approx -\text{Tr} \ln \not{p} - \text{Tr} [\not{p}^{-1} M] - \frac{1}{2} \text{Tr} [\not{p}^{-1} M \not{p}^{-1} M] - \dots, \quad (\text{C.1.5})$$

were the shortcut $M = g(\sigma + i\gamma^5 \vec{\tau} \vec{\pi})$ is used. Applying $(\not{p})^{-1} = \not{p}/p^2$ and the fact that the trace of an odd number of Dirac matrices vanishes one notes that only powers of $\not{p}^{-1} M \not{p}^{-1} M$ remain in the sum (besides the $\ln \not{p}$ -term). Using

$$\not{p}^{-1} M \not{p}^{-1} M = \frac{\not{p}}{p^2} g(\sigma + i\gamma^5 \vec{\tau} \vec{\pi}) \frac{\not{p}}{p^2} g(\sigma + i\gamma^5 \vec{\tau} \vec{\pi}) \quad (\text{C.1.6})$$

$$= \frac{\not{p}}{p^2} \gamma^\mu g(\sigma - i\gamma^5 \vec{\tau} \vec{\pi}) \frac{p_\mu}{p^2} g(\sigma + i\gamma^5 \vec{\tau} \vec{\pi}) \quad (\text{C.1.7})$$

and

$$\phi(x)p_\mu = p_\mu\phi(x) + [\phi(x), p_\mu] = p_\mu\phi(x) - i\partial_\mu\phi(x), \quad (\text{C.1.8})$$

for any field $\phi(x)$ one arrives at

$$\begin{aligned} \not{p}^{-1}M\not{p}^{-1}M &= \frac{\not{p}}{p^2}\not{p}g(\sigma - i\gamma^5\vec{\tau}\vec{\pi})\frac{1}{p^2}g(\sigma + i\gamma^5\vec{\tau}\vec{\pi}) \\ &\quad - i\frac{\not{p}}{p^2}\left(\not{p}g(\sigma - i\gamma^5\vec{\tau}\vec{\pi})\right)\frac{1}{p^2}g(\sigma + i\gamma^5\vec{\tau}\vec{\pi}). \end{aligned} \quad (\text{C.1.9})$$

Employing the operator identity (for invertible A)

$$[A^{-1}, B] = -A^{-2}[A, B] - A^{-3}[A, [A, B]] - A^{-4}[A, [A, [A, B]]] - \dots \quad (\text{C.1.10})$$

with $A = p^2$ and $B = \sigma, \pi$ the $1/p^2$ term in (C.1.9) can be commuted to the left. The nested commutators in (C.1.10) are computed by utilizing recursively the identity

$$[p^2, \phi] = \square\phi + 2ip^\mu\partial_\mu\phi. \quad (\text{C.1.11})$$

Inspecting (C.1.11) one sees that each commutator with p^2 contributes at least one derivative of ϕ leading to the observation that terms in (C.1.10) with n commutators imply at least n derivatives of the meson fields. Thus, one finds

$$[p^{-2}, \sigma \text{ or } \pi] = 0 + \mathcal{O}(\partial\sigma, \partial\vec{\pi}), \quad (\text{C.1.12})$$

leading to

$$\not{p}^{-1}M\not{p}^{-1}M = \frac{1}{p^2}g(\sigma - i\gamma^5\vec{\tau}\vec{\pi})g(\sigma + i\gamma^5\vec{\tau}\vec{\pi}) + \mathcal{O}(\partial\sigma, \partial\vec{\pi}) \quad (\text{C.1.13})$$

$$= \frac{1}{p^2}m^2 + \mathcal{O}(\partial\sigma, \partial\vec{\pi}) \quad (\text{C.1.14})$$

with $m^2 = g^2(\sigma^2 + \vec{\pi}^2)$. Taking only zero derivative terms, the higher powers of $\not{p}^{-1}M\not{p}^{-1}M$ in the expansion (C.1.5) result in

$$(\not{p}^{-1}M\not{p}^{-1}M)^n = \left(\frac{1}{p^2}\right)^n (m^2)^n \mathbf{1}_D + \mathcal{O}(\partial\sigma, \partial\vec{\pi}) \quad (\text{C.1.15})$$

with $\mathbb{1}_D$ denoting the unity matrix in DIRAC space. Then, the complete expansion (C.1.5) gives

$$\Omega_{\bar{q}q} \approx -\text{Tr} \ln \not{p} - \frac{1}{2} \text{Tr} \left[\frac{m_q^2}{p^2} \mathbb{1}_D \right] - \frac{1}{4} \text{Tr} \left[\left(\frac{m_q^2}{p^2} \right)^2 \mathbb{1}_D \right] - \dots + \mathcal{O}(\partial\sigma, \partial\pi^a). \quad (\text{C.1.16})$$

It can easily be checked that this is exactly the expansion of a noninteracting Fermi gas with mass m

$$-\text{Tr} \ln [\not{p} - m_q] = -\text{Tr} \ln \not{p} - \sum_n \frac{1}{2n} \text{Tr} \left[\left(\frac{m_q^2}{p^2} \right)^n \mathbb{1} \right], \quad (\text{C.1.17})$$

thus verifying (4.2.11).

C.1.2. First-order correction

The evaluation of (C.1.11) to next to leading order gives a correction to (C.1.12):

$$[p^{-2}, \phi] = -\frac{2i}{p^4} p^\mu \partial_\mu \phi + \mathcal{O}((\partial\phi)^2). \quad (\text{C.1.18})$$

Setting

$$B_\pm := (\sigma \pm i\gamma^5 \vec{\tau} \vec{\pi}), \quad (\text{C.1.19})$$

$$A := p^2, \quad (\text{C.1.20})$$

$$B' := \not{\partial}(\sigma - i\gamma^5 \vec{\tau} \vec{\pi}) \quad (\text{C.1.21})$$

makes the structure of (C.1.9) apparent

$$\not{p}^{-1} M \not{p}^{-1} M = g^2 \not{p} A^{-1} \not{p} B_- A^{-1} B_+ - i g^2 \not{p} A^{-1} B' A^{-1} B_+. \quad (\text{C.1.22})$$

Commuting B and A^{-1} in the first term and A^{-1} and B' in the second moves all momentum dependent terms to the left and all space-time dependent terms to the right. The necessary relations up to first order in the derivatives are

$$B_- A^{-1} = A^{-1} B_- + \frac{2i}{p^4} p^\mu \partial_\mu B_- + \mathcal{O}(\partial^2), \quad (\text{C.1.23})$$

$$B' A^{-1} = A^{-1} B' + \mathcal{O}(\partial^2). \quad (\text{C.1.24})$$

Applying this to (C.1.9) yields

$$\not{p}^{-1}M\not{p}^{-1}M = g^2\not{p}A^{-1}\not{p}\left(A^{-1}B_- + \frac{2i}{p^4}p^\mu\partial_\mu B_-\right)B_+ - ig^2\not{p}A^{-2}B'B_+ + \mathcal{O}(\partial^2) \quad (\text{C.1.25})$$

$$= g^2\not{p}^2A^{-2}B_-B_+ + g^2\frac{2i}{p^6}p^\mu\not{p}^2\partial_\mu B_-B_+ - ig^2\not{p}A^{-2}B'B_+ + \mathcal{O}(\partial^2) \quad (\text{C.1.26})$$

$$= g^2\mathbb{1}_D A^{-1}(\sigma^2 + (\vec{\tau}\vec{\pi})^2) + g^2\frac{2i}{p^4}p^\mu\mathbb{1}_D(\partial_\mu B_-)B_+ - ig^2\not{p}A^{-2}B'B_+ + \mathcal{O}(\partial^2) \quad (\text{C.1.27})$$

$$= g^2\mathbb{1}_D A^{-1}(\sigma^2 + \vec{\pi}^2) + g^2\frac{i}{p^4}\left(2p^\mu\mathbb{1}_D - \not{p}\gamma^\mu\right)(\partial_\mu B_-)B_+ + \mathcal{O}(\partial^2) \quad (\text{C.1.28})$$

$$= g^2\mathbb{1}_D A^{-1}(\sigma^2 + \vec{\pi}^2) + g^2\frac{i}{p^4}\gamma^\mu\not{p}(\partial_\mu B_-)B_+ + \mathcal{O}(\partial^2). \quad (\text{C.1.29})$$

Applying $m^2 = g^2(\sigma^2 + \vec{\pi}^2)$ and introducing the shortcut $b' := g^2ip^{-4}\gamma^\mu\not{p}(\partial_\mu B_-)B_+$ one obtains

$$\not{p}^{-1}M\not{p}^{-1}M = \mathbb{1}_D\frac{m^2}{p^2} + b' + \mathcal{O}(\partial^2). \quad (\text{C.1.30})$$

In (C.1.5), the n -th power of this is needed. Expanding $(\not{p}^{-1}M\not{p}^{-1}M)^n$ up to first order in the derivative yields (note from its definition that b' is first order in the derivatives)

$$\left(\not{p}^{-1}M\not{p}^{-1}M\right)^n = \left(\mathbb{1}_D\frac{m^2}{p^2}\right)^n + n\left(\mathbb{1}_D\frac{m^2}{p^2}\right)^{n-1}b' + \mathcal{O}((b')^2) \quad (\text{C.1.31})$$

$$= \left(\frac{m^2}{p^2}\right)^n\mathbb{1}_D + n\left(\frac{m^2}{p^2}\right)^{n-1}b' + \mathcal{O}((b')^2). \quad (\text{C.1.32})$$

This is to be inserted into (C.1.5)

$$\Omega_{\bar{q}q} \approx -\text{Tr} \ln \not{p} - \text{Tr} \left[\sum_{n=1}^{\infty} \frac{1}{2n} (\not{p}^{-1}M\not{p}^{-1}M)^n \right] \quad (\text{C.1.33})$$

$$= -\text{Tr} \ln \not{p} - \text{Tr} \left[\sum_{n=1}^{\infty} \frac{1}{2n} \left(\frac{m^2}{p^2}\right)^n \mathbb{1}_D + \frac{1}{2n} n \left(\frac{m^2}{p^2}\right)^{n-1} b' \right] + \mathcal{O}((b')^2) \quad (\text{C.1.34})$$

$$= -\text{Tr} \ln \not{p} - \text{Tr} \left[\sum_{n=1}^{\infty} \frac{1}{2n} \left(\frac{m^2}{p^2}\right)^n \mathbb{1}_D \right] - \frac{1}{2} \text{Tr} [b'] \sum_{n=0}^{\infty} \left(\frac{m^2}{p^2}\right)^n + \mathcal{O}(b'^2). \quad (\text{C.1.35})$$

The first two terms yield the leading order result, while the third trace is the first-order correction in the form of a geometric series:

$$\Omega_{\bar{q}q} = -\text{Tr} \ln \left[\not{p} - \tilde{m} \right] \Bigg|_{\tilde{m}=m} - \frac{1}{2} \text{Tr} [b'] \frac{p^2}{p^2 - m^2} + \mathcal{O}(b'^2). \quad (\text{C.1.36})$$

The DIRAC part of the b' trace can be executed with the result

$$\Omega_{\bar{q}q} = -\text{Tr} \ln \left[\not{p} - \tilde{m} \right] \Bigg|_{\tilde{m}=m} - \frac{1}{2} \text{Tr} [b'] \frac{p^2}{p^2 - m^2} + \mathcal{O}(b'^2) \quad (\text{C.1.37})$$

$$\begin{aligned} &= -\text{Tr} \ln \left[\not{p} - \tilde{m} \right] \Bigg|_{\tilde{m}=m} - 2g^2 i \text{Tr} \frac{p^\mu}{p^2} \frac{1}{p^2 - m^2} [\sigma \partial_\mu \sigma \mathbb{1}_{2 \times 2} + \tau^a \tau^b \pi_a \partial_\mu \pi_b] \\ &\quad + \mathcal{O}(b'^2). \end{aligned} \quad (\text{C.1.38})$$

Applying (B.3.3) and evaluating the flavor trace yields

$$\Omega_{\bar{q}q} = -\text{Tr} \ln \left[\not{p} - \tilde{m} \right] \Bigg|_{\tilde{m}=m} - 4g^2 i \text{Tr} \frac{p^\mu}{p^2} \frac{1}{p^2 - m^2} [\sigma \partial_\mu \sigma + \vec{\pi} \partial_\mu \vec{\pi}] + \mathcal{O}(b'^2) \quad (\text{C.1.39})$$

$$= -\text{Tr} \ln \left[\not{p} - \tilde{m} \right] \Bigg|_{\tilde{m}=m} - 2i \text{Tr} \frac{p^\mu}{p^2} \frac{1}{p^2 - m^2} \partial_\mu m^2 + \mathcal{O}(b'^2). \quad (\text{C.1.40})$$

It is satisfying that the second term indeed is a small correction if the meson fields (and thus m^2) are only slowly varying.

D. Inverting perturbed matrices

We apply

$$M^{-1} = M_0^{-1} \sum_{n=0}^{\infty} (-\Delta_M M_0^{-1})^n, \quad M = M_0 + \Delta_M \quad (\text{D.1.1})$$

valid for invertible matrices M and M_0 . A heuristic derivation of (D.1.1) can be obtained by noting

$$M^{-1} = (M_0 + \Delta_M)^{-1} = M_0^{-1} (1 - (-M_0 \Delta_M))^{-1} \quad (\text{D.1.2})$$

which is then written as a geometric series, leading to (D.1.1). With $M_b^a \equiv M(x_a, x_b)$ this relations can be reformulated for the continuum limit in the language of functional derivatives with the only changes being $\partial/\partial\phi_i \rightarrow \delta/\delta\phi(x)$ and the matrix multiplication replaced by an integral $A_b^a B_c^b \rightarrow \int db A(x_a, b) B(b, x_c)$.

Application to the photon propagator

Setting in (D.1.1) $M(z, z') \equiv ((G_\gamma^0)_{\mu\nu}(z, z'))^{-1} = M_0(z, z') + \Delta M(z, z')$ with $M_0(z, z') = \overline{G}_{\mu\nu}^\gamma(z, z')^{-1}$ and $\Delta M(z, z') = [-e^2 \pi^+(z) \pi^-(z) g_{\mu\nu}] \delta(z - z')$ one gets

$$(G_\gamma^0)_{\mu\nu}(z, z') = \overline{G}_{\mu\nu}^\gamma + \int d^4x \overline{G}_{\mu\rho}^\gamma(z, x) [e^2 \pi^+(x) \pi^-(x) g^{\rho\kappa}] \overline{G}_{\kappa\nu}^\gamma(x, z') + \mathcal{O}(e^4), \quad (\text{D.1.3})$$

which is applied in (4.2.28).

Application to the quark propagator

Setting $M(z, z') \equiv ((G_q^0)_{\sigma, \pi}(z, z'))^{-1}$, $M_0(z, z') = (G_q^0)_{v,0}(z, z')^{-1}$ and $\Delta M = [-g\Delta(z) - gi\gamma^5\tau_a\pi^a(z)]\delta(z - z')$ one obtains

$$\begin{aligned} (G_q^0)_{\sigma, \pi}(z, z') &= (G_q^0)_{v,0}(z, z') - \int d^4x (G_q^0)_{v,0}(z, x) A(x) (G_q^0)_{v,0}(x, z') \\ &\quad - \iint d^4x d^4y (G_q^0)_{v,0}(z, x) A(x) (G_q^0)_{v,0}(x, y) A(y) (G_q^0)_{v,0}(y, z') \\ &\quad - \iint d^4x d^4y (G_q^0)_{v,0}(z, y) A(y) (G_q^0)_{v,0}(y, x) A(x) (G_q^0)_{v,0}(x, z') \\ &\quad + \mathcal{O}(\Delta^3, \vec{\pi}^3), \end{aligned} \tag{D.1.4}$$

$$A(z) = -g\Delta(z) - gi\gamma^5\tau_a\pi^a(z). \tag{D.1.5}$$

Replacing on both sides of the equation $\Delta(z)$ by $\delta/\delta\eta_\sigma(z)$ and $\pi^a(z)$ by $\delta/\delta\eta_{\pi^a}(z)$ one arrives at

$$\begin{aligned} \widehat{(G_q^0)}_{\sigma, \pi}(z, z') &= (G_q^0)_{v,0}(z, z') - \int d^4x (G_q^0)_{v,0}(z, x) \hat{A}(x) (G_q^0)_{v,0}(x, z') \\ &\quad - \iint d^4x d^4y (G_q^0)_{v,0}(z, x) \hat{A}(x) (G_q^0)_{v,0}(x, y) \hat{A}(y) (G_q^0)_{v,0}(y, z') \\ &\quad - \iint d^4x d^4y (G_q^0)_{v,0}(z, y) \hat{A}(y) (G_q^0)_{v,0}(y, x) \hat{A}(x) (G_q^0)_{v,0}(x, z') \\ &\quad + \mathcal{O}\left(\frac{\delta^3}{\delta\eta_\sigma^3}, \frac{\delta^3}{\delta\eta_\pi^3}\right), \end{aligned} \tag{D.1.6}$$

$$\hat{A}(z) = -g\frac{\delta}{\delta\eta_\sigma(z)} - gi\gamma^5\tau_a\frac{\delta}{\delta\eta_{\pi^a}(z)}, \tag{D.1.7}$$

which is used in Section 4.3.

E. Thermodynamic formulas in LFA

In this appendix, the formulas for thermodynamic quantities within the LFA are collected (see [MME04] for a detailed derivation). First, the set of equations which determines self consistently the meson masses and the thermal expectation value v of the sigma field is given. Given these, the thermodynamic quantities can be calculated applying a field averaging procedure:

$$m_\sigma^2 = 2\lambda v^2 + g^2 \left\langle \left(\frac{\Delta}{\langle \Delta^2 \rangle} - \frac{1}{v} \right) (v + \Delta) A(m^2) \right\rangle + \frac{H}{v}, \quad (\text{E.1.1})$$

$$m_\pi^2 = 2\lambda \left(\frac{1}{3} \langle \pi^2 \rangle - \langle \Delta^2 \rangle \right) + g^2 \left\langle \left(\frac{\pi^2}{\langle \pi^2 \rangle} - \frac{v + \Delta}{v} \right) A(m^2) \right\rangle + \frac{H}{v}, \quad (\text{E.1.2})$$

$$0 = g^2 \langle (v + \Delta) A(m^2) \rangle + \lambda v (v^2 + 3 \langle \Delta^2 \rangle + \langle \pi^2 \rangle - \zeta) - H, \quad (\text{E.1.3})$$

$$\langle \Delta^2 \rangle = F_\sigma^{\text{vac}} + \frac{1}{2\pi^2} \int d|\vec{p}| \frac{|\vec{p}|^2}{E_p^\sigma} n_B(E_p^\sigma), \quad (\text{E.1.4})$$

$$\langle \pi^2 \rangle = F_\pi^{\text{vac}} + \frac{1}{2\pi^2} \int d|\vec{p}| \frac{|\vec{p}|^2}{E_p^\sigma} n_B(E_p^\sigma), \quad (\text{E.1.5})$$

$$A(m^2) = F_q^{\text{vac}} + \frac{2N_f N_c}{2\pi^2} \int d|\vec{p}| \frac{|\vec{p}|^2}{E_p^q} (n_F(E_p^q) - n_{\bar{F}}(E_p^q)). \quad (\text{E.1.6})$$

The thermal averaging $\langle f(\sigma, |\vec{\pi}|) \rangle$ is done according to (4.2.27). The vacuum fluctuation contributions $F_{\sigma,\pi,q}^{\text{vac}}$ depend on the renormalization scheme. In Tab. E.1, the contributions for two different renormalization schemes as well as the unrenormalized (and hence infinite) term are given. In this thesis, these terms have been ignored, *i.e.* here $F_{\sigma,\pi,q}^{\text{vac}} = 0$.

After solving self consistently the set of equations (E.1.1) – (E.1.6), various thermodynamic quantities can be evaluated:

$$n = \left\langle \frac{1}{(2\pi)^3} \int d^3p (n_F(E_q) - n_{\bar{F}}(E_q)) \right\rangle, \quad (\text{E.1.7})$$

$$(\text{E.1.8})$$

	divergent	here	\overline{MS}	MME
F_q^{vac}	$\frac{2N_f N_c}{(2\pi)^3} \int d^3 p E_q$	0	$-\frac{2N_f N_c}{32\pi^2} m_q^4 \ln \frac{m_q^2}{\mu^2}$	$-\frac{2N_f N_c}{32\pi^2} \left(m_q^4 \ln \frac{m_q^2}{\Lambda^2} + f_{MME}(m_q, \Lambda) \right)$
F_σ^{vac}	$\frac{1}{(2\pi)^3} \int d^3 p \frac{E_\sigma}{2}$	0	$\frac{1}{64\pi^2} m_\sigma^4 \ln \frac{m_\sigma^2}{\mu^2}$	$\frac{1}{64\pi^2} \left(m_\sigma^4 \ln \frac{m_\sigma^2}{\Lambda^2} + f_{MME}(m_\sigma, \Lambda) \right)$
F_π^{vac}	$\frac{3}{(2\pi)^3} \int d^3 p \frac{E_\pi}{2}$	0	$\frac{3}{64\pi^2} m_\pi^4 \ln \frac{m_\pi^2}{\mu^2}$	$\frac{3}{64\pi^2} \left(m_\pi^4 \ln \frac{m_\pi^2}{\Lambda^2} + f_{MME}(m_\pi, \Lambda) \right)$

Table E.1.: Vacuum fluctuation contributions $F_{q,\sigma,\pi}^{\text{vac}}$ within the \overline{MS} renormalization scheme in dimensional regularization (fourth column) and with the renormalization scheme used in [MME04] (rightmost column) using $f_{MME}(m, x) = (3m^2 - x^2)(x^2 - m^2)/2$. The remaining two columns give the unrenormalized expression (second column) and the values used in this thesis (third column).

$$\begin{aligned}
e = & \langle U(v + \Delta, \vec{\pi}) \rangle - \frac{1}{2} m_\sigma^2 \langle \Delta^2 \rangle - \frac{1}{2} m_\pi^2 \langle \boldsymbol{\pi}^2 \rangle + F_\sigma^{\text{vac}} + F_\pi^{\text{vac}} \\
& + \frac{1}{(2\pi)^3} \int d^3 p E_\sigma n_B(E_\sigma) + \frac{3}{(2\pi)^3} \int d^3 p E_\pi n_B(E_\pi) \\
& + \langle F_q^{\text{vac}} \rangle + \frac{2N_f N_c}{(2\pi)^3} \int d^3 p \langle E_q [n_F(E_q) + n_{\bar{F}}(E_q)] \rangle,
\end{aligned} \tag{E.1.9}$$

$$\begin{aligned}
\langle U(v + \Delta, \vec{\pi}) \rangle = & \frac{1}{4} \lambda \left(3 \left(v^2 + \langle \Delta^2 \rangle \right)^2 + \left(v^2 + \langle \boldsymbol{\pi}^2 \rangle \right)^2 + \frac{2}{3} \langle \boldsymbol{\pi}^2 \rangle^2 \right. \\
& \left. + 2 \langle \Delta^2 \rangle \langle \boldsymbol{\pi}^2 \rangle - 2\zeta \left(v^2 + \langle \Delta^2 \rangle + \langle \boldsymbol{\pi}^2 \rangle - \frac{1}{2} \zeta \right) - 3v^4 \right),
\end{aligned} \tag{E.1.10}$$

$$s = \frac{1}{T} (e + p - \mu n). \tag{E.1.11}$$

The quark number susceptibility and the heat capacity are obtained by differentiation of the net quark density and the entropy density, respectively:

$$\chi_{\mu\mu} = \frac{\partial n}{\partial \mu}, \quad \chi_{TT} = \frac{\partial s}{\partial T}. \tag{E.1.12}$$

F. Matrix elements

F.1. FEYNMAN rules

With the generating functional, as derived in Chapter 4, the FEYNMAN rules depicted in Fig. F.1 have to be applied. Vertices and propagators are those derived in Chapter 4. The normalization of the incoming or outgoing particles has to be chosen consistently to the propagators leading to the factors $\sqrt{2}$ for the mesons. With these rules at hand we can write down the formulas for the matrix elements depicted in Fig. 4.3

The MANDELSTAM variables are defined according to:

$$\begin{aligned}
 s &= (p+q)^2 = (k+z)^2 = m^2 + 2pq + q^2 = k^2 + 2kz + m^2, \\
 t &= (z-p)^2 = (q-k)^2 = 2m^2 - 2zp = q^2 - 2qk + k^2, \\
 u &= (k-p)^2 = (z-q)^2 = k^2 - 2kp + m^2 = m^2 - 2zq + q^2.
 \end{aligned}
 \tag{F.1.1}$$

F.2. COMPTON scattering with sigma mesons

There are only two diagrams contributing to the COMPTON process with σ mesons at tree level. Diagrammatically, they are represented by the first two diagrams in the upper row of Fig. 4.3. Applying the FEYNMAN rules depicted in Fig. F.1 one finds the following two expressions:

$$M_{C1} = \bar{u}(z)_{f,s} (-i) g_{1f'} \frac{\not{p} - \not{k} + m}{u - m^2} i e q_f \gamma^\mu \epsilon(k)_\mu^* u(p)^{r,f'} \tag{F.2.1}$$

$$= g e \epsilon(k)_\mu^* q_f \bar{u}(z)_{f,s} \frac{\not{p} - \not{k} + m}{u - m^2} \gamma^\mu u(p)^{r,f}, \tag{F.2.2}$$

$$M_{C2} = g e \epsilon(k)_\mu^* q_f \bar{u}(z)_{f,s} \gamma^\mu \frac{\not{k} + \not{z} + m}{s - m^2} u(p)^{r,f}. \tag{F.2.3}$$

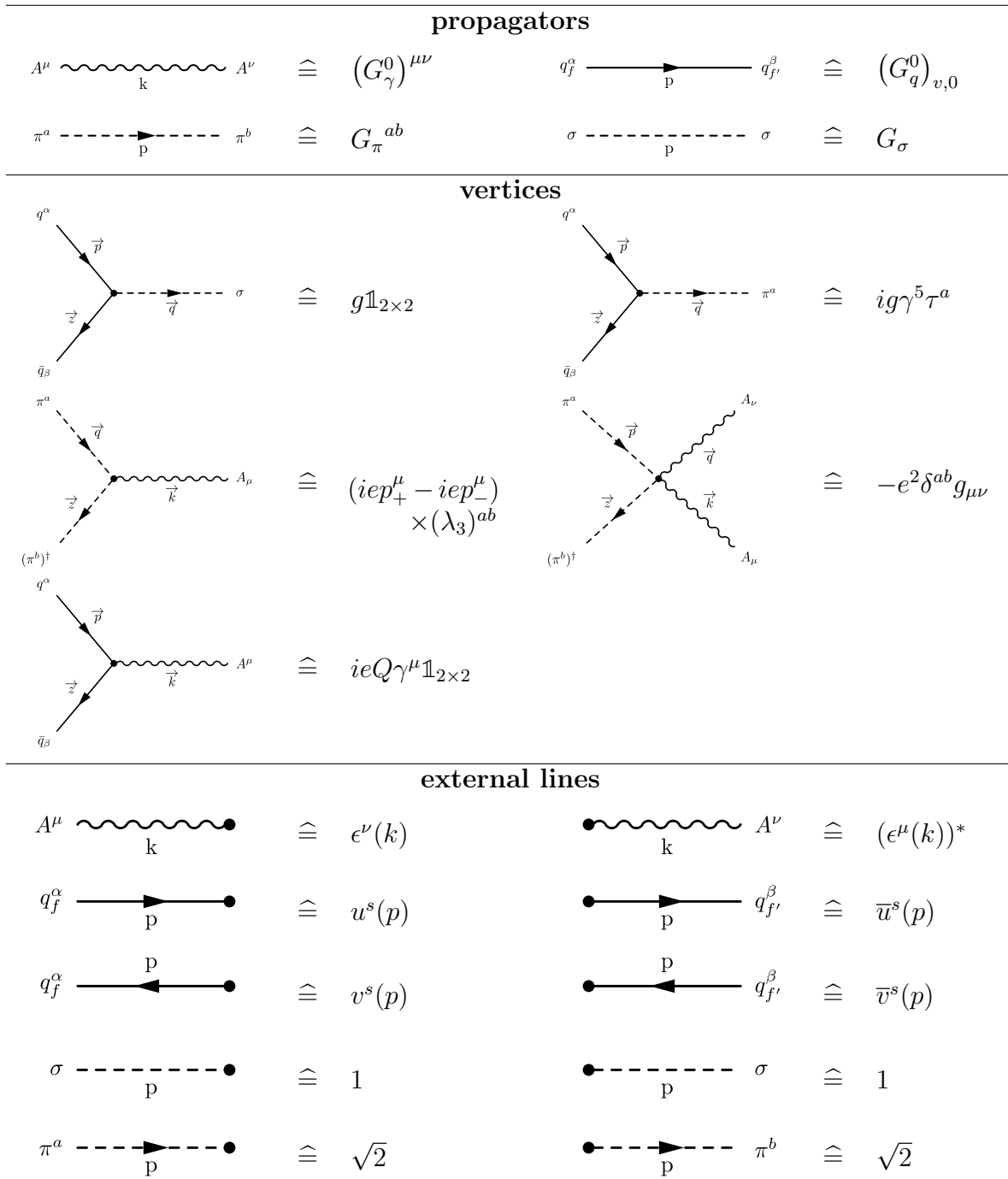


Figure F.1.: Momentum space FEYNMAN rules corresponding to the derivation in Chapter 4. The propagators $(G_\gamma^0)^{\mu\nu}$, $(G_q^0)_{v,0}$, G_π^{ab} and G_σ are those defined in Chapter 4, g and e are the quark-meson and electromagnetic coupling (*cf.* (2.1.1) and (4.1.1)), respectively, Q is the charge operator and τ^a as in (4.1.2). The photon polarization four-vector is denoted by ϵ^μ and the asterisk denotes complex conjugation. At the pion-photon vertex p^+ and p^- are the momenta of the incoming π^+ and π^- meson, respectively and λ_3 is the respective GELL-MANN matrix. The spinors u^s and v^s denote the particle and anti-particle solutions of the DIRAC equation and \bar{u}^s and \bar{v}^s denote the respective DIRAC-adjoint spinors (*cf.* notation in [PS95]).

The matrix elements can be simplified with a bit of Dirac algebra (cf. [PS95]):

$$(\not{p} + m)\gamma^\mu u(p)^{r,f} = 2p^\mu u(p)^{r,f}, \quad (\text{F.2.4})$$

$$u(z)_{f,s}\gamma^\mu(\not{z} + m) = 2u(z)_{f,s}z^\mu \quad (\text{F.2.5})$$

resulting in

$$M_{C1} = ge\epsilon(k)_\mu^* q_f \bar{u}(z)_{f,s} \frac{2p^\mu - \not{k}\gamma^\mu}{u - m^2} u(p)^{r,f}, \quad (\text{F.2.6})$$

$$M_{C2} = ge\epsilon(k)_\mu^* q_f \bar{u}(z)_{f,s} \frac{\gamma^\mu \not{k} + 2z^\mu}{s - m^2} u(p)^{r,f}. \quad (\text{F.2.7})$$

Both contributions are added ($M \equiv M_{C1} + M_{C2}$):

$$M = ge\epsilon(k)_\mu^* q_f \bar{u}(z)_{f,s} \left(\frac{2p^\mu - \not{k}\gamma^\mu}{u - m^2} + \frac{\gamma^\mu \not{k} + 2z^\mu}{s - m^2} \right) u(p)^{r,f}. \quad (\text{F.2.8})$$

The squared and spin-, flavour- and polarisation summed/averaged matrix element then reads:

$$\frac{1}{2} \sum_{r,s,\epsilon,f} |M|^2 = \sum_{r,s,\epsilon,f} ge\epsilon(k)_\mu^* q_f \bar{u}(z)_{f,s} \left(\frac{2p^\mu - \not{k}\gamma^\mu}{u - m^2} + \frac{\gamma^\mu \not{k} + 2z^\mu}{s - m^2} \right) u(p)^{r,f} \quad (\text{F.2.9})$$

$$\begin{aligned} & \times ge\epsilon(k)_\nu q_f \bar{u}(p)_{r,f} \left(\frac{2p^\nu - \not{k}\gamma^\nu}{u - m^2} + \frac{\gamma^\nu \not{k} + 2z^\nu}{s - m^2} \right)^\dagger u(z)^{f,s} \\ & = - \sum_f g^2 (q_f)^2 e^2 g_{\mu\nu} \text{Tr}_{\text{Dirac}} \left[\left(\frac{2p^\mu - \not{k}\gamma^\mu}{u - m^2} + \frac{\gamma^\mu \not{k} + 2z^\mu}{s - m^2} \right) (\not{p} + m) \right. \\ & \quad \left. \times \left(\frac{2p^\nu - \not{k}\gamma^\nu}{u - m^2} + \frac{\gamma^\nu \not{k} + 2z^\nu}{s - m^2} \right) (\not{z} + m) \right] \end{aligned} \quad (\text{F.2.10})$$

$$\begin{aligned} & = - g^2 e^2 \sum_f (q_f)^2 \\ & \quad \times \left(\frac{I}{(u - m^2)^2} + \frac{II}{(s - m^2)^2} + \frac{III + IV}{(u - m^2)(s - m^2)} \right) \end{aligned} \quad (\text{F.2.11})$$

with

$$I = \text{Tr}_{\text{Dirac}} \left[(2p^\mu - \not{k}\gamma^\mu) (\not{p} + m) (2p_\mu - \gamma_\mu \not{k}) (\not{z} + m) \right], \quad (\text{F.2.12})$$

$$II = \text{Tr}_{\text{Dirac}} \left[(\gamma^\mu \not{k} + 2z^\mu) (\not{p} + m) (\not{k}\gamma_\mu + 2z_\mu) (\not{z} + m) \right], \quad (\text{F.2.13})$$

$$III = \text{Tr}_{\text{Dirac}} \left[(2p^\mu - \not{k}\gamma^\mu) (\not{p} + m) (\not{k}\gamma_\mu + 2z_\mu) (\not{z} + m) \right], \quad (\text{F.2.14})$$

$$IV = \text{Tr}_{\text{Dirac}} [(\gamma^\mu \not{k} + 2z^\mu)(\not{p} + m)(2p_\mu - \gamma_\mu \not{k})(\not{z} + m)]. \quad (\text{F.2.15})$$

Applying the procedure outlined in Appendix B.4.2 based on the reduction formula (B.4.12) these traces can be evaluated yielding

$$I = 16p^2 \left((pz) - (kz) + m_q^2 \right) + 16m_q^2 \left(k^2 - (kp) \right) - 16(kp)(kz) + 8k^2(pz), \quad (\text{F.2.16})$$

$$II = 16z^2 \left((kp) + (pz) + m_q^2 \right) + 16m_q^2 \left(k^2 + (kz) \right) - 16(kp)(kz) + 8k^2(pz), \quad (\text{F.2.17})$$

$$\begin{aligned} III &= 16 \left((pz) - (kz) \right) \left((kp) + (pz) \right) \\ &\quad + 8m_q^2 \left((kp) + 2(pz) - (kz) \right) + 8m_q^2 k^2 - 8p^2(kz) + 8(kp)z^2, \end{aligned} \quad (\text{F.2.18})$$

$$IV = III. \quad (\text{F.2.19})$$

These can be rewritten in terms of the MANDELSTAM variables resulting in ($p^2 = z^2 = m_q^2$, $q^2 = m_\sigma^2$, $k^2 = 0$)

$$\begin{aligned} \frac{1}{2} \sum |\mathcal{M}_{q\sigma \rightarrow q\gamma}|^2 &= -\frac{5}{9} g^2 e^2 \left((4m_q^2 - m_\sigma^2) \left(\frac{8m_q^2}{(u - m_q^2)^2} + \frac{8m_q^2}{(s - m_q^2)^2} \right. \right. \\ &\quad \left. \left. + 8 \frac{(2m_q^2 - m_\sigma^2)}{(u - m_q^2)(s - m_q^2)} \right) \right. \\ &\quad \left. + 4 \frac{s + 7m_q^2 - 2m_\sigma^2}{u - m_q^2} + 4 \frac{u + 7m_q^2 - 2m_\sigma^2}{s - m_q^2} + 8 \right) \end{aligned} \quad (\text{F.2.20})$$

for the fully summed and averaged squared matrix element. If we now set the fermion masses zero (*i.e.* in the WIGNER-WEYL phase in the chiral limit), this reduces to

$$\frac{1}{2} \sum |\mathcal{M}_{q\sigma \rightarrow q\gamma}|^2 = -\frac{5}{9} g^2 e^2 \left(8 \frac{m_\sigma^4}{us} + 4 \frac{s - 2m_\sigma^2}{u} + 4 \frac{u - 2m_\sigma^2}{s} + 8 \right). \quad (\text{F.2.21})$$

The annihilation matrix elements are related to the Compton matrix elements by crossing symmetries and can be obtained by $s \leftrightarrow t$.

F.3. COMPTON scattering with pions

The three contributing diagrams for the process $q + \pi \rightarrow q + \gamma$ (upper row in Fig. 4.3) translate into the following expression for the matrix element:

$$M_{C3} = \bar{u}(z)_{f,s} g \gamma^5 (\tau^a)_{f'}^f \frac{\not{z} - \not{q} + m}{u - m^2} i e q_f \gamma^\mu \epsilon(k)_\mu^* u(p)^{r,f'}, \quad (\text{F.3.1})$$

$$M_{C4} = \bar{u}(z)_{f,s} i e q_f \gamma^\mu \epsilon(k)_\mu^* \frac{\not{p} + \not{q} + m}{s - m^2} g \gamma^5 (\tau^a)_{f'}^f u(p)^{r,f'}, \quad (\text{F.3.2})$$

$$M_{C5} = \bar{u}(z)_{f,s} g \gamma^5 (\tau^a)_{f'}^f u(p)^{r,f'} \frac{1}{t - m_\pi^2} i e q_a (2q^\mu - k^\mu) \epsilon(k)_\mu^* \quad (\text{F.3.3})$$

with q_a being the charge of the corresponding pions: $q_\pm = \pm 1, q_0 = 0$. This can be rewritten using the GELL-MANN matrix λ_3 :

$$\lambda_3 := \begin{pmatrix} 1 & 0 & 0 \\ 0 & -1 & 0 \\ 0 & 0 & 0 \end{pmatrix}, \quad (\text{F.3.4})$$

$$M_{C5} = \bar{u}(z)_{f,s} \tilde{g} \gamma^5 \left(\tau^b (\lambda_3)_b^a \right)_{f'}^f u(p)^{r,f'} \frac{1}{t - m_\pi^2} i e (2q^\mu + k^\mu) \epsilon(k)_\mu^*. \quad (\text{F.3.5})$$

The matrix elements can be simplified a bit using some Dirac algebra:

$$\bar{u}(z)_{f,s} \gamma^5 (\not{z} + m) = 0, \quad (\text{F.3.6})$$

$$(\not{p} + m) \gamma^5 u(p)^{r,f'} = 0, \quad (\text{F.3.7})$$

$$(2q^\mu - k^\mu) \epsilon(k)_\mu^* = 2q^\mu \epsilon(k)_\mu^* \quad (\text{F.3.8})$$

yielding for $M_{C3} - M_{C5}$

$$M_{C3} = i e q_f \tilde{g} (\tau^a)_{f'}^f \epsilon(k)_\mu^* \bar{u}(z)_{f,s} \gamma^5 \frac{-\not{q}}{u - m^2} \gamma^\mu u(p)^{r,f'}, \quad (\text{F.3.9})$$

$$M_{C4} = i e q_f \tilde{g} (\tau^a)_{f'}^f \epsilon(k)_\mu^* \bar{u}(z)_{f,s} \gamma^\mu \frac{\not{q}}{s - m^2} \gamma^5 u(p)^{r,f'}, \quad (\text{F.3.10})$$

$$M_{C5} = 2 i e \tilde{g} q^\mu \epsilon(k)_\mu^* (\tau^b)_{f'}^f (\lambda_3)_b^a \bar{u}(z)_{f,s} \frac{1}{t - m_\pi^2} \gamma^5 u(p)^{r,f'}. \quad (\text{F.3.11})$$

The three elements are added ($M := M_{C3} + M_{C4} + M_{C5}$)

$$\begin{aligned}
M &= ieg\epsilon(k)_\mu^* \bar{u}(z)_{f,s} \\
&\times \left(q_{f'}(\tau^a)_{f'}^f \gamma^5 \frac{-\not{q}}{u-m^2} \gamma^\mu + q_f(\tau^a)_{f'}^f \gamma^\mu \frac{\not{q}}{s-m^2} \gamma^5 + \gamma^5 (\tau^b)_{f'}^f (\lambda_3)_b^a \frac{2q^\mu}{t-m_\pi^2} \right) \quad (\text{F.3.12}) \\
&\times u(p)^{r,f'},
\end{aligned}$$

squared and summed/averaged over all spins, polarizations and flavors. This results in

$$\begin{aligned}
\frac{1}{2} \sum_{\substack{r,s,\epsilon \\ f,f',a}} |M|^2 &= \frac{1}{2} \sum_{r,s,\epsilon,f,f',a} ieg\epsilon(k)_\mu^* \bar{u}(z)_{f,s} \\
&\times \left(q_{f'}(\tau^a)_{f'}^f \frac{-\gamma^5 \not{q} \gamma^\mu}{u-m^2} + q_f(\tau^a)_{f'}^f \frac{\gamma^\mu \not{q} \gamma^5}{s-m^2} + \gamma^5 (\tau^b)_{f'}^f (\lambda_3)_b^a \frac{2q^\mu}{t-m_\pi^2} \right) \\
&\times u(p)^{r,f'} (-i) eg\epsilon(k)_\nu \bar{u}(p)_{r,f'} \\
&\times \left(q_{f'}(\tau^{a\dagger})_{f'}^f \frac{-\gamma^\nu \not{q} \gamma^5}{u-m^2} + q_f(\tau^{a\dagger})_{f'}^f \frac{\gamma^5 \not{q} \gamma^\nu}{s-m^2} + \gamma^5 (\tau^{c\dagger})_{f'}^f (\lambda_3)_c^a \frac{2q^\nu}{t-m_\pi^2} \right) \\
&\times u(z)^{f,s}, \\
&= -\frac{1}{2} \sum_{f,f',a} e^2 g^2 g_{\mu\nu} \text{Tr}_{\text{Dirac}} \left[(\not{z} + m) \right. \\
&\times \left(q_{f'}(\tau^a)_{f'}^f \frac{-\gamma^5 \not{q} \gamma^\mu}{u-m^2} + q_f(\tau^a)_{f'}^f \frac{\gamma^\mu \not{q} \gamma^5}{s-m^2} + \gamma^5 (\tau^b)_{f'}^f (\lambda_3)_b^a \frac{2q^\mu}{t-m_\pi^2} \right) \\
&\times (\not{p} + m) \\
&\times \left. \left(q_{f'}(\tau^{a\dagger})_{f'}^f \frac{-\gamma^\nu \not{q} \gamma^5}{u-m^2} + q_f(\tau^{a\dagger})_{f'}^f \frac{\gamma^5 \not{q} \gamma^\nu}{s-m^2} + \gamma^5 (\tau^{c\dagger})_{f'}^f (\lambda_3)_c^a \frac{2q^\nu}{t-m_\pi^2} \right) \right], \\
&= -\frac{e^2 g^2}{2} \left(\frac{I}{(u-m^2)^2} + \frac{II}{(s-m^2)^2} + \frac{III}{(t-m_\pi^2)^2} \right. \\
&+ 2 \frac{IV}{(u-m^2)(s-m^2)} + 2 \frac{V}{(u-m^2)(t-m_\pi^2)} \quad (\text{F.3.13}) \\
&\left. + 2 \frac{VI}{(s-m^2)(t-m_\pi^2)} \right).
\end{aligned}$$

With

$$I = \sum_{f,f',a} q_{f'}(\tau^a)_{f'}^f q_f(\tau^{a\dagger})_{f'}^f g_{\mu\nu} \text{Tr}_{\text{Dirac}} \left[\gamma^5 \not{q} \gamma^\mu (\not{p} + m) \gamma^\nu \not{q} \gamma^5 (\not{z} + m) \right], \quad (\text{F.3.14})$$

$$II = \sum_{f,f',a} (q_f)^2 (\tau^a)_{f'}^{f'} (\tau^a)_f^f g_{\mu\nu} \text{Tr}_{\text{Dirac}} \left[\gamma^\mu \not{q} \gamma^5 (\not{p} + m) \gamma^5 \not{q} \gamma^\nu (\not{z} + m) \right], \quad (\text{F.3.15})$$

$$III = \sum_{f,f',a} g_{\mu\nu} (\tau^b)_{f'}^f (\lambda_3)_b^a (\tau^{c\dagger})_{f'}^{f'} (\lambda_3)_c^a \text{Tr}_{\text{Dirac}} \left[\gamma^5 2q^\mu (\not{p} + m) \gamma^5 2q^\nu (\not{z} + m) \right], \quad (\text{F.3.16})$$

$$IV = - \sum_{f,f',a} q_{f'} q_f (\tau^a)_{f'}^f (\tau^{a\dagger})_f^{f'} g_{\mu\nu} \text{Tr}_{\text{Dirac}} \left[\gamma^5 \not{q} \gamma^\mu (\not{p} + m) \gamma^5 \not{q} \gamma^\nu (\not{z} + m) \right], \quad (\text{F.3.17})$$

$$V = - \sum_{f,f',a,c} g_{\mu\nu} q_{f'} (\tau^a)_{f'}^f (\tau^{c\dagger})_f^{f'} (\lambda_3)_c^a \text{Tr}_{\text{Dirac}} \left[\gamma^5 \not{q} \gamma^\mu (\not{p} + m) \gamma^5 2q^\nu (\not{z} + m) \right], \quad (\text{F.3.18})$$

$$VI = \sum_{f,f',a,c} q_f (\tau^a)_{f'}^f (\tau^{c\dagger})_f^{f'} (\lambda_3)_c^a g_{\mu\nu} \text{Tr}_{\text{Dirac}} \left[\gamma^\mu \not{q} \gamma^5 (\not{p} + m) \gamma^5 2q^\nu (\not{z} + m) \right]. \quad (\text{F.3.19})$$

For the evaluation of the expressions I - VI one needs the adjoint τ^a :

$$(\tau^+)^\dagger = \frac{1}{\sqrt{2}} (\tau^1 + i\tau^2)^\dagger = \sqrt{2} \begin{pmatrix} 0 & 1 \\ 0 & 0 \end{pmatrix}^\dagger = \frac{1}{\sqrt{2}} (\tau^1 - i\tau^2) = \tau^-, \quad (\text{F.3.20})$$

$$(\tau^-)^\dagger = \frac{1}{\sqrt{2}} (\tau^1 - i\tau^2)^\dagger = \sqrt{2} \begin{pmatrix} 0 & 0 \\ 1 & 0 \end{pmatrix}^\dagger = \frac{1}{\sqrt{2}} (\tau^1 + i\tau^2) = \tau^+, \quad (\text{F.3.21})$$

$$\tau^+ (\tau^+)^\dagger = \tau^+ \tau^- = \mathbb{1} + \tau^3, \quad (\text{F.3.22})$$

$$\tau^- (\tau^-)^\dagger = \tau^- \tau^+ = \mathbb{1} - \tau^3, \quad (\text{F.3.23})$$

$$\tau^0 \equiv \tau^3 \Rightarrow \tau^0 (\tau^0)^\dagger = (\tau^3)^2 = \mathbb{1}. \quad (\text{F.3.24})$$

Evaluating and simplifying as described in Appendix B.4.2 yields

$$I = \frac{5}{3} (16(qp)(qz) - 8q^2(pz) + 16m_q^2 q^2), \quad (\text{F.3.25})$$

$$II = \frac{5}{3} (16(qz)(qp) - 8q^2(zp) + 16m_q^2 q^2) = I, \quad (\text{F.3.26})$$

$$III = -64q^2(pz) + 64q^2 m_q^2, \quad (\text{F.3.27})$$

$$IV = -\frac{1}{3} (8m_q^2 q^2 + 16(qp)(qz)), \quad (\text{F.3.28})$$

$$V = 16m_q^2 q^2 - 16q^2(pz), \quad (\text{F.3.29})$$

$$VI = -16q^2(pz) + 16q^2 m_q^2 = V. \quad (\text{F.3.30})$$

Rewriting these in terms of MANDELSTAM variables and inserting into (F.3.13) gives

$$\begin{aligned} \frac{1}{2} \sum |M|^2 = & -e^2 g^2 \left(-\frac{10}{3} \left(\frac{s - m_q^2}{u - m_q^2} + \frac{u - m_q^2}{s - m_q^2} \right) \right. \\ & + \frac{20}{3} m_\pi^2 m_q^2 \left(\frac{1}{(u - m_q^2)^2} + \frac{1}{(s - m_q^2)^2} \right) \\ & + \frac{4}{3} - \frac{4}{3} \frac{m_\pi^2 (s + u - m_\pi^2)}{(u - m_q^2)(s - m_q^2)} \\ & \left. + 8 \frac{m_\pi^2 t}{t - m_\pi^2} \left(\frac{1}{u - m_q^2} + \frac{1}{s - m_q^2} + \frac{2}{t - m_\pi^2} \right) \right). \end{aligned} \quad (\text{F.3.31})$$

where the squared four-momenta were evaluated using $p^2 = z^2 = m_q^2$, $q^2 = m_\pi^2$ and $k^2 = 0$.

For the case of massless pions (*e.g.* in the NAMBU-GOLDSTONE phase in the chiral limit) this simplifies considerably:

$$\frac{1}{2} \sum |M|^2 = e^2 g^2 \left(\frac{10}{3} \left(\frac{s - m_q^2}{u - m_q^2} + \frac{u - m_q^2}{s - m_q^2} \right) - \frac{4}{3} \right). \quad (\text{F.3.32})$$

F.4. Annihilations and anti-COMPTON

The annihilation diagrams are related to the respective COMPTON diagrams by crossing symmetries which translate into the exchange of MANDELSTAM variables. To be specific, changing from COMPTON to annihilation diagrams (which corresponds diagrammatically to bending the outgoing fermion line to the left and the incoming meson line to the right, *cf.* Fig. 4.3) is equivalent to switch s and t in the formulas. Thus, the matrix element for annihilations into a σ meson and a photon reads

$$\begin{aligned} \frac{1}{2} \sum |\mathcal{M}_{q\bar{q} \rightarrow \sigma\gamma}|^2 = & -\frac{5}{9} g^2 e^2 \left((4m^2 - m_\sigma^2) \left(\frac{8m^2}{(u - m^2)^2} + \frac{8m^2}{(t - m^2)^2} \right) \right. \\ & \left. + 8 \frac{(2m^2 - m_\sigma^2)}{(u - m^2)(t - m^2)} \right) \\ & + 4 \frac{t + 7m^2 - 2m_\sigma^2}{u - m^2} + 4 \frac{u + 7m^2 - 2m_\sigma^2}{t - m^2} + 8 \Big). \end{aligned} \quad (\text{F.4.1})$$

This result is symmetric *w.r.t.* the interchange $u \leftrightarrow t$, which reflects the crossing symmetries of the S matrix.

That for the annihilation into a pion and a photon is

$$\begin{aligned}
\frac{1}{2} \sum |\mathcal{M}_{q\bar{q} \rightarrow \pi\gamma}|^2 = & -e^2 g^2 \left(-\frac{10}{3} \left(\frac{t-m^2}{u-m^2} + \frac{u-m^2}{t-m^2} \right) \right. \\
& + \frac{20}{3} m_\pi^2 m^2 \left(\frac{1}{(u-m^2)^2} + \frac{1}{(t-m^2)^2} \right) \\
& + \frac{4}{3} - \frac{4}{3} \frac{m_\pi^2 (t+u-m_\pi^2)}{(u-m^2)(t-m^2)} \\
& \left. + 8 \frac{m_\pi^2 s}{s-m_\pi^2} \left(\frac{1}{u-m^2} + \frac{1}{t-m^2} + \frac{2}{s-m_\pi^2} \right) \right). \tag{F.4.2}
\end{aligned}$$

The matrix elements for anti-COMPTON processes coincide with the matrix element for the respective COMPTON process:

$$\sum |\mathcal{M}_{\bar{q}\sigma \rightarrow \bar{q}\gamma}|^2 = \sum |\mathcal{M}_{q\sigma \rightarrow q\gamma}|^2, \tag{F.4.3}$$

$$\sum |\mathcal{M}_{\bar{q}\pi \rightarrow \bar{q}\gamma}|^2 = \sum |\mathcal{M}_{q\pi \rightarrow q\gamma}|^2. \tag{F.4.4}$$

G. Comments on the photon production formulas

G.1. The MCLERRAN-TOIMELA formula

We follow here the derivation in [KG06, GK91]. The starting point is an S -matrix element that gives the transition amplitude from an initial $|i\rangle$ state to a final state $|f\rangle$. We will consider only reactions which involve one photon with momentum k^ν and polarization ϵ^μ . The transition rate $R_{i\rightarrow f}$ between these states is

$$R_{i\rightarrow f} = \frac{1}{V\delta t} |S_{fi}|^2. \quad (\text{G.1.1})$$

The S -matrix element in the one-photon approximation (which corresponds to no back-reaction of the emitted photons) is given by

$$S_{fi} = \left\langle f \left| \int d^4x A^\mu(x) \hat{J}_\mu(x) \right| i \right\rangle \quad (\text{G.1.2})$$

with the electromagnetic current operator $\hat{J}_\mu(x)$. The one-photon approximation (or equivalently the leading term in a perturbation expansion *w.r.t.* the electromagnetic coupling) requires the use of the unperturbed photon field

$$A^\mu = \frac{\epsilon^\mu}{\sqrt{2\omega V}} (e^{-ikx} + e^{ikx}). \quad (\text{G.1.3})$$

The somewhat awkward prefactor is necessary to obtain the correct value for the energy of a single photon. Assuming translation invariance for the current

$$\langle f | \hat{J}_\mu(x) | i \rangle = e^{i(p_f - p_i)x} \langle f | \hat{J}_\mu(0) | i \rangle \quad (\text{G.1.4})$$

one arrives at

$$R_{i \rightarrow f} = \frac{1}{V\delta t} \langle f | \int d^4x A^\mu(x) \hat{J}_\mu(x) | i \rangle \langle i | \int d^4y A^\nu(y) \hat{J}_\nu(y) | f \rangle \quad (\text{G.1.5})$$

$$= \frac{1}{V\delta t} \int d^4x d^4y \frac{\epsilon^\mu}{\sqrt{2\omega V}} (e^{-ikx} + e^{ikx}) \frac{\epsilon^\nu}{\sqrt{2\omega V}} (e^{-iky} + e^{iky}) \times \langle f | \hat{J}_\mu(x) | i \rangle \langle i | \hat{J}_\nu(y) | f \rangle, \quad (\text{G.1.6})$$

$$= \frac{1}{V\delta t} \int d^4x d^4y \frac{\epsilon^\mu \epsilon^\nu}{2\omega V} (e^{-ikx} + e^{ikx}) (e^{-iky} + e^{iky}) e^{i(p_f - p_i)x} e^{-i(p_f - p_i)y} \times \langle f | \hat{J}_\mu(0) | i \rangle \langle i | \hat{J}_\nu(0) | f \rangle, \quad (\text{G.1.7})$$

$$= \frac{1}{V\delta t} \int d^4y \frac{\epsilon^\mu \epsilon^\nu}{2\omega V} ((2\pi)^4 \delta(-k + p_f - p_i) + (2\pi)^4 \delta(k + p_f - p_i)) (e^{-i(k+p_f-p_i)y} + e^{-i(-k+p_f-p_i)y}) \langle f | \hat{J}_\mu(0) | i \rangle \langle i | \hat{J}_\nu(0) | f \rangle, \quad (\text{G.1.8})$$

$$= \frac{(2\pi)^4 \epsilon^\mu \epsilon^\nu}{2\omega V} (\delta(p_f - p_i - k) + \delta(p_f - p_i + k)) \langle f | \hat{J}_\mu(0) | i \rangle \langle i | \hat{J}_\nu(0) | f \rangle, \quad (\text{G.1.9})$$

with the first delta distribution corresponding to absorption and the second one to emission processes. Summing over the final states and averaging over the initial states with a thermal weight $1/Z \langle i | \exp\{\beta(\hat{H} - \mu\hat{N})\} | i \rangle$, where \hat{H} is the Hamiltonian and \hat{N} the number operator and $Z = \sum_i \langle i | \exp\{\beta(\hat{H} - \mu\hat{N})\} | i \rangle$ is the partition function, one obtains

$$R \equiv \frac{1}{Z} \sum_{f,i} R_{i \rightarrow f} e^{\beta(E_i - \mu N_i)} \quad (\text{G.1.10})$$

$$= - \frac{g^{\mu\nu} (2\pi)^4}{2\omega V} \frac{1}{Z} \sum_{f,i} e^{\beta(E_i - \mu N_i)} \delta(p_f - p_i + k) \langle f | \hat{J}_\mu(0) | i \rangle \langle i | \hat{J}_\nu(0) | f \rangle \quad (\text{G.1.11})$$

$$= - \frac{g^{\mu\nu} (2\pi)^4}{2\omega V} \frac{1}{Z} \sum_{f,i} \frac{V}{(2\pi)^3} \int dK [3] e^{\beta(E_i - \mu N_i)} \delta(p_f - p_i + k) \langle f | \hat{J}_\mu(0) | i \rangle \langle i | \hat{J}_\nu(0) | f \rangle \\ =: \int dK [3] \frac{dR[3]}{dK[3]}. \quad (\text{G.1.12})$$

This corresponds to the differential rate

$$\omega \frac{dR[3]}{dK[3]} = - g^{\mu\nu} \pi \frac{1}{Z} \sum_{f,i} e^{\beta(E_i - \mu N_i)} \delta(k + p_f - p_i) \langle f | \hat{J}_\mu(0) | i \rangle \langle i | \hat{J}_\nu(0) | f \rangle \quad (\text{G.1.13})$$

$$= \frac{g^{\mu\nu} \pi}{(2\pi)^3} f_{\mu\nu}^-(k) \quad (\text{G.1.14})$$

with

$$f_{\mu\nu}^\pm(k) = \pm \frac{1}{Z} \sum_{f,i} e^{\beta(E_i - \mu N_i)} (2\pi)^3 \delta(p_f - p_i \pm k) \langle f | \hat{J}_\mu(0) | i \rangle \langle i | \hat{J}_\nu(0) | f \rangle \quad (\text{G.1.15})$$

being the spectral function of the current-current correlator associated to emission and absorption, respectively [KG06]. The retarded current correlation function

$$f_{\mu\nu}^{\text{ret}}(\omega, \vec{k}) = \int \frac{d\omega'}{(2\pi)} \frac{(f_{\mu\nu}^+(\omega', \vec{k}) + f_{\mu\nu}^-(\omega', \vec{k}))}{\omega' - \omega - i\epsilon} \quad (\text{G.1.16})$$

is up to order e^2 identical to the retarded photon propagator $G_{\mu\nu}^{\gamma, \text{ret}}$. Using the detailed balance relation $f_{\mu\nu}^+ = -e^{\beta\omega} f_{\mu\nu}^-$ and inserting the inverted (G.1.16) into (G.1.14) yields for the differential rate

$$\omega \frac{dR[3]}{dK[3]} = \frac{g^{\mu\nu}}{(2\pi)^3} \frac{1}{e^{\beta\omega} - 1} \text{Im} G_{\mu\nu}^{\gamma, \text{ret}} \quad (\text{G.1.17})$$

which is the MCLERRAN-TOIMELA formula (3.1.1)

G.2. The optical theorem

The discussion follows closely the one in [PS95]. From the unitarity of the S -matrix follows a useful identity for the T -matrix. The T -matrix is defined as the part of the S -matrix that corresponds to scattering, *i.e.*

$$S = \mathbb{1} + iT. \quad (\text{G.2.1})$$

The unitarity of the S -matrix

$$\mathbb{1} = S^\dagger S \quad (\text{G.2.2})$$

yields for the T -matrix

$$i(T^\dagger - T) = T^\dagger T. \quad (\text{G.2.3})$$

In the case of forward scattering, *i.e.* the case of identical initial and final state this reads

$$i(T_{ii}^* - T_{ii}) = 2\text{Im}T_{ii} = \sum_f |T_{fi}|^2. \quad (\text{G.2.4})$$

where T_{fi} is that element of the matrix T , that connects the initial state $|i\rangle$ with the final state $|f\rangle$. The left hand side, *i.e.* the imaginary part of the forward scattering amplitude being connected to the propagator by the LSZ theorem, can be related to the damping of a particles wave function as well as to the finite width of a resonance in scattering experi-

ments. The right hand side in turn is proportional to the total probability of the particle to scatter into any possible finite state. The optical theorem (G.2.4) thus can be interpreted as stating that the reason for damping are scattering processes. The somewhat handwaving derivation above in turn points to the unitarity (*i.e.* the conservation of probability) as the fundamental property that causes this connection. Equation (G.2.4) similarly applies to the invariant matrix elements $\mathcal{M}_{i \rightarrow f}$ connected to T_{fi} by

$$T_{fi} = (2\pi)^4 \delta^{(4)}(P_f - P_i) \mathcal{M}_{i \rightarrow f}, \quad (\text{G.2.5})$$

where P_i and P_f denote the total four-momentum of the initial and final states, respectively [PS95]:

$$\text{Im} \mathcal{M}_{i \rightarrow i} = \sum_f (2\pi)^4 (\delta^{(4)}(P_f - P_i)) |\mathcal{M}_{i \rightarrow f}|^2 \quad (\text{G.2.6})$$

with the sum running over all possible states $|f\rangle$, especially over all possible momenta compatible with energy-momentum conservation, represented by the delta distribution. Equations (G.2.4) and (G.2.6) are the optical theorem.

In the derivation of the photon emissivity in Chapter 4, the optical theorem is used to transform the MCLERRAN-TOIMELA formula (3.1.1) into the form known from kinetic theory with the CUTKOSKY cutting rules [Cut60] being the diagrammatic equivalent to (G.2.6).

H. Phase space integration

H.1. Solving the integrals

The general formula for the differential rate $\omega d^7N/d^3k d^4x$ for $2 \rightarrow 2$ processes (incoming momenta: p_1, p_2 ; outgoing momenta: q, k with k corresponding to the photon and $R \equiv d^4N/d^4x$) is (*cf.* (4.4.1))

$$\begin{aligned} \omega \frac{d^3R}{d^3k} = & \int \frac{d^3p_1}{2E_1(2\pi)^3} \frac{d^3p_2}{2E_2(2\pi)^3} \frac{d^3z}{2E_q(2\pi)^3} (2\pi)^4 \delta^{(4)}(p_1 + p_2 - q - k) \\ & \times n_{F/B}(p_1) n_{F/B}(p_2) (1 - n_{F/B}(q)) |M(s, u)|^2. \end{aligned} \quad (\text{H.1.1})$$

The first step is the evaluation of the q integration using the momentum conserving delta distribution followed by the introduction of the MANDELSTAM variable s , which is done by inserting $1 = \int ds \delta(s - (p_1 + p_2)^2)$:

$$\begin{aligned} \omega \frac{d^3R}{d^3k} = & \frac{1}{(2\pi)^5} \int \frac{d^3p_2}{2E_2} \frac{d^3p_1}{2E_1} \delta(E_1 + E_2 - E_q - \omega) \\ & \times \int ds \delta(s - p_1^2 - p_2^2 - 2E_1E_2 + 2\vec{p}_1\vec{p}_2) n_F(E_1) n_B(E_2) \\ & \times \bar{n}_F(\omega - E_1 - E_2) |M(s, t)|^2 \frac{1}{2E_q}. \end{aligned} \quad (\text{H.1.2})$$

Afterwards, p_1 is transformed into spherical coordinates $d^3p_1 \rightarrow |\vec{p}_1|^2 d|\vec{p}_1| d\cos\theta_{12} d\phi_{12}$. These coordinates are adjusted such that the q direction of the spherical coordinates coincides with the direction of \vec{p}_2 ($\Rightarrow \vec{p}_1\vec{p}_2 = |\vec{p}_1||\vec{p}_2| \cos\theta_{12}$). Then the azimuthal integration can be carried out easily by virtue of the delta distribution in the second line of (H.1.2)

resulting in

$$\begin{aligned} \omega \frac{d^3 R}{d^3 k} &= \frac{1}{(2\pi)^5} \int \frac{d^3 p_2}{2E_2} |\vec{p}_1|^2 \frac{d|\vec{p}_1| d\phi_{12}}{2E_1} \int ds |M(s, t)|^2 \frac{\theta(1 - c_2^2)}{2|\vec{p}_1||\vec{p}_2|} \\ &\quad \times n_F(E_1) n_B(E_2) \bar{n}_F(\omega - E_1 - E_2) \frac{1}{2E_q} \delta(E_1 + E_2 - E_q - \omega) \end{aligned} \quad (\text{H.1.3})$$

with

$$c_2 := \frac{-s + p_1^2 + p_2^2 + 2E_1 E_2}{2|\vec{p}_1||\vec{p}_2|} \equiv \cos(\theta_{12}). \quad (\text{H.1.4})$$

Similarly a second MANDELSTAM variable is introduced by inserting $1 = \int dt \delta(t - (p_2 - k)^2)$. Afterwards the differential $d^3 p_2$ is transformed into spherical coordinates and simplified analogously. This time the q direction of the spherical momentum coordinates points in direction of the photon three-momentum \vec{k} :

$$\begin{aligned} \omega \frac{d^3 R}{d^3 k} &= \frac{1}{(2\pi)^5} \int \frac{|\vec{p}_2|^2 d|\vec{p}_2| d\phi_{2k}}{2E_2} \frac{|\vec{p}_1|^2 d|\vec{p}_1| d\phi_{12}}{2E_1} \int ds dt \frac{\theta(1 - c_2^2)}{2|\vec{p}_1||\vec{p}_2|} \frac{\theta(1 - c_1^2)}{2|\vec{p}_2||\vec{k}|} \\ &\quad \times |M(s, t)|^2 n_F(E_1) n_B(E_2) \bar{n}_F(\omega - E_1 - E_2) \frac{1}{2E_q} \delta(E_1 + E_2 - E_q - \omega), \end{aligned} \quad (\text{H.1.5})$$

with

$$c_1 := \frac{t - p_2^2 - k^2 + 2E_2 \omega}{2|\vec{p}_2||\vec{k}|} \equiv \cos(\theta_{2k}). \quad (\text{H.1.6})$$

Now, the energy conserving delta distribution can be evaluated. For this purpose one transforms the argument of the delta distribution ,

$$\frac{1}{2E_q} \delta(E_q - (E_1 + E_2 - \omega)) = \delta(E_q^2 - (E_1 + E_2 - \omega)^2), \quad (\text{H.1.7})$$

and expands the quadratic terms. The angles θ_{12}, θ_{2k} between \vec{p}_1 and \vec{p}_2 as well as between \vec{p}_2 and \vec{k} are determined by (H.1.4) and (H.1.6), respectively. Thus

$$\begin{aligned} E_q^2 - (E_1 + E_2 - \omega)^2 &= q^2 + \left(|\vec{p}_1|^2 + |\vec{p}_2|^2 + |\vec{k}|^2 + 2|\vec{p}_1||\vec{p}_2|c_2 \right. \\ &\quad \left. - 2|\vec{p}_1||\vec{k}| \cos(\theta_{1k}) - 2|\vec{p}_2||\vec{k}|c_1 \right) - (E_1 + E_2 - \omega)^2, \end{aligned}$$

which can be simplified considerably yielding that the energy conserving delta distribution can be rewritten according to

$$\delta\left(E_q^2 - (E_1 + E_2 - \omega)^2\right) = \frac{\delta(c_0 - \cos(\theta_{1k}))}{2|\vec{p}_1||\vec{k}|} \quad (\text{H.1.8})$$

with

$$c_0 := \frac{q^2 + p_2^2 - s - t + 2E_1\omega}{2|\vec{p}_1||\vec{k}|}, \quad (\text{H.1.9})$$

which gives for the rate

$$\begin{aligned} \frac{d^3R}{d^3k} &= \frac{1}{8|\vec{k}|^2(2\pi)^5} \int \frac{d|\vec{p}_2|d\phi_{2k}}{2E_2} \frac{d|\vec{p}_1|d\phi_{12}}{2E_1} \int ds dt \theta(1 - c_2^2)\theta(1 - c_1^2) \\ &\quad \times n_F(E_1)n_B(E_2)\bar{n}_F(\omega - E_1 - E_2)|M(s, t)|^2\delta(c_0 - \cos(\theta_{1k})). \end{aligned} \quad (\text{H.1.10})$$

Now, the next goal is to express $\cos(\theta_{1k})$ in terms of one of the remaining integration variables and using the delta distribution to execute the corresponding integration. The angle ϕ_{12} is defined to be between the projections of \vec{p}_1 onto a plane perpendicular to \vec{p}_2 and some normalized vector \vec{e}_v lying in that plane, *i.e.*

$$\cos \phi_{12} = \frac{(\vec{e}_1\vec{e}_v)}{\sqrt{1 - (\vec{e}_1\vec{e}_2)^2}} \quad (\text{H.1.11})$$

with $e_1 = \vec{p}_1/|\vec{p}_1|$. Because of the delta distributions that have already been evaluated, it is known (*cf.* (H.1.4) and (H.1.6)) that $\vec{e}_2\vec{e}_1 = \cos(\theta_{12}) = c_2$ and $\vec{e}_2\vec{e}_k = \cos(\theta_{2k}) = c_1$. It remains to specify which vector \vec{e}_v is used for reference. Since the only physical vector is \vec{k} , the projection k_\perp of \vec{k} onto the plane perpendicular to \vec{p}_2 is chosen. Then ϕ_{12} can be expressed in terms of θ_{1k} by ($e_2 = \vec{p}_2/|\vec{p}_2|$)

$$\cos \phi_{12} = \frac{(\vec{e}_1(\mathbb{1} - \vec{e}_2 \circ \vec{e}_2)\vec{k})}{|\vec{k}_\perp|\sqrt{1 - (\vec{e}_1\vec{e}_2)^2}} \quad (\text{H.1.12})$$

with the direct product $\vec{a} \circ \vec{b}$ of two vectors \vec{a} and \vec{b} acting on a third vector \vec{c} according to $(\vec{a} \circ \vec{b})\vec{c} = \vec{a}(\vec{b}\vec{c})$, which yields after some straightforward algebra

$$\cos \phi_{12} = \frac{\cos \theta_{1k} - c_2c_1}{\sqrt{1 - c_1^2}\sqrt{1 - c_2^2}}, \quad (\text{H.1.13})$$

$$\cos \theta_{1k} = \sqrt{1 - c_1^2}\sqrt{1 - c_2^2} \cos \phi_{12} + c_2c_1. \quad (\text{H.1.14})$$

Inserting into the rate formula gives

$$\begin{aligned} \omega \frac{d^3 R}{d^3 k} &= \frac{1}{8|\vec{k}|^2 (2\pi)^5} \int \frac{d|\vec{p}_2| d\phi_{2k}}{2E_2} \frac{d|\vec{p}_1| d\phi_{12}}{2E_1} \int ds dt \theta(1 - c_2^2) \theta(1 - c_1^2) \\ &\times n_F(E_1) n_B(E_2) \bar{n}_F(\omega - E_1 - E_2) |M(s, t)|^2 \frac{\delta\left(\frac{c_0 - c_2 c_1}{\sqrt{1 - c_1^2} \sqrt{1 - c_2^2}} - \cos \phi_{12}\right)}{\sqrt{1 - c_1^2} \sqrt{1 - c_2^2}}. \end{aligned} \quad (\text{H.1.15})$$

The ϕ_{12} integration is evaluated using the substitution

$$\xi := \cos \phi_{12} \quad , \quad d\xi = \sqrt{1 - \xi^2} d\phi_{12}. \quad (\text{H.1.16})$$

Besides replacing ϕ_{12} and $d\phi_{12}$ according to (H.1.16) a factor of two has to be inserted since when ϕ_{12} runs from 0 to 2π each value of ξ is taken twice:

$$\begin{aligned} \omega \frac{d^3 R}{d^3 k} &= \frac{2}{8|\vec{k}|^2 (2\pi)^5} \int \frac{d|\vec{p}_2| d\phi_{2k}}{2E_2} \frac{d|\vec{p}_1| d\xi}{2E_1} \int ds dt |M(s, t)|^2 \theta(1 - c_2^2) \theta(1 - c_1^2) \\ &\times n_F(E_1) n_B(E_2) \bar{n}_F(\omega - E_1 - E_2) \frac{\delta(c_3 - \xi)}{\sqrt{1 - \xi^2} \sqrt{1 - c_1^2} \sqrt{1 - c_2^2}} \end{aligned} \quad (\text{H.1.17})$$

with

$$c_3 := \frac{c_0 - c_2 c_1}{\sqrt{1 - c_1^2} \sqrt{1 - c_2^2}}. \quad (\text{H.1.18})$$

Now, the integration *w.r.t.* ξ can be done easily:

$$\begin{aligned} \omega \frac{d^3 R}{d^3 k} &= \frac{1}{16|\vec{k}|^2 (2\pi)^4} \int \frac{d|\vec{p}_2|}{E_2} \frac{d|\vec{p}_1|}{E_1} \int ds dt |M(s, t)|^2 \\ &\times \frac{n_F(E_1) n_B(E_2) \bar{n}_F(\omega - E_1 - E_2) \theta(1 - c_3^2) \theta(1 - c_2^2) \theta(1 - c_1^2)}{\sqrt{1 - c_3^2} \sqrt{1 - c_1^2} \sqrt{1 - c_2^2}}. \end{aligned} \quad (\text{H.1.19})$$

The denominator is expanded:

$$\zeta^2 := (1 - c_3^2)(1 - c_1^2)(1 - c_2^2) \quad (\text{H.1.20})$$

$$\begin{aligned} &= \frac{1}{(2|\vec{p}_2| |\vec{k}| |\vec{p}_1|)^2} \left(-|\vec{k}|^2 (\hat{s} - 2E_1 E_2)^2 - |\vec{p}_1|^2 (\hat{t} + 2E_2 \omega)^2 - |\vec{p}_2|^2 (\hat{u} + 2E_1 \omega)^2 \right. \\ &\quad \left. + 4|\vec{p}_1|^2 |\vec{p}_2|^2 |\vec{k}|^2 - (\hat{u} + 2E_1 \omega)(\hat{s} - 2E_1 E_2)(\hat{t} + 2E_2 \omega) \right) \end{aligned} \quad (\text{H.1.21})$$

with the shortcuts:

$$\hat{s} := s - p_1^2 - p_2^2, \quad \hat{t} := t - p_2^2 - k^2, \quad \hat{u} := q^2 + p_2^2 - s - t = u - p_1^2 - k^2. \quad (\text{H.1.22})$$

This is a nicely symmetric result that is inserted into (H.1.19). Then the $|\vec{p}_2|$ and $|\vec{p}_1|$ integrations are transformed into E_1 and E_2 integrations yielding

$$\omega \frac{d^3 R}{d^3 k} = \frac{1}{8|\vec{k}|(2\pi)^4} \int ds dt |M(s, t)|^2 \int dE_2 dE_1 \times \frac{n_F(E_1)n_B(E_2)\bar{n}_F(\omega - E_1 - E_2)\theta(1 - c_3^2)\theta(1 - c_2^2)\theta(1 - c_1^2)}{\zeta'}, \quad (\text{H.1.23})$$

where the shortcut $\zeta' := 2|\vec{p}_2||\vec{k}||\vec{p}_1|\zeta$ is used. The HEAVISIDE step functions $\theta(1 - c_2^2)$ and $\theta(1 - c_1^2)$ are equivalent to the restriction of s and t to the physical region, *i.e.* to the limits s_0 and t_{\pm} given in (B.5.12) and (B.5.16), and thus can be omitted.

As can be seen from (H.1.20) the numerator is zero if and only if $(1 - c_3^2)$, $(1 - c_2^2)$ or $(1 - c_1^2)$ vanish. As just discussed, the latter two are zero only at the limits of the s and t integrations. The $\theta(1 - c_3^2)$ can be eliminated from (H.1.23) by appropriately setting the limits of the energy integrations, which in turn means that the energy integration is limited by the zeros of the numerator.

Thus, by setting the limits of the s , t and the energy integrations appropriately all θ functions can be dropped.

$$\omega \frac{d^3 R}{d^3 k} = \frac{1}{8|\vec{k}|(2\pi)^4} \int_{s_0}^{\infty} ds \int_{t_-}^{t^+} dt |M(s, t)|^2 \int_{c_3 \leq 1} dE_2 dE_1 \times \frac{n_F(E_1)n_B(E_2)\bar{n}_F(\omega - E_1 - E_2)}{\zeta'}, \quad (\text{H.1.24})$$

The numerator ζ' in (H.1.24) is transformed by substituting $E_2 =: \nu - E_1$. The result is sorted *w.r.t.* powers of E_1 yielding

$$\begin{aligned} \zeta'^2 = & E_1^2(-(\hat{u} + \hat{t})^2 + 4k^2(\hat{s} + p_2^2 + p_1^2)) \\ & + E_1(\nu(-8k^2p_1^2 + 2\hat{u}^2 + 2\hat{t}\hat{u} - 4k^2\hat{s}) + \omega(-4p_1^2\hat{t} + 4\hat{u}p_2^2 - 2\hat{t}\hat{s} + 2\hat{s}\hat{u})) \\ & + \nu^2(4k^2p_1^2 - \hat{u}^2) + 2\nu\omega(2p_1^2\hat{t} - \hat{s}\hat{u}) + p_1^2(4|\vec{k}|^2p_2^2 + \hat{t}^2) - |\vec{k}|^2\hat{s}^2 + \hat{u}^2p_2^2 \\ & - \hat{t}\hat{s}\hat{u} \end{aligned} \quad (\text{H.1.25})$$

$$\begin{aligned}
&= E_1^2 \left(-(-s + q^2 - k^2)^2 + 4k^2 s \right) \\
&\quad + E_1 \left(\nu \left(+2k^2(k^2 - u - s - p_1^2 - q^2 + 2p_2^2) - 2(s - q^2)(u - p_1^2) \right) \right. \\
&\quad \quad + \omega \left(2q^2(-p_1^2 - s + p_2^2) - 2s(p_1^2 - s + p_2^2) \right. \\
&\quad \quad \quad \left. \left. + 2k^2(-p_2^2 - s + p_1^2) + 4us \right) \right) \\
&\quad + \nu^2(-u^2 - p_1^4 - k^4 + 2up_1^2 + 2uk^2 + 2p_1^2 k^2) \\
&\quad + 2\nu\omega \left(-(u + p_1^2 - k^2)(s + p_1^2 - p_2^2) + 2p^2(p_1^2 + q^2 - p_2^2 - k^2) \right) \\
&\quad + p_1^2(s(p_2^2 + k^2 - u) + (q^2 - p_2^2 + p_1^2 - s - u)(q^2 - k^2)) \\
&\quad - |\vec{k}|^2(s^2 + p_1^4 + p_2^4 - 2sp_1^2 - 2sp_2^2 - 2p_1^2 p_2^2) + p_2^2(k^2 - u)(k^2 + s - q^2) \\
&\quad + s(u + s - q^2)(u - k^2).
\end{aligned} \tag{H.1.26}$$

H.2. Limits of the ν integration

The limits of the ν integration can be found by inspecting $s = (q + k)^2$:

$$s = (E_q + \omega)^2 - (\vec{k} + \vec{q})^2 \tag{H.2.1}$$

$$= \nu^2 - |\vec{k}|^2 - |\vec{q}|^2 - 2|\vec{k}||\vec{q}|\cos\theta_{2k}. \tag{H.2.2}$$

With $|\vec{q}|^2 = q^2 - E_q^2$ and $\nu = E_q + \omega$ as well as $|\cos\theta_{2k}| \leq 1$ this yields

$$s \leq \nu^2 - \omega^2 + k^2 + q^2 - E_q^2 + 2|\vec{k}|\sqrt{E_q^2 - q^2}. \tag{H.2.3}$$

After a number of straightforward steps, the following inequality holds (for the definition of λ see (4.4.10)):

$$0 \geq \lambda(s, q^2, k^2) + 4\nu\omega q^2 + 4\omega^2 s - 4\nu\omega s - 4k^2\nu\omega + 4k^2\nu^2 =: f_\nu. \tag{H.2.4}$$

In order of obtaining the limits for the ν integration $f_\nu = 0$ has to be solved with the result

$$\nu_\pm = \frac{\omega(s - q^2 + k^2)}{2k^2} \pm \frac{|\vec{k}|}{2k^2} \sqrt{\lambda(s, q^2, k^2)}. \tag{H.2.5}$$

In the limit $k^2 \rightarrow 0$ (which is the only relevant case for this work) this reduces to

$$\nu_+ = \infty, \quad \nu_- \equiv \nu_{\min} = \frac{s - q^2}{4\omega} + \frac{\omega s}{s - q^2}, \tag{H.2.6}$$

which are the limits of the ν integration used in Section 4.4.1.

H.3. Simplifying the denominator

The right side of (H.1.26) is quadratic in E_1 and thus the zeros *w.r.t.* E_1 can be calculated exactly. With the definitions

$$\begin{aligned}\zeta'^2 &= AE_1^2 + BE_1 + C, \\ A &= -(\hat{u} + \hat{t})^2 + 4k^2(\hat{s} + p_2^2 + p_1^2), \\ B &= \nu(-8k^2p_1^2 + 2\hat{u}^2 + 2\hat{t}\hat{u} - 4k^2\hat{s}) + \omega(-4p_1^2\hat{t} + 4\hat{u}p_2^2 - 2\hat{t}\hat{s} + 2\hat{s}\hat{u}), \\ C &= \nu^2(4k^2p_1^2 - \hat{u}^2) + 2\nu\omega(2p_1^2\hat{t} - \hat{s}\hat{u}) + p_1^2(4|\vec{k}|^2p_2^2 + \hat{t}^2) \\ &\quad - |\vec{k}|^2\hat{s}^2 + \hat{u}^2p_2^2 - \hat{t}\hat{s}\hat{u}\end{aligned}\tag{H.3.1}$$

the zeros are

$$E_1^\pm = \frac{-B \pm \sqrt{B^2 - 4AC}}{2A},\tag{H.3.2}$$

$$4A^2\Delta^2 := B^2 - 4AC,\tag{H.3.3}$$

which can be interpreted more easily by defining $E_1^\pm = -B/(2A) \pm \Delta$. Before going on another shortcut is introduced:

$$\tilde{s} := s - q^2 + k^2 \Rightarrow \hat{t} + \hat{u} = -\tilde{s}.\tag{H.3.4}$$

The limits of the MANDELSTAM variable u (*cf.* (B.5.15)) can be expressed in terms of \tilde{s} as

$$\hat{u}_\pm = -\frac{1}{2s} \left(\tilde{s}(\hat{s} + 2p_1^2) \pm \sqrt{(\hat{s}^2 - 4p_1^2p_2^2)(\tilde{s}^2 - 4sk^2)} \right).\tag{H.3.5}$$

\hat{u}_\pm are the zeros of the parabola

$$\hat{f}_u := 4s^2(\hat{u} - \hat{u}_+)(\hat{u} - \hat{u}_-)\tag{H.3.6}$$

$$= 4s^2\hat{u}^2 + 4s\hat{u}(\tilde{s}(\hat{s} + 2p_1^2)) + \left(\tilde{s}^2(\hat{s} + 2p_1^2)^2 - (\hat{s}^2 - 4p_1^2p_2^2)(\tilde{s}^2 - 4sk^2) \right).\tag{H.3.7}$$

Collecting the coefficients of the various powers of ν in $B^2 - 4AC =: a\nu^2 + b\nu + c$ and simplifying afterwards yields after a simple yet lengthy calculation

$$a = 4\frac{k^2}{s}\hat{f}_u,\tag{H.3.8}$$

$$b = -\frac{4\omega\tilde{s}}{s}\hat{f}_u,\tag{H.3.9}$$

$$c = \frac{1}{s} \hat{f}_u \left(4s|\vec{k}|^2 + \tilde{s}^2 \right), \quad (\text{H.3.10})$$

which gives

$$\Delta^2 = \frac{1}{s} \hat{f}_u \left(4k^2\nu^2 - 4\nu\omega\tilde{s} + 4s|\vec{k}|^2 + \tilde{s}^2 \right). \quad (\text{H.3.11})$$

As can be checked easily, the term in brackets is exactly f_ν of (H.2.4) whose zeros determine the limits of the ν integration. Thus, the final expression for Δ simply reads

$$\Delta^2 = \frac{1}{s} \hat{f}_u f_\nu \quad (\text{H.3.12})$$

with \hat{f}_u and f_ν being the parabolas whose zeros define the borders of integration for \hat{u} and ν , respectively (*cf.* (H.3.7) and (H.2.4)).

From a numeric point of view, being able to write Δ^2 as a product of relatively simple terms is extremely helpful, because u , u_\pm , ν and ν_{\min} all can be numerically large, even when Δ^2 is not. In such a case (which inevitably occurs during the evaluation of the phase space integrals, especially when s is large) numerically large terms are subtracted from each other yielding almost zero. However, due to the finite numerical precision the relative numerical error of the difference might become large possibly making Δ^2 negative and thus the limits of the E_1 integration complex. This imposes rather severe problems if an expanded expression of Δ^2 is used for the definition of the E_1 -limits of integration as simple fixes of the possible negative results for Δ^2 introduce numerical errors that cannot be ignored (they even may be of the same order of magnitude as the result). However, when using the product structure of Δ^2 , especially $\hat{f}_u \propto (\hat{u} - \hat{u}_+)(\hat{u} - \hat{u}_-)$ and $f_\nu \propto (\nu - \nu_{\min})$, the relative error can be made as small as 10^{-14} for double¹ precision.

¹ *i.e.* 64 bit floating-point numbers.

H.4. The rate formula

Putting everything together ($R \equiv d^4N/d^4x$, $E \equiv E_1$) one finds as the final formula for the rate

$$\omega \frac{d^7N}{d^3k d^4x} = \frac{1}{16\omega(2\pi)^7} \int_{s_0}^{\infty} \frac{ds}{s - q^2} \int_{t_-}^{t_+} dt |M(s, t)|^2 \quad (\text{H.4.1})$$

$$\times \int_{\nu_{\min}}^{\infty} d\nu \int_{E^-}^{E^+} dE \frac{n_F(E) n_B(\nu - E) \bar{n}_F(\omega - \nu)}{\sqrt{(E - E^-)(E^+ - E)}},$$

$$\nu_{\min} = \frac{s - q^2}{4\omega} + \frac{\omega s}{s - q^2}, \quad (\text{H.4.2})$$

$$E^{\pm} = \bar{E} \pm \Delta, \quad (\text{H.4.3})$$

$$\bar{E} = \frac{(s + p_1^2 - p_2^2)\omega(s - q^2) + (u - p_1^2)(2\omega s - \nu(s - q^2))}{(s - q^2)^2}, \quad (\text{H.4.4})$$

with λ defined as in (4.4.10), Δ^2 as in (H.3.12) and s_0 , u_{\pm} and t_{\pm} as given in (B.5.12), (B.5.15) and (B.5.16).

I. Approximations of the rate formulas

I.1. BOLTZMANN approximation

As mentioned in the main text, in large parts of the phase diagram, it is reasonable to replace the FERMI and BOSE distribution functions by their classical analog, the BOLTZMANN distribution function:

$$n_F(x) \approx e^{-(x-\mu)/T}, \quad (\text{I.1.1})$$

$$n_B(x) \approx e^{-x/T}. \quad (\text{I.1.2})$$

The distribution functions of the outgoing particles can then be set to unity. For the COMPTON case, the formula for the rate (*cf.* (4.4.2)) then reads

$$\begin{aligned} \omega \frac{d^7 N_{q\sigma/\pi \rightarrow q\gamma}}{d^3 k d^4 x} &= \frac{1}{16\omega(2\pi)^7} \int_{s_0}^{\infty} \frac{ds}{s - m_q^2} \int_{t^-}^{t^+} dt |M(s, t)|^2 \\ &\times \int_{\nu_{\min}}^{\infty} d\nu \int_{E^-}^{E^+} dE \frac{e^{-(E-\mu)/T} e^{-(\nu-E)/T}}{\sqrt{(E - E^-)(E^+ - E)}}. \end{aligned} \quad (\text{I.1.3})$$

The E -dependence in the exponents cancel and thus the E and ν integration can be executed with the result

$$\omega \frac{d^7 N_{q\sigma/\pi \rightarrow q\gamma}}{d^3 k d^4 x} = \frac{T e^{\mu/T}}{32\omega(2\pi)^6} \int_{s_0}^{\infty} \frac{ds}{s - m_q^2} e^{-\nu_{\min}(s)/T} \int_{t^-}^{t^+} dt |M(s, t)|^2. \quad (\text{I.1.4})$$

The t -integral is expressed with the vacuum cross section $\sigma(s)$ according to (B.5.30)

$$\omega \frac{d^7 N_{q\sigma/\pi \rightarrow q\gamma}}{d^3 k d^4 x} = \frac{T e^{\mu/T}}{4\omega(2\pi)^5} \int_{s_0}^{\infty} \frac{ds}{s - m_q^2} e^{-\nu_{\min}(s)/T} \lambda(s, m_q^2, m_{\sigma,\pi}^2) \sigma_{q\sigma/\pi \rightarrow q\gamma}(s). \quad (\text{I.1.5})$$

The annihilation and anti-COMPTON rates are treated analogously:

$$\begin{aligned} \omega \frac{d^7 N_{q\bar{q} \rightarrow \sigma/\pi \gamma}}{d^3 k d^4 x} &= \frac{1}{16\omega(2\pi)^7} \int_{s_0}^{\infty} \frac{ds}{s - m_{\pi,\sigma}^2} \int_{t^-}^{t^+} dt |M(s, t)|^2 \\ &\quad \times \int_{\nu_{\min}}^{\infty} d\nu \int_{E^-}^{E^+} dE \frac{e^{-(E-\mu)/T} e^{-(\nu-E+\mu)/T}}{\sqrt{(E-E^-)(E^+-E)}} \\ &= \frac{T}{4\omega(2\pi)^5} \int_{s_0}^{\infty} \frac{ds}{s - m_{\pi,\sigma}^2} s(s - 4m_q^2) e^{-(\nu_{\min})/T} \sigma_{q\bar{q} \rightarrow \sigma/\pi \gamma}(s), \end{aligned} \quad (\text{I.1.6})$$

$$\begin{aligned} \omega \frac{d^7 N_{\bar{q}\sigma/\pi \rightarrow \bar{q}\gamma}}{d^3 k d^4 x} &= \frac{1}{16\omega(2\pi)^7} \int_{s_0}^{\infty} \frac{ds}{s - m_q^2} \int_{t^-}^{t^+} dt |M(s, t)|^2 \\ &\quad \times \int_{\nu_{\min}}^{\infty} d\nu \int_{E^-}^{E^+} dE \frac{e^{-(E+\mu)/T} e^{-(\nu-E)/T}}{\sqrt{(E-E^-)(E^+-E)}} \\ &= \frac{T e^{-\mu/T}}{4\omega(2\pi)^5} \int_{s_0}^{\infty} \frac{ds}{s - m_q^2} e^{-\nu_{\min}(s)/T} \lambda(s, m_q^2, m_{\sigma,\pi}^2) \sigma_{\bar{q}\sigma/\pi \rightarrow \bar{q}\gamma} \end{aligned} \quad (\text{I.1.7})$$

$$= e^{-2\mu/T} \omega \frac{d^7 N_{q\sigma/\pi \rightarrow q\gamma}}{d^3 k d^4 x}. \quad (\text{I.1.8})$$

Equations (I.1.5), (I.1.6) and (I.1.7) are the result quoted in (4.5.2).

I.2. Approximations for the s integration

To gain some insight into the spectra, the integrand of the s integration is approximated. It is reasonable to assume that the shape of the integrand is dominated by the exponential and that the power law corrections to it (*i.e.* the cross sections as well as the other s -dependent terms beside the exponential) are slowly changing. In this section, the exponent $-\nu_{\min}(s)/T$ is TAYLOR expanded around the largest value in the range of integration. Two

cases have to be considered: either the maximum of the exponent is within the range of integration or it is not. Both cases require different approximations leading to notable differences in the differential photon spectra.

ν_{\min} as well as its first and second derivative *w.r.t.* s are (*cf.* (H.2.6))

$$\nu_{\min} = \frac{s - m_z^2}{4\omega} + \omega + \frac{\omega m_z^2}{s - m_z^2}, \quad (\text{I.2.1})$$

$$\frac{\partial \nu_{\min}}{\partial s} = \frac{1}{4\omega} - \frac{\omega m_z^2}{(s - m_z^2)^2}, \quad (\text{I.2.2})$$

$$\frac{\partial^2 \nu_{\min}}{\partial s^2} = 2 \frac{\omega m_z^2}{(s - m_z^2)^3}. \quad (\text{I.2.3})$$

The extrema are at $s = s_1$ given by

$$s_1 = 2\omega m_z + m_z^2. \quad (\text{I.2.4})$$

The value of ν_{\min} and its second derivative at this point are

$$\nu_{\min}(s_1) = m_z + \omega, \quad (\text{I.2.5})$$

$$\left. \frac{\partial^2 \nu_{\min}}{\partial s^2} \right|_{s=s_1} = \frac{1}{4\omega^2 m_z}. \quad (\text{I.2.6})$$

Two cases are to be distinguished: either the position s_1 of the minimum of ν_{\min} is within the s integration range, *i.e.* $s_1 \geq s_0$ (case a), or it is not, *i.e.* $s_1 < s_0$ (case b).

1.2.1. Case (a), the Gaussian approximation

If $s_1 \geq s_0$ it is reasonable to TAYLOR expand ν_{\min} around its minimum up to second order. The exponential term $\exp\{-\nu_{\min}/T\}$ then becomes a Gaussian which can be integrated:

$$\nu_{\min} = m_z + \omega + \frac{1}{8\omega^2 m_z} (s - s_1)^2 + \mathcal{O}((s - s_1)^3). \quad (\text{I.2.7})$$

The other s -dependent factors besides $\exp\{-\nu_{\min}/T\}$ are expected to vary slowly with s and can be set to their value at the minimum of ν_{\min} . If s_1 and s_0 are not too close ($s_1 - s_0 \gtrsim 2\omega\sqrt{m_z T}$) one makes only a relatively small error by shifting the lower limit to

$-\infty$. Then the integrals in (I.1.5), (I.1.6) and (I.1.8) have the form

$$C \int_{-\infty}^{\infty} dx e^{-\frac{x^2}{2\alpha^2}} = C\sqrt{2\pi\alpha^2} \quad (\text{I.2.8})$$

and can be solved yielding

$$\omega \frac{d^7 N_{q\sigma/\pi \rightarrow q\gamma}}{d^3 k d^4 x} = \frac{T e^{\mu/T}}{4\omega(2\pi)^5} e^{-(m_q+\omega)/T} \sqrt{8\pi\omega^2 m_q T} \frac{\lambda(s_1, m_q^2, m_{\sigma,\pi}^2) \sigma_{q\sigma/\pi \rightarrow q\gamma}(s_1)}{s_1 - m_q^2} \quad (\text{I.2.9})$$

$$= \frac{T e^{\mu/T}}{4\omega(2\pi)^5} e^{-(m_q+\omega)/T} \sqrt{8\pi\omega^2 m_q T} \frac{\lambda(s_1, m_q^2, m_{\sigma,\pi}^2) \sigma_{q\sigma/\pi \rightarrow q\gamma}(s_1)}{2\omega m_q} \quad (\text{I.2.10})$$

$$= \frac{T^{3/2}}{4\omega m_q^{1/2} (2\pi)^{9/2}} e^{-(m_q+\omega-\mu)/T} \lambda(s_1, m_q^2, m_{\sigma,\pi}^2) \sigma_{q\sigma/\pi \rightarrow q\gamma}(s_1), \quad (\text{I.2.11})$$

$$\omega \frac{d^7 N_{q\bar{q} \rightarrow \sigma/\pi \gamma}}{d^3 k d^4 x} = \frac{T^{3/2}}{4\omega m_{\pi,\sigma}^{1/2} (2\pi)^{9/2}} e^{-(m_{\pi,\sigma}+\omega)/T} s_1 (s_1 - 4m_q^2) \sigma_{q\bar{q} \rightarrow \sigma/\pi \gamma}(s_1), \quad (\text{I.2.12})$$

$$\omega \frac{d^7 N_{\bar{q}\sigma/\pi \rightarrow \bar{q}\gamma}}{d^3 k d^4 x} = \frac{T^{3/2}}{4\omega m_q^{1/2} (2\pi)^{9/2}} e^{-(m_q+\omega+\mu)/T} \lambda(s_1, m_q^2, m_{\sigma,\pi}^2) \sigma_{q\sigma/\pi \rightarrow q\gamma}(s_1), \quad (\text{I.2.13})$$

which is the result given in (4.5.8).

I.2.2. Case (b), the exponential approximation

If the minimum of ν_{\min} is outside the integration range it is sufficient to expand ν_{\min} to linear order. The integrand is expanded around s_0 since from there the largest contribution to the integral comes. Thus

$$\begin{aligned} \nu_{\min}(s) &\approx \nu_{\min}(s_0) + \left(\frac{1}{4\omega} - \frac{\omega m_z^2}{\tilde{s}_0^2} \right) (s - s_0) \\ &=: a + b(s - s_0) \end{aligned} \quad (\text{I.2.14})$$

with $a \equiv \nu_{\min}(s_0)$ and $b = (\tilde{s}_0^2 - 4\omega^2 m_z^2)/(4\omega \tilde{s}_0^2)$. Similar to the Gaussian approximation the s dependent factors, except $\exp\{-\nu_{\min}(s)/T\}$, are set to a typical value they obtain within the integration range. As $\exp\{-\nu_{\min}(s)/T\}$ is largest at $s = s_0$ these s dependent factors are evaluated at $s = s_0$. However, in certain regions of the phase diagram some of these factors are not defined at s_0 . In this case, the evaluation at s_0 is understood as the

limit when $s \rightarrow s_0$. With

$$C \int_{s_0}^{\infty} ds e^{-a/T - b/T(s-s_0)} = C e^{-a/T} \frac{T}{b} \quad (\text{I.2.15})$$

the integrals in (I.1.5), (I.1.6) and (I.1.8) can be evaluated with the results

$$\omega \frac{d^7 N_{q\sigma/\pi \rightarrow q\gamma}}{d^3 k d^4 x} = \frac{T^2 e^{\mu/T}}{4\omega(2\pi)^5} \frac{\lambda(s_2, m_q^2, m_{\sigma,\pi}^2) \sigma_{q\sigma/\pi \rightarrow q\gamma}(s_2)}{b(s_0 - m_q^2)} e^{-a/T} \quad (\text{I.2.16})$$

$$= \frac{T^2 e^{-a/T}}{(2\pi)^5} e^{\mu/T} \frac{(s_0 - m_q^2) \lambda(s_0, m_q^2, m_{\sigma,\pi}^2) \sigma_{q\sigma/\pi \rightarrow q\gamma}(s_0)}{(s_0 - m_q^2)^2 - 4\omega^2 m_q^2}, \quad (\text{I.2.17})$$

$$\omega \frac{d^7 N_{q\bar{q} \rightarrow \sigma/\pi\gamma}}{d^3 k d^4 x} = \frac{T^2}{4\omega(2\pi)^5 b} e^{-a/T} \frac{s(s - 4m_q^2)}{s - m_{\pi,\sigma}^2} \sigma_{q\bar{q} \rightarrow \sigma/\pi\gamma}(s) \quad (\text{I.2.18})$$

$$= \frac{T^2 e^{-a/T}}{(2\pi)^5} \frac{(s_0 - m_{\sigma,\pi}^2) s_0 (s_0 - 4m_q^2)}{(s_0 - m_{\sigma,\pi}^2)^2 - 4\omega^2 m_{\sigma,\pi}^2} \sigma_{q\bar{q} \rightarrow \sigma/\pi\gamma}(s), \quad (\text{I.2.19})$$

and the anti-COMPTON emissivity $\omega d^7 N_{q\sigma/\pi \rightarrow \bar{q}\gamma} / d^3 k d^4 x$ according to (I.1.8). Although the annihilation matrix elements diverge for $s \rightarrow s_0$ if $m_{\sigma,\pi} \geq 2m_q$ the complete expression (I.2.19) does not. However, for the ease of notation the prescription of taking the limit is suppressed.

Bibliography

- [A⁺96] R. ALBRECHT ET AL.: *Limits on the production of direct photons in 200-A/GeV S-32 + Au collisions.* Phys. Rev. Lett. **76**, 3506 (1996)
- [A⁺98] G. AGAKISHIEV ET AL.: *Low mass $e^+ e^-$ pair production in 158/A-GeV Pb - Au collisions at the CERN SPS, its dependence on multiplicity and transverse momentum.* Phys. Lett. **B422**, 405 (1998)
- [A⁺99a] K. ACKERSTAFF ET AL.: *Measurement of the strong coupling constant $\alpha(s)$ and the vector and axial vector spectral functions in hadronic tau decays.* Eur. Phys. J. **C7**, 571 (1999)
- [A⁺99b] H. APPELSHAUSER ET AL.: *Baryon stopping and charged particle distributions in central Pb + Pb collisions at 158-GeV per nucleon.* Phys. Rev. Lett. **82**, 2471 (1999)
- [A⁺00a] M. C. ABREU ET AL.: *Dimuon and charm production in nucleus-nucleus collisions at the CERN SPS.* Eur. Phys. J. **C14**, 443 (2000)
- [A⁺00b] M. M. AGGARWAL ET AL.: *Observation of direct photons in central 158-A-GeV Pb-208 + Pb-208 collisions.* Phys. Rev. Lett. **85**, 3595 (2000)
- [A⁺00c] A. L. S. ANGELIS ET AL.: *Excess of continuum dimuon production at masses between threshold and the J / Psi in S - W interactions at 200-GeV/c/nucleon.* Eur. Phys. J. **C13**, 433 (2000)
- [A⁺03] D. ADAMOVA ET AL.: *Enhanced production of low mass electron pairs in 40-AGeV Pb - Au collisions at the CERN SPS.* Phys. Rev. Lett. **91**, 042301 (2003)
- [A⁺05a] G. AGAKICHIEV ET AL.: *$e^+ e^-$ pair production in Pb - Au collisions at 158-GeV per nucleon.* Eur. Phys. J. **C41**, 475 (2005)
- [A⁺05b] I. ARSENE ET AL.: *Quark gluon plasma and color glass condensate at RHIC? The Perspective from the BRAHMS experiment.* Nucl. Phys. **A757**, 1 (2005)

- [A⁺08a] D. ADAMOVA ET AL.: *Modification of the rho-meson detected by low-mass electron-positron pairs in central Pb-Au collisions at 158-A-GeV/c*. Phys. Lett. **B666**, 425 (2008)
- [A⁺08b] G. AGAKISHIEV ET AL.: *Study of dielectron production in C+C collisions at 1-A-GeV*. Phys. Lett. **B663**, 43 (2008)
- [A⁺08c] C. ALT ET AL.: *Pion and kaon production in central Pb + Pb collisions at 20-A and 30-A-GeV: Evidence for the onset of deconfinement*. Phys. Rev. **C77**, 024903 (2008)
- [A⁺09a] R. ARNALDI ET AL.: *Evidence for the production of thermal-like muon pairs with masses above 1-GeV/c**2 in 158-A-GeV Indium-Indium Collisions*. Eur. Phys. J. **C59**, 607 (2009)
- [A⁺09b] R. ARNALDI ET AL.: *NA60 results on thermal dimuons*. Eur. Phys. J. **C61**, 711 (2009)
- [A⁺10a] A. ADARE ET AL.: *Detailed measurement of the e⁺e⁻ pair continuum in p + p and Au+Au collisions at $\sqrt{s_{NN}} = 200$ GeV and implications for direct photon production*. Phys. Rev. **C81**, 034911 (2010)
- [A⁺10b] A. ADARE ET AL.: *Enhanced production of direct photons in Au+Au collisions at $\sqrt{s_{NN}} = 200$ GeV and implications for the initial temperature*. Phys. Rev. Lett. **104**, 132301 (2010)
- [A⁺12a] A. ADARE ET AL.: *Evolution of π^0 suppression in Au+Au collisions from $\sqrt{s_{NN}} = 39$ to 200 GeV*. Phys. Rev. Lett. **109**, 152301 (2012)
- [A⁺12b] A. ADARE ET AL.: *J/ ψ suppression at forward rapidity in Au+Au collisions at $\sqrt{s_{NN}} = 39$ and 62.4 GeV*. Phys. Rev. **C86**, 064901 (2012)
- [A⁺12c] A. ADARE ET AL.: *Observation of direct-photon collective flow in $\sqrt{s_{NN}} = 200$ GeV Au+Au collisions*. Phys. Rev. Lett. **109**, 122302 (2012)
- [A⁺12d] S. AFANASIEV ET AL.: *Measurement of Direct Photons in Au+Au Collisions at $\sqrt{s_{NN}} = 200$ GeV*. Phys. Rev. Lett. **109**, 152302 (2012)
- [A⁺13] L. ADAMCZYK ET AL.: *Elliptic flow of identified hadrons in Au+Au collisions at $\sqrt{s_{NN}} = 7.7$ -62.4 GeV*. Phys. Rev. **C88**, 014902 (2013)
- [A⁺14a] L. ADAMCZYK ET AL.: *Beam-energy dependence of charge separation along the magnetic field in Au+Au collisions at RHIC*. Phys. Rev. Lett. **113**, 052302 (2014)
- [A⁺14b] L. ADAMCZYK ET AL.: *Beam energy dependence of moments of the net-*

- charge multiplicity distributions in Au+Au collisions at RHIC.* Phys. Rev. Lett. **113**, 092301 (2014)
- [A⁺14c] L. ADAMCZYK ET AL.: *Energy Dependence of Moments of Net-proton Multiplicity Distributions at RHIC.* Phys. Rev. Lett. **112**, 032302 (2014)
- [A⁺15] N. M. ABDELWAHAB ET AL.: *Energy Dependence of K/π , p/π , and K/p Fluctuations in Au+Au Collisions from $\sqrt{s_{NN}} = 7.7$ to 200 GeV.* Phys. Rev. **C92**, 021901 (2015)
- [ABMN08] M. ASAKAWA, S. A. BASS, B. MÜLLER AND C. NONAKA: *Transverse Velocity Dependence of the Proton-Antiproton Ratio as a Signature of the QCD Critical Point.* Phys. Rev. Lett. **101**, 122302 (2008)
- [ABMRS11] A. ANDRONIC, P. BRAUN-MUNZINGER, K. REDLICH AND J. STACHEL: *The thermal model on the verge of the ultimate test: particle production in Pb-Pb collisions at the LHC.* J. Phys. **G38**, 124081 (2011)
- [ADD16] N. G. ANTONIOU, N. DAVIS AND F. K. DIAKONOS: *Has the QCD critical point been observed at RHIC?* arXiv:1607.01326 [nucl-th] (2016)
- [AF85] I. J. R. AITCHISON AND C. M. FRASER: *Derivative Expansions of Fermion Determinants: Anomaly Induced Vertices, Goldstone-Wilczek Currents and Skyrme Terms.* Phys. Rev. **D31**, 2605 (1985)
- [AFKS06] Y. AOKI, Z. FODOR, S. D. KATZ AND K. K. SZABO: *The QCD transition temperature: Results with physical masses in the continuum limit.* Phys. Lett. **B643**, 46 (2006)
- [AGKZ98] P. AURENCHE, F. GELIS, R. KOBES AND H. ZARAKET: *Bremsstrahlung and photon production in thermal QCD.* Phys. Rev. **D58**, 085003 (1998)
- [AGZ00a] P. AURENCHE, F. GELIS AND H. ZARAKET: *KLN theorem, magnetic mass, and thermal photon production.* Phys. Rev. **D61**, 116001 (2000)
- [AGZ00b] P. AURENCHE, F. GELIS AND H. ZARAKET: *Landau-Pomeranchuk-Migdal effect in thermal field theory.* Phys. Rev. **D62**, 096012 (2000)
- [AHM00] M. ASAKAWA, U. W. HEINZ AND B. MÜLLER: *Fluctuation probes of quark deconfinement.* Phys. Rev. Lett. **85**, 2072 (2000)
- [AIS12] H. ABUKI, D. ISHIBASHI AND K. SUZUKI: *Crystalline chiral condensates off the tricritical point in a generalized Ginzburg-Landau approach.* Phys. Rev. **D85**, 074002 (2012)

- [ALZ15] A. AYALA, M. LOEWE AND R. ZAMORA: *Inverse magnetic catalysis in the linear sigma model with quarks*. Phys. Rev. **D91**, 016002 (2015)
- [AMY01a] P. B. ARNOLD, G. D. MOORE AND L. G. YAFFE: *Photon emission from quark gluon plasma: Complete leading order results*. JHEP **12**, 009 (2001)
- [AMY01b] P. B. ARNOLD, G. D. MOORE AND L. G. YAFFE: *Photon emission from ultrarelativistic plasmas*. JHEP **11**, 057 (2001)
- [AMY02] P. B. ARNOLD, G. D. MOORE AND L. G. YAFFE: *Photon and gluon emission in relativistic plasmas*. JHEP **06**, 030 (2002)
- [And16] E. ANDRONOV: *Transverse momentum and multiplicity fluctuations in Ar+Sc collisions at the CERN SPS from NA61/SHINE*. In ‘10th International Workshop on Critical Point and Onset of Deconfinement (CPOD 2016) Wroclaw, Poland, May 30-June 4, 2016’, (2016)
- [ASRS08] M. G. ALFORD, A. SCHMITT, K. RAJAGOPAL AND T. SCHÄFER: *Color superconductivity in dense quark matter*. Rev. Mod. Phys. **80**, 1455 (2008)
- [AvS01] R. ALKOEFER AND L. VON SMEKAL: *The Infrared behavior of QCD Green’s functions: Confinement dynamical symmetry breaking, and hadrons as relativistic bound states*. Phys. Rept. **353**, 281 (2001)
- [B+96] R. BAUR ET AL.: *Search for direct photons from S - Au collisions at 200-GeV/u*. Z. Phys. **C71**, 571 (1996)
- [B+98a] R. BARATE ET AL.: *Measurement of the spectral functions of axial - vector hadronic τ decays and determination of $\alpha_s(M_\tau^2)$* . Eur. Phys. J. **C4**, 409 (1998)
- [B+98b] S. A. BASS ET AL.: *Microscopic models for ultrarelativistic heavy ion collisions*. Prog. Part. Nucl. Phys. **41**, 255 (1998)
- [B+01] B. B. BACK ET AL.: *Baryon rapidity loss in relativistic Au+Au collisions*. Phys. Rev. Lett. **86**, 1970 (2001)
- [B+12] A. BAZAVOV ET AL.: *The chiral and deconfinement aspects of the QCD transition*. Phys. Rev. **D85**, 054503 (2012)
- [B+17] A. BAZAVOV ET AL.: *The QCD Equation of State to $\mathcal{O}(\mu_B^6)$ from Lattice QCD* (2017)
- [Bay62] G. BAYM: *Selfconsistent approximation in many body systems*. Phys. Rev. **127**, 1391 (1962)
- [BB10a] B. BÄUCHLE AND M. BLEICHER: *Direct photon calculations in heavy-ion*

- collisions at $\sqrt{s_{NN}} = 62.4 - 200$ AGeV in a (3+1) dimensional hybrid approach.* Phys. Rev. **C82**, 064901 (2010)
- [BB10b] B. BÄUCHLE AND M. BLEICHER: *Hybrid model calculations of direct photons in high-energy nuclear collisions.* Phys. Rev. **C81**, 044904 (2010)
- [BBF⁺15] R. BELLWIED, S. BORSANYI, Z. FODOR, J. GÜNTHER, S. D. KATZ, C. RATTI AND K. K. SZABO: *The QCD phase diagram from analytic continuation.* Phys. Lett. **B751**, 559 (2015)
- [BC15] M. BUBALLA AND S. CARIGNANO: *Inhomogeneous chiral condensates.* Prog. Part. Nucl. Phys. **81**, 39 (2015)
- [BDM⁺14] C. BONATI, M. D'ELIA, M. MARITI, M. MESITI, F. NEGRO AND F. SANFILIPPO: *Curvature of the chiral pseudocritical line in QCD.* Phys. Rev. **D90**, 114025 (2014)
- [BGG⁺12] O. BUSS, T. GAITANOS, K. GALLMEISTER, H. VAN HEES, M. KASKULOV, O. LALAKULICH, A. B. LARIONOV, T. LEITNER, J. WEIL AND U. MOSEL: *Transport-theoretical Description of Nuclear Reactions.* Phys. Rept. **512**, 1 (2012)
- [BI02] J.-P. BLAIZOT AND E. IANCU: *The Quark gluon plasma: Collective dynamics and hard thermal loops.* Phys. Rept. **359**, 355 (2002)
- [BK61] G. BAYM AND L. P. KADANOFF: *Conservation Laws and Correlation Functions.* Phys. Rev. **124**, 287 (1961)
- [BK73] E. BYCKLING AND K. KAJANTIE: *Particle kinematics*, Wiley, London (1973). ISBN 0471128856
- [BK09] E. S. BOWMAN AND J. I. KAPUSTA: *Critical Points in the Linear Sigma Model with Quarks.* Phys. Rev. **C79**, 015202 (2009)
- [BKM99] S. BINNER, J. H. KUHN AND K. MELNIKOV: *Measuring sigma($e^+e^- \rightarrow$ hadrons) using tagged photon.* Phys. Lett. **B459**, 279 (1999)
- [BNNR92] R. BAIER, H. NAKKAGAWA, A. NIEGAWA AND K. REDLICH: *Production rate of hard thermal photons and screening of quark mass singularity.* Z. Phys. **C53**, 433 (1992)
- [BP90] E. BRAATEN AND R. D. PISARSKI: *Soft Amplitudes in Hot Gauge Theories: A General Analysis.* Nucl. Phys. **B337**, 569 (1990)
- [BR00] B. BERDNIKOV AND K. RAJAGOPAL: *Slowing out-of-equilibrium near the QCD critical point.* Phys. Rev. **D61**, 105017 (2000)

- [BSSB14] T. BEISITZER, R. STIELE AND J. SCHAFFNER-BIELICH: *Supernova Equation of State with an extended $SU(3)$ Quark-Meson Model*. Phys. Rev. **D90**, 085001 (2014)
- [Bul79] M. BULMER: *Principles of Statistics*, Dover Publications (1979). ISBN 9780486637600
- [CB09] W. CASSING AND E. L. BRATKOVSKAYA: *Parton-Hadron-String Dynamics: an off-shell transport approach for relativistic energies*. Nucl. Phys. **A831**, 215 (2009)
- [CBS14] S. CARIGNANO, M. BUBALLA AND B.-J. SCHAEFER: *Inhomogeneous phases in the quark-meson model with vacuum fluctuations*. Phys. Rev. **D90**, 014033 (2014)
- [CG07] W. N. COTTINGHAM AND D. A. GREENWOOD: *An introduction to the standard model of particle physics*, Cambridge Univ. Press, Cambridge (2007). ISBN 0521852498
- [CHYZ89] M. E. CARRINGTON, T. H. HANSSON, H. YAMAGISHI AND I. ZAHED: *Linear Response of Hot Gluons*. Annals Phys. **190**, 373 (1989)
- [CJJ⁺74] A. CHODOS, R. L. JAFFE, K. JOHNSON, C. B. THORN AND V. F. WEISKOPF: *A New Extended Model of Hadrons*. Phys. Rev. **D9**, 3471 (1974)
- [CJT74] J. M. CORNWALL, R. JACKIW AND E. TOMBOULIS: *Effective Action for Composite Operators*. Phys. Rev. **D10**, 2428 (1974)
- [CORW06] J. CLEYMANS, H. OESCHLER, K. REDLICH AND S. WHEATON: *Comparison of chemical freeze-out criteria in heavy-ion collisions*. Phys. Rev. **C73**, 034905 (2006)
- [Cow80] R. A. COWLEY: *Structural phase transitions I – Landau theory*. Advances in Physics **29** 1, 1 (1980)
- [CR99] J. CLEYMANS AND K. REDLICH: *Chemical and thermal freezeout parameters from 1 to 200 AGeV*. Phys. Rev. **C60**, 054908 (1999)
- [Cut60] R. E. CUTKOSKY: *Singularities and discontinuities of Feynman amplitudes*. J. Math. Phys. **1**, 429 (1960)
- [CW73] S. R. COLEMAN AND E. J. WEINBERG: *Radiative Corrections as the Origin of Spontaneous Symmetry Breaking*. Phys. Rev. **D7**, 1888 (1973)
- [Das06] A. DAS: *Field theory : a path integral approach*, World Scientific, Hackensack, NJ (2006) 2nd edn. ISBN 9812568476

- [Das15] S. DAS: *Chemical freeze-out parameters in Beam Energy Scan Program of STAR at RHIC*. EPJ Web Conf. **90**, 10003 (2015)
- [DATD16] A. M. DIAB, A. I. AHMADOV, A. N. TAWFIK AND E. A. E. DAHAB: *SU(4) Polyakov linear-sigma model at finite temperature and density*. In ‘38th International Conference on High Energy Physics (ICHEP 2016) Chicago, IL, USA, August 03-10, 2016’, (2016)
- [dFP02] P. DE FORCRAND AND O. PHILIPSEN: *The QCD phase diagram for small densities from imaginary chemical potential*. Nucl. Phys. **B642**, 290 (2002)
- [DKM15] H.-T. DING, F. KARSCH AND S. MUKHERJEE: *Thermodynamics of strong-interaction matter from Lattice QCD*. Int. J. Mod. Phys. **E24**, 1530007 (2015)
- [EGR15] W. I. ESHRAIM, F. GIACOSA AND D. H. RISCHKE: *Phenomenology of charmed mesons in the extended Linear Sigma Model*. Eur. Phys. J. **A51**, 112 (2015)
- [EHKT88] H. T. ELZE, U. W. HEINZ, K. KAJANTIE AND T. TOIMELA: *High Temperature Gluon Matter in the Background Gauge*. Z. Phys. **C37**, 305 (1988)
- [FAR17] B. FRIMAN, G. ALMASI AND K. REDLICH: *Modeling chiral criticality*. Acta Physica Polonica B **CPOD 2016** (2017)
- [FGP12] G. N. FERRARI, A. F. GARCIA AND M. B. PINTO: *Chiral Transition Within Effective Quark Models Under Magnetic Fields*. Phys. Rev. **D86**, 096005 (2012)
- [FHK⁺11] B. FRIMAN, C. HOHNE, J. KNOLL, S. LEUPOLD, J. RANDRUP, R. RAPP AND P. SENGER, (eds.): *The CBM physics book: Compressed baryonic matter in laboratory experiments* vol. 814 of *Lect. Notes Phys.*, Springer, Berlin (2011)
- [Fis06] C. S. FISCHER: *Infrared properties of QCD from Dyson-Schwinger equations*. J. Phys. **G32**, R253 (2006)
- [FK02] Z. FODOR AND S. D. KATZ: *A New method to study lattice QCD at finite temperature and chemical potential*. Phys. Lett. **B534**, 87 (2002)
- [FKP10] L. FERRONI, V. KOCH AND M. B. PINTO: *Multiple Critical Points in Effective Quark Models*. Phys. Rev. **C82**, 055205 (2010)
- [FKRS11] B. FRIMAN, F. KARSCH, K. REDLICH AND V. SKOKOV: *Fluctuations as probe of the QCD phase transition and freeze-out in heavy ion collisions at LHC and RHIC*. Eur. Phys. J. **C71**, 1694 (2011)

- [FKS07] Z. FODOR, S. D. KATZ AND C. SCHMIDT: *The Density of states method at non-zero chemical potential*. JHEP **03**, 121 (2007)
- [Flo10] W. FLORKOWSKI: *Phenomenology of ultra-realistic heavy-ion collisions*, World Scientific, Singapore (2010). ISBN 9789814280662
- [FM07] E. FRAGA AND A. MOCSY: *Connecting an effective model of confinement and chiral symmetry to lattice QCD*. Braz. J. Phys. **37**, 281 (2007)
- [FP67] L. D. FADDEEV AND V. N. POPOV: *Feynman Diagrams for the Yang-Mills Field*. Phys. Lett. **B25**, 29 (1967)
- [FP97] B. FRIMAN AND H. J. PIRNER: *P wave polarization of the rho meson and the dilepton spectrum in dense matter*. Nucl. Phys. **A617**, 496 (1997)
- [Fra85] C. M. FRASER: *Calculation of Higher Derivative Terms in the One Loop Effective Lagrangian*. Z. Phys. **C28**, 101 (1985)
- [Fri96] B. FRIMAN: *Medium effects in low mass lepton pair production*. Nucl. Phys. **A610**, 358C (1996)
- [Fri14] B. FRIMAN: *Probing the QCD phase diagram with fluctuations*. Nucl. Phys. **A928**, 198 (2014)
- [Fuk08] K. FUKUSHIMA: *Phase diagrams in the three-flavor Nambu-Jona-Lasinio model with the Polyakov loop*. Phys. Rev. **D77**, 114028 (2008). [Erratum: Phys. Rev.D78,039902 (2008)]
- [Gal10] C. GALE: *Photon Production in Hot and Dense Strongly Interacting Matter*. Landolt-Börnstein **23**, 445 (2010)
- [Gaz08] M. GAZDZICKI: *Onset of Deconfinement and Critical Point: NA49 and NA61/SHINE at the CERN SPS*. Eur. Phys. J. ST **155**, 37 (2008)
- [GHJ+15] C. GALE, Y. HIDAKA, S. JEON, S. LIN, J.-F. PAQUET, R. D. PISARSKI, D. SATOW, V. V. SKOKOV AND G. VUJANOVIC: *Production and Elliptic Flow of Dileptons and Photons in a Matrix Model of the Quark-Gluon Plasma*. Phys. Rev. Lett. **114**, 072301 (2015)
- [Gie12] H. GIES: *Introduction to the functional RG and applications to gauge theories*. Lect. Notes Phys. **852**, 287 (2012)
- [GK91] C. GALE AND J. I. KAPUSTA: *Vector dominance model at finite temperature*. Nucl. Phys. **B357**, 65 (1991)
- [GML60] M. GELL-MANN AND M. LEVY: *The axial vector current in beta decay*. Nuovo Cim. **16**, 705 (1960)

-
- [GMOR68] M. GELL-MANN, R. J. OAKES AND B. RENNER: *Behavior of current divergences under $SU(3) \times SU(3)$* . Phys. Rev. **175**, 2195 (1968)
- [GSW62] J. GOLDSTONE, A. SALAM AND S. WEINBERG: *Broken Symmetries*. Phys. Rev. **127**, 965 (1962)
- [GSZ13] V. V. GOLOVIZNIN, A. M. SNIGIREV AND G. M. ZINOVJEV: *Towards azimuthal anisotropy of direct photons*. JETP Lett. **98**, 61 (2013)
- [GT12] U. S. GUPTA AND V. K. TIWARI: *Revisiting the Phase Structure of the Polyakov-quark-meson Model in the presence of Vacuum Fermion Fluctuation*. Phys. Rev. **D85**, 014010 (2012)
- [Haw75] S. W. HAWKING: *Particle Creation by Black Holes*. Commun. Math. Phys. **43**, 199 (1975)
- [Hei09] U. W. HEINZ: *Early collective expansion: Relativistic hydrodynamics and the transport properties of QCD matter*. Landolt-Börnstein **23**, 240 (2009)
- [Heu11] J. M. HEUSER: *The Compressed Baryonic Matter Experiment at FAIR*. EPJ Web Conf. **13**, 03001 (2011)
- [HHR16] N. P. M. HOLT, P. M. HOHLER AND R. RAPP: *Thermal photon emission from the $\pi\rho\omega$ system*. Nucl. Phys. **A945**, 1 (2016)
- [HK94] T. HATSUDA AND T. KUNIHIRO: *QCD phenomenology based on a chiral effective Lagrangian*. Phys. Rept. **247**, 221 (1994)
- [HPS11] T. K. HERBST, J. M. PAWLOWSKI AND B.-J. SCHAEFER: *The phase structure of the Polyakov-quark-meson model beyond mean field*. Phys. Lett. **B696**, 58 (2011)
- [Hö14] C. HÖHNE: *Measurement of dileptons with the CBM experiment at FAIR*. Nucl. Phys. **A931**, 735 (2014)
- [Ios15] I. IOSILEVSKIY: *Entropic and enthalpic phase transitions in high energy density nuclear matter*. In ‘Compact Stars in the QCD Phase Diagram IV Prerow, Germany, September 26-30, 2014’, (2015)
- [IZ05] C. ITZYKSON AND J.-B. ZUBER: *Quantum field theory*, Dover Publications, Mineola (2005). ISBN 0486445682
- [K⁺16] F. KARSCH ET AL.: *Conserved Charge Fluctuations from Lattice QCD and the Beam Energy Scan*. Nucl. Phys. **A956**, 352 (2016)
- [KBHP16] I. KARPENKO, M. BLEICHER, P. HUOVINEN AND H. PETERSEN: *Estimat-*

- ing η/s of QCD matter at high baryon densities.* J. Phys. Conf. Ser. **668**, 012063 (2016)
- [KG06] J. I. KAPUSTA AND C. GALE: *Finite-temperature field theory: Principles and applications*, Cambridge University Press, Cambridge (2006). ISBN 9780521820820
- [KH] P. F. KOLB AND U. W. HEINZ: *Hydrodynamic description of ultrarelativistic heavy ion collisions.* arXiv:0305084 [nucl-th]
- [KHB14] I. KARPENKO, P. HUOVINEN AND M. BLEICHER: *A 3+ 1 dimensional viscous hydrodynamic code for relativistic heavy ion collisions.* Computer Physics Communications **185**, 3016 (2014)
- [KKL⁺11] O. KACZMAREK, F. KARSCH, E. LAERMANN, C. MIAO, S. MUKHERJEE, P. PETRECKY, C. SCHMIDT, W. SOELDNER AND W. UNGER: *Phase boundary for the chiral transition in (2+1) -flavor QCD at small values of the chemical potential.* Phys. Rev. **D83**, 014504 (2011)
- [KKM05] M. KAWASAKI, K. KOHRI AND T. MOROI: *Big-Bang nucleosynthesis and hadronic decay of long-lived massive particles.* Phys. Rev. **D71**, 083502 (2005)
- [KKW96] F. KLINGL, N. KAISER AND W. WEISE: *Effective Lagrangian approach to vector mesons, their structure and decays.* Z. Phys. **A356**, 193 (1996)
- [KLS91] J. I. KAPUSTA, P. LICHARD AND D. SEIBERT: *High-energy photons from quark - gluon plasma versus hot hadronic gas.* Phys. Rev. **D44**, 2774 (1991). [Erratum: Phys. Rev. D47, 4171 (1993)]
- [Koc97] V. KOCH: *Aspects of chiral symmetry.* Int. J. Mod. Phys. **E6**, 203 (1997)
- [KR11] F. KARSCH AND K. REDLICH: *Probing freeze-out conditions in heavy ion collisions with moments of charge fluctuations.* Phys. Lett. **B695**, 136 (2011)
- [KSS05] P. KOVTUN, D. T. SON AND A. O. STARINETS: *Viscosity in strongly interacting quantum field theories from black hole physics.* Phys. Rev. Lett. **94**, 111601 (2005)
- [KSW16] P. KOVÁCS, Z. SZÉP AND G. WOLF: *Existence of the critical endpoint in the vector meson extended linear sigma model.* Phys. Rev. **D93**, 114014 (2016)
- [KT09] T. KAHARA AND K. TUOMINEN: *Effective models of two-flavor QCD: From small towards large $m(q)$.* Phys. Rev. **D80**, 114022 (2009)

- [Kug97] T. KUGO: *Eichtheorie*, Springer, Berlin , Heidelberg (1997). ISBN 354062063X
- [L⁺94] C. LOURENCO ET AL.: *J / psi, psi-prime and muon pair production in p - W and S - U collisions*. Nucl. Phys. **A566**, 77C (1994)
- [Lac15] R. A. LACEY: *Indications for a Critical End Point in the Phase Diagram for Hot and Dense Nuclear Matter*. Phys. Rev. Lett. **114**, 142301 (2015)
- [Lat12] J. M. LATTIMER: *The nuclear equation of state and neutron star masses*. Ann. Rev. Nucl. Part. Sci. **62**, 485 (2012)
- [LBC15] O. LINNYK, E. L. BRATKOVSKAYA AND W. CASSING: *Direct photon production in heavy-ion collisions at RHIC and LHC*. PoS **BaldinISHEP-PXXII**, 084 (2015)
- [Lee69] B. W. LEE: *Renormalization of the sigma model*. Nucl. Phys. **B9**, 649 (1969)
- [LFK⁺13] P. M. LO, B. FRIMAN, O. KACZMAREK, K. REDLICH AND C. SASAKI: *Polyakov loop fluctuations in SU(3) lattice gauge theory and an effective gluon potential*. Phys. Rev. **D88**, 074502 (2013)
- [Lin80] A. D. LINDE: *Infrared Problem in Thermodynamics of the Yang-Mills Gas*. Phys. Lett. **B96**, 289 (1980)
- [LKCB13] O. LINNYK, V. P. KONCHAKOVSKI, W. CASSING AND E. L. BRATKOVSKAYA: *Photon elliptic flow in relativistic heavy-ion collisions: hadronic versus partonic sources*. Phys. Rev. **C88**, 034904 (2013)
- [LKS⁺15] O. LINNYK, V. KONCHAKOVSKI, T. STEINERT, W. CASSING AND E. L. BRATKOVSKAYA: *Hadronic and partonic sources of direct photons in relativistic heavy-ion collisions*. Phys. Rev. **C92**, 054914 (2015)
- [LL80] L. D. LANDAU AND E. M. LIFSCHITZ: *Relativistische Quantentheorie [1/2]*, Akad.-Verl., Berlin (1980) 4th edn.
- [LNT⁺15] T.-G. LEE, E. NAKANO, Y. TSUE, T. TATSUMI AND B. FRIMAN: *Landau-Peierls instability in a Fulde-Ferrell type inhomogeneous chiral condensed phase*. Phys. Rev. **D92**, 034024 (2015)
- [LR00] J. T. LENAGHAN AND D. H. RISCHKE: *The O(N) model at finite temperature: Renormalization of the gap equations in Hartree and large N approximation*. J. Phys. **G26**, 431 (2000)
- [LRSB00] J. T. LENAGHAN, D. H. RISCHKE AND J. SCHAFFNER-BIELICH: *Chiral*

- symmetry restoration at nonzero temperature in the $SU(3)_r \times SU(3)_l$ linear sigma model.* Phys. Rev. **D62**, 085008 (2000)
- [LTJ⁺14] R. A. LACEY, A. TARANENKO, J. JIA, D. REYNOLDS, N. N. AJITANAND, J. M. ALEXANDER, Y. GU AND A. MWAI: *Beam energy dependence of the viscous damping of anisotropic flow in relativistic heavy ion collisions.* Phys. Rev. Lett. **112**, 082302 (2014)
- [LX17] X. LUO AND N. XU: *Search for the QCD Critical Point with Fluctuations of Conserved Quantities in Relativistic Heavy-Ion Collisions at RHIC : An Overview.* Nucl. Sci. Tech. **28**, 112 (2017)
- [MBC⁺13] R. MARTY, E. BRATKOVSKAYA, W. CASSING, J. AICHELIN AND H. BERREHRAH: *Transport coefficients from the Nambu-Jona-Lasinio model for $SU(3)_f$.* Phys. Rev. **C88**, 045204 (2013)
- [McD15] D. McDONALD: *Overview of results from phase I of the Beam Energy Scan program at RHIC.* EPJ Web Conf. **95**, 01009 (2015)
- [MCF10] A. J. MIZHER, M. N. CHERNODUB AND E. S. FRAGA: *Phase diagram of hot QCD in an external magnetic field: possible splitting of deconfinement and chiral transitions.* Phys. Rev. **D82**, 105016 (2010)
- [MFR15] K. MORITA, B. FRIMAN AND K. REDLICH: *Criticality of the net-baryon number probability distribution at finite density.* Phys. Lett. **B741**, 178 (2015)
- [MME04] A. MOCSY, I. MISHUSTIN AND P. ELLIS: *Role of fluctuations in the linear sigma model with quarks.* Phys. Rev. **C70**, 015204 (2004)
- [MMY17] A. MONNAI, S. MUKHERJEE AND Y. YIN: *Phenomenological Consequences of Enhanced Bulk Viscosity Near the QCD Critical Point.* Phys. Rev. **C95**, 034902 (2017)
- [MT85] L. D. MCLERRAN AND T. TOIMELA: *Photon and Dilepton Emission from the Quark - Gluon Plasma: Some General Considerations.* Phys. Rev. **D31**, 545 (1985)
- [Mus11] G. MUSULMANBEKOV: *The NICA/MPD project at JINR.* Nucl. Phys. **A862-863**, 244 (2011)
- [NA05] C. NONAKA AND M. ASAKAWA: *Hydrodynamical evolution near the QCD critical end point.* Phys. Rev. **C71**, 044904 (2005)
- [Nah16] M. NAHRGANG: *The QCD Critical Point and Related Observables.* Nucl. Phys. **A956**, 83 (2016)

- [NS06] G. M. NEWMAN AND D. T. SON: *Response of strongly-interacting matter to magnetic field: Some exact results*. Phys. Rev. **D73**, 045006 (2006)
- [NSS⁺10] E. NAKANO, B. J. SCHAEFER, B. STOKIC, B. FRIMAN AND K. REDLICH: *Fluctuations and isentropes near the chiral critical endpoint*. Phys. Lett. **B682**, 401 (2010)
- [NT05] E. NAKANO AND T. TATSUMI: *Chiral symmetry and density wave in quark matter*. Phys. Rev. **D71**, 114006 (2005)
- [O⁺14] K. A. OLIVE ET AL.: *Review of Particle Physics*. Chin. Phys. **C38**, 090001 (2014)
- [Oll08] J.-Y. OLLITRAULT: *Relativistic hydrodynamics for heavy-ion collisions*. Eur. J. Phys. **29**, 275 (2008)
- [P⁺97] R. J. PORTER ET AL.: *Dielectron cross-section measurements in nucleus-nucleus reactions at 1-A/GeV*. Phys. Rev. Lett. **79**, 1229 (1997)
- [PGR10] D. PARGANLIJA, F. GIACOSA AND D. H. RISCHKE: *Vacuum Properties of Mesons in a Linear Sigma Model with Vector Mesons and Global Chiral Invariance*. Phys. Rev. **D82**, 054024 (2010)
- [PKW⁺13] D. PARGANLIJA, P. KOVACS, G. WOLF, F. GIACOSA AND D. H. RISCHKE: *Meson vacuum phenomenology in a three-flavor linear sigma model with (axial-)vector mesons*. Phys. Rev. **D87**, 014011 (2013)
- [PS95] M. E. PESKIN AND D. V. SCHROEDER: *An Introduction to quantum field theory*, Westview Press, Boulder (1995). ISBN 9780201503975
- [PSD03] K. PAECH, H. STÖCKER AND A. DUMITRU: *Hydrodynamics near a chiral critical point*. Phys. Rev. **C68**, 044907 (2003)
- [PW84] R. D. PISARSKI AND F. WILCZEK: *Remarks on the Chiral Phase Transition in Chromodynamics*. Phys. Rev. **D29**, 338 (1984)
- [Ran04] J. RANDRUP: *Spinodal decomposition during the hadronization stage at RHIC?* Phys. Rev. Lett. **92**, 122301 (2004)
- [Rap11] R. RAPP: *Theory of Soft Electromagnetic Emission in Heavy-Ion Collisions*. Acta Phys. Polon. **B42**, 2823 (2011)
- [RC06] J. RANDRUP AND J. CLEYMANS: *Maximum freeze-out baryon density in nuclear collisions*. Phys. Rev. **C74**, 047901 (2006)
- [RC16] J. RANDRUP AND J. CLEYMANS: *Exploring high-density baryonic matter: Maximum freeze-out density*. Eur. Phys. J. **52**, 218 (2016)

- [Rey05] K. REYGERS: *Direct-photon production from SPS to RHIC energies*. Eur. Phys. J. **C43**, 393 (2005)
- [RR07] P. ROMATSCHKE AND U. ROMATSCHKE: *Viscosity Information from Relativistic Nuclear Collisions: How Perfect is the Fluid Observed at RHIC?* Phys. Rev. Lett. **99**, 172301 (2007)
- [RvHH14] R. RAPP, H. VAN HEES AND M. HE: *Properties of Thermal Photons at RHIC and LHC*. Nucl. Phys. **A931**, 696 (2014)
- [RW94] C. D. ROBERTS AND A. G. WILLIAMS: *Dyson-Schwinger equations and their application to hadronic physics*. Prog. Part. Nucl. Phys. **33**, 477 (1994)
- [S⁺05] S. SCHAEEL ET AL.: *Branching ratios and spectral functions of tau decays: Final ALEPH measurements and physics implications*. Phys. Rept. **421**, 191 (2005)
- [SAR⁺98] S. SARKAR, J.-E. ALAM, P. ROY, A. K. DUTT-MAZUMDER, B. DUTTA-ROY AND B. SINHA: *Photons from hadronic matter at finite temperature*. Nucl. Phys. **A634**, 206 (1998)
- [Sas14] C. SASAKI: *Fate of charmed mesons near chiral symmetry restoration in hot matter*. Phys. Rev. **D90**, 114007 (2014)
- [Sch03] T. SCHÄFER: *Quark matter*. In ‘Mesons and quarks. Proceedings, Workshop, Mumbai, India, January 28-February 1, 2003’, 185–233. (2003)
- [SDF⁺01] O. SCAVENIUS, A. DUMITRU, E. S. FRAGA, J. T. LENAGHAN AND A. D. JACKSON: *First order chiral phase transition in high-energy collisions: Can nucleation prevent spinodal decomposition?* Phys. Rev. **D63**, 116003 (2001)
- [See11] E. SEEL: *Thermodynamics of the $O(4)$ linear and nonlinear models within the auxiliary field method*. Acta Phys. Polon. Supp. **4**, 733 (2011)
- [SFN⁺10] V. SKOKOV, B. FRIMAN, E. NAKANO, K. REDLICH AND B.-J. SCHAEFER: *Vacuum fluctuations and the thermodynamics of chiral models*. Phys. Rev. **D82**, 034029 (2010)
- [SFR11] V. SKOKOV, B. FRIMAN AND K. REDLICH: *Quark number fluctuations in the Polyakov loop-extended quark-meson model at finite baryon density*. Phys. Rev. **C83**, 054904 (2011)
- [SFR12] V. SKOKOV, B. FRIMAN AND K. REDLICH: *Non-perturbative dynamics and charge fluctuations in effective chiral models*. Phys. Lett. **B708**, 179 (2012)

- [She80] M. A. SHER: *Effects of Phase Transitions on the Evolution of the Early Universe*. Phys. Rev. **D22**, 2989 (1980)
- [SK09] R. SCHULZE AND B. KÄMPFER: *Cold quark stars from hot lattice QCD*. arXiv:0912.2827 [nucl-th] (2009)
- [SM12] C. SASAKI AND I. MISHUSTIN: *The Phase structure of a chiral model with dilatons in hot and dense matter*. Phys. Rev. **C85**, 025202 (2012)
- [SMMR01] O. SCAVENIUS, A. MOCSY, I. N. MISHUSTIN AND D. H. RISCHKE: *Chiral phase transition within effective models with constituent quarks*. Phys. Rev. **C64**, 045202 (2001)
- [Sol14] R. A. SOLTZ: *PHENIX beam energy scan results*. Nucl. Phys. **A931**, 780 (2014)
- [SPW07] B.-J. SCHAEFER, J. M. PAWLOWSKI AND J. WAMBACH: *The Phase Structure of the Polyakov–Quark–Meson Model*. Phys. Rev. **D76**, 074023 (2007)
- [SR15] C. SASAKI AND K. REDLICH: *Correlations between light and heavy flavors near the chiral crossover*. Phys. Rev. **D91**, 074021 (2015)
- [Sre07] M. SREDNICKI: *Quantum field theory*, Cambridge University Press, Cambridge (2007). ISBN 9780521864497
- [SRK14] J. STEINHEIMER, J. RANDRUP AND V. KOCH: *Non-equilibrium phase transition in relativistic nuclear collisions: Importance of the equation of state*. Phys. Rev. **C89**, 034901 (2014)
- [SRS99] M. A. STEPANOV, K. RAJAGOPAL AND E. V. SHURYAK: *Event-by-event fluctuations in heavy ion collisions and the QCD critical point*. Phys. Rev. **D60**, 114028 (1999)
- [SSB16] R. STIELE AND J. SCHAFFNER-BIELICH: *Phase diagram and nucleation in the Polyakov-loop-extended Quark-Meson truncation of QCD with the unquenched Polyakov-loop potential*. Phys. Rev. **D93**, 094014 (2016)
- [SSFR10] V. SKOKOV, B. STOKIC, B. FRIMAN AND K. REDLICH: *Meson fluctuations and thermodynamics of the Polyakov loop extended quark-meson model*. Phys. Rev. **C82**, 015206 (2010)
- [ST09] T. SCHÄFER AND D. TEANEY: *Nearly Perfect Fluidity: From Cold Atomic Gases to Hot Quark Gluon Plasmas*. Rept. Prog. Phys. **72**, 126001 (2009)
- [SW05] B.-J. SCHAEFER AND J. WAMBACH: *The Phase diagram of the quark meson model*. Nucl. Phys. **A757**, 479 (2005)

- [SW09] B.-J. SCHAEFER AND M. WAGNER: *The Three-flavor chiral phase structure in hot and dense QCD matter*. Phys. Rev. **D79**, 014018 (2009)
- [SW12] B. J. SCHAEFER AND M. WAGNER: *QCD critical region and higher moments for three flavor models*. Phys. Rev. **D85**, 034027 (2012)
- [SWW10] B.-J. SCHAEFER, M. WAGNER AND J. WAMBACH: *Thermodynamics of (2+1)-flavor QCD: Confronting Models with Lattice Studies*. Phys. Rev. **D81**, 074013 (2010)
- [Tiw12] V. K. TIWARI: *Exploring criticality in the QCD-like two quark flavour models*. Phys. Rev. **D86**, 094032 (2012)
- [TJGS17] D. THAKUR, S. JAKHAR, P. GARG AND R. SAHOO: *Estimation of Stopped Protons at Energies Relevant for a Beam Energy Scan at the BNL Relativistic Heavy-Ion Collider*. Phys. Rev. **C95**, 044903 (2017)
- [TRG04] S. TURBIDE, R. RAPP AND C. GALE: *Hadronic production of thermal photons*. Phys. Rev. **C69**, 014903 (2004)
- [Tse10] I. TSERRUYA: *Electromagnetic Probes*. Landolt-Börnstein **23**, 176 (2010)
- [TSvSW14] R.-A. TRIPOLT, N. STRODTHOFF, L. VON SMEKAL AND J. WAMBACH: *Spectral Functions for the Quark-Meson Model Phase Diagram from the Functional Renormalization Group*. Phys. Rev. **D89**, 034010 (2014)
- [VAGP15] V. VOVCHENKO, D. V. ANCHISHKIN, M. I. GORENSTEIN AND R. V. POBEREZHNYUK: *Scaled variance, skewness, and kurtosis near the critical point of nuclear matter*. Phys. Rev. **C92**, 054901 (2015)
- [VGS⁺16] V. VOVCHENKO, M. I. GORENSTEIN, L. M. SATAROV, I. N. MISHUSTIN, L. P. CSERNAI, I. KISEL AND H. STÖCKER: *Entropy production in chemically nonequilibrium quark-gluon plasma created in central Pb+Pb collisions at energies available at the CERN Large Hadron Collider*. Phys. Rev. **C93**, 014906 (2016)
- [vHGR11] H. VAN HEES, C. GALE AND R. RAPP: *Thermal Photons and Collective Flow at the Relativistic Heavy-Ion Collider*. Phys. Rev. **C84**, 054906 (2011)
- [vHHR15] H. VAN HEES, M. HE AND R. RAPP: *Pseudo-Critical Enhancement of Thermal Photons in Relativistic Heavy-Ion Collisions*. Nucl. Phys. **A933**, 256 (2015)
- [vHK02] H. VAN HEES AND J. KNOLL: *Renormalization in selfconsistent approxi-*

- mations schemes at finite temperature. 1. Theory.* Phys. Rev. **D65**, 025010 (2002)
- [VKG⁺16] V. VOVCHENKO, I. A. KARPENKO, M. I. GORENSTEIN, L. M. SATAROV, I. N. MISHUSTIN, B. KÄMPFER AND H. STÖCKER: *Electromagnetic probes of a pure-gluon initial state in nucleus-nucleus collisions at energies available at the CERN Large Hadron Collider.* Phys. Rev. **C94**, 024906 (2016)
- [VW91] U. VOGL AND W. WEISE: *The Nambu and Jona Lasinio model: Its implications for hadrons and nuclei.* Prog. Part. Nucl. Phys. **27**, 195 (1991)
- [Wei65] S. WEINBERG: *Infrared photons and gravitons.* Phys. Rev. **140**, B516 (1965)
- [Wei05a] S. WEINBERG: *The Quantum theory of fields. Vol. 1: Foundations,* Cambridge University Press, Cambridge (2005). ISBN 9780521670531
- [Wei05b] S. WEINBERG: *The quantum theory of fields. Vol. 2: Modern applications,* Cambridge University Press, Cambridge (2005). ISBN 9780521550024
- [Wel83] H. A. WELDON: *Simple Rules for Discontinuities in Finite Temperature Field Theory.* Phys. Rev. **D28**, 2007 (1983)
- [WK15a] F. WUNDERLICH AND B. KÄMPFER: *Photon emission rates near the critical point in the linear sigma model.* PoS **CPOD2014**, 027 (2015)
- [WK15b] F. WUNDERLICH AND B. KÄMPFER: *Photon emission within the linear sigma model.* J. Phys. Conf. Ser. **599**, 012019 (2015)
- [WK16] F. WUNDERLICH AND B. KÄMPFER: *Imprints of a critical point on photon emission.* Eur. Phys. J. **A52**, 262 (2016)
- [WK17] F. WUNDERLICH AND B. KÄMPFER: *Photon emissivity in the vicinity of a critical point - A case study within the quark meson model.* Nucl. Phys. **A959**, 27 (2017)
- [WYK16] F. WUNDERLICH, R. YARESKO AND B. KÄMPFER: *Arguing on entropic and enthalpic first-order phase transitions in strongly interacting matter.* J. Mod. Phys. **7**, 852 (2016)
- [YFS61] D. R. YENNIE, S. C. FRAUTSCHI AND H. SUURA: *The infrared divergence phenomena and high-energy processes.* Annals Phys. **13**, 379 (1961)
- [YMK10] R. YARESKO, M. G. MUSTAFA AND B. KÄMPFER: *Relativistic Expansion of Electron-Positron-Photon Plasma Droplets and Photon Emission.* Phys. Plasmas **17**, 103302 (2010)
- [Ynd02] F. J. YNDURÁIN: *Low-energy pion physics.* arXiv:0212282 [hep-ph] (2002)

- [Ynd06] F. J. YNDURÁIN: *The theory of quark and gluon interactions*, Springer, Berlin, Heidelberg (2006) 4th edn. ISBN 354033209X
- [ZJ02] J. ZINN-JUSTIN: *Quantum field theory and critical phenomena*. Int. Ser. Monogr. Phys. **113**, 1 (2002)

Erklärung

Hiermit versichere ich, dass ich die vorliegende Arbeit ohne unzulässige Hilfe Dritter und ohne Benutzung anderer als der angegebenen Hilfsmittel angefertigt habe. Die aus fremden Quellen direkt oder indirekt übernommenen Gedanken sind als solche kenntlich gemacht. Die Arbeit wurde bisher weder im Inland noch im Ausland in gleicher oder ähnlicher Form einer anderen Prüfungsbehörde vorgelegt.

Berlin, am 24.07.2017

Falk Wunderlich

Acknowledgement

I want to express my thanks to all people who helped me making this work becoming a success.

I gratefully thank Prof. Burkhard Kämpfer for continuously guiding me with patience, humor and good advice on my journey through the fascinating field of the physics of strongly interacting matter, always offering illuminating discussions and valuable ideas for my research as well as giving me the opportunity to present my work at various conferences.

I thank Prof. Roland Sauerbrey, Prof. Peter Joehnk, Prof. Thomas Cowan and Prof. Ulrich Schramm for the excellent working conditions at the Helmholtz-Zentrum Dresden-Rossendorf in general and, especially, at the Institute of Radiation Physics. Furthermore I thank Prof. Matthias Vojta for hosting our group in the rooms of the Institute of Theoretical Physics at the TU Dresden.

Many thanks are also for the past and present members of our group, especially Dr. Thomas Buchheim for numerous discussions and helpful advice in the past years. Furthermore, I also thank Andreas Otto and Rico Zöllner for their help with all major and minor problems, such as crazy L^AT_EX-output or programming advice as well as for proof-reading this thesis.

Also for proofreading, I want to thank Dr. Zita Hüsges, Marco Viebach, Dr. Stefan Lange, Dr. Ulrike Schnoor and Silke Bosch.

Finally, special thanks are for my wife Sarah and my daughter Laura, for their loving support in all situations, for patience and many happy hours together.